Quantitative photogrammetrische Analyse von Sturzprozessen in den Alpen und auf La Réunion

Dissertation

zur Erlangung des Doktorgrades Dr. rer. nat.

an der

Mathematisch-Geographischen Fakultät

der

Katholischen Universität Eichstätt-Ingolstadt

vorgelegt von

Kerstin Wegner

aus Nürnberg

Eichstätt, 2026

Datum der mündlichen Prüfung: 04.02.2026

Referent: Prof. Dr. Michael Becht

Koreferent: Apl. Prof. Dr. Florian Haas

Für meine Eltern.

Zusammenfassung

Sturzprozesse stellen einen wesentlichen geomorphologischen Prozess dar und nehmen insbesondere in Hochgebirgsregionen eine bedeutsame Rolle in der Prozessmorphologie ein. Sie beeinflussen die langfristige Relief- und Landschaftsentwicklung sowie den Sedimenttransport und die Sedimentproduktion.

In mehreren wissenschaftlichen Studien wird von einer zunehmenden Häufigkeit von Sturzprozessen berichtet. Als Hauptursache für diese Entwicklung wird die fortschreitende Klimaveränderung diskutiert.

Obwohl Sturzprozesse überwiegend in hochalpinen und abgelegenen Regionen auftreten, stellen sie aufgrund der zunehmenden Besiedlung und anthropogenen Nutzung des Alpenraums ein ernst zu nehmendes Naturgefahrenpotential für Mensch und Infrastruktur dar. Die Stabilität von Felswänden stellt ein komplexes Phänomen dar, das sich durch eine hohe Variabilität in Bezug auf Frequenz und Magnitude auszeichnet.

In der vorliegenden Dissertation wurden Felswände und Schutthalden in verschiedenen hochalpinen und geomorphologisch aktiven Untersuchungsgebieten, darunter die Drei Zinnen (Italien), Gampenalm (Italien), Dreitorspitze (Deutschland), Zwieselbachtal (Österreich) sowie der Krater Dolomieu auf La Réunion, mit Hilfe multitemporaler terrestrischer Fotografien, terrestrischer historischer Fotoaufnahmen, terrestrischen Laserscannings sowie automatisierter Kamerasysteme mit photogrammetrischen Verfahren analysiert.

Ziel dieser Dissertation ist es, zu prüfen, inwiefern historische Bilddaten in Kombination mit terrestrischen digitalen Fotografien und TLS zur Rekonstruktion vergangener Veränderungen der Felsoberfläche beitragen können. Dazu wurde die bekannte Felsformation Drei Zinnen in den Dolomiten (Italien) ausgewählt. Die Ergebnisse zeigen, dass nach aufwendiger und individueller Bearbeitung der Datensätze eine Quantifizierung der Oberflächenveränderungen an steilen Felswänden möglich ist. Volumenänderungen von 101 m^3 und 1.873 m^3 konnten für zwei Bereiche an den Felswänden für einen Zeitraum von 1970 bis 2018 bestimmt werden. Aussagen zum Einfluss des Klimawandels bleiben jedoch aufgrund der begrenzten Datenverfügbarkeit und Auflösung spekulativ.

Zur Untersuchung der Sturz- und Prozessdynamik unter aktuellen Prozessbedingungen, insbesondere zur Vermeidung von Überlagerungen von unterschiedlich auftretenden Prozessen wie Muren oder Rutschungen, wurden am Dolomieu Krater Fotoaufnahmen eines fest installierten, automatisierten Kamerasystems (Webcam) zur kontinuierlichen Datenerfassung genutzt. Durch hochfrequente Daten soll eine Differenzierung der stattfindenden Einzelprozesse ermöglicht werden. Anhand der TLS-Daten sowie ergänzender terrestrischer digitaler Fotoaufnahmen konnten neben sturzprozessbedingten Bereichen zwei weitere Areale mit Gesteinsablagerungen identifiziert werden. Für den Zeitraum von 2010 bis 2016 ließen sich dabei erfolgreich Oberflächenveränderungen berechnen. Die durch Sturzprozesse geprägten Bereiche zeigen Volumenänderungen von 18.606 m^3 bzw. 2.921 m^3. In den beiden weiteren, durch Ablagerungen gekennzeichneten Gebieten wurden Veränderungen von 2.995 m^3 und

20.430 m^3 festgestellt. Für zukünftige Untersuchungen dieser Art wird jedoch empfohlen, das Kamerasystem so zu positionieren und auszurichten, dass es den Anforderungen der Photogrammetrie entspricht.

Eine weitere Untersuchung am Dolomieu-Krater auf La Réunion widmet sich dem Einfluss von Niederschlag und Seismizität auf Hanginstabilitäten. Ziel ist unter anderem die Bewertung der Eignung von TLS und Photogrammetrie zur Validierung von Volumenangaben, die auf seismischen Aufzeichnungen basieren. Im ersten Schritt wurde auf Grundlage seismischer Daten ein Katalog mit Informationen der Lage und den Volumina der Felsstürze im Krater erstellt. Ergänzend dazu erfolgten TLS-Messungen sowie digitale terrestrische Fotoaufnahmen entlang des Kraterrandes. Mithilfe photogrammetrischer Auswertungen konnte das Volumen der größten Ablagerung im nordwestlichen Kraterbereich ermittelt werden, das sich auf rund 80.000 m^3 beläuft. Die seismischen Daten führten zu einer Volumenschätzung von etwa 100.000 m^3.

Neben der Quantifizierung von Oberflächenveränderungen und der entsprechenden Nutzung von TLS-Daten wird im Rahmen der Dissertation außerdem die Frage beantwortet, ob sich aus solchen hochaufgelösten topographischen Daten Prozesszusammenhänge von Sturzprozessen ableiten lassen. Untersucht wurden die Einflüsse von Blockgröße, -form, Lithologie und Rauigkeit auf die Reichweite von Sturzprozessen in mehreren Gebieten des Alpenraums (Gampenalm, Dreitorspitze, Zwieselbachtal) und am Krater Dolomieu unter unterschiedlichen geologischen Bedingungen. Die Analysen zeigen eine komplexe Beziehung zwischen Blockgröße und Blockform in Bezug auf die Reichweite der abgelagerten Blöcke innerhalb der unterschiedlichen lithologischen Bedingungen. Aus den Ergebnissen kann jedoch weder eine Bestätigung noch eine Ablehnung der Theorie der gravitativen Sortierung abgeleitet werden. Zwischen Blockgröße und -form sowie Reichweite konnte kein eindeutiger Zusammenhang festgestellt werden. Die Ergebnisse deuten darauf hin, dass die Blockgröße nicht die alleinige Einflussgröße ist und vielmehr ein komplexes Zusammenspiel mehrerer geomorphologischer Faktoren die Reichweite bestimmt.

Abstract

Rockfall processes constitute a key geomorphological mechanism and, in particular, play a major role in the morphodynamics of high mountain regions. They influence long-term relief and landscape evolution as well as sediment production and sediment transport.

Several scientific studies report an increase in the frequency of rockfalls. Progressive climate change is discussed as the principal driver of this development.

Although rockfalls occur predominantly in high-alpine and remote areas, they pose a serious natural hazard potential to people and infrastructure due to the ongoing expansion of settlement and anthropogenic land use in the Alpine region. The stability of rock faces is a complex phenomenon characterized by pronounced variability in event frequency and magnitude.

In this dissertation, rock faces and talus slopes were investigated in several high-alpine, geomorphologically active study areas, including the Tre Cime di Lavaredo (Italy), Gampenalm (Italy), Dreitorspitze (Germany), Zwieselbachtal (Austria) and the Dolomieu Crater on La Réunion, using multitemporal terrestrial photographs, historical terrestrial photo archives, terrestrial laser scanning (TLS) and automated camera systems processed with photogrammetric methods.

The aim of the dissertation is to examine to what extent historical imagery, in combination with terrestrial digital photography and TLS, can be used to reconstruct past changes in rock-surface morphology. For this purpose, the well-known rock formation of the Tre Cime di Lavaredo in the Dolomites (Italy) was selected. The results show that, following meticulous and dataset-specific processing, the quantification of surface changes on steep rock faces is feasible. For two areas of the cliffs, volume changes of 101 m^3 and 1,873 m^3 were determined for the period 1970 to 2018. However, statements regarding the influence of climate change remain speculative owing to limited data availability and resolution.

To analyse rockfall and process dynamics under current conditions, particularly to avoid overlap with other processes such as debris flows or landslides, continuous data acquisition from a fixed, automated camera system (webcam) was employed at the Dolomieu Crater. The use of high-frequency data is intended to enable a differentiation of individual active processes. Based on TLS data and complementary terrestrial digital photographs, two additional areas of rock deposition were identified alongside rockfall-dominated sectors. For the period 2010–2016, surface changes were successfully computed. The rockfall-dominated areas exhibit volume changes of 18,606 m^3 and 2,921 m^3. In the two further areas characterised by accumulations, changes of 2,995 m^3 and 20,430 m^3 were observed. For future studies of this kind, it is recommended that the camera system be positioned and aligned to meet photogrammetric requirements.

A further investigation at the Dolomieu Crater (La Réunion) addresses the influence of precipitation and seismicity on slope instabilities. One objective is to address the suitability of TLS and photogrammetry for validating volume estimates derived from seismic records. In a first step, a catalogue of rockfalls, including location and volume, was compiled from seismic data. TLS surveys and terrestrial dig-

ital photography along the crater rim were then carried out. Photogrammetric analysis yielded an estimate of approximately 80,000 m^3 for the largest deposit in the north-western crater area, while the seismic data suggested a volume of around 100,000 m^3.

Beyond the quantification of surface changes and the use of TLS data, the dissertation also investigates whether high-resolution topographic datasets permit inference of process relationships for rockfalls. Specifically, the effects of block size, block shape, lithology, and surface roughness on runout distance were examined across several Alpine sites (Gampenalm, Dreitorspitze, Zwieselbachtal) and at the Dolomieu Crater, under contrasting geological conditions. The analyses reveal a complex relationship between block size and block shape with respect to the runout of deposited blocks within different lithological settings. The results neither confirm nor refute the theory of gravitational sorting. No unequivocal relationship between block size and shape on the one hand and runout on the other was identified. Instead, the findings indicate that block size is not the sole controlling facter; rather, a multifactorial interplay of geomorphological conditions governs runout distances.

Danksagung

Die vorliegende Dissertation wäre ohne die Unterstützung vieler Menschen nicht möglich gewesen, denen ich an dieser Stelle meinen Dank aussprechen möchte.

Mein besonderer Dank gilt meinem Doktorvater, Prof. Dr. Michael Becht, für seine kontinuierliche Unterstützung, sowohl persönlich als auch fachlich, seinen fachlichen und konstruktiven Austausch sowie die wertvollen Hinweise während der gesamten Promotionszeit. Darüber hinaus danke ich ihm für seine strategische Begleitung, die Ermöglichung von Geländeaufenthalten, für die Förderung von Tagungsbesuchen und Publikationen.

Ebenso danke ich meinem Zweitgutachter, apl. Prof. Dr. Florian Haas. Ohne ihn wäre die konzeptionelle Ausarbeitung dieser Dissertation nicht möglich gewesen. Ich bedanke mich nicht nur für die Betreuung während der Promotionszeit, sondern auch für die Vielzahl an hilfreichen Kommentaren und konstruktiver Kritik, die die Qualität dieser Arbeit maßgeblich verbessert haben. Aber selbstverständlich auch für die persönliche Unterstützung. Daneben war aber auch immer der Austausch in der Mensa, Cafeteria oder auf dem Flur für mich von großer Bedeutung. Nicht zu vergessen die vielen gemeinsamen Geländeaufenthalte, vor allem der auf La Réunion.

Ein ebenfalls großes Dankeschön geht an Prof. Dr. Tobias Heckmann. Der wichtige und maßgebliche Input zu allen GIS-bezogenen und statistischen Themen waren für die Beantwortung einiger Fragestellungen von großer Bedeutung. Dazu gehören aber auch die vielen bereichernden fachlichen Diskussionen außerhalb des Büros.

Meinen Kolleginnen und Kollegen Dr. Sarah Betz-Nutz, Georgia Kahlenberg, Dr. Manuel Stark, Dr. Moritz Altmann, Dr. Fabian Fleischer, Dr. Jakob Rom und Dr. Peter Fischer möchte ich ganz herzlich für die schöne Zeit, die sehr gute kollegiale Zusammenarbeit und den ständigen Austausch einen großen Dank aussprechen. Ob dies im Büro oder im Gelände war, die Diskussionen und Unterstützung waren stets mehr als bereichernd.

Außerdem gilt ein weiterer großer Dank Prof. Dr. Anne Mangeney. Ohne die finanzielle Unterstützung durch das ERC Projekt „*Slidequakes*“ wären die Geländeaufenthalte auf La Réunion nicht realisierbar gewesen. Ich bedanke mich auch für die vielzähligen fachlichen Gespräche zu Beginn der Promotion. Bei Dr. Virginie Durand bedanke ich mich ebenfalls herzlich für die Unterstützung während der gemeinsamen Geländearbeiten, sowohl in den Dolomiten als auch auf La Réunion. Nicht nur während der Arbeit war es eine schöne kollegiale Zeit, sondern auch bei Freizeitaktivitäten auf La Réunion. Dem gesamten Team des vulkanologischen Observatoriums, unter anderem Dr. Aline Peltier, Dr. Nicolas Villeneuve und Dr. Philippe Kowalski danke ich für die sehr gute kollegiale Zusammenarbeit während der Datenaufnahme und Unterstützung vor Ort zu allen fachlichen und administrativen Fragestellungen sowie für die schöne Zeit auf La Réunion.

Nicht zuletzt möchte ich meiner Familie und meinen Freunden danken.

Meinen Mädels (Franzi, Sani, Katrin, Marísa (+Bernhard), Kathrin, Farina, Charlotte, Tani) danke ich von ganzem Herzen für die anhaltende Unterstützung während dieser gesamten Zeit der Promotion. Ihr habt mir in allen Phasen mit Eurem Verständnis, Eurer Geduld und aufmunternden Worten immer wieder die Kraft gegeben weiterzumachen.

Außerdem danke ich meinen Rennradlers für ihre Unterstützung, wenn ich wieder mentale Kraft während gemeinsamer Ausfahrten getankt habe.

Besonderer Dank gilt meinem Partner Olaf für seine bedingungslose Unterstützung während der Promotionszeit. Du warst zu jeder Zeit, vor allem bei Schwierigkeiten und diversen herausfordernden Phasen stets an meiner Seite und ich konnte mich auf Dich verlassen. Dies bedeutet mir unendlich viel.

Nicht in Worte zu fassen ist der Dank an meine Eltern, Petra und Wolfgang Wegner, die mir zum einen eine lange Ausbildung ermöglicht haben und mich zum anderen bei allen Vorhaben und Themen immer unterstützt haben. Vor allem bei Schwierigkeiten wart ihr mit Rat und Tat an meiner Seite. Dafür bin ich Euch mehr als dankbar.

Inhaltsverzeichnis

Abbildungsverzeichnis

Tabellenverzeichnis

Abkürzungsverzeichnis

ALS	Airborne Laserscanning
AOI	Area Of Interest
DGM	Digitales Geländemodell
DoD	Digital Elevation Model of Difference (auch Differenzhöhenmodell)
DTM	Digital Terrain Model
ERC	European Research Council
GCP	Ground Control Point
dGPS	differential Global Positioning System
GNSS	Global Navigation Satellite System
ICP	Iterative Closest Point (Algorithmus)
IPCC	Intergovernmental Panel on Climate Change
LiDAR	Light Detection and Ranging
LoD	Level of Detection
m. ü.d.M.	Meter über dem Meeresspiegel (ellipsoidische Höhe)
MVS	Multi-View Stereo
<q10, q10-q25, ..., >q90	Bezeichnet das jeweilige x-% Quantil
SfM	Structure from Motion
TLS	Terrestrial Laserscanning
UAS	Unmanned Aerial System (unbemanntes Luftfahrzeug; Drohne)

Liste der in der Arbeit enthaltenen Publikationen und Erklärungen zur Autorschaft

Die folgenden Publikationen sind in Zusammenarbeit mit Kolleginnen und Kollegen des Lehrstuhls für Physische Geographie an der Katholischen Universität Eichstätt-Ingolstadt sowie im Rahmen von Kooperationen mit internationalen Forschungsinstituten erarbeitet worden. Alle enthaltenen Beiträge waren Bestandteil eines Peer-Review Verfahrens und sind Gegenstand von Veröffentlichungen in Fachzeitschriften.

Alle von mir verfassten Beiträge, deren Erstautorin ich bin, wurden im Rahmen meiner Dissertation am Lehrstuhl für Physische Geographie der Katholischen Universität Eichstätt-Ingolstadt erarbeitet. Diese wissenschaftlichen Arbeiten habe ich als Wissenschaftlerin selbst durchgeführt. Dabei war ich von der Datenaufnahme über die Aufbereitung, Auswertung und Analyse bis zur Veröffentlichung hauptverantwortlich.

Einer der nachfolgend aufgeführten Artikel, bei denen ich die Ko-Autorenschaft innehabe, entstand in Kooperation mit Prof. Dr. Anne Mangeney (Université Paris Cité, Institut de physique du globe de Paris (IPGP) – Institut für Geophysik Paris), Dr. Virginie Durand (Université Côte d'Azur, Université Paris Cité) sowie Dr. Nicolas Villeneuve (Université de la Réunion) und der gesamten Arbeitsgruppe des vulkanologischen Observatoriums auf der Insel La Réunion. Hier war ich sowohl bei der Datenaufnahme als auch -auswertung beteiligt.

Nachfolgend werden alle Publikationen sowie mein Anteil daran im Detail dargestellt.

Publikation I

Kerstin Wegner, Manuel Stark, Florian Haas, Michael Becht (2023): Suitability of terrestrial archival imagery for SfM-MVS based surface reconstruction of steep rock walls for the detection of rockfalls. In: *Journal of Geomorphology*, 7–39, doi: 10.1127/jgeomorphology/2023/0775.

Die Publikation ist im *Journal of Geomorphology* erschienen. Sie beschäftigt sich mit der Oberflächenrekonstruktion sowie der Quantifizierung von Sturzprozessen mittels SfM-MVS von steilen Felswänden der Drei Zinnen in den Dolomiten (Südtirol, Italien). Die Auswahl des Untersuchungsgebietes wurde in gemeinsamer Abstimmung mit Apl. Prof. Dr. Florian Haas getroffen. Die Analysen und Auswertungen basieren sowohl auf historischen terrestrischen Fotos (1970) als auch auf einem LiDAR Datensatz (TLS, 2018) sowie terrestrischen digitalen Fotografien (2018). Die historischen terrestrischen Fotos wurden von mir in einer zeitlich aufwendigen Recherche in diversen Archiven und privat geführten Fotohäusern ausgewählt. Der TLS-Datensatz wurde von mir mit Unterstützung meines Kollegen Dr. Manuel Stark und einer studentischen Hilfskraft aufgenommen. Um basierend auf den Daten Volumina quantifizieren zu können, wurden zunächst individuelle Arbeitsschritte zur Datenprozessierung entwickelt. Dies passierte in Absprache mit meinem Kollegen Dr. Manuel Stark. Die anschließende Analyse

und Interpretation oblagen mir. Ich war verantwortlich für die Erstellung des Manuskripts sowie für die Gestaltung aller Abbildungen mit abschließender Überarbeitung durch die Ko-Autorenschaft.

Publikation II

Kerstin Wegner, Florian Haas, Tobias Heckmann, Anne Mangeney, Virginie Durand, Nicolas Villeneuve, Philippe Kowalski, Aline Peltier, Michael Becht (2021): Assessing the effect of lithological setting, block characteristics and slope topography on the runout length of rockfalls in the Alps and on the island of La Réunion. In: *Natural Hazards and Earth System Sciences*, 21, 1159–1177, doi: 10.5194/nhess-21-1159-2021.

Die Studie ist in der Zeitschrift *Natural Hazards and Earth System Sciences* der EGU – European Geosciences Union GmbH erschienen. Sie untersucht die Reichweite einzelner Felsblöcke von Sturzprozessen in diversen Untersuchungsgebieten mit unterschiedlichen lithologischen Bedingungen. Für die Untersuchung wurden reichweitenbeeinflussende Faktoren wie die Lithologie, die Blockgröße und -form aber auch geomorphometrische Parameter wie die Rauigkeit und die Hangneigung analysiert. Dafür wurden hochaufgelöste LiDAR Datensätze (TLS) der Schutthalden verwendet. Für die vergleichende Studie wurden drei unterschiedliche Untersuchungsflächen in den Europäischen Alpen und eine auf La Réunion (Krater Dolomieu des Vulkans Piton de la Fournaise) selektiert. Die Auswahl dieser Gebiete erfolgte in Abstimmung mit Apl. Prof. Dr. Florian Haas. Die TLS-Datensätze der Flächen in den Alpen waren bereits vorhanden und wurden von Apl. Prof. Dr. Florian Haas in anderen Projekten aufgenommen. Die Daten (TLS, dGPS) auf La Réunion habe ich sowohl mit Apl. Prof. Dr. Florian Haas als auch den Kollegen des vulkanischen Observatoriums auf La Réunion (Dr. Virginie Durand, Dr. Nicolas Villeneuve, Dr. Philippe Kowalski) selbst generiert. Die Daten wurden von mir ausgewertet und analysiert. Die Darstellung und Interpretation der Ergebnisse erfolgten in meiner Verantwortung. Das Manuskript und die Abbildungen wurden von mir angefertigt. Die finale Überarbeitung erfolgte jedoch in Zusammenarbeit mit der gesamten Ko-Autorenschaft.

Publikation III

Kerstin Wegner, Virginie Durand, Nicolas Villeneuve, Anne Mangeney, Philippe Kowalski, Aline Peltier, Antoine Protin, Manuel Stark, Michael Becht, Florian Haas (2024): Multitemporal Quantification of the Geomorphodynamics on a Slope within the Cratère Dolomieu at the Piton de la Fournaise (La Réunion, Indian Ocean) Using Terrestrial LiDAR Data, Terrestrial Photographs, and Webcam Data. In: *Geosciences,* 14, 1–22, doi: 10.3390/geosciences14100259.

Diese Veröffentlichung ist im Journal *Geosciences* in Kooperation mit Prof. Dr. Anne Mangeney im Rahmen des ERC („*European Research Council*“) Projekts „*Slidequakes*“ und der Arbeitsgruppe des vulkanologischen Observatoriums auf La Réunion erschienen. Sie beschäftigt sich mit der multitemporalen Analyse und Quantifizierung von Sturzprozessen in dem seismisch hochaktiven Gebiet des Kraters Dolomieu im aktiven Vulkan Piton de la Fournaise auf La Réunion. Für die Auswertung wurden neben

TLS, terrestrische photogrammetrische Fotografien sowie Webcam-basierte Fotos verwendet. Während mehrerer Feldkampagnen in den Jahren 2014 (TLS, terrestrische digitale Fotos), 2015 (terrestrische digitale Fotos) und 2016 (terrestrische digitale Fotos) wurden die Datensätze von mir und Apl. Prof. Dr. Florian Haas aufgenommen. Die anschließende Aufbereitung der benötigten Datensätze und die Durchführung der Analysen erfolgten ebenfalls von mir. Dies gilt auch für die Darstellung und Interpretation der Ergebnisse. Die Erstellung des Manuskripts sowie die Gestaltung der Abbildungen wurden von mir durchgeführt, wobei eine abschließende Überarbeitung des Manuskripts ebenfalls durch die gesamte Ko-Autorenschaft vorgenommen wurde.

Publikation IV

Virginie Durand, Anne Mangeney, Florian Haas, Xiaoping Jia, Fabian Bonilla, Aline Peltier, Clément Hibert, Valérie Ferrazzini, Philippe Kowalski, Frédéric Lauret, Christophe Brunet, Claudio Satriano, **Kerstin Wegner**, Arthur Delorme, Nicolas Villeneuve (2018): On the Link Between External Forcings and Slope Instabilities in the Piton de la Fournaise Summit Crater, Reunion Island. In: *Journal of Geophysical Research: Earth Surface*, 123, 2422–2442, doi: 10.1029/2017JF004507.

Die Publikation ist im *Journal of Geophysical Research: Earth Surface* ebenfalls im Rahmen des ERC-Projekts „*Slidequakes*“ in Kooperation mit Prof. Dr. Anne Mangeney veröffentlicht. Darin wurden die Auswirkungen verschiedener Einflüsse wie Regen und Seismizität auf die Instabilität von Hängen des Kraters des aktiven Vulkans Piton de la Fournaise auf La Réunion untersucht. Dazu wurde ein Katalog mit seismischen Aufzeichnungen für einen Zeitraum von 2014–2016 mit Informationen über die Standorte und Volumina von Sturzprozessen im Krater des Vulkans Piton de la Fournaise erstellt. Die Validierung dieser Daten erfolgte durch die Auswertung von TLS-Messungen sowie die photogrammetrische Analyse von Bildern einer Digitalkamera. Während zweier Feldkampagnen im Jahr 2014 (TLS) und 2016 (digitale terrestrische Fotografien) wurden die Datensätze von mir und Apl. Prof. Dr. Florian Haas aufgenommen. Ebenfalls erfolgte von mir die anschließende Aufbereitung der notwendigen Datensätze, um sie Dr. Virginie Durand für ihre weiteren Analysen zur Verfügung zu stellen. Die entsprechenden Kapitel wurden von mir erstellt. Außerdem war ich an der Überarbeitung des Manuskripts beteiligt.

1 Einleitung

> "*A geomorphic system is a structure of interacting processes and landforms that function individually and jointly to form a landscape complex.*"
>
> (Chorley, et al., 1984, p. 5)

Die Formulierung von Chorley et al. (1984) macht deutlich, dass in der geomorphologischen Prozessforschung einzelne landschaftsformende Prozesse nicht für sich alleinstehend betrachtet werden können und diese nicht isoliert auftreten, sondern dabei immer Interaktionen mit anderen stattfinden Prozessen involviert sind. Da Landformen komplexe und prozessuale vielschichtige Systeme darstellen, ist es notwendig, diese zu strukturieren und zu differenzieren. Dies kann mit Hilfe des Modells eines Kaskadensystems umgesetzt werden.

Es kann damit beschrieben werden, dass Sedimente, die Teil eines Gesamtsystems sind, in ein Subsystem, einer Landform, weitertransportiert werden (Heckmann & Schwanghart, 2013; Messenzehl, et al., 2014). Die auftretenden Prozesse haben einen Weitertransport des Materials in das nächste Subsystem oder zunächst eine Ablagerung in vorhandene Zwischenspeicher zur Folge. Die gängige Prozesskette im Hochgebirge nimmt ihren Ausgangspunkt an einer Felswand, an der Gesteinsblöcke durch beispielsweise Frostsprengung, resultierend in Steinschlag, abgetragen werden. Das so transportierte Material lagert sich anschließend entweder innerhalb eines Hanges oder auf einer Sturzhalde ab. Der Sedimenttransfer ist abhängig von der Kopplung innerhalb eines Subsystems und der Subsysteme untereinander sowie von Prozessfrequenzen und -magnituden (Harvey, 2001; Messenzehl, et al., 2014).

Bereits Chorley et al. (1984) sprechen bei steilen Felshängen von komplexen Systemen, die selbst ein Subsystem in einem geomorphologischen *„Process-Response-System*" sind. In einem solchen System stehen die Form- und Prozessvariablen jedoch auch in einer Wechselwirkung, die durch negative Rückkopplungen gekennzeichnet ist (Dikau, et al., 2019). Dies hat zur Folge, dass die mit der Zeit räumlich anwachsende Schutthalde zu einer Verkleinerung der freien Felswand und damit zu einer Verringerung der potenziellen Verfügbarkeit von Festgestein führt (Dikau, et al., 2019). Ein solches System hängt entscheidend vom eingetragenen, umgesetzten und ausgetragenen Material und dessen Energie ab. Auf diese Weise kann jede Veränderung des eingetragenen Materials zu einer Veränderung im Austrag führen und dementsprechend auch im übergeordneten geomorphologischen System wirksam sein (Chorley, et al., 1984).

Die Formung der Landschaft durch geomorphologische Prozesse, die in dieser Dissertation anhand von Sturzprozessen[1] thematisiert wird, ist vor allem in Hochgebirgsregionen von Bedeutung. In diesen Gebieten findet eine Vielzahl individueller formgebender Prozesse statt, wie z.B. gravitative Prozesse und fluviale Transporte, die miteinander interagieren (Hungr & Evans, 1988; Krautblatter & Dikau, 2007; Bennett, et al., 2012; Frattini, et al., 2012).

Um diese formgebenden Prozesse in ihrer Gesamtheit erfassen und rekonstruieren sowie für valide Untersuchungen und Analysen zur Prozessaktivität von Sturzereignissen nutzbar machen zu können, ist eine hochauflösende Datengrundlage unabdingbar. Insbesondere die Rekonstruktion von Gelände- und Felsoberflächen erfordert eine hohe räumliche Auflösung. Die zeitliche Auflösung spielt ebenfalls eine entscheidende Rolle, denn nur so können Prozessdynamiken und -interaktionen erfasst werden. Des Weiteren sind eine Quantifizierung und Bilanzierung abgelagerten Materials erforderlich.

Um aktuell stattfindende Prozesse zu quantifizieren, eignen sich dafür vor allem hochauflösende Fernerkundungsmethoden. Dazu gehören das geodätische Messverfahren des terrestrischen (TLS: „*terrestrial laserscanning*“) und luftgestützten (ALS: „*airborne laserscanning*“) Laserscannings (LiDAR: „*light detection and ranging*“), aber auch die Verwendung von aufgenommenen digitalen Fotos.

Die Kombination digitalisierter (ehemals analoger) Fotografien mit „*Structure from Motion*“ (SfM)-mit „*Multi View Stereo*“ (MVS) Algorithmen erlaubt die Erweiterung der Untersuchungszeiträume in die Vergangenheit und somit die Möglichkeit der Quantifizierung historischer Prozesse.

Im folgenden Kapitel 2 wird der aktuelle Forschungsstand zu Sturzprozessen erläutert. Darauf aufbauend werden im anschließenden Kapitel 3 die Fragestellungen und Ziele dieser Dissertation formuliert, welche in den zugrunde liegenden Publikationen behandelt und beantwortet werden. Anschließend in Kapitel 4 erfolgt eine Beschreibung der Erfassungsmethoden des terrestrischen Laserscannings sowie der digitalen Photogrammetrie. Daran schließt sich Kapitel 6 an, in dem die einzelnen Publikationen kurzzusammengefasst sind, gefolgt von Kapitel 7 mit den Artikel selbst. Danach folgen eine Zusammenfassung und Diskussion der wichtigsten Forschungsergebnisse (Kapitel 8). Abgeschlossen wird die Arbeit durch ein Fazit und einen Ausblick in Kapitel 9 (Abbildung 1).

[1] In der vorliegenden Dissertation wird der Begriff „*Sturzprozess(e)*“ synonym für die unterschiedlichen Bezeichnungen in Bezug auf die Volumenklassifizierung verwendet.
Die folgende Tabelle gibt einen Überblick über die differenzierte Nomenklatur der Sturzprozesse mit jeweiligen Volumenangabe (Whalley, 1974). Im Englischen wird dabei von „rockfalls“ gesprochen.
Evans & Hungr (1993) führten zusätzlich den Begirff des „*fragmental rockfall*“ ein. Er beschreibt, dass sich einzelne Fragmente als unabhängige starre Körper bewegen, die durch episodische Stöße mit dem Untergrund interagieren (Evans & Hungr, 1993; Bourrier, et al., 2013).

Bezeichnung	**Volumen [m^3]**
Steinschlag	< 10
Blockschlag	10-100
Felssturz	100-10^5
Bergsturz	> 10^6

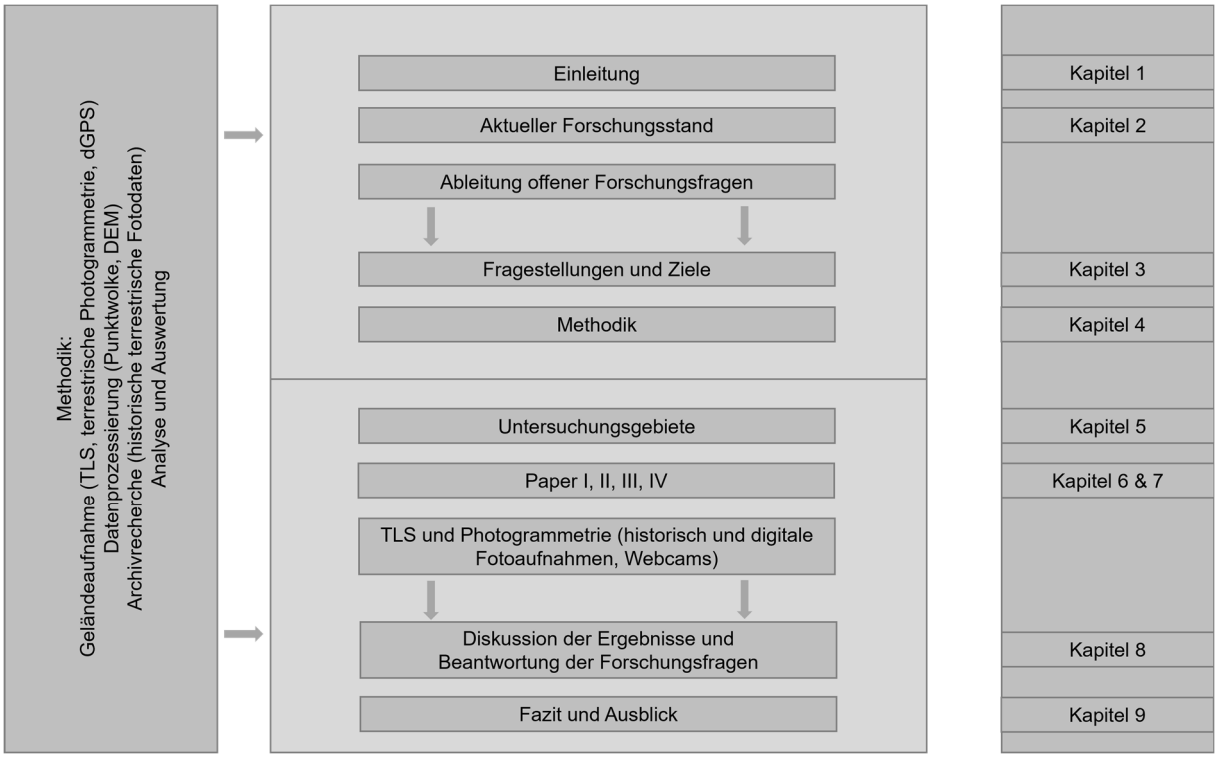

Abbildung 1. Konzeptioneller Aufbau der Arbeit.

2 Stand der Forschung

> "*Rockfalls are probably the most frequently observed mass movement in mountain areas and yet few data are available on the frequency, size and controls of rockfall activity.*"
>
> (Luckman, 1976, p. 287)

2.1 Sturzprozesse

Die Instabilität von Felswänden ist ein komplexes Phänomen, das weltweit unter unterschiedlichen geologischen, topographischen und klimatischen Bedingungen auftritt. Felswände können praktisch überall dort instabil werden und versagen, wo das lokale Relief ausreicht, um Schwerkraftspannungen zu erzeugen (Terzaghi, 1962; Brunsden & Prior, 1984; Dikau, et al., 1996; Wyllie & Mah, 2004).

Sturzprozesse lassen sich definieren als die Bewegung von verwittertem und losem Gestein im freien Fall an einem steilen Hang unter dem Einfluss der Gravitation (Cruden & Varnes 1996; Luckman, 2013). Sobald die inneren und äußeren Spannungen die Widerstandsfähigkeit der Gesteinsmasse übersteigen, werden die Felswände instabil, und das zerfallende Material kann sich lösen.

Ein gängiger morphometrischer Ansatz zur Beurteilung der Hangstabilität basiert auf der Festlegung kritischer Neigungswinkel, oberhalb derer insbesondere Felswände als instabil eingestuft werden können. Hierfür werden unterschiedliche Schwellenwerte angegeben, darunter > 60° (Guzzetti, et al., 2003), > 45° (Jaboyedoff & Labiouse, 2003) sowie > 37° (Frattini, et al., 2008).

Nach Rapp (1960) können Sturzprozesse in zwei grundlegende Arten differenziert werden. Bei *„primary rockfalls"* kommt es aufgrund der Instabilität der Felswand dazu, dass das Gestein unmittelbar herausbricht und hangabwärts transportiert wird. *„Secondary rockfalls"* sind jene, bei denen abgelöstes und im Hang in Zwischenspeichern temporär abgelagertes Material erneut mobilisiert und weiter hangabwärts bewegt wird (Rapp, 1960; Becht, 1995; Krautblatter & Dikau, 2007).

Die Größe des abgelösten Materials kann bei Sturzprozessen variieren. Sie kann einzelne Gesteinsblöcke, mehrere Blöcke oder fragmentierte Gesteinsmassen umfassen, die sich zunächst im freien Fall befinden und erst während der Flugbahn in einen anderen Bewegungsmechanismus wie den des Aufprallens, Rollens oder Gleitens wechseln (Flageollet & Weber, 1996; Luckman, 2013; Crosta, et al., 2015). Diese drei Hauptbewegungsarten wurden zum ersten Mal von Ritchie (1963) in experimentellen Versuchen festgestellt. In Abhängigkeit von der Hangneigung kommt es zu unterschiedlichen Bewegungsmechanismen. Das Gesteinsmaterial befindet sich im freien Fall an steilen, überhängenden

Felsabschnitten sowie bei Hangneigungen von 70° bis 90° (Dorren, 2003). Bei weniger als 70° Neigung dominieren Sprungbewegungen, während hingegen unterhalb von 45° Neigung die Gesteinsblöcke meistens Rollen (Dorren, 2003).

Im Gegensatz zu anderen gravitativen Massenbewegungen treten Sturzprozesse plötzlich auf und sind durch ein hohes Maß an Bewegungsenergie gekennzeichnet (Corominas, et al., 2017). Nach Experimenten von Broili (1974) gehen etwa 75–86 % der beim initialen Fall gewonnenen kinetischen Energie beim ersten Oberflächenkontakt verloren (Evans & Hungr, 1993). Gleichzeitig zerfallen einzelne Gesteinsblöcke in der Regel beim ersten Aufprall auf dem Hang in mehrere Gesteinsfragmente. Nach dem initialen Aufprall können die fragmentierten Blöcke entweder auf der Stelle verbleiben oder, was üblicher ist, sich in unterschiedliche Richtungen seitlich über den Hang verteilen (Evans & Hungr, 1993; Crosta & Agliardi, 2004). Infolge jedes Aufpralls wird Energie durch den Stoß entweder absorbiert oder aber in Rotationsenergie umgewandelt (di Prisco & Vecchiotti, 2006). Die meiste Blockgeschwindigkeit geht jedoch im oberen Bereich des Hangs unterhalb der Felswand verloren. Dies liegt daran, dass sich die Energie der Gesteinsblöcke proportional zur Aufprallgeschwindigkeit verteilt, wie in Experimenten von Pfeiffer & Bowen (1989) gezeigt wurde. Die wesentlichen Einflussfaktoren auf die Energiedissipation sind die Fallhöhe und der Aufprallwinkel (Li, et al., 2016), die Blockform (Glover, et al., 2015), die Dichte und das Gewicht des fallenden Blocks (Vilajosana, et al., 2008) sowie die gegenseitige Kollision der Gesteinsblöcke während der Bewegung (Erismann & Abele, 2001). Darüber hinaus wird die Energiedissipation maßgeblich von den genannten Gesteinseigenschaften und der Pufferkapazität des darunterliegenden Materials gesteuert, auf das der Aufprall erfolgt (Pichler, et al., 2005; Schellenberg, et al., 2008). Die wesentlichsten Parameter sind Blockgröße, Blockform, Gesteinsfestigkeit und Brüche, Elastizität sowie Hohlräume zwischen Blöcken, Schnee- und Vegetationsdecke (Crosta & Agliardi, 2004; Dorren, et al., 2006; Frattini, et al., 2012).

Das Verständnis des komplexen Zusammenspiels externer und interner Faktoren, die Hanginstabilitäten begünstigen, vorbereiten und auslösen, stellt eine wissenschaftliche Herausforderung dar.

Eine mögliche Herangehensweise, um ein Verständnis für das Auftreten von Sturzprozessen zu erhalten, ist die Beziehung zwischen der Grenze der Stabilität der Felswand sowie der Frequenz und Magnitude von destabilisierenden Faktoren (Glade & Crozier, 2005).

Vorbereitende („*preparatory*“) Faktoren, wie glaziale Entlastung und Belastung, aber auch Gefrier-Auftau-Zyklen von Permafrost, können die Stabilität von Felswänden beeinflussen, ohne dabei einen Sturzprozess zu initiieren (Glade & Crozier, 2005). Auslösende („*triggering*“) Faktoren sind externe Parameter wie vulkanische oder seismische Aktivität, aber auch Niederschlag (Durand, et al., 2018; Durand, et al., 2023). Diese können die Felswand in einen instabilen Zustand versetzen und einen Sturzprozess verursachen (Glade & Crozier, 2005; Hibert, et al., 2017). Grundvoraussetzende („*preconditioning*“) Faktoren sind hingegen statisch und inhärent, die nicht nur die Stabilität beeinflussen, sondern auch als eine Art Katalysator wirken, um andere dynamische und destabilisierende Faktoren effektiver wirken zu lassen (Glade & Crozier, 2005). Dazu gehören die Lithologie, die Topographie des Hanges, die Vegetation, Verwitterungsprozesse, die Solarstrahlung und das Wurzelwachstum (Meißl, 1998; Glade & Crozier, 2005; Jaboyedoff & Derron, 2005; Krautblatter & Dikau, 2007; Frattini,

et al., 2012; Crosta, et al., 2015). Jedoch können sich verschiedene Auslösemechanismen überschneiden, überlagern oder nacheinander auftreten. Dies erschwert die Zuordnung einzelner Prozesse, insbesondere wenn die Reaktion des Systems zeitlich verzögert erfolgt (Dietze, et al., 2017).

Untersuchungen belegen, dass insbesondere in geomorphologisch aktiven Regionen externe Faktoren wie Seismizität und Niederschlag eine zentrale Rolle für die Auslösung von Sturzprozessen spielen (Burtin, et al., 2014; Dietze, et al., 2017). Publikation IV zeigt am Krater Dolomieu, dass diese Triggerfaktoren signifikant zur Destabilisierung der Kraterwände beitragen (Durand, et al., 2018). Insbesondere die Validierung seismisch abgeleiteter Volumina stellt eine methodische Herausforderung dar, da bislang kaum Vergleiche mit TLS oder Photogrammetrie vorliegen (Salvini, et al., 2013; Vanneschi, et al., 2019). Außerdem mangelt es am kombinierten Einsatz der beiden Methoden Seismik mit TLS und Photogrammetrie. Es existieren kaum Forschungsarbeiten, die explizit Volumendaten aus Photogrammetrie und TLS mit seismisch geschätzten Volumina vergleichen oder validieren (Salvini, et al., 2013; Vanneschi, et al., 2019).

Obwohl Sturzprozesse oft in abgelegenen Gebirgsregionen vorkommen, stellen sie mancherorts, aufgrund der bereits vorhandenen und prognostizierten Veränderungen im klimatischen Gesamtsystem, ein Gefahrenpotential für die Bevölkerung und lokale Infrastruktur dar (Pfeiffer & Bowen, 1989; Volkwein, et al., 2011; Frattini, et al., 2012; Heiser, et al., 2017; Vanneschi, et al., 2019). Vor allem aufgrund der zunehmenden Besiedlung und möglicher klimatischer Veränderungen in hochalpinen Regionen ist zu erwarten, dass das Naturgefahrenpotenzial weiter zunimmt.

Insbesondere Sturzprozesse in hochalpinen Geosystemen reagieren sensibel auf einen klimatischen Wandel (Magnin, et al., 2017; Gallach, et al., 2020; Legay, et al., 2021). Vornehmlich kann eine Veränderung der Lufttemperatur und des Niederschlags Auswirkungen auf den Permafrostabbau sowie Verwitterungsprozesse nach sich ziehen (Paranunzio, et al., 2016; Viani, et al., 2020; Fischer, et al., 2012). Dies wiederum kann zu einer signifikanten Beeinträchtigung der Stabilität von Felswänden und zu Veränderungen in Frequenz und Magnitude von Sturzprozessen führen (McGuire, 2010; Fischer, et al., 2012; Paranunzio, et al., 2016; Gallach, et al., 2020; Viani, et al., 2020; Legay, et al., 2021; Mourey, et al., 2021; Stoffel, et al., 2024).

In den letzten Jahrzehnten wurden weltweit vermehrt sowohl katastrophale als auch kleinere Felsstürze in Gebirgsregionen registriert (Fischer, et al., 2012; Ravanel & Deline, 2015). Es wird vermutet, dass die derzeitige globale Erwärmung die Hauptursache für diese Entwicklung ist. So berichtet das „*Intergovernmental Panel on Climate Change*“ (IPCC), dass Veränderungen im klimatischen System direkten Einfluss auf hochalpine Geosysteme haben (IPCC, 2021). Die Temperaturen in den Europäischen Alpen sind vom 19. bis zum Beginn des 21. Jahrhunderts um zwei Grad Celsius angestiegen (EEA, 2009). Regionale Klimamodelle berechnen steigende Temperaturen bis zum Ende des 21. Jahrhunderts von +3.1 °C bis +4.3 °C (Kotlarski, et al., 2023).

Insbesondere aufgrund der zunehmenden Häufigkeit von Sturzereignissen sind Informationen über die räumliche Ablagerung und die Reichweite des herausgebrochenen Materials für die Gefahrenanalyse von entscheidender Bedeutung (Lambert, et al., 2013; Caviezel, et al., 2019).

Diese beiden Faktoren sind jedoch durch eine starke Unsicherheit und räumliche Variabilität gekennzeichnet (Crosta & Agliardi, 2004). Eine zuverlässige Vorhersage über die Ablagerung des Materials ist aufgrund der Vielzahl an interagierenden und beeinflussenden Faktoren sowie den Kontaktreaktionen des stürzenden Materials kompliziert (Crosta & Agliardi, 2004).

Parameter, die die Reichweite und die Trajektorie der Gesteinsblöcke beeinflussen sind makro-topographische Kenngrößen wie die Hangneigung, die Fallhöhe und Krümmungseigenschaften des Hanges (Meißl, 1998; Crosta & Agliardi, 2004; Frattini, et al., 2012; Leine, et al., 2014). Weitere zu berücksichtigende Parameter sind mikro-topographische Einflussgrößen. Dazu gehören sowohl die Oberflächeneigenschaften des Hanges wie beispielsweise die Rauigkeit, als auch vorhandene Schutzmaßnahmen (Meißl, 1998; Crosta & Agliardi, 2004; Gratchev & Saeidi, 2019). Die Eigenschaften des Sturzmaterials selbst, wie das Volumen, die Größe und Form der Gesteinsblöcke sowie die Lithologie haben weiteren Einfluss auf die Ablagerung und die Reichweite (Kirkby, 1975; Meißl, 1998; Crosta & Agliardi, 2004; Haas, et al., 2012; Leine, et al., 2014). Sie werden als dynamische Faktoren bezeichnet, da sie sich im Zusammenhang mit der Interaktion von Hangeigenschaften und der Blockdynamik verändern (Crosta & Agliardi, 2004).

Darüber hinaus beeinflussen die kinematischen Eigenschaften der Blöcke und die Restitutionsparameter die Ablagerung (Azzoni & de Freitas, 1995; Jaboyedoff & Labiouse, 2011; Ji, et al., 2019; Sandeep, et al., 2020).

Bisher gibt es jedoch nur wenige Arbeiten, die den Einfluss von Blockform, Blockgröße und Hangtopographie auf die Reichweite untersucht haben (Azzoni & de Freitas, 1995; Haas, et al., 2012; Caviezel, et al., 2019; Caviezel, et al., 2021).

In verschiedenen Studien wurde die Ablagerung der Gesteinsblöcke auf dem Schuttkegel als eine Form der gravitativen Sortierung („*gravitational sorting*“) charakterisiert. Dabei finden sich größere Blöcke im unteren Teil und kleinere Blöcke im oberen Teil des Schuttkegels (Statham, 1973; Messenzehl & Dikau, 2017; Kenner, 2019). Popescu et al. (2017) schlussfolgern, dass die Größe der Felsblöcke zum Hangfuß hin allmählich zunimmt, was auch von Copons et al. (2009) bestätigt wird, die in ihren Analysen eine Abhängigkeit zwischen dem Volumen der Felsblöcke und der Reichweite feststellen.

Haas et al. (2012) kommen in ihren Analysen zu dem Ergebnis, dass sowohl die Größe als auch die Form der Blöcke einen entscheidenden Einfluss auf die Reichweite haben. Dabei konnten auch komplexe Beziehungen zwischen Blockgröße und Reichweite festgestellt werden, die durch die jeweilige Blockform beeinflusst werden. Allerdings werden die Ergebnisse der gravitativen Sortierung durch die von ihnen durchgeführten Analysen nicht bestätigt. Die Autoren zeigen, dass es auch Gesteinsblöcke gibt, die trotz großen Volumens kürzere Reichweiten erzielen (Haas, et al., 2012). Aufgrund der Unterschiede in der Blockform und -größe, die durch verschiedene lithologische Gegebenheiten entstehen, weisen sie abschließend darauf hin, dass derartige Untersuchungen unter mehreren unterschiedlichen lithologischen Bedingungen erfolgen müssen (Haas, et al., 2012).

Räumlich hochaufgelöste Datensätze sind entscheidend für die präzise Erfassung der Reichweite einzelner Gesteinsblöcke und die detaillierte Quantifizierung spezifischer Sturzprozesse. Diese umfassenden Daten bilden zudem die Grundlage für zuverlässige Analysen der Prozessaktivität von Sturzereignissen sowie für die Rekonstruktion von Oberflächen vor dem Abgang der Massenbewegungen.

Um solche hochaufgelösten Daten zu gewinnen, kommen insbesondere zwei Methoden zum Einsatz: das terrestrische Laserscanning (TLS) und die digitale Photogrammetrie mit der Verwendung von (historisch, aktuellen) terrestrischen Bilddaten.

Bei der Quantifizierung der Sturzprozesse zeigen die Ergebnisse der Studien jedoch eine erhebliche Streuung. Guerin et al. (2020) quantifizieren in ihren Untersuchungen im Yosemite Valley (Kalifornien, USA) Volumina von Sturzprozessen, die zwischen 0,02 m^3 und 2.844 m^3 liegen. Diese Volumenangaben beziehen sich auf Einzelereignisse, die zwischen 2010 und 2016 mit TLS erfasst wurden. Ergänzend zu diesen Analysen nutzten sie historische Fotoaufnahmen mit Blickwinkel auf die Felswand, die aus einem Hubschrauber aufgenommen wurden (Guerin, et al., 2020). Über einen Zeitraum von 34 Jahren (1976–2010) quantifizierten sie für vier Sturzprozesse Volumina von 93 m^3 bis 2.019 m^3 (Guerin, et al., 2020).

Im Vergleich dazu fallen die Ergebnisse von Strunden et al. (2015) in eine deutlich kleinere Volumenklasse. Für einen kürzeren Zeitraum von 18 Monaten wurden Volumina zwischen 0,06 ± 0,01 m^3 und 119,34 ± 1,70 m^3 berechnet. Für ihre Analysen wurden über den Untersuchungszeitraum eine TLS-Aufnahme pro 1,5–2 Monate aufgenommen. Auch in diesem Fall handelt sich um Einzelereignisse.

In einer weiteren Studie von Guerin et al. (2020) quantifizieren sie für den Zeitraum 2005–2016 insgesamt 307 Sturzprozesse im Mont-Blanc-Massiv (Frankreich). Die Oberflächenveränderungen der einzelnen Sturzprozesse zeigen eine große Spannweite, mit Volumina zwischen 0,002 m^3 und 41.810 m^3 (Guerin, et al., 2020).

Diese Vergleiche verdeutlichen die unterschiedliche Variation der Volumina je nach Untersuchungsgebiet und -zeitraum. Ein möglicher Erklärungsansatz hierfür liegt in der unzureichenden zeitlichen Auflösung der Datenaufnahme. Infolgedessen kann es zur Überlagerung einzelner Prozesse kommen, die in den Analysen nicht eindeutig differenziert werden können.

Überschreitet das zeitliche Intervall zwischen zwei Messungen die Wiederkehrperiode einzelner Ereignisse, besteht das Risiko, dass mehrere Sturzprozesse fälschlichreweise als ein einziges, zusammenhängendes Ereignis erfasst werden (Williams, et al., 2019). Dies kann zu einer systematischen Verzerrung der Magnitude-Frequenz-Verteilung führen (Williams, et al., 2019). Während kleinere Ereignisse tendenziell unterschätzt werden, kann das Volumen größerer Prozesse überschätzt erscheinen, da es sich möglicherweise um die Akkumulation mehrerer kleinerer Prozesse handelt (Stock, et al., 2012; Royán, et al., 2015; Kromer, et al., 2017). Diese Problematik ist besonders relevant, da gerade die kleinvolumigen Ereignisse in der Regel die höchste Auftretenshäufigkeit aufweisen.

Für die Analyse von Prozessdynamiken ist eine hohe zeitliche Auflösung essenziell. So kommen Williams et al. (2019) in ihrer Analyse zu dem Ergebnis, dass das Aufnahmeintervall nicht nur die Quantität, sondern auch die Qualität der erfassten Daten beeinflusst. Langfristige Untersuchungen mit großen Zeitabständen unterschätzen systematisch die Häufigkeit kleinerer Ereignisse und verzerren damit die Magnitude-Frequenz-Beziehung (Williams, et al., 2019).

Anhand der Ergebnisse der Studien wird ersichtlich, dass ein zentrales Problem darin besteht, dass viele Untersuchungen nur über einen kurzen Zeitraum hinweg durchgeführt werden. Dies limitiert die Möglichkeit, eine Magnituden-Frequenz-Beziehung abzuleiten, die für das Verständnis von Sturzprozessen entscheidend ist. Langfristige Zeitreihen sind daher unerlässlich, um die Morphodynamik von Sturzprozessen präzise zu erfassen und zu analysieren.

Historische Aufzeichnungen bieten dagegen die Möglichkeit, Sturzereignisse über längere Zeiträume hinweg zu untersuchen. Zahlreiche Studien fokussieren sich hingegen auf kurzfristige Zeiträume und berücksichtigen dabei oft nicht die langfristige Morphodynamik, die durch historische Daten erfasst werden kann. Solche Daten sind von zentraler Bedeutung, um Analysen im Kontext langfristiger Entwicklungen zu ermöglichen.

Solange keine historischen Fotoaufnahmen verwendet werden, können aufgrund der zum Teil zeitlich begrenzten Projektlaufzeiten dementsprechend auch nur die in diesem Zeitraum auftretenden Sturzprozesse analysiert werden. Durch die photogrammetrische Auswertung von digitalisierten, vor allem historischen Fotografien, sollten die Analysen weiter in die Vergangenheit ausgeweitet werden.

Bei steilen Felswänden bieten terrestrische Fotografien insbesondere aufgrund der Bild-Objekt-Geometrie (dem Winkel zwischen der Objektebene und dem Objektiv) Vorteile. Im Vergleich zur Luftbildfotografie ermöglicht sie eine bessere Perspektive und damit eine genauere Rekonstruktion der komplexen Oberflächenstruktur (Benjamin, et al., 2020; Guerin, et al., 2020). Müller et al. (2014) berichten von einer Zunahme vertikaler Fehler in luftgestützten photogrammetrischen digitalen Höhenmodellen in Bereichen mit einer Hangneigung von über 40°, was eine direkte Einschränkung für das Monitoring von Felswänden mithilfe von Luftbildern darstellt.

In ihrer Studie setzten Guerin et al. (2020) luftgestützte Bilddaten erfolgreich ein, um Steinschlagereignisse im Yosemite Valley (Californien, USA) über einen Zeitraum von 34 Jahren zu analysieren und zu quantifizieren. An dieser Stelle ist jedoch zu betonen, dass es sich bei der Datenaufnahme nicht um eine Nadiraufnahme handelt, sondern um eine Schrägansicht auf die Felswand, auch wenn die Aufnahme luftgestützt erfolgte. Die Autoren erreichen für die stabilen Bereiche in zwei SfM-Punktwolken aus dem Jahr 1976 eine Genauigkeit von 28 cm bzw. 42 cm für ein doppeltes Konfidenzintervall (Guerin, et al., 2020).

Im Gegensatz dazu existiert bislang keine Studie, die gezielt historische terrestrische Bilddaten zur Quantifizierung von Steinschlagereignissen verwendet.

Diese aufgezeigten Forschungslücken sollten an einer Untersuchungsfläche im regionalen Kontext der europäischen Alpen verortet sein, wie beispielsweise den Drei Zinnen oder auf La Réunion am Krater Dolomieu.

Trotz der Verwendung historischer Fotoaufnahmen kann es zu Überlagerungen von Sturzprozessen kommen, deren Differenzierung in der Auswertung erschwert werden kann. Dies kann insbesondere in geomorphologisch hochaktiven Gebieten der Fall sein. Dazu zählt La Réunion, da dort im Zusammenhang mit einer verstärkten seismischen Aktivität auch eine Zunahme von Sturzprozessen zu verzeichnen ist (Hibert, et al., 2017).

Treten mehrere Prozesse in engem zeitlichem Abstand auf, ist eine klare Abgrenzung dieser erschwert. Das Problem wird noch verstärkt, wenn die Frequenz der Ereignisse deutlich höher ist als die Häufigkeit der Datenerfassung. Eine längere und optimalerweise permanente Beobachtungsdauer sowie eine räumlich hoch aufgelöste Datenbasis sind daher für eine differenzierte Analyse dieser Ereignisse notwendig.

Die Arbeit von Mastrantoni et al. (2024) beschäftigt sich mit dem Monitoring einer Rutschung in Italien mittels festinstallierter Kamerasysteme, wobei die Datenaufnahme etwas über ein Jahr hinweg erfolgte und alle drei Stunden ein Foto gemacht wurde. Allerdings quantifizieren sie in ihren Ergebnissen keine Volumina der Oberflächenveränderungen, sondern geben nur die Fläche an.

In einer weiteren Studie wird eine Felswand in Spanien ebenfalls mit einem fest installierten Kamerasystem erfasst (Blanch, et al., 2024). Im Zeitraum von 2018 bis 2020 wurden zwei Sturzprozesse mit einem Volumen von 1 m^3 und 107 m^3 quantifiziert. Es ist jedoch anzumerken, dass es in beiden Fällen bei der Betrachtung der Ergebnisse keine Schwierigkeit gab, einzelne Prozesse voneinander zu differenzieren.

Auch wenn sich einige Arbeiten mit dem Monitoring von Vulkanen mittels Webcams, deren Aktivität sowie der Entwicklung der äußeren Vulkanflanken befassen (Falsaperla, et al., 2006; Calvari, et al., 2016; Coltelli, et al., 2017), fehlt es an Untersuchungen, die längere Zeiträume einbeziehen und auch speziell die inneren Flanken aktiver Vulkane in den Fokus nehmen. Die Analysen von Mastrantoni et al. (2024) und Blanch et al. (2024) decken ebenfalls keine längeren Zeiträume ab.

Die Voraussetzungen für die Nutzung solcher Daten sind ein möglichst langer Zeitraum, in dem die Webcams an einem festen Standort betrieben wurden und die Sicherstellung, dass die Daten über diesen Zeitraum hinweg angemessen archiviert wurden.

3 Fragestellungen und Ziele

„Die wahre Entdeckungsreise besteht nicht darin, neue Landschaften zu suchen, sondern mit neuen Augen zu sehen.“

(Marcel Proust, o.J.)

Das Potenzial historischer terrestrischer Fotografien zur Quantifizierung von Sturzprozessen wurde in bisherigen Forschungsarbeiten kaum genutzt.

Um Kenntnisse über Frequenz-Magnituden Beziehung zu erhalten und um eine Rekonstruktion früherer Felsoberflächen zu erreichen, sind Messungen über mehrere Dekaden notwendig. Gerade im Hinblick auf aktuelle Klimaveränderungen ist das Wissen über die Prozessdynamik vergangener Perioden von enormer Bedeutung. Erst vorhandene Langzeit- und Kurzzeitstudien ermöglichen die Einordnung aktueller Prozessraten und -dynamiken in einen langfristigen Kontext. In vielen Studien werden jedoch Datensätze verwendet, die nur wenige Jahre umfassen (Abellán, et al., 2011; Strunden, et al., 2015; Kenner, 2019).

Für die Rekonstruktion langfristiger Veränderungen der Felswand bzw. des Ausbruchbereichs von Sturzmaterial müssen historische Fotoaufnahmen herangezogen werden. Für deren Auswertung ist das terrestrische SfM-Verfahren besonders geeignet, wobei adäquate Bilder aus Archiven zuvor recherchiert werden müssen. Aufgrund der besseren Aufnahmegeometrie terrestrischer Standorte im Vergleich zur vertikalen Fotografie der Felswand bieten sich terrestrische Aufnahmen hier besonders an.

Vor allem im Hochgebirge kann es aufgrund der starken Geomorphodynamik zu einer Überlagerung verschiedener Ereignisse kommen, was die Differenzierung von Einzelereignissen erschwert. Dieses Problem tritt besonders dann auf, wenn der zeitliche Abstand zwischen den Datensätzen etwa bei Luftbildern groß ist. Die Folge sind Ungenauigkeiten in der Bestimmung von Frequenz und Magnitude. Fest installierte, automatisierte terrestrische Kamerasysteme ermöglichen jedoch eine Verdichtung der Zeitreihen, wodurch Einzelereignisse, insbesondere in geomorphologisch hochaktiven Gebieten, in der Datenauswertung besser differenziert und einzeln analysiert werden können. Allerdings sollte das Kamerasystem nach photogrammetrischen Bedingungen installiert sein, da ansonsten die Datenauswertung und das Erstellen von Höhenmodellen erschwert wird.

In diesem Zusammenhang wurde der Krater Dolomieu auf La Réunion als Untersuchungsgebiet ausgewählt, da er aufgrund seiner ausgeprägten seismischen Aktivität eine besonders hohe Geomorphodynamik aufweist. Diese ist durch eine Frequenz von monatlich über 1.000 Sturzereignissen sowie

Magnituden mit Einzelvolumina von bis zu 1.000 m^3 gekennzeichnet (Durand, et al., 2018). Infolgegessen ergeben sich optimale Voraussetzungen für die Auswertung webcambasierter Bilddaten, um die Vielzahl an stattfindenden Prozessen mit hoher zeitlicher Auflösung zu erfassen und zu analysieren.

Zum besseren Verständnis der Prozessaktivität in Bezug auf die Reichweite einzelner Blöcke von Sturzprozessen sind Analysen, insbesondere vergleichende Untersuchungen in unterschiedlichen Lithologien, erforderlich. Die meisten Arbeiten befassen sich jedoch damit nur mit Einzeluntersuchungen oder erfolgen unter Laborbedingungen.

Publikation I beschäftigt sich mit der Rekonstruktion von steilen Felswänden und der Quantifizierung von Sturzprozessen mittels historisch terrestrischer Fotoaufnahmen. Der Fokus der zweiten Publikation liegt auf der Analyse von reichweitenbeeinflussenden Faktoren von Sturzprozessen. Die Publikationen III und IV befassen sich mit der Quantifizierung von Sturzprozessen mit Hilfe von stationären Webcams. Darüber hinaus geht es um den kombinierten Einsatz von TLS und photogrammetrischen Fotoaufnahmen zur Volumenbestimmung von Sturzereignissen. Diese eingesetzten Methoden sollen als Referenz dienen, um die Genauigkeit der aus seismischen Daten berechneten Volumina der Sturzprozesse zu validieren.

Aus dem aktuellen Stand der Forschung lassen sich folgende Fragestellungen ableiten, die in den in dieser Arbeit enthaltenen Publikationen behandelt wurden:

1) Wie gut kann durch den Einsatz von multitemporalen historischen terrestrischen Fotographien in Kombination mit TLS und aktuellen terrestrischen digitalen Fotoaufnahmen eine Analyse und Quantifizierung der Veränderung der Felswandoberfläche durchgeführt werden? Darüber hinaus stellt sich die Frage, welche spezifischen Herausforderungen sich im Zusammenhang mit der Integration dieser Datensätze ergeben.
2) Lässt sich mittels des Einsatzes räumlich hochauflösender topographischer Daten ein Erkenntnisgewinn bezüglich der Prozesszusammenhänge und -abläufe von Sturzprozessen erzielen? In diesem Kontext soll untersucht werden, inwiefern die Faktoren Blockgröße, -form, Lithologie und Rauigkeit der Schutthalde die Reichweite von Sturzprozessen beeinflussen, wobei die Analysen in mehreren Untersuchungsgebieten mit unterschiedlichen Lithologien erfolgen.
3) Können neue Erkenntnisse über die Dynamik von Sturzprozessen in einem seismisch und geomorphologisch hoch aktiven Untersuchungsgebiet durch den Einsatz eines automatisierten Kamerasystems (fest installierte Webcams) mit hoher räumlicher und zeitlicher Auflösung gewonnen werden?
4) Welchen Einfluss üben die Faktoren Regen und Seismizität auf Sturzprozesse aus und in welcher Form eignen sich sowohl TLS als auch Photogrammetrie, um die auf Basis seismischer Aufzeichnungen abgeleiteten Volumina zu verifizieren?

4 Methodik

> "[...] *in recent decades, considerable attention has been given to using terrestrial laser scanning (TLS), airborne laser scanner (ALS) LiDAR, and close-range photogrammetry techniques in rock slope investigations.*"
>
> (Cirillo, et al., 2024)

Im Rahmen dieser Arbeit sowie zur Beantwortung der oben genannten Forschungsfragen wurden unterschiedliche Daten für die Analysen recherchiert und aufbereitet.

Die technischen Spezifikationen und Aufnahmeparameter sind zum einen in Tabelle 1 für die TLS Daten als auch in Tabelle 2 und Tabelle 3 für die photogrammetrischen Datensätze zusammenfassend dargestellt. Für darüber hinausgehende Details zu den jeweiligen Datensätzen wird auf die entsprechenden Publikationen verwiesen.

4.1 LiDAR

Eine zentrale Grundlage aller Publikationen bilden Datensätze für alle Untersuchungsflächen, die sowohl mit dem terrestrischen Laserscanner der Firma Riegl „*LMS-Z420i*" (Publikation I) als auch mit dem „*VZ-4000*" (Publikationen II, III, IV) aufgenommen wurden.

Das in den letzten beiden Jahrzehnten entwickelte Messverfahren LiDAR, lässt sich in terrestrisches LiDAR (terrestrial, TLS) und luftgestütztes LiDAR (airborne, ALS) differenzieren.

Zum einen können damit Daten von abgelegenen Untersuchungsflächen berührungslos aufgenommen werden, zum anderen werden die Oberflächen durch die Messung nicht beeinflusst. Die zeitliche und räumliche Auflösung und Genauigkeit im einstelligen Zentimeterbereich (Smith, et al., 2016) ermöglichen, basierend auf generierten 3D-Modellen, die Ableitung diverser Reliefparameter sowie die Lokalisierung von Erosionsprozessen und deren Prozessdynamik auf Hang- und Einzugsgebietsskala (Neugirg, et al., 2016). Ein weiterer Vorteil von LiDAR ist die Möglichkeit, die Aufnahmeintervalle selbst zu definieren (Carrivick, et al., 2013).

In der geomorphologischen Prozessforschung gehört LiDAR aufgrund der genannten Vorteile mittlerweile zur Standardmethode für die Erfassung topographischer Parameter und die anschließende Quantifizierung von Erosionsvolumina und -raten. Daher findet LiDAR in einer Vielzahl von Studien mit unterschiedlichen Fragestellungen Anwendung. Die Forschungsbereiche können dabei in unterschiedliche Kategorien gegliedert werden.

Zunächst einmal geht es um die allgemeine Visualisierung und Prozessdarstellung (Glenn, et al., 2006; Jones, et al., 2007; Markus, et al., 2023). Dies umfasst auch die Quantifizierung geomorphologischer Prozesse mithilfe multitemporaler Daten (Glenn, et al., 2006; Kasperski, et al., 2010; Abellán, et al., 2011; Haas, et al., 2012; Salvini, et al., 2013; Sala, et al., 2019).

LiDAR wird auch eingesetzt, um Forschungsfragen zur Analyse von Hangrutschungsprozessen infolge seismischer Aktivität zu beantworten (Walter, et al., 2012; Hibert, et al., 2014; Dietze, et al., 2017). Ein weiterer Anwendungsbereich beschäftigt sich mit der Ableitung und Analyse von morphometrischen Oberflächenparametern wie z.B. der Hangneigung oder der Rauigkeit (Rahman, et al., 2006; Hollaus, et al., 2011; Haas, et al., 2012; Milenković, et al., 2015; Wegner, et al., 2021).

Spezielle Forschungsarbeiten befassen sich mit der Modellierung der Reichweite von Gesteinsblöcken und den diese beeinflussenden Parametern (Meißl, 1998; Frattini, et al., 2012; Haas, et al., 2012; Leine, et al., 2014; Gratchev & Saeidi, 2019; Caviezel, et al., 2021). Die geringe Anzahl existierender Arbeiten, die sich mit der Reichweitenanalyse beschäftigen, beschränkt sich vorallem auf die Analyse einzelner Untersuchungsgebiete oder auf Laborexperimente (Glover, et al., 2015; Wang, et al., 2018; Gratchev & Saeidi, 2019).

Im Gegensatz zu den genannten Vorteilen von LiDAR weist die Aufnahmemethode einige Limitierungen auf. Dazu zählen Abschattungseffekte, vor allem bei TLS, aufgrund der vorhandenen Topographie der Untersuchungsfläche. Diese können durch aufwendige Nachbearbeitung, aber auch mittels unterschiedlicher Aufnahmeperspektiven durch mehrere Aufnahmepositionen im Untersuchungsgebiet minimiert werden. Allerdings hat dies einen Genauigkeitsverlust zur Folge. Auch wenn zusätzliche materialspezifische und geräteabhängige Fehlerquellen vorhanden sind, kann dieser Genauigkeitsverlust dazu führen, dass die Untersuchungsfläche nicht vollständig hoch aufgelöst aufgenommen werden kann. Dazu zählen auch Elemente wie z.B. Wasser, Schnee, Feuchtigkeit und Vegetationsbedeckung. Da die Größe der aufzunehmenden Fläche bei TLS meist limitiert ist, bietet hier ALS einen Vorteil, da ein größeres Gebiet mit einer günstigeren Aufnahmegeometrie (Nadiraufnahme) aufgenommen werden kann. Jedoch verfügt TLS bei steilen Flächen (z.B. Felswände) wiederum über einige Vorteile, aufgrund der Geometrie der Erfassung. Solange kein schwenkbarer Sensor bei der ALS Datenaufnahme zum Einsatz kommt, zeigen Geländemodelle, die auf luftgestützten Aufnahmen basieren, insbesondere bei steilen Felswänden mit einer Neigung von über 40°, größere Fehler (Müller, et al., 2014). Weitere auftretende Fehler gehen mit dem *„footprint“* (auftreffendes Infrarotsignal) einher. Dieser wird durch die Strahlendivergenz mit zunehmender Entfernung vom Messobjekt größer. Weitere Limitierungen von TLS sind das Gewicht und das Equipment (Gerät, Akkus, Stative) (Smith, et al., 2016). Das kann eine Datenaufnahme in komplexen Topographien wie auf steilen Schuttkegeln erschweren. In einigen Fällen bietet sich die Kombination von TLS und ALS an. Nicht unbeachtet sollte jedoch der hohe finanzielle Aufwand in Bezug auf Beschaffungs- und Unterhaltkosten gelassen werden und hängt damit vom Budget eines jeden Projekts ab (Smith, et al., 2016).

Auf Grundlage der LiDAR Daten wurden für alle Gebiete Höhenmodelle auf Basis der Punktwolken erstellt. Zudem dienten die hochaufgelösten 3D-Punktwolken zur Analyse von Hangneigungen und Oberflächenrauigkeiten. Darüber hinaus wurden die TLS-Daten zur Referenzierung der jeweiligen SfM-MVS-Datensätze herangezogen.

Die folgende Tabelle 1gibt einen Überblick über die gerätespezifischen Parameter der beiden verwendeten Modelle.

Tabelle 1. Spezifikationen für die beiden eingesetzten Modelle Riegl VZ-4000 und LMS-Z420i (Riegl, 2010; Riegl, 2020). Für die Datenaufnahme auf La Réunion und bei den Drei Zinnen kam der VZ-4000 zur Anwendung, für die restlichen Untersuchungsgebiete Gampenalm, Dreitorspitze und Zwieselbachtal der LMS-Z420i.

	VZ-4000	**LMS-Z420i**
Max. Messbereich	4.000 m	1.000 m
Min. Messbereich	5 m	2 m
Sichtfeld (vertikal × horizontal)	60° × 360°	80° × 360°
Messfrequenz	23.000 Punkte s^{-1}	8.000 Punkte s^{-1}
Genauigkeit	15 mm	10 mm
Präzision	10 mm	4–8 mm
Laserwellenlänge	Nahinfrarot	Nahinfrarot
Laserstrahldivergenz	0.15 mrad	0.25 mrad

4.2 Photogrammetrie

Im Rahmen der Untersuchungen dieser Dissertation wurden neben hochauflösenden digitalen terrestrischen Fotografien (Tabelle 2) auch solche von automatisierten, stationären Webcams genutzt (Tabelle 3). Zudem kamen historische terrestrische Fotografien zum Einsatz, die in verschiedenen Archiven sowie in einer privaten Sammlung recherchiert wurden (Tabelle 4) (Universalarchiv der Deutschen Fotothek für Kunst und Kulturgeschichte, Dresden; Amt für Film und Medien, Bozen; Fotohaus Heimhuber, Sonthofen).

Tabelle 2. Spezifikationen für die verwendeten digitalen terrestrischen Kamerasysteme.

	Kamerasystem 1	**Kamerasystem 2**	**Kamerasystem 3**	**Kamerasystem 4**
Gerätetyp	Sony Alpha 6000	Pentax Kx	Canon EOS 1DS Mark III	Nikon D610
Auflösung	24.3 MP	12.2 MP	21.1 MP	24.3 MP
Brennweite	16 mm	28 mm	35 mm	32 mm
Blendenzahl	F/9	F/11	F/8	F/4.5
Anzahl aufgenommener Fotos	221	496	92	133
Anzahl verwendeter Fotos	118	4	4	4

Tabelle 3. Spezifikationen für die beiden Webcamsysteme.

	Webcam 1	**Webcam 2**
Gerätetyp	Pentax K200D	Canon EOS350D
Auflösung	10.2 MP	8 MP
Brennweite	18 mm	20 mm
Blendenzahl	1/200	1/40
Anzahl aufgenommener Fotos	390	485
Anzahl verwendeter Fotos	4	8

Tabelle 4. Spezifikationen für die recherchierten historischen terrestrischen Fotoaufnahmen. Allerdings wurden für die weitere Prozessierung und Quantifizierung der Oberflächenveränderungen in Publikation 1 lediglich die Fotografien aus dem Jahr 1970 verwendet.

Jahr	**Anzahl der Fotos**	**Dimension [pixel]**	**Scanauflösung [dpi]**	**Originalformat**	**Farbe**	**Datenquelle**
1902–1930	6	6,520 × 4,162	1.2000	Negativ Glassplatte	Graustufe	Universalarchiv der deutschen Fotothek für Kunst- und Kulturgeschichte (Dresden, Deutschland)
1914	2	11,000 × 8,250	300	Negativ Glassplatte	Graustufe	Universalarchiv der deutschen Fotothek für Kunst- und Kulturgeschichte (Dresden, Deutschland)
1964	7	8,315 × 8,315	1.200	Rollfilm negativ	Graustufe	Fotohaus Heimhuber (Privatarchiv, Sonthofen, Deutschland)
1965	2	6,520 × 4,162	1.200	Rollfilm negativ	Graustufe	Amt für Film und Medien (Bozen, Italien)
1970	42	8,580 × 8,800	4.000	Rollfilm negativ	Graustufe	Amt für Film und Medien (Bozen, Italien)
1979	7	8,409 × 8,409	1.200	Rollfilm negativ	Graustufe	Fotohaus Heimhuber (Privatarchiv, Sonthofen, Deutschland)

In den letzten Jahrzehnten haben die Fortschritte in der Vermessungstechnik, vor allem in der Fernerkundung, die Fähigkeit, die Erdoberfläche quantitativ zu erfassen und zu charakterisieren, stark weiterentwickelt (Smith, et al., 2016; Eltner, et al., 2017). Dazu zählt die Photogrammetrie, die fast so alt ist wie die Fotografie selbst.

Ziel der Photogrammetrie ist die Rekonstruktion dreidimensionaler Geländeoberflächen aus Bildaufnahmen und die Ableitung von Punktwolken, digitalen Höhenmodellen und weiteren Eigenschaften wie z.B. topographischen Parametern (Eltner, et al., 2016; Aber, et al., 2019). Die Datenaufnahme kann entweder auf der Basis terrestrischer Fotoaufnahmen erfolgen oder durch „*Unmanned Aerial Systems*“ (UAS) generiert werden.

Die Weiterentwicklung der letzten Jahrzehnte, photogrammetrische Prinzipien mit Algorithmen zu verknüpfen, führte zu einer signifikanten Verbesserung in der 3D Oberflächenrekonstruktion (Eltner, et al., 2016; Aber, et al., 2019).

Die in den Publikationen (I, III, IV) dieser Dissertation verwendeten Fotodatensätze (historische, aktuelle terrestrische Fotoaufnahmen, Webcams) weisen signifikante Unterschiede in den Bildeigenschaften (z.B. Bildqualität, Format, Auflösung, Objektivgeometrie etc.) auf. Daher war es notwendig, die Einstellungen innerhalb der SfM-MVS-Prozessierung individuell an die jeweiligen Datensätze anzupassen. Detaillierte Ausführungen dazu sind in den einzelnen Publikationen (I, III, IV) zu finden.

Vor der Durchführung des tatsächlichen SfM-MVS Workflows (Abbildung 2), erfolgte eine Filterung der verwendeten Bilder in den Publikationen. In einem zweistufigen Prozess wurden zunächst unscharfe und verschwommene Bilder anhand einer visuellen Bildinspektion ausgeschlossen. Anschließend schätzte eine automatische Bildqualitätsanalyse in Metashape Pro (Version 1.5.5) den normierten dimensionslosen Wert [0;1] (0 = niedrige Qualität, 1 = hohe Qualität). Bilder mit einem Wert < 0,5 flossen nicht in die weitere Prozessierung ein.

Im Folgenden werden die einzelnen Schritte des SfM-MVS Workflows (Abbildung 2) erläutert. Weitere Informationen dazu sind in Westoby et al. (2012), Eltner et al. (2016), Smith et al. (2016), Aber et al. (2019) zu finden.

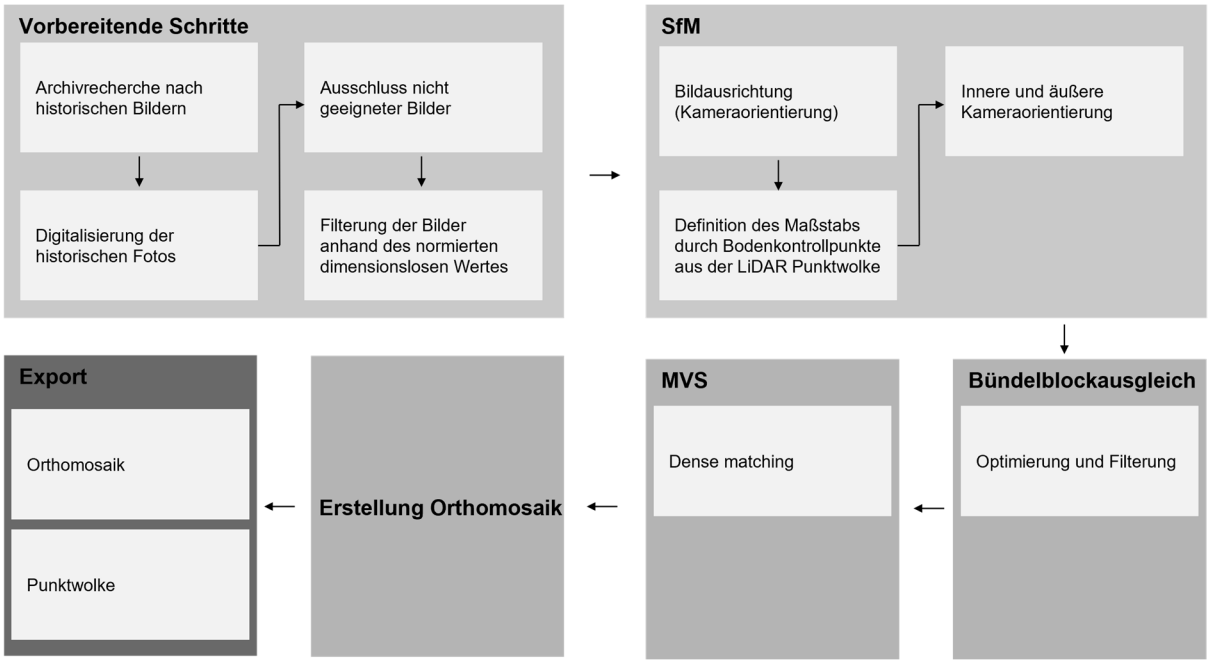

Abbildung 2. Arbeitsschritte des SfM-MVS-Workflows für die verwendeten terrestrischen Fotodatensätze zur Erstellung von Orthomosaiken und Punktwolken mit Metashape Pro.

SfM Photogrammetrie lässt sich in drei wesentliche Verarbeitungsschritte zusammenfassen:

> (1) Identifizierung und Abgleich homologer Bildpunkte in sich überlappenden Bildern, die von verschiedenen Positionen aus aufgenommen wurden.
> (2) Bündelblockausgleich: Rekonstruktion des Aufnahmeschemas (d.h. innere und äußere Kameraorientierung) und Generierung einer dünnen Punktwolke („*sparse cloud*“) (d.h. 3D-Koordinaten der übereinstimmenden Bildpunkte).
> (3) Verdichtung der rekonstruierten Punktwolke durch MVS zu einer sogenannten „*dense cloud*“ (Eltner, et al., 2017).

In einem ersten Schritt werden aus einem Datensatz bestehend aus mehreren Fotos, die über eine gewisse Überlappung verfügen, sogenannte „*keypoints*“ extrahiert (Smith, et al., 2016; Aber, et al., 2019). Die Überlappung zwischen den einzelnen Fotografien sollte deutlich über einem Wert von > 40 % liegen (Goodbody, et al., 2021). Demgegenüber werden, auch in Abhängigkeit vom Untersuchungsdesign, das in diesem Fall auf UAV basiert, 90 % laterale und 70 % Bildüberlappung in Flugrichtung vorgeschlagen (de Lima, et al., 2021). Ponti et al. (2024) kommen in ihren Untersuchungen zum Permafrostmonitoring zu dem Resultat, dass eine Überlappung von > 60 % sinnvoll ist. Es ist jedoch zu beachten, dass eine Erhöhung der Bildüberlappung immer mit einer Zunahme der Rechenleistung einhergeht (Torres-Sánchez, et al., 2017).

Bei keypoints handelt es sich um korrespondierende Bildmerkmale. Basierend darauf können die einzelnen Fotos einander zugeordnet werden (Smith, et al., 2016; Eltner, et al., 2016). Bevor dies jedoch stattfinden kann, müssen „*feature points*“ (Korrespondenzen) identifiziert werden, die die Basis für die keypoints sind (Smith, et al., 2016). In diesem Schritt werden korrespondierende keypoints in den Bildern identifiziert und deren euklidischer Abstand zueinander berechnet. Punkte, die über keine ausreichende Übereinstimmung verfügen, werden eliminiert (Smith, et al., 2016). Snavely et al. (2008) definieren dafür einen dimensionslosen Mindestwert für diese Übereinstimmung von < 0.6. Der sich nun anschließende Bearbeitungsschritt ist das eigentliche SfM Verfahren. Ausgehend von den geometrisch korrekten Merkmalskorrespondenzen verwenden SfM Algorithmen zum Bündelblockausgleich („*bundle adjustment*“), um die 3D-Geometrie (oder Struktur) einer Szene, die verschiedenen Kamerapositionen (externe Kalibrierung) und die kamerainternen Parameter (interne Kalibrierung) zu schätzen (Smith, et al., 2016; Aber, et al., 2019). SfM benötigt für diesen Prozess keine separaten Informationen über die Kamerakalibrierung, sondern verwendet dafür die Metadaten des Bildes („*EXIF tags*“) (Smith, et al., 2016). Kameraparameter wie die Brennweite und die Verzeichnung spielen eine entscheidende Rolle in der SfM-Bearbeitung und können, wenn sie vorhanden sind, zur Verbesserung der Ergebnisse beitragen. Allerdings stehen für die historischen terrestrischen Fotos (Publikation I) keine entsprechenden Metadaten zur Verfügung. Aus diesem Grund erfolgt die Schätzung aller Objektivparameter mithilfe der internen Autokalibrierungsfunktion der Software.

Als Ergebnis wird eine sparse cloud erstellt. Das ist eine dünne Punktwolke bestehend aus „*tie points*“ in einem beliebig (un)skalierten Koordinatensystem und geschätzten Kamerakalibrierungsparametern sowie den geschätzten Kamerapositionen (Westoby, et al., 2012; Smith, et al., 2016; Aber, et al., 2019). Um diese generierte sparse cloud nun zu skalieren und zu georeferenzieren, können „*ground*

control points“ (GCPs, Bodenkontrollpunkte) verwendet werden (Smith, et al., 2016). Diese können entweder vorher im Untersuchungsgebiet verteilte und eingemessene (dGPS/GNSS („*differential Global Positioning System“/„global navigation satellite system*“) Bodenkontrollpunkte sein oder aus einem vorhandenen LiDAR Datensatz extrahiert werden (Smith, et al., 2016). Mit Hilfe dieser Bodenkontrollpunkte ist es möglich, das 3D-Modell mit einem geographischen Koordinatensystem zu versehen. Außerdem können Verzerrungsfehler korrigiert und die Lagegenauigkeit des Modells verbessert werden. Da im Gelände keine GCPs installiert und vermessen werden konnten, wurden in den Publikationen I, III und IV die Koordinaten der GCPs aus Strukturen extrahiert, die sowohl in der LiDAR Punktwolke als auch in den Fotografien vorhanden und im Beobachtungszeitraum unverändert waren.

Zur Erstellung der sparse cloud werden je drei globale Translations- und Rotationsparameter sowie ein Skalierungsfaktor benötigt (Smith, et al., 2016).

Die sparse cloud enthält häufig eine Vielzahl fehleranfälliger Messungen, die gefiltert werden müssen, um die Qualität des nachfolgenden Bündelblockausgleichs zu verbessern. Daher kommen bestimmte Filteroperationen zum Einsatz, die auf der Rekonstruktionsunsicherheit („*reconstruction uncertainty*“), der Projektionsgenauigkeit („*projection accuracy*“) und des Reprojektionsfehlers („*reprojection error*“) basieren, um fehlerhafte Anschlusspunkte zu entfernen. Die Projektionsgenauigkeit gibt an, mit welcher Genauigkeit die tie points lokalisiert wurden.

Hohe Rekonstruktionsunsicherheiten sind typisch für Punkte, die aus Kamerapositionen mit kurzer Grundlinie (geringer Abstand zwischen den Kamerapositionen wie bei historischen terrestrischen Aufnahmen) resultieren (Agisoft LCC 2019). In Kombination mit flachen Winkeln zwischen den Projektionslinien der Bilder kann dies zu einer hohen Unsicherheit bei der Rekonstruktion der 3D-Koordinaten führen. Als Folge können diese Punkte erheblich von der Objektoberfläche abweichen, was zu Rauschen in den photogrammetrischen Punktwolken führt und daher eliminiert werden muss.

Schließlich wird ein dritter Filtervorgang verwendet, um Punkte mit hohen Reprojektionsfehlern zu entfernen, die auf schlechte Bildprojektionen sowie auf eine falsche Zuordnung der erkannten Merkmale zurückzuführen sind. Diese Filterung von tie points ist immer ein Kompromiss zwischen der Entfernung möglichst vieler schlecht projizierter Punkte und dem Erhalt einer ausreichenden Anzahl von Punkten mit hoher Lagegenauigkeit zur Gewährleistung einer lückenlosen Oberflächenrekonstruktion.

Um die Kameraparameter und die rekonstruierte Geometrie zu optimieren, kann nach dem Hinzufügen der GCPs und der Filterung, der Bündelblockausgleich erneut durchgeführt werden (Smith, et al., 2016).

Der letzte Schritt ist die Anwendung von MVS-Algorithmen auf die bereits skalierte und georeferenzierte sparse cloud und die Kameraparameter (Smith, et al., 2016). Das Resultat der genannten Bearbeitungsschritte ist eine dense cloud.

Aufgrund der berührungslosen Aufnahme eignet sich die photogrammetrische Auswertung von terrestrischen Bildern, um schwer zugängliche Untersuchungsflächen aufzunehmen und diese nicht zu be-

einträchtigen (Smith, et al., 2016). Außerdem können Daten von unterschiedlich großen Gebieten generiert werden, deren Größen von 10^{-2} bis 10^{6} m^2 variieren (Smith & Vericat, 2015). Während hingegen für die Aufnahme mit LiDAR schweres Equipment benötigt wird, ist bei SfM der Umfang dessen um ein Vielfaches geringer (Smith, et al., 2016).

Allerdings kann es auch zu Problemen bezüglich der Abschattung kommen. Dies kann im Gegensatz zu LiDAR aufgrund der Vervielfachung der Aufnahmepositionen leichter gelöst werden, wodurch auch die Menge an tie points erhöht wird (Smith, et al., 2016).

Weitere Probleme im Hinblick auf die Verarbeitung und Auswertbarkeit ergeben sich, wie bei den in Publikation I und III verwendeten Fotografien, aus den Qualitäten der Aufnahmen selbst. Dies betrifft vor allem eine zu geringe Bildüberlappung von deutlich < 40 % (James, et al., 2017). Vorhandene qualitative Unterschiede in den Aufnahmen, beispielsweise Beleuchtungsunterschiede, Abschattungen, unterschiedliche Texturen sowie unterschiedliche Aufnahmepositionen und -zeiten beeinflussen die Weiterverarbeitung der Datensätze (Baltsavias, 1999) und können diese auch unmöglich machen. Folglich können keine Verknüpfungpunkte gesetzt werden. Auch wenn, bedingt durch den technologischen Fortschritt, heutige Rechner leistungsstärker sind als vor einigen Jahren, können große Datenmengen zu Limitationen bezüglich der Rechenzeit führen.

Trotz der genannten Limitationen ist SfM für geomorphologische Fragestellungen von großem Wert. Daher findet es in einer Vielzahl von jüngeren Forschungsgebieten Anwendung, wie z. B. für die Analyse von Massenbewegungen (Niethammer, et al., 2012; Lucieer, et al., 2014; Stumpf, et al., 2015; Eker, et al., 2017), in der Analyse von Steinschlagdynamik (Salvini, et al., 2013; Casagli, et al., 2017; Vanneschi, et al., 2019; Guerin, et al., 2020; Gallo, et al., 2021), in der Glaziologie (Fugazza, et al., 2018; Vivero & Lambiel, 2019; Geissler, et al., 2021), für die Quantifizierung von Prozessen an Steilküsten (Mancini, et al., 2013; Jaud, et al., 2019; Laporte-Fauret, et al., 2019), für das Monitoring von aktiven Vulkanen (James & Varley, 2012; Bretar, et al., 2013; Derrien, et al., 2020) und auch in der fluvialen Geomorphologie (Bakker & Stuart, 2017; Hemmelder, et al., 2018).

Die überwiegende Mehrheit der bisher genannten Studien befasst sich mit der Erfassung der aktuellen geomorphologischen Dynamik. Um die Untersuchungszeiträume weiter in die Vergangenheit auszudehnen, bietet sich hier die Fusion von digitalisierten (ehemals analogen) historischen Fotos mit SfM-MVS an.

Die Verwendung historischer Fotografien spielt dabei eine entscheidende Rolle. So existieren bereits zahlreiche Studien, die sich mit langfristigen Veränderungen z.B. der Blockgletscherdynamik (Fleischer, et al., 2021), der Gletscherdynamik oder des Sedimenthaushalts (Betz, et al., 2019; Altmann, et al., 2020; Stark, et al., 2022) innerhalb des letzten Jahrzehnts beschäftigen. Als Datengrundlage für diese Studien dienten vor allem historische Luftbilder, die je nach Region gut katalogisiert sind und in den meisten Fällen für wissenschaftliche Arbeiten zur Verfügung stehen.

Allerdings sind Studien, die Luftaufnahmen zur Bestimmung der historischen Steinschlagdynamik verwenden, selten. Basierend auf intensiver Recherche existiert lediglich folgende Studie von Guerin et

al. (2020), die Steinschlagereignisse über einen Zeitraum von mehreren Jahren analysiert und quantifiziert. In ihrer Arbeit kombinierten sie historische Luftbild-SfM mit terrestrischem SfM und TLS, um Steinschlagereignisse im Yosemite-Nationalpark in Kalifornien (USA) zu detektieren und zu quantifizieren, wobei jedoch keine historischen terrestrischen Bilder verwendet wurden (Guerin, et al., 2020). Ravanel & Deline (2010) haben in ihrer Studie historische Fotografien, die einen Zeitraum von 1860 bis 2008 abdecken und terrestrisches Laserscanning zur Quantifizierung von Felsstürzen im Mont-Blanc-Massiv verwendet.

Da die digitale Photogrammetrie nicht auf Luftbilder beschränkt ist, erscheint die Verwendung historischer terrestrischer Bilder zur Erkennung von Sturzprozessen, insbesondere an vertikalen Felswänden, sehr lohnend. Vor allem im Hinblick auf die Kosteneffizienz sind historische terrestrische Bildaufnahmen deutlich kostengünstiger verfügbar als z.B. UAV-Befliegungen. Ebenso sind keine Spezialausrüstungen oder spezielle Flugkenntnisse erforderlich.

Wenn historische Bilder die Anforderungen der SfM-MVS-Algorithmen erfüllen (z.B. ausreichende Bildüberlappung, Entropie, Auflösung, etc.), bieten sie großes Potenzial für multitemporale Reliefanalysen und Auswertungen geomorphologischer Prozesse über Zeitspannen von mehreren Jahrzehnten (Eltner, et al., 2016; Guerin, et al., 2020; Stark, et al., 2022). Die Vorteile der terrestrischen Fotografie liegen vor allem in der Bild-Objekt-Geometrie (Winkel zwischen Objektebene und Objektiv), die eine bessere Rekonstruktion der komplexen Oberflächenstrukturen im Vergleich zu Luftbildern an den steilen Felswänden ermöglicht (Benjamin, et al., 2020; Guerin, et al., 2020). Trotz intensiver Recherche konnten keine Studien gefunden werden, die sich mit der Analyse und Quantifizierung von Felsstürzen auf der Grundlage historischer terrestrischer Bilder beschäftigen.

Insbesondere in Gebieten wie auf La Réunion, wo Sturzprozesse mit hoher Frequenz auftreten, eignen sich stationäre Webcams zur Datenerfassung. Dies führt zu einer präziseren Quantifizierung der einzelnen Ereignisse. Zudem eröffnen sich dadurch Möglichkeiten für genauere und detailliertere Analysen der geomorphologischen Dynamik. Solche Webcams können auch über die zeitlich begrenzte Projektlaufzeit hinaus eingesetzt werden.

5 Untersuchungsgebiete

> "*Die Dolomiten sind die schönsten Bauwerke der Welt.*"
>
> (Reinhold Messner, o.J.)

Für diese Arbeit wurden fünf Untersuchungsgebiete in Hochgebirgsregionen ausgewählt. Vier dieser Gebiete befinden sich in den Europäischen Alpen (Gampenalm, Drei Zinnen, Dreitorspitze, Zwieselbachtal). Ein Gebiet liegt auf dem französischen Übersee-Département La Réunion. Die in den Alpen liegende Untersuchungsflächen befinden sich in Deutschland, Österreich und Italien. Das Untersuchungsgebiet auf La Réunion ist der Vulkankrater Dolomieu des aktiven Vulkans Piton de la Fournaise.

Die untersuchten Gebiete unterscheiden sich sowohl hinsichtlich der lithologischen Verhältnisse als auch in Bezug auf die klimatischen Bedingungen. Alle Gebiete zeichnen sich durch rezente Sturzprozessaktivität und eine deutlich erkennbare Felswand mit zugehörigem Hang aus. Die ausgewählten Untersuchungsgebiete repräsentieren unterschiedliche Sturzprozesse wie Felsstürze und Blockstürze. Jedoch spielt deren Differenzierung hinsichtlich der unterschiedlichen Volumina für die Auswertungen und Analysen eine untergeordnete Rolle. Dies begründet sich primär damit, dass für Publikation I Oberflächenveränderungen auf Basis von historischen Fotoaufnahmen berechnet wurden, deren Bildqualität die tatsächlich dektiertbaren Veränderungen erschweren kann. Für die Analysen in Publikation II ist eine volumenbasierte Einteilung irrelevant, da dort Reichweitenuntersuchungen von einzelnen Gesteinsblöcken unternommen wurden. Eine volumenbasierte Klassifikation ist vor allem in der Planung für Schutzbauwerke oder für die Gefahrenzonierung relevant. Ein weiteres Kriterium für die Auswahl der Gebiete war, dass sowohl die Felswände als auch die Schuttkegel deutlich und vollständig sichtbar sind, um eine vollständige Datenerfassung zu gewährleisten. Lediglich für die Untersuchungsfläche der Drei Zinnen (Publikation I) spielte der Schuttkegel für die Analyse eine untergeordnete Rolle, da sich die Arbeit vor allem auf die Felswand konzentriert. Mit Blick auf die historischen terrestrischen Fotoaufnahmen war es für diese Publikation wichtig, ein Untersuchungsgebiet zu finden, das bekannt ist, um sicherzustellen, dass eine ausreichende Quantität und Qualität an Datenmaterial vorhanden sind.

Auf die morphologischen und geologischen Bedingungen sowie auf weitere Unterscheidungsmerkmale in den einzelnen Untersuchungsgebieten wird im Folgenden näher eingegangen. Für eine detaillierte bildliche Darstellung der Untersuchungsgebiete sowie der Hänge und Schuttkegel wird auf die entsprechenden Publikationen verwiesen. Zunächst gibt Tabelle 5 einen Überblick über die Eigenschaften und lithologischen Merkmale der Untersuchungsgebiete gefolgt von zwei Übersichtskarten, die die Lage der Untersuchungsgebiete darstellen (Abbildung 3, Abbildung 4).

Tabelle 5. Ausgewählte Untersuchungsgebiete mit Eigenschaften der Höhenlage, Lithologie, Gebirgsgruppe, klimatischen Angaben sowie der jeweiligen Publikation.

	La Réunion	Gampenalm	Drei Zinnen	Dreitorspitze	Zwieselbachtal
Höhe [M. ü.d.M.]	2.632	2.450	2.999	2.682	2.278
Lithologie	Basalt	Muschelkalk, Kalkstein, Psephite	Hauptdolomit	Muschelkalk, Dolomit	Gneiss, Glimmer, metamorphe Granite
Gebirgsgruppe	Piton de la Fournaise	Dolomiten	Dolomiten	Wettersteingebirge	Stubaier Alpen
Länge [m] Schutthalde	250	250	600	300	55
Länge [m] Felswand	150	150	500	100	60
Exposition	Norden	Norden	Süden	Norden	Norden
Mittlerer jährlicher Niederschlag [mm yr^{-1}]	3.000–4.250	862,2	700–1.000	1.500	820
Mittlere jährliche Temperatur [°C]	13,8	7,8	7–10	6,7	3,1
Publikation	II, III, IV	II	I	II	II

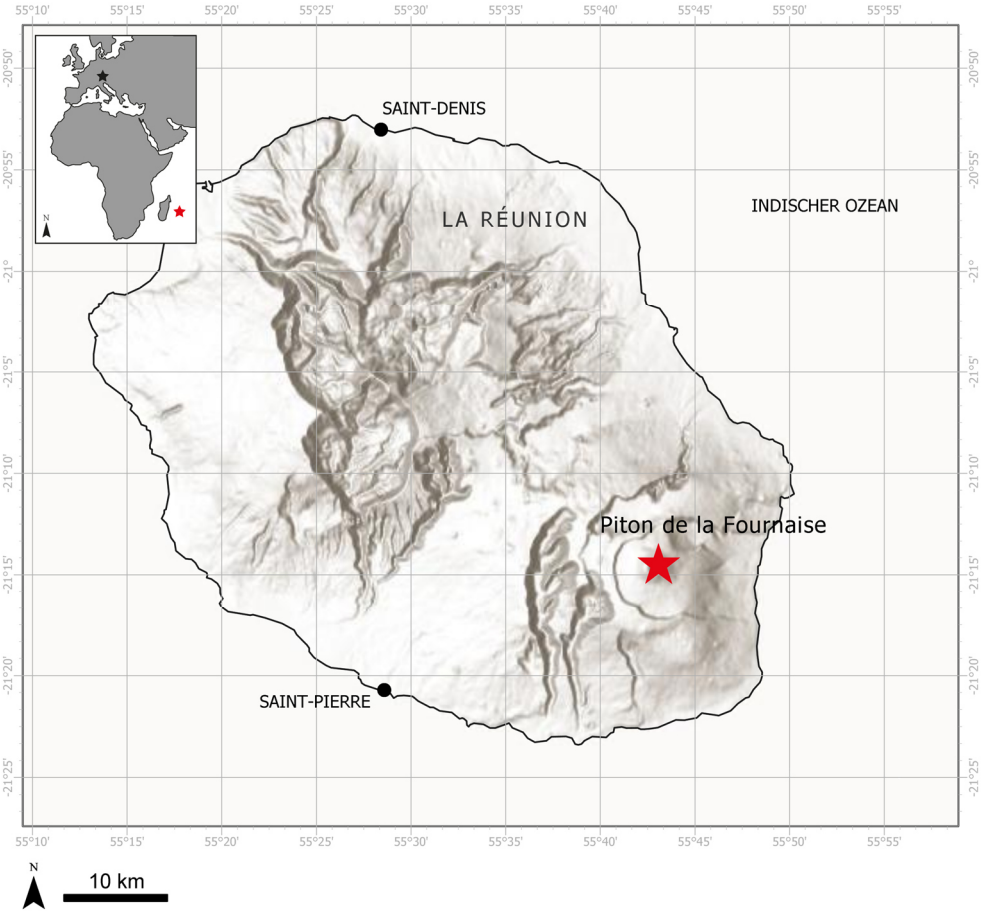

Abbildung 3. Lage des Untersuchungsgebiets, Krater Dolomieu des Piton de la Fournaise, auf der Insel La Réunion (Datenquelle der Landesgrenzen: Esri World_Countries; Datenquelle des Hillshades: Esri World Hillshade (WGS84)).

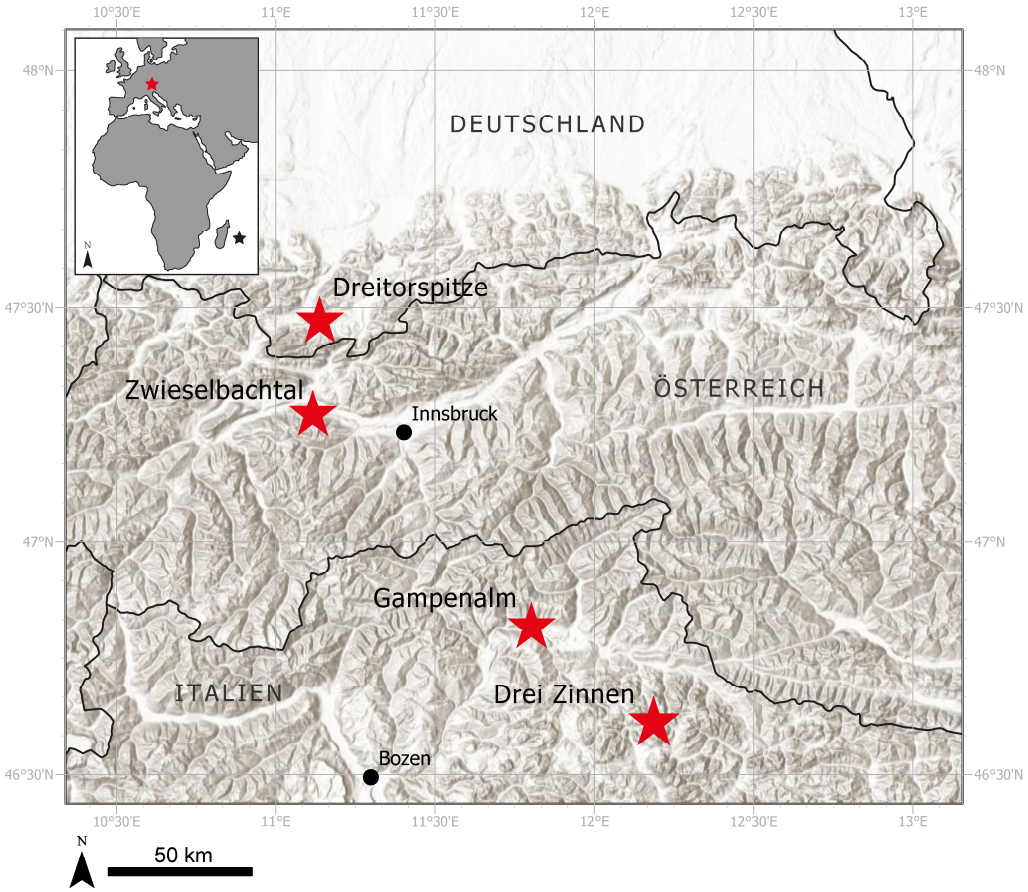

Abbildung 4. Lage der ausgewählten Untersuchungsgebiete in den Europäischen Alpen (Datenquelle der Landesgrenzen: Esri World_Countries; Datenquelle des Hillshades: Esri World Hillshade (WGS84)).

5.1 La Réunion (Piton de la Fournaise, Frankreich)

Die Insel La Réunion liegt im westlichen Indischen Ozean, etwa 700 km östlich von Madagaskar und 180 km südwestlich von Mauritius (Abbildung 3). Sie besteht aus zwei großen Schildvulkanen: dem inaktiven Piton des Neiges und dem Piton de la Fournaise, einem der aktivsten Vulkane der Welt (Peltier, et al., 2009; Roult, et al., 2012). Für den Zeitraum von 1950 bis 2013 wurden 93 Eruptionen dokumentiert (Staudacher, et al., 2016). Im Mittel kommt es zu zwei Eruptionen pro Jahr (Gailler, et al., 2022).

Der Piton de la Fournaise ist durch eine große hufeisenförmige Caldera gekennzeichnet, deren lokaler Name „*Enclos*“ lautet (Chevrel, et al., 2021). Dies ist eine 8 km breite Struktur, die im Osten zum Meer hin offen und von Klippen von bis zu 100 m Höhe im Westen, Norden und Süden umgeben ist (Chevrel, et al., 2021). Der Gipfel ist durch eine 1,1×0,8 km große und 340 m tiefe Caldera („*Cratère Dolomieu*“) gekennzeichnet (Urai, et al., 2007), die durch wiederholte Einstürze entstanden ist, wobei sich der letzte Einsturz im April 2007 ereignete (Michon, et al., 2007). Im Westen wird der Krater Dolomieu von einem kleineren (0,38×0,23 km) Krater eingefasst („*Cratère Bory*“).

Die Zusammensetzung der Lava dieses Vulkans ist hauptsächlich bimodal mit einer Kombination aus aphyrischen und olivinreichen Basalten (Peltier, et al., 2009; Lénat, et al., 2012). Aufgrund der hohen

tektonischen Belastung (Merle, et al., 2010; Staudacher, et al., 2016), der hohen vulkanischen Aktivität, der Deformation und seismischen Aktivität (Sens-Schönfelder, et al., 2014; Peltier, et al., 2018), sowie der Schichtung verschiedener Lavaströme, ist der Rand sehr instabil und daher anfällig für hohe Sturzprozessaktivität (Hibert, et al., 2017; Durand, et al., 2018).

Sowohl die Felswand als auch der Schuttkegel sind sehr junge Landformen, da die geomorphologische Formung erst unmittelbar nach dem Einsturz und der Entstehung der Caldera im Jahr 2007 begonnen hat. Neben der Ablagerung in der Caldera durch vulkanische Produkte tragen auch geomorphologische Prozesse wesentlich zur Neugestaltung dieser jungen Landschaft bei. Diese zeichnen sich durch hohe Magnituden bei gleichzeitig kurzen Frequenzen aus. Die hohe geomorphologische Aktivität ist auf die Kombination aus seismischer Aktivität, topographischen Gegebenheiten sowie hohen Niederschlagsmengen zurückzuführen (Hibert, et al., 2017; Durand, et al., 2018). Der mittlere jährliche Niederschlag beträgt 3.000–4.250 mm (Garcin, et al., 2005).

In einigen Einzugsgebieten des Vulkans wurden sogar deutlich höhere Werte registriert. Eine Klimastation am südlichen Rand des Kraters Dolomieu hat für den Zeitraum von 2010 bis 2016 einen mittleren Jahresniederschlag von 7.469 mm und ein Maximum von 9.890 mm im Jahr 2015, gemessen (OVPF & IPGP, 2008). Besonders während der Regenzeit kommt es zu intensiven Niederschlagsereignissen, die nachweislich zur Auslösung von Steinschlagprozessen beitragen (Hibert, et al., 2017; Durand, et al., 2023). Die Kombination aus jungem Alter, intensiven klimatischen Bedingungen und geologisch instabilen Strukturen schafft somit ideale Voraussetzungen für die hohe Frequenz von gravitativen Massenbewegungen im Untersuchungsgebiet.

5.2 Gampenalm (Südtirol, Italien)

Das Untersuchungsgebiet Gampenalm befindet sich in Südtirol (Italien) im oberen Tal Val di Funes (Abbildung 4). Dies ist ein Seitental des Eisacktals und gehört zu den westlichen Dolomiten.

Die Felswand der Untersuchungsfläche ist nach Norden hin exponiert und besteht aus Dolomiten, Kalksteinen und Psephiten aus der mittleren bis unteren Trias (Bosellini, et al., 2003). Diese massiven Dolomite werden von dünnen und teilweise instabilen Schichten der Buchenstein-, Contrin- und Peres-Formationen (Kalkstein und Psephite) unterlagert (Bosellini, et al., 2003). Diese lithologischen Verhältnisse mit häufigen Diskontinuitäten, Kluftsystemen und wechselnden Gesteinsfestigkeiten begünstigen Steinschlagprozesse (Frattini, et al., 2008). Der Schuttkegel ist von Steinschlag- und Murgangablagerungen dominiert und von alpinen Wiesen bedeckt.

Der Höhenunterschied zwischen der Oberkante der Felswand und den untersten Teilen des entsprechenden Schuttkegels beträgt etwa 400 m (2.050 bis 2.450 m ü.d.M.). Solche Höhenunterschiede ermöglichen eine hohe potenzielle Energie für herabstürzendes Material und damit eine hohe Relevanz für die Analyse von Reichweiten und Volumina von Sturzprozessen (Agliardi & Crosta, 2003).

Das Gebiet unterliegt einem alpinen Klima mit einer mittleren jährlichen Niederschlagsmenge von 1.000 bis 1.200 mm und eine mittlere Jahrestemperatur von 8–10 °C (Crespi, et al., 2021).

Das Untersuchungsgebiet weist eine ausgeprägte saisonale Schneedecke auf, wobei die Hauptschneeschmelzperiode von April bis Ende Mai reicht. Diese Phase ist entscheidend für das Auftreten hydrologisch gesteuerter Instabilitäten. Frost-Tau-Zyklen im Frühjahr sowie intensive Niederschläge im Sommer stellen ebenfalls bedeutende Auslöser für Sturzprozesse dar (Bonometti, et al., 2025).

5.3 Drei Zinnen (Südtirol, Italien)

Die Drei Zinnen befinden sich im Nordosten Italiens in den Sextner Dolomiten, die zu den Südalpen gehören und sich im nordöstlichsten Teil der Dolomiten befinden (Abbildung 4). Das Massiv besteht aus drei steil aufragenden Gipfeln: der „*Cima Grande*“ (2.999 m ü.d.M.) (Große Zinne), der „*Cima Ovest*“ (2.973 m ü.d.M.) (Westliche Zinne) und der „*Cima Piccola*“ (2.857 m ü.d.M.) (Kleine Zinne), die in die „*Punta di Frida*“ (2.792 m ü.d.M.) und den „*Preußturm*“ (2.700 m ü.d.M.) unterteilt ist (Abbildung 4).

Stratigraphisch sind die Sextener Dolomiten hauptsächlich aus Hauptdolomit aufgebaut, der in den flachen Gewässern des Urozeans Tethys vor etwa 200 bis 220 Millionen Jahren abgelagert wurde (Flügel, 2010). Die ausgeprägte horizontale Schrägstellung verleiht dem Gestein eine auffällige horizontale Struktur (Gianolla, et al., 2018). Der Hauptdolomit ist von vertikalen sowie subvertikalen Kluftsystemen durchzogen, welche maßgeblich zur Ausbildung einer hohen strukturellen Instabilität beitragen (Marchi, et al., 2008).

Demnach stellen die südexponierten Kanten und Felswände der einzelnen Gipfel auch vertikale Kluft- und Bruchflächen dar (Gianolla, et al., 2018). Das Plateau um die Drei Zinnen selbst wird durch den massiven Schlern-Dolomit aufgebaut. In der vertikalen Gesteinsabfolge werden der Schlern und der Hauptdolomit von den verwitterungsanfälligen und verformbaren Raibler Schichten unterlagert (Marchi, et al., 2008). Letztere bestehen hauptsächlich aus sandig-mergeligem Gestein, die eine geringere mechanische Festigkeit aufweisen und daher zur Ausbildung von Schicht- oder Denudationsterrassen neigen (Soldati, et al., 2004). Diese geologische Konstellation führt zu einer strukturellen Instabilität der überlagernden Dolomitgesteine, da die rückschreitende Erosion sowie die plastische Deformation der Raibler Schichten zu einer sukzessiven Unterhöhlung der Felspartien beitragen (Marchi, et al., 2008). Folglich entsteht ein erhöhtes Potenzial für Sturzprozesse.

An den Drei Zinnen sind Sturzprozesse ein zentrales geomorphologisches Phänomen, da das stark zerklüftete Hauptdolomitgestein durch Frost-Tau-Zyklen, tektonische Schwächezonen und intensive Witterungsprozesse in zunehmendem Maße destabilisiert wird (Gianolla, et al., 2018; Draebing & Krautblatter, 2019). Der häufige Wechsel zwischen Frost- und Tauphasen, insbesondere im Frühling und Herbst, fördert die Frostsprengung, bei der eindringendes Wasser in Klüfte eindringt, gefriert, sich ausdehnt und dadurch mechanischen Druck auf die Gesteinsmassen ausübt (Luethi, et al., 2015; Draebing, et al., 2017).Dadurch entstehen zunächst kleinere Spalten und anschließend größere Gesteinslockerungen, die in Sturzereignissen resultieren können.

Auch klimatische Ereignisse wie intensive Niederschläge oder plötzliche Schneeschmelzen, verstärken die Prozesse der Destabilisierung. Studien zeigen, dass erhöhte Feuchtigkeitswerte die Kohäsion

innerhalb des klüftigen Gesteinsverbands zusätzlich herabsetzen und damit die Wahrscheinlichkeit von Sturzprozessen signifikant erhöhen (Bonometti, et al., 2025).

Das Untersuchungsgebiet ist durch ein ausgeprägt kontinentales Klima gekennzeichnet. Die Jahresdurchschnittstemperatur beträgt 7–10 °C. Die Jahresniederschlagswerte liegen zwischen 700–1.000 mm, wobei die Niederschläge hauptsächlich im Sommer durch konvektive Ereignisse und im Winter in Form von Schnee auftreten (Cassol, 2008).

5.4 Dreitorspitze (Bayern, Deutschland)

Die Dreitorspitze ist ein markantes Bergmassiv, das sich im süd-östlichen Teil des Wettersteingebirges befindet (Deutschland) (Abbildung 4). Sie besteht aus mehreren Gipfeln, darunter die Partenkirchner Dreitorspitze (2.633 m ü. A.) und die Leutascher Dreitorspitze (2.681 m ü. A.), wobei die Leutascher Dreitorspitze als Hauptgipfel gilt und auch als Karlsspitze bekannt ist.

Die Dreitorspitze erhebt sich als eindrucksvolle Formation über dem umliegenden Karstplateau und stellt aufgrund ihrer geomorphologischen und geologischen Charakteristika ein bedeutendes Gebiet für die Analyse gravitativer Massenbewegungen dar.

Das Gebiet des Wettersteingebirges zählt tektonisch zur Lechtaldecke des Oberostalpin. Das Gebiet der Dreitorspitze wird durch dickbankigen Wettersteinkalk dominiert. Dieser entstand in einem tropisch-warmen Flachwassermilieu vor etwa 240 Millionen Jahren im Übergang von der mittleren zur oberen Trias. An der Basis befinden sich sehr reine Kalke, die von Riffkalken überlagert werden. Die stark bankige Lagerung sowie die ausgeprägte Klüftung machen den Wettersteinkalk besonders anfällig für hangabwärts gerichtete Massenbewegungen (Toschek, 2012).

Die lithologische Struktur des Wettersteinkalks ist durch ein ausgeprägtes Kluftsystem geprägt. Dieses, bestehend aus vertikalen und schräg geneigten Trennflächen, begünstigt die Entstehung und Mobilisierung von instabilen Felsmassen. Die Kluftweite, -orientierung und -vernetzung bestimmen maßgeblich das potenzielle Volumen und die Mobilität einzelner Felsstürze (Krautblatter, et al., 2012). Die klimatischen Randbedingungen wirken in Kombination mit der Geologie als Hauptauslöser für Sturzprozesse.

Das Gebiet um die Dreitorspitze ist durch ein hochalpines Klima mit einem mittleren Jahresniederschlag von ca. 1.500 mm und einer Jahresdurchschnittstemperatur von 6,7°C geprägt. Die hohe Niederschlagsrate sowie häufige Frostwechsel im Frühling und Herbst führen zu verstärkter Frostsprengung, dem Hauptprozess der physikalischen Verwitterung in Kalksteinregionen (Matsuoka & Murton, 2008). Infolge dieser Prozesse kommt es zur mechanischen Auflockerung von Gesteinsverbänden, was insbesondere im steilen Gelände zur Entstehung von Sturzprozessen führen kann.

Trotz der hohen Druckfestigkeit kann der Wettersteinkalk durch Frost-Tau-Zyklen und hydrothermale Verwitterung stark geschwächt werden, da dies zu einer sukzessiven Schwächung entlang von Klüften und Trennflächen führt, was die Stabilität von Felswänden erheblich reduziert (Krautblatter, et al., 2012).

Sturzprozesse im Bereich der Dreitorspitze äußern sich in Form von Felsstürzen, Steinschlägen sowie seltener Blockstürze. Besonders markant ist der geomorphologische Einfluss dieser Prozesse im Bereich der steilen Nord- und Ostflanken, wo rezente Abbruchkanten, Schuttkegel sowie aktive Blockfelder auftreten. Diese Strukturen zeugen von der dynamischen Entwicklung der Hänge und der fortwährenden Massenumlagerung (Heckmann & Schwanghart, 2013).

5.5 Zwieselbachtal (Stubaier Alpen, Österreich)

Das Zwieselbachtal liegt im Bereich der kristallinen Zentralalpen (Stubaier Alpen) und ist ein Seitental des Horlachtals, einem rechten Seitental des Ötztales (Österreich) (Abbildung 4). Das Horlachtal, oberhalb von Niederthai, erstreckt sich über eine Höhenlage von von 1.606 m ü.d.M. bis 3.389 m ü.d.M. Damit umfasst es ein breites Höhenspektrum, das sowohl subalpine als auch hochalpine geomorphodynamische Prozesse begünstigt (Rom, et al., 2023).

Die im Einzugsgebiet auf 1.959 m ü.d.M. Höhe gelegene meteorologische Station Horlachalm hat im Zeitraum 1991 bis 2020 eine mittlere Jahresniederschlagssumme von 817 mm und eine mittlere Jahreslufttemperatur von 3,1 ºC gemessen (Fleischer, et al., 2023; Rom, et al., 2023). Durch seine Lage in den Zentralalpen ist das Horlachtal vor advektiven Niederschlägen geschützt, was zu geringeren Jahresniederschlagssummen führt als in den nördlich angrenzenden Alpenregionen–(Becht, 1995; Geitner, 1999).

Die heutige Talform des Zwieselbachtals resultiert maßgeblich aus der pleistozänen Vergletscherung. Glaziale Erosionsformen wie Kare, Trogtäler, Hängetäler und Moränenablagerungen zeugen von intensiven glazialen Umformungsprozessen. Die Gesteinsgrundlage des Zwieselbachtals besteht vorwiegend aus stark beanspruchtem Schiefergneis, Amphibolit und metamorphen Granitoiden, die in Ost-West-Richtung streichen und parallel zur Haupttalrichtung verlaufen (Becht, 1995; Heckmann, et al., 2014). Diese Lithologien zeichnen sich durch eine hohe tektonische Vorbelastung und intensive Klüftung aus, wodurch sie als besonders verwitterungsanfällig gelten. Solche strukturellen Schwächezonen begünstigen die Initiierung von Sturzprozessen, indem sie das Gestein mechanisch auflockern und zur Ausbildung von potenziellen Bruchflächen führen (Hergarten & Neugebauer, 1999).

Infolge dieser geologischen Prädisposition weist das Zwieselbachtal eine hohe Sturzprozessaktivität auf, die sich durch ausgedehnte Schuttkegel, Blockhalden und rezente Felsabgänge widerspiegelt. Zahlreiche Hangpartien zeigen Anzeichen gravitativer Massenumlagerungen, wobei besonders die Übergangsbereiche zwischen steilen Felswänden und flacheren Talbereichen durch extensive Schuttakkumulation geprägt sind. Diese geomorphologischen Formen stellen nicht nur Hinweise auf rezente Sturzprozesse dar, sondern spiegeln auch die kontinuierliche Wirkung dieser Prozesse wider.

6 Kurzzusammenfassung der einzelnen Veröffentlichungen

6.1 Publikation I

Kerstin Wegner, Manuel Stark, Florian Haas, Michael Becht (2023): Suitability of terrestrial archival imagery for SfM-MVS based surface reconstruction of steep rock walls for the detection of rockfalls. In: *Journal of Geomorphology*, 7–39, doi: 10.1127/jgeomorphology/2023/0775.

Die Publikation befasst sich mit der 3D-Oberflächenrekonstruktion von steilen Felswänden der Drei Zinnen (Dolomiten, Italien) auf der Basis von SfM-MVS. Ziel ist die Quantifizierung von Sturzprozessen über lange Zeiträume durch die Kombination historischer und aktueller Datensätze.

Zu den Datengrundlagen zählen TLS-Daten aus dem Jahr 2018, digitale terrestrische Fotografien desselben Jahres sowie historische terrestrische Bildaufnahmen aus dem Jahr 1970. Während die TLS- und historischen Bilddaten primär zur Erfassung und Quantifizierung der Sturzprozesse herangezogen wurden, dienten die aktuellen Fotografien als wesentliche Referenzgrundlage für die Ko-Registrierung der verschiedenen Datensätze. Zusätzlich wurden sie für eine zweidimensionale Kartierung der Veränderungen an den Felswänden verwendet, um den räumlichen Verlauf der Prozesse detailliert zu dokumentieren. Aufgrund fehlender Kontrollpunkte wurden stabile Bereiche innerhalb des TLS-Datensatzes genutzt, um Referenzpunkte für die Georeferenzierung des historischen SfM-Datensatzes zu extrahieren.

Zur Vermeidung systematischer Fehler und zur Sicherstellung einer präzisen Auswertung erfolgte die Registrierung in einem zweistufigen Verfahren. Im ersten Schritt wird ein großflächiger Bereich als AOI („*area of interest*“) definiert, der das gesamte Prozessgebiet sowie angrenzende Zonen umfasst. In einem zweiten Schritt erfolgt eine gezielte Eingrenzung innerhalb dieses Rahmens, um den Fokus auf das relevante Teilgebiet zu richten und die Genaugikeit der Registrierung zu erhöhen.

Die Suche nach historischen terrestrischen Aufnahmen ist eine große Herausforderung, da sie in der Regel nicht strukturiert in Archiven aufbewahrt werden. Die Wahl der Drei Zinnen als Untersuchungsgebiet basierte auf der Erwartung einer hohen Verfügbarkeit geeigneter historischer Aufnahmen. Dennoch entsprach eine Vielzahl der gefundenen Bilder nicht den Anforderungen der SfM Photogrammetrie. Ursächlich waren unter anderem ungünstige Perspektiven, geringe Überlappung, niedrige Auflösung oder ungeeignete Belichtungsverhältnisse.

Während mit TLS und der digitalen Photogrammetrie Oberflächenveränderungen meist nur über kurze Untersuchungszeiträume erfasst werden können, ermöglichen historische Datensätze eine weit in die Vergangenheit zurückreichende Oberflächenrekonstruktion. Der Vergleich von Ergebnissen aus Langzeit- und Kurzzeitstudien erlaubt eine Einordnung aktueller Prozessraten und Dynamiken in einen langfristigen Kontext.

Dabei bietet hier die Zusammenführung von digitalisierten, ehemals analogen, Fotografien, insbesondere terrestrischen historischen Aufnahmen, mit SfM-MVS, die Möglichkeit, Untersuchungszeiträume

weiter in die Vergangenheit auszudehnen. Weiter gestatten multitemporale hochauflösende Geländemodelle, die aus TLS und SfM Photogrammetrie generiert werden, die Quantifizierung von Oberflächenveränderungen mit Hilfe eines Höhenmodells der Differenzen („*DTM of Difference*“ (DoD)).

Die Analyse der Oberflächenveränderungen in zwei ausgewählten Untersuchungsbereichen ergab Volumenveränderungen von -101,28 m^3 beziehungsweise -1872,87 m^3 im Zeitraum von 1970 bis 2018.

Allerdings werden in der Publikation auch die Limitierungen aufgezeigt. So wurde überraschenderweise nur eine geringe Anzahl an historischen terrestrischen Fotos gefunden, wobei die Qualität der Fotos zum Teil nicht den Anforderungen der SfM Photogrammetrie entsprach. Leider ist die Frage, ob historische Bilder für die Oberflächenrekonstruktion von steilen Felswänden geeignet sind, nicht generell anhand von spezifischen Parametern wie Auflösung, Anzahl der Aufnahmen oder Objekt-Sensor-Abstand zu beantworten. Eine gründliche Überprüfung und Aufbereitung der Daten sind unerlässlich, um die Eignung der einzelnen Datensätze beurteilen zu können. Dazu gehört vor allem eine ständige Kontrolle während der einzelnen Verarbeitungsschritte, die individuell an den Datensatz angepasst werden müssen.

Trotz der methodischen Herausforderungen und Einschränkungen hinsichtlich Datenqualität und Verfügbarkeit, zeigt die Studie, dass die Kombination historischer und aktueller Bilddaten grundsätzlich geeignet ist, um Sturzprozesse und morphologische Veränderungen zu quantifizieren. Dies gilt unter der Voraussetzung, dass die Datensätze bestimmte Qualitätskriterien erfüllen und individuelle Bearbeitungsschritte gewählt werden.

6.2 Publikation II

Kerstin Wegner, Florian Haas, Tobias Heckmann, Anne Mangeney, Virginie Durand, Nicolas Villeneuve, Philippe Kowalski, Aline Peltier, Michael Becht (2021): Assessing the effect of lithological setting, block characteristics and slope topography on the runout length of rock-falls in the Alps and on the island of La Réunion. In: *Natural Hazards and Earth System Sciences*, 21, 1159–1177, doi: 10.5194/nhess-21-1159-2021.

Mit dieser Studie wird der Einfluss von lithologischen Bedingungen, aber auch morphometrischen Eigenschaften der Felsblöcke und Schutthaldencharakteristiken auf die Reichweite einzelner abgelagerter Gesteinsblöcke von Sturzprozessen in unterschiedlichen Untersuchungsgebieten analysisiert.

Diese Informationen werden verwendet, um den Zusammenhang zwischen Blockgröße, -form und -lithologie auf der einen Seite und der Reichweite auf der anderen Seite zu untersuchen. Für diese vergleichende Analyse wurden vier Untersuchungsgebiete mit unterschiedlichen lithologischen Bedingungen ausgewählt. Dazu gehören drei Gebiete in den Europäischen Alpen (Gampenalm, Dreitorspitze, Zwieselbachtal) und ein Ablagerungsbereich an den inneren Flanken des Kraters Dolomieu des Vulkans Piton de la Fournaise auf La Réunion.

Die Studie verwendet hochauflösende digitale Geländemodelle (DGM) und Punktwolken aus TLS-Messungen. Auf der Basis der räumlich hochaufgelösten TLS-Daten der einzelnen Untersuchungsflächen

konnten die drei Achsen jedes Blocks durch manuelle Vermessung in der Punktwolke erfasst werden. Anhand dessen wurde sowohl das Blockvolumen als auch das Achsenverhältnis berechnet. Lediglich die Größe und Form der auf der Schutthalde abgelagerten Gesteinsblöcke sind bekannt. Informationen zur ursprünglichen Dimension der Blöcke vor dem Abbruchereignis liegen nicht vor. Um außerdem die Reichweite eines jeden Felsblocks zu bestimmen, wurde dafür der euklidische Abstand vom Ausbruchbereich zum entsprechenden Felsblock in der Punktwolke gemessen. Da jedoch die Schutthalden der Untersuchungsflächen stark divergieren, wurden die Auslauflängen für jeden einzelnen Block für den Bereich von [0, 1] normiert, um eine Vergleichbarkeit zu gewährleisten.

Zur Analyse des Einflusses der morphometrischen Eigenschaften des Hanges wurden die Neigung, Krümmung und Rauhigkeit auf Basis der hochauflösenden Geländedaten abgeleitet. Die Rauigkeit kann dabei als Indikator für die Partikelgrößenverteilung des Schuttkegels dienen. Dieser Parameter kann weitere Informationen über die gravitative Sortierung liefern, die bei einer Vergröberung im unteren Bereich des Hanges auftritt und/oder zu einer Konzentration von gröberem Material am Hangfuß führt.

Die Analysen zeigen eine komplexe Beziehung zwischen Blockgröße und der Blockform in Bezug auf die Reichweite der abgelagerten Blöcke mit Unterschieden zwischen verschiedenen lithologischen Bedingungen. Allerdings belegen die Ergebnisse, dass die Theorie der gravitativen Sortierung weder bestätigt noch verworfen werden kann. Es konnte kein eindeutiger Zusammenhang zwischen Blockgröße, Blockform und Reichweite festgestellt werden. Die Blockform wirkt jedoch in den beiden Gebieten Gampenalm und Dreitorspitze wie ein moderierender Faktor. Gesteinsblöcke mit einem kleineren axialen Verhältnis verfügen über größere Reichweiten. Die Ergebnisse variieren jedoch in Abhängigkeit davon, ob die abgelagerten Blöcke eindeutig einem Sturzereignis zugeordnet werden können (Gampenalm, Dreitorspitze) oder ob eine solche Zuordnung nicht möglich ist (Piton de la Fournaise, Zwieselbachtal). Basierend auf den vorliegenden Daten kann daher angenommen werden, dass die Blockgröße nicht die alleinige kontrollierende Variable darstellt.

Die auf TLS-Punktwolken gestützte Rauhigkeitsanalyse zeigt eine deutliche Übereinstimmung mit der Einzelblockanalyse hinsichtlich des Zusammenhangs zwischen Reichweite und Blockvolumen. Daraus lässt sich schließen, dass für solche Analysen die Verwendung der Rauigkeit anstelle von zeitaufwändigen Einzelblockmessungen geeignet ist. Diese Analysen können nicht nur auf der Grundlage von TLS Daten durchgeführt werden, sondern auch mit Hilfe von ALS Daten oder photogrammetrischen Höhenmodellen, sofern die Punktdichte ausreicht, um Blöcke einer bestimmten Größe zu erfassen.

6.3 Publikation III

Kerstin Wegner, Virginie Durand, Nicolas Villeneuve, Anne Mangeney, Philippe Kowalski, Aline Peltier, Antoine Protin, Manuel Stark, Michael Becht, Florian Haas (2024): Multitemporal Quantification of the Geomorphodynamics on a Slope within the Cratère Dolomieu at the Piton de la Fournaise (La Réunion, Indian Ocean) Using Terrestrial LiDAR Data, Terrestrial Photographs, and Webcam Data. In: *Geosciences,* 14, 1–22, doi: 10.3390/geosciences14100259.

In dieser Studie wird die Geomorphodynamik am Piton de la Fournaise (La Réunion) über einen Zeitraum von sechs Jahren (2010–2016) anhand multitemporaler Datensätze untersucht. Zum Einsatz kamen ein fest installiertes automatisiertes Kamerasystem (zwei Webcams), terrestrisches LiDAR sowie hochauflösende terrestrische Fotografien. Ziel war die Analyse von Volumenveränderungen in vier ausgewählten Untersuchungsflächen, die durch Ablagerungen gravitativer Massenbewegungen geprägt sind.

Generell ist die Erfassung von Prozessen mit hoher Magnitude, aber niedriger Frequenz problematisch und kann mit den derzeitigen Messverfahren kaum oder nur mit sehr hohem Aufwand erfolgen. Da es sich in den meisten Fällen jedoch um stichprobenartige Erhebungen handelt, ist es möglich, die Magnitude, nicht aber die Frequenz solcher Ereignisse zu bestimmen. Prozesse wie Murgänge oder Sturzprozesse können jedoch wesentlich zur Sedimentbilanz beitragen. In Hochgebirgsregionen ergibt sich neben der nicht exakt erfassbaren Häufigkeit ein weiteres Problem aufgrund der unterschiedlichen Prozesse, deren Ablagerungen sich stark überlagern, so dass eine Differenzierung zwischen den Ereignissen nicht möglich ist. Dieses Problem wird umso ausgeprägter, je geringer die zeitliche Auflösung zwischen den einzelnen Datensätzen ist, beispielsweise bei Luftbildern. Dies führt bei der Bestimmung von Frequenz und Magnitude zu Ungenauigkeiten.

Daher bieten sich terrestrische Aufnahmen an, um Veränderungen mit höherer zeitlicher Auflösung an steilen Hängen zu erfassen. Wenn die Voraussetzungen für eine photogrammetrische Auswertung gegeben sind, können mehrere Fotoaufnahmen verwendet werden, um mit einer sehr hohen zeitlichen Auflösung Einzelereignisse räumlich zu kartieren und zu identifizieren. Auf diese Weise ist es möglich, die Frequenz von Ereignissen über die Zeit sehr genau zu bestimmen. Mit SfM oder LiDAR lassen sich solche Einzelereignisse anschließend quantifizieren und in ihrer Magnitude bestimmen. Für die Analysen wurden die am nördlichen Kraterrand installierten Webcams verwendet. Allerdings sind sie nicht nach stereophotogrammetrischen Prinzipien ausgerichtet, da sie ursprünglich nicht für solche Untersuchungen vorgesehen waren.

Zusätzlich wurden Daten aus terrestrischen LiDAR Aufnahmen und hochauflösenden terrestrischen Fotos ergänzend zur Datenerfassung genutzt. Diese Datensätze wurden in den Jahren 2014, 2015 und 2016 erhoben. Die Auswertung der Webcamdaten bezieht sich auf den Zeitraum 2009–2013. Letztendlich konnten aufgrund von Qualitätsmängeln und ungünstigen Witterungsbedingungen nur Bildpaare der Webcams für die Jahre 2010 bis 2012 verwendet werden. Für die beiden ausgewählten Untersuchungsflächen mit sturzprozessdominierten Bereichen wurde für den Zeitraum 2010 bis 2016 eine Volumenänderung von 18.604 m^3 bzw. 2.921 m^3 berechnet. Darüber hinaus konnte für zwei weitere Bereiche am Hang eine Volumenänderung, ebenfalls für den Zeitraum von 2010 bis 2016, berechnet werden. Diese beträgt 2.995 m^3 bzw. 20.430 m^3.

Neben der erfolgreichen Quantifizierung unterstreichen die Ergebnisse die methodischen Herausforderungen bei der Integration unterschiedlicher Datensätze.

6.4 Publikation IV

Virginie Durand, Anne Mangeney, Florian Haas, Xiaoping Jia, Fabian Bonilla, Aline Peltier, Clément Hibert, Valérie Ferrazzini, Philippe Kowalski, Frédéric Lauret, Christophe Brunet, Claudio Satriano, Kerstin Wegner, Arthur Delorme, Nicolas Villeneuve (2018): On the Link Between External Forcings and Slope Instabilities in the Piton de la Fournaise Summit Crater, Reunion Island. In: *Journal of Geophysical Research: Earth Surface*, 123, 2422–2442, doi: 10.1029/2017JF004507.

In der Publikation wurden die Auswirkungen von Regen und Seismizität auf die Instabilität der Hänge des aktiven Vulkans Piton de la Fournaise auf La Réunion untersucht. Der Vulkan Piton de la Fournaise bietet dafür eine ideale Umgebung, um die Reaktion instabiler Hänge auf verschiedene Einflüsse zu untersuchen. Anhand seismischer Aufzeichnungen wurde ein Lage- und Volumenkatalog der Felsstürze im Krater Dolomieu erstellt. Die Validierung erfolgte durch Vergleich der Standorte und Volumina mit den aus den photogrammetrischen Daten abgeleiteten Werten. Es wurden 10.477 Steinschläge in den Jahren 2014 bis 2016 analysiert. Die seismischen Signale, die von den Sturzprozessen an vier Messstationen erzeugt werden, dienen dazu, diese zu lokalisieren. Anschließend werden die abgeleiteten Standorte und Volumina anhand der Ergebnisse aus den photogrammetrischen Daten validiert.

Die LiDAR Daten wurden im November 2014 im Rahmen einer zweitägigen Feldkampagne mit einem terrestrischen Laserscanner erfasst. Im Jahr 2016 wurden unter Einsatz von zwei verschiedenen Kamerasystemen terrestrische Fotos entlang des Kraterrands aufgenommen. Um die Qualität des photogrammetrischen Modells zu verbessern, wurden die Scanpositionen verwendet, aber auch einige zusätzliche Kamerapositionen dazwischen eingefügt.

Auf Grundlage der photogrammetrischen Auswertung wurde für die größte Ablagerung in der nordwestlichen Kraterzone ein Volumen von 80.000 m^3 ermittelt. Die seismische Analyse ergab im Vergleich dazu ein Gesamtvolumen von ca. 100.000 m^3.

Die Analyse legt nahe, dass es in diesem Bereich des Kraterrandes zu einer Absenkung kommt. Diese Annahme wird durch das Fehlen seismischer Aktivität in dieser Zone gestützt, da solche Senkungen seismisch unauffällig sind. Dies steht im Einklang mit vorhandenen negativen Oberflächenveränderungen und dem Fehlen entsprechender Ablagerungen, die sich aus den photogrammetrischen Daten ergeben. Die Analyse kommt zu dem Ergebnis, dass wiederholte Erschütterungen durch die vielen seismischen Ereignisse in Verbindung mit der Einwirkung von Niederschlag das Wachstum von Rissen in stark zerklüftetem (oder körnigem) Material bewirken, was zum Einsturz großer Volumen führt. Externe Faktoren wie Niederschläge und seismische Aktivität haben gezeigt, dass sie potenziell die Häufigkeit und das Volumen von Felsstürzen erhöhen können, wobei die Auswirkungen in Bezug auf das Volumen größer sind.

Diese Studie verdeutlicht, dass zur besseren Erklärung der Destabilisierung von Hängen durch externe Einflüsse, insbesondere durch die Auswirkungen geringer Seismizität, umfassende und systematische

Daten notwendig sind. Das Vorhandensein eines umfangreichen seismischen Datensatzes sowie photogrammetrische Daten ermöglichte einen Vergleich der Lage und des Volumens der Felsstürze, die mit Hilfe dieser beiden Datentypen erfasst wurden.

7 Publikationen

7.1 Suitability of terrestrial archival imagery for SfM-MVS based surface reconstruction of steep rock walls for the detection of rockfalls

Journal of Geomorphology
Stuttgart, July 2023

Suitability of terrestrial archival imagery for SfM-MVS based surface reconstruction of steep rock walls for the detection of rockfalls

Kerstin Wegner[1,*], Manuel Stark[1], Florian Haas[1], Michael Becht[1]

[1] Chair of Physical Geography, Catholic University of Eichstätt-Ingolstadt, Eichstätt, 85072, Germany
* Corresponding author: kwegner@ku.de

With 12 figures and 7 tables

Abstract: Rockfalls are a common geomorphological process on steep rock slopes and therefore play an important role in the geomorphological dynamics of high mountain regions. Using multi-temporal high-resolution terrain models (DTMs) generated from remote sensing data from Light Detection and Ranging (LiDAR) and Structure-from-Motion (SfM) photogrammetry, surface changes can be calculated using a DTM of Difference (DoD). Whereas surface changes can usually only be covered over short investigation periods with terrestrial laser scanning (TLS) and digital photogrammetry, historical data sets enable surface reconstruction far back into the past. Therefore, our work focuses on the combined use of TLS data, terrestrial digital and terrestrial historical images to quantify rockfalls on the steep rock faces of the *Tre Cime di Lavaredo* in the Dolomites, Italy. The reconstruction of the topography of the rock faces from past times was preceded by an intense and time-consuming search for historical terrestrial photographs. After a complex data preparation and the development of a processing workflow adapted to the data, we were able to quantify the surface changes caused by rockfalls for the observation period 1970–2018. For two areas, we calculated surface changes of -101.28 m³ and -1,872.87 m³. Our study demonstrates the potential and limitations of historical terrestrial images for a long-term geomorphic change detection analysis of rockfalls. This specific workflow, depending on the quality of the images, has to be adapted for each dataset while constant controls of the intermediate results are indispensable.

Keywords: historical terrestrial images; lidar; terrestrial laser scanning; structure from motion; rockfalls; long-term change detection

1 Introduction

The shaping of the landscape by geomorphological processes is particularly visible in high mountains, in which a multitude of individual processes and their interaction are involved. The magnitude and frequency of these processes are determined by relief and climate forcing. This process, driven e.g. by frost weathering, transports material from the rock faces to the associated scree slopes (e.g. Hungr & Evans 1988, Krautblatter & Dikau 2017). Due to the anthropogenic use of these landscapes, frequently occurring gravitational processes, in particular, pose a major threat to infrastructures and settlement areas (e.g. Pfeiffer & Bowen 1989, Ravanel et al. 2010, Volkwein et al. 2011, Frattini et al. 2012, Heiser et al. 2017, Vanneschi et al. 2019). This shows the high importance of evaluating the process dynamics of such events in the context of natural hazard analysis. Based on the combination of climatic forcing and process dynamics, the dynamics of geomorphic processes of high alpine geosystems are highly sensitive to climate variability (e.g. Magnin et al. 2017, Gallach et al. 2020, Legay et al. 2021). Consequently, changes in air temperature and precipitation inevitably affect geomorphodynamics and thus rockfall processes (Paranunzio et al. 2016, Gallach et al. 2020, Legay et al. 2021). In particular, thawing of permafrost leads to instability of the rock faces and mountain slopes (Ravanel & Deline 2010, Viero et al. 2013, Paranunzio et al. 2016, Gallach et al. 2020, IPCC 2021, Legay et al. 2021)

LiDAR (light detection and ranging) techniques, either airborne laser scanning (ALS) or terrestrial laser scanning (TLS), can be used to obtain precise topographic information to determine process variables and process areas (e.g. Abellán et al. 2011, Haas et al. 2012, Heckmann et al. 2012, Salvini et al. 2013, Royán et al.

DOI: 10.1127/jgeomorphology/2023/0775

2014, Strunden et al. 2015, Obanawa & Hayakawa 2018, Sala et al. 2019, Guerin et al. 2020a, b). Since data acquisition is coupled with high equipment and survey costs, high temporal resolution monitoring with e.g. TLS or robot tachymeters is normally carried out in particularly endangered settings only. Therefore, such data in high mountains are only available selectively and only with poor temporal resolution.

The use of digital photogrammetric methods has recently provided geosciences with another method for recording topography. Using Structure from Motion (SfM) (Ullman 1979), 3D terrain surfaces can be reconstructed from at least two photos consisting of different perspectives with a certain degree of image overlap (Eltner et al. 2016, Linder 2016, Aber et al. 2019). SfM can be coupled with multi-view stereo (MVS) algorithms for the densification of the SfM-based 3D point clouds to reconstruct the surface in detail (Carrivick et al. 2016). Due to the cost-effective use of the technology in contrast to e.g. LiDAR measurements, higher temporal resolution can be established, which allows capturing the geomorphological process dynamics in a high resolution. Based on these advantages, SfM-MVS is used in a wide range of geosciences research, such as for the analysis of rockfall dynamics (e.g. Salvini et al. 2013, Casagli et al. 2017, Vanneschi et al. 2019, Guerin et al. 2020a, Gallo et al. 2021), the monitoring of landslides (e.g. Stumpf et al. 2015, Eker et al. 2018) or glacial process research (e.g. Vivero & Lambiel 2019, Geissler et al. 2021) and in a multitude of other research fields (e.g. Jaud et al. 2019, Laporte-Fauret 2019, Derrien et al. 2020, Hemmelder et al. 2018).

The comparison of results from long-term and short-term studies allows classifying current process rates and dynamics in a long-term context. This allows to investige the influence of climate change on geomorphodynamics over longer periods. Here, the fusion of digitised (formerly analogue) photographs, particularly historical photographs, with SfM-MVS offers the possibility to extend the investigation periods further into the past. Numerous studies already exist that focus on long-term changes of, e.g., rock glacier dynamics (e.g. Fleischer et al. 2021), glacier dynamics or morphological sediment budgets (e.g. Betz et al. 2019, Altmann et al. 2020, Stark et al. 2022) within the past decades. The data used for these studies were primarily historical aerial photographs, which are well catalogued depending on the region and in most cases are available for scientific work. Due to high slope angles and typically extreme geometries of rock faces, the use of aerial imagery to capture historical rockfall dynamics is problematic. For example, Müller et al. (2014) reported an increase of vertical errors in airborne photogrammetric digital elevation models (DEMs) in areas in >40° slope, which poses a direct limitation to the monitoring of rock cliffs with aerial photography. Guerin et al. (2020a) used for their study aerial photography to analyse and quantify rockfall events over 41 years (Guerin et al. 2020a). Likewise, Ravanel & Deline (2010, 2008) used historical photographs, laser ranging with inclinometer and terrestrial laser scanning in their studies to quantify rockfalls both before and after the LIA (Little Ice Age) on the Mont Blanc Massif. However, the images used do not have the requirements for digital photogrammetry.

When historical terrestrial images meet the requirements of the SfM-MVS algorithms it offers great potential for multitemporal DTM analysis and the analyses of geomorphological processes over time spans of several decades (Eltner et al. 2016, Guerin et al. 2020a, Stark et al. 2022). In the case of steep rock faces, the advantage of terrestrial photography lies primarily in the image-object geometry (angle between object plane and lens), which, compared to aerial photography, allows a better view and consequently a more accurate reconstruction of the complex surface structures (Benjamin et al. 2020, Guerin et al. 2020a). Despite intensive research, we could not find any studies dealing with the analysis and quantification of rockfalls based on historical terrestrial imagery. The present study aims to close this research gap and to show that the combination of historical terrestrial photos and recent TLS data contains crucial potential and enables the analysis and quantification of rockfalls. This would provide the possibility to investigate rockfall dynamics into the past and to improve the understanding of e.g. the influence of changes in the climate forcing.

However, existing SfM-MVS processing workflows need to be adapted for such historical datasets, taking into account the diverse qualities and resolutions of the images. In addition to the technical aspects, the collection of historical terrestrial images is a major challenge, as they are usually not stored in a structured way in archives. Therefore, we choose a quite famous study area for which we would expect many existing historical images from different perspectives. Thus, we have chosen the *Tre Cime di Lavaredo* as one of the best-known rock formations in the Alps and we assumed that some suitable images are available, not only in public or war archives, but also in private archives. The present work was carried out using several historical terrestrial datasets starting from 1914 and two self-collected data sets from 2018 (terrestrial LiDAR and digital terrestrial photography).

2 Study site

The *Tre Cime di Lavaredo* are located in the northeast of Italy in the Sesto Dolomites, which belong to the Southern

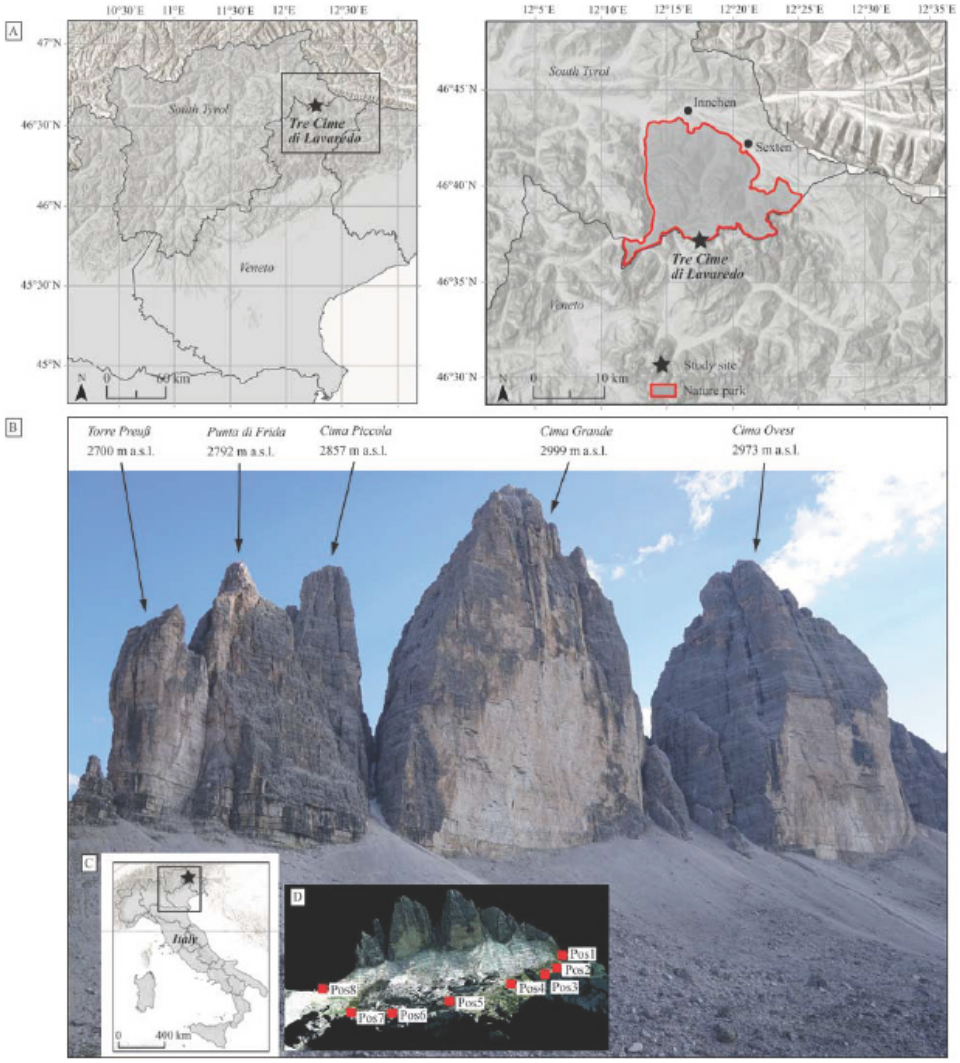

Fig. 1. Geographical location **(A, C)** of the study site (46°37'7" N, 12°18'20" E) and an image of the north-exposed rock faces of the *Tre Cime di Lavaredo* **(B)**. It was taken during the field campaign in July 2018 (own photo, view in south direction). **(D)** shows the eight TLS scan positions (Source of the overview base map: ESRI, HERE, Garmin, OpenStreetMap contributors and the GIS user community).

Alps and are located in the most north-eastern part of the Dolomites (Fig. 1). The massif consists of three steep vertical prominent peaks, the *Cima Grande* (2999 m a.s.l.), the *Cima Ovest* (2973 m a.s.l.) and the *Cima Piccola* (2857 m a.s.l.), which is separated into the *Punta di Frida* (2792 m a.s.l.) and the *Preußturm* (2700 m a.s.l.). Stratigraphically the Sexten Dolomites are mainly composed of dolomite ("Hauptdolomit"), which was deposited in the shallow waters of the Tethys Ocean about 200 to 220 million years ago. Their pronounced horizontal

banking gives the rock a striking horizontal structure. Vertical fissures, in combination with horizontal banking, are responsible for rock fragmentation along these faults. The edges and rock wall faces of the individual peaks also represent vertical fissure and fault surfaces. The plateau around the *Tre Cime di Lavaredo* itself is built up by the bulk Schlern dolomite. The Schlern and main dolomite are underlain by the weathering-prone and deformable Raibler layers. Their horizon, mostly composed of sandy-marly rock, shows layered or denudation terraces in the terrain and thus forms the unstable base on which the *Tre Cime di Lavaredo* stand. Consequently, retrogressive erosion of the Raibler layers also leads to destabilisation of the main dolomite rocks.

The study site is characterised by a typical alpine climate. The average annual temperature lies between 7–10°. The annual precipitation values are between 700–1000 mm (Autonome Provinz Bozen-Südtirol 2008).

The *Tre Cime di Lavaredo* are certainly one of the most important photo motifs of the Dolomites, if not of the entire European Alps. Easy access as well as the nearby refuge, allowed early touristic use. The rock faces were already a sought-after object for rock climbers at the beginning of alpinism (first ascent in 1869). Due to the multifaceted use, numerous photographs from different time periods, angles and distances exist.

3 Materials and methods

The method chapter outlines the data acquisition (TLS, terrestrial digital imagery), the archive research (historical terrestrial images) as well as a description of the processing of the different data sets with special attention to co-registration and adapted processing workflow.

3.1 Data acquisition

3.1.1 Terrestrial laser scanning

During a campaign on 27th of July 2018, we acquired TLS data with a terrestrial 3D long-range laser scanner (Riegl VZ-4000), which serves as a reference data set for the photogrammetric data and for additional analysis. The data collection took place during dry weather conditions and covered the north-facing rock walls. Due to the very complex topography of the study site, eight scan positions were acquired to minimize TLS shadowing effects (Neugirg et al. 2016) in order to capture the current topography in high resolution and with high accuracy. The data set was used as reference for the photogrammetric data and their analysis. The TLS specifications and survey parameters are given in Tables 1 and 2.

3.1.2 Terrestrial digital imagery

Simultaneously to the TLS survey, 118 terrestrial images were recorded using a Sony alpha 6000 system camera at two different height levels (chest and overhead level). The camera is equipped with a pre-calibrated sigma ILCE-6000 lens with a fixed focal length of 16 mm, yielding an absolute pixel size/pixel pitch (Eltner et al. 2016) of 4.07 µm. Aperture settings were defined automatically and were only slightly adjusted according to the light conditions. For all other survey parameters, see Table 3.

3.1.3 Archive research

An elaborate and time-consuming data research was necessary to find historical terrestrial images that meet the requirements of photogrammetric principles. Our research included official archives such as the German Alpine Association (Deutscher Alpenverein e.V., DAV) or the Office for Film and Media in Bolzano, South Tyrol, as well as online databases of Alpine and local history societies, museums and private archives. We also tried to identify the photographers of images in various books about the region (e.g. climbing books). The research yielded six data sets with an overall of 66 photographs of varying quality covering a period of more than 120 years from now. A large number of image sets did not fulfil the previously mentioned requirements of the SfM processing, such as high image overlaps (Torres-Sánchez et al. 2018), sufficient image quality (Bakker & Lane 2017) or resolution (Mosbrucker et al. 2017) and therefore, had to be excluded from the 3D object reconstruction.

Table 4 gives an overview of the historical images that were selected for further photogrammetric processing. After digitation all data were stored as digital images in uncompressed TIFF file format.

3.2 Data processing

3.2.1 Terrestrial laser scanning

Before the processing of LiDAR point clouds all artificial- and flying-points (e.g. dust, insect, birds) were manually removed. Since we were unable to install reference-points on the rock walls of the *Tre Cime di Lavaredo*, we manually co-registered the point clouds from the various scan positions (coarse registration on the base of well-distributed common points). Afterwards we used the RiSCAN PRO (Version 2.4) integrated iterative closest point (ICP) algorithm (Multi Station Adjustment tool, e.g. Zhang 1994, Micheletti et al. 2015) to finally register all scan positions to a common local reference frame (detailed description of the workflow in Haas et al. 2016) with a mean standard deviation of 0.026 m. After, the point cloud (56 million points in total; point density 20.16 points/m²) was exported in LAZ file format. To

Table 1. TLS specifications (Riegl Laser Measurement Systems GmbH, 2020). The values refer to measurements at a rate of 30 kHz (* = milliradian).

Parameter	Riegl VZ-4000
Max. measurement range	4,000 m
Min. measurement range	5 m
Field of view	60° (vertical) × 360° (horizontal)
Measurement rate	Max. 23,000 pts./s
Accuracy	15 mm
Precision	10 mm
Laser wavelength	Near-infrared
Laser beam divergence	0.15 mrad*

Table 2. TLS survey parameters.

Survey parameters	
No. of scan positions	8
Measurement frequency	30 kHz (23,000 points/s)
Humidity	30%
Temperature	24°C
Measurement distance	350–1,800 m

Table 3. Terrestrial digital imagery survey parameters.

Survey parameters	
Resolution	24.3 MP
Sensor	APS-C CMOS
Image overlap (horizontal and vertical)	>85%
Sensor-object distance	350–1,800 m

Table 4. Overview of the historical image data from archive research.

Year	Image count	Dimension [pixel]	Scan resolution [dpi]	Original format	Colour	Data source
1902–1930	6	6,520 × 4,162	1,200	Negative glass plates	greyscale	Universalarchiv der Deutschen Fotothek für Kunst- und Kulturgeschichte (Dresden, Germany)
1914	2	11,000 × 8,250	300	Negative glass plates	greyscale	Universalarchiv der Deutschen Fotothek für Kunst- und Kulturgeschichte (Dresden, Germany)
1964	7	8,315 × 8,315	1,200	Rollfilm negative	greyscale	Fotohaus Heimhuber (private archive)
1965	2	6,520 × 4,162	1,200	Rollfilm negative	greyscale	Amt für Film und Medien in Bozen, Sütirol, Italy
1970	42	8,580 × 8,800	4,000	Rollfilm negative	greyscale	Amt für Film und Medien in Bozen, Sütirol, Italy
1979	7	8,409 × 8,409	1,200	Rollfilm negative	greyscale	Fotohaus Heimhuber (private archive)

combine the LiDAR point clouds with the SfM raster datasets, we performed all further analyses in a 2.5D GIS environment. To obtain a z-coordinate perpendicular to the rock face, it was necessary to rotate the LiDAR point clouds (*transform pointcloud* tool in SAGA LIS, Conrad et al. 2015, Laserdata Information System, LIS: https://laserdata.at/, last access: 20.10.2022). For the georeferencing and scaling of the rock walls and the selected process areas, we extracted so-called control points (CPs) from the LiDAR point cloud. These CPs were used for all further SfM processing of historical data (see Chapter 3.2.2).

3.2.2 Image processing

Both, the historical and the high-resolution images from 2018 were processed with the same workflow (Fig. 2) with certain exceptions. Due to the significant differences between the image properties of the historical and the 2018 photo data (e.g. image quality, format, resolution, lens geometry, etc.), the settings within the SfM-MVS

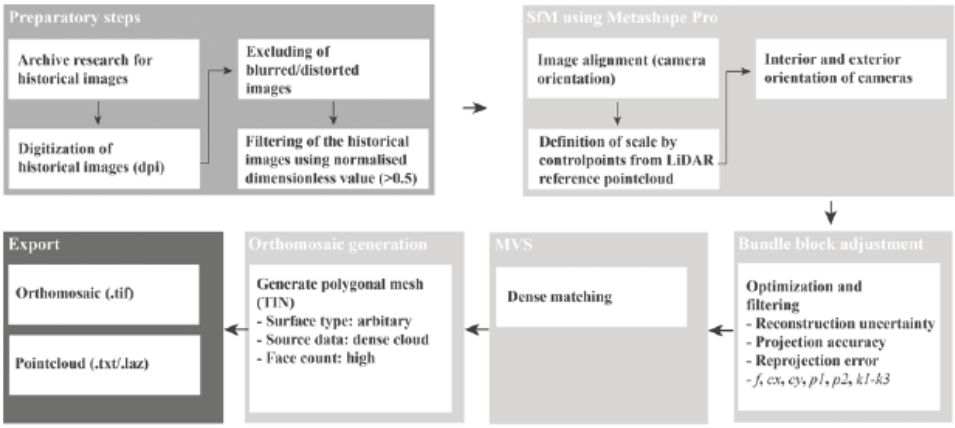

Fig. 2. Processing steps and SfM as well as MVS workflow for all images to create photomosaics and point clouds using Metashape Pro (Version 1.5.5, Agisoft LLC 2019).

processing, such as matching and densification quality, chosen camera model etc., had to be adjusted individually to the respective data set. In order to find the optimal settings, a series of test calculations were performed and the results were checked against quality and accuracy. Additionally, we filtered all images of low quality in a two-step approach. First, all blurred and fuzzy images were excluded based on visual image inspections before we applied an automatic image quality estimation (normalized dimensionless value [0;1] / 0 = low quality, 1 = high quality) within Metashape Pro (Version 1.5.5, Agisoft LLC 2019). Images with a value <0.5 were excluded from further processing. From a total of 270 photographs only six image sets (in total 66 photographs) of different dates proved to be suitable for the 3D reconstruction. All unnecessary image elements such as the sky, clouds, talus cones etc. were masked to exclude them from the image alignment.

A standard SfM-MVS workflow (Fig. 2) was performed to process all remaining images into 3D point clouds. Additionally, we calculated rectified photomosaics for all image data. The workflow contains the major steps i) camera orientation and calibration (SfM), ii) model scaling, iii) bundle block adjustments and iv) dense image matching (MVS) and is briefly described in, e.g. James et al. (2017a).

The CPs from the LiDAR data (see Chapter 3.2.1) were used to facilitate scene triangulation and reconstruction (Westoby et al. 2012) and to define and optimize exterior orientation parameters (scale, rotation and translation) of the image sets (James et al. 2017a). To improve the reconstruction quality of the photogrammetric data, different CP configurations were used and adjusted according to the respective data sets (James et al. 2017a, Tonkin & Midgley 2016, Agüera-Vega et al. 2017, Sanz-Ablanedo et al. 2018, Cabo et al. 2021). CP coordinates were extracted for structures that were readily apparent in both the LiDAR point cloud and the historical images and had not changed during the observation period. Based on careful visual observation of the respective results and the achieved RMSE of CP placement (Verma & Bourke 2019), the final parameters were chosen and the models were calculated. Due to the extreme angles between the rock faces and the camera in certain photos of the 1964/65 and 1970 data, the calculation of a model that depicts all rock faces together was abandoned and instead each rock face was calculated in a separate project of its own CP distribution (Fig. 3).

Camera parameters, such as focal length or distortion, are crucial to SfM processing. If available, these can be used to improve the results. Unfortunately, in the case of the historical terrestrial photographs no such metadata were available. Consequently, we estimated all lens parameters using the software`s internal autocalibration function. The SfM approach results in a first sparse 3D-pointcloud (tie-points) for the image data. These sparse point clouds typically contain a large number of error-prone measures which need to be filtered to improve the following bundle adjustment. Therefore, we applied certain filter operations based on the reconstruction uncertainty, projection accuracy and reprojection error for the subsequent removal of error-prone tie-points.

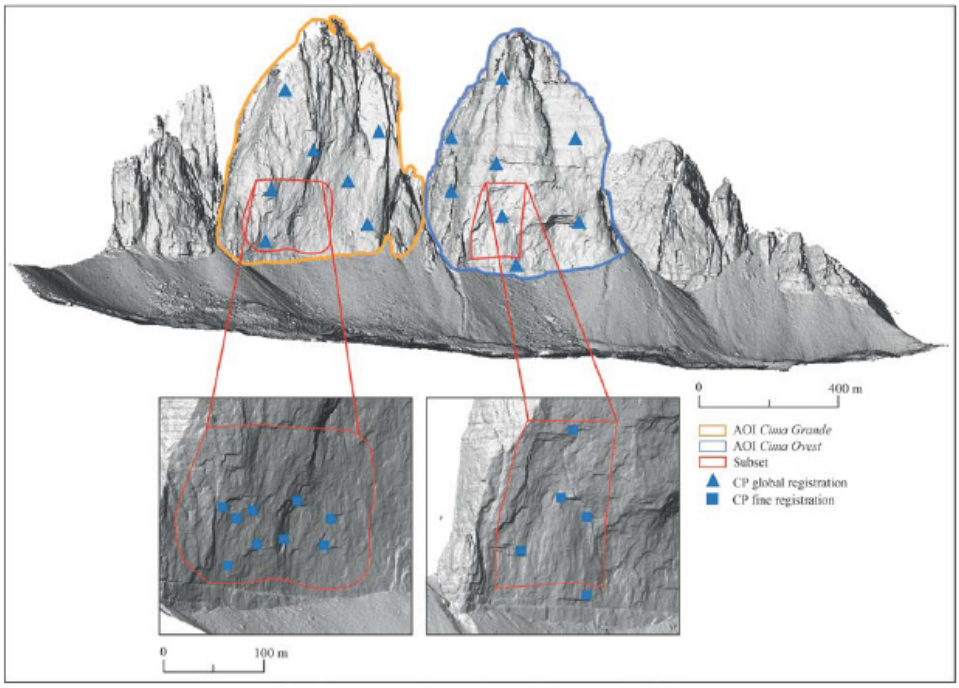

Fig. 3. Hillshade of the *Tre Cime di Lavaredo*, showing the two study areas *Cima Grande* and *Cima Ovest*. The two areas ("subset") investigated in more detail are highlighted with red polygons. Distribution of CPs on the two rock faces of *Cima Grande* and *Cima Ovest*. The triangles represent the CPs used for the first global registration step for each rock face. Using the squares, a fine registration for both rock faces was performed to increase the accuracy of the model for the corresponding area in which the rockfall occurred. View in south direction.

The projection accuracy indicates the localisation accuracy of tie-points. High reconstruction uncertainties are typical for points calculated from camera poses with a short baseline (small distance between camera positions as in the case of historical terrestrial photographs) (Agisoft LCC 2019). Together with flat angles between the projection lines of the images this can lead to high reconstruction uncertainties of the 3D coordinates. Consequently, these points can deviate considerably from the object surface, leading to noise in the photogrammetric point clouds and thus needs to be eliminated. Finally, a third filtering was used to remove points with a high reprojection error, due to poor image projections as well as by incorrect assignment of detected features. Tie-point filtering is always subject to the trade-off of removing as many poorly projected points as possible while retaining enough points with high positional accuracy to ensure seamless surface reconstruction. Although Mertes et al. (2017) and Warrick et al. (2017), among others, provide some information on the thresholds and number of tie-points used in the respective studies, they point out that no official guidelines exist in this regard and that filter settings should always depend on the given project conditions (Mayer et al. 2018). After the filtering process, the initially estimated camera parameters are optimized in the bundle adjustment. Here, the focal length (f), the principal point offsets in x and y coordinates (cx, cy) as well as radial ($k1$, $k2$ and $k3$) and two tangential distortion coefficients ($p1$, $p2$) were used for the optimization before the densification of tie-points (MVS) was applied to all data. Metashape Pro provides several quality settings for the densification of tie-points. This is especially relevant to data with low resolution and poor quality as those datasets tend to produce large gaps if the quality parameters are chosen too high. The depth filter settings for detecting outliers have been set to moderate for all

Table 5. Parameter settings for SfM processing of archival image data in Metashape Pro (Version 1.5.5).

Year	Subset	Alignment quality	Marker count / RMSE [m]	Dense cloud accuracy	Depth filter
1902–1930	*Cima Grande*	Low	No alignment possible	Medium	Moderate
	Cima Ovest				
1914	*Cima Grande*	Low	7 / 1.45	Medium	Moderate
	Cima Ovest		6 / 3.14		
1964	*Cima Grande*	Medium	6 / 1.83	High	Moderate
1965	*Cima Ovest*	Medium	6 / 2.08	High	Moderate
1970	*Cima Piccola*	Medium	10 / 0.56	High	Moderate
	Cima Grande		7 / 0.32		
	Cima Ovest		8 / 0.47		
1979	*Cima Grande*	Medium	8 / 1.94	High	Moderate
	Cima Ovest		6 / 3.57		

data (Agisoft LLC 2019). To detect and calculate volumetric changes in the rock face (along the z-axis) in a 2.5D approach (raster DTM), all point clouds and photomosaics were rotated along the x-axis and the new reference plane was spanned along the x- and y-axes. All derived point clouds were exported as ASCI.txt files and the respective rectified photomosaics were stored in uncompressed TIFF files. The entire workflow of image processing is shown in Figure 2. Table 5 summarises the parameter settings for the SfM processing of the historical datasets.

3.2.3 Two-step co-referencing of SfM and LiDAR point clouds

As we expected significant differences in resolution, accuracy and coverage of the various photogrammetric point clouds due to different data quality (James et al. 2017b, James et al. 2020, Stark et al. 2022), we aimed to minimize these differences using the ICP algorithm (see chapter 3.2.1) while taking care that the co-registration was carried out on data with similar point densities. Therefore, the LiDAR point density was adjusted (point cloud thinning) according to the density of the respective SfM point clouds. The adjustment of the individual point clouds was done for each of the *Tre Cime di Lavaredo* individually. After, we derived a first DTM of Difference (DoD) in order to identify areas with clearly visible surface changes. In total, we identified four areas for further in-depth-analyses. Despite the initial co-registration, the DTMs may still contain small systematic errors. These are minimized by a second co-registration step based on the stable surfaces near the respective process area. After, all point clouds were exported as single LAZ files for further analyses.

3.2.4 Co-referencing of photomosaics

To identify the changes on the rock faces over the epochs and match them with the results of the DoD analysis, all photomosaics were co-registered using the georeferencing function (splines) in ArcGIS Pro (version 2.7.0, Esri Inc.). This referencing was done for the areas, where clearly visible changes occurred over the observation period. Between 50–150 CPs were set per registration step to achieve a final registration accuracy of less than 0.5 m (RMSE). The photomosaic of 2018 served as reference for the co-registration. Figure 4 shows the overall workflow of the present study.

3.3 Data analysis

3.3.1 DoD analysis and LoD calculation

After the co-registration all pointclouds were imported into SAGA LIS for further processing and analysis. The point clouds were aggregated with a bilinear resampling scheme (Conrad et al. 2015) to a common DTM resolution of 0.75 m. The chosen resolution is a trade-off between the best realizable resolution and the minimum number of "no-data" cells. In the case of multiple points corresponding to one grid cell the mean z-value of the respective points was used for the aggregation. Additionally, hill shades were calculated for better visualisation of rock wall structures. The DTMs are then used to create DoD for the respective periods. Since all point clouds are subject to uncertainty due to data acquisition and co-registration, which is reflected in the DTMs generated from them (Haas et al. 2016), a level/ limit of detection (LoD) (e.g. Brasington et al. 2003, Lane et al. 2003, Bennett et al. 2012, Fey & Wichmann 2017) was used to separate measurement errors from actual topographic changes.

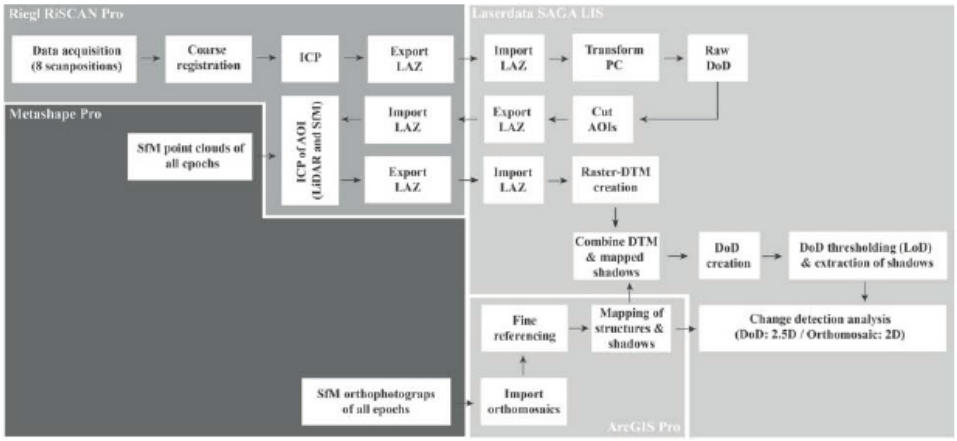

Fig. 4. Overall workflow of data processing of the TLS, terrestrial digital imagery and terrestrial historical data sets. The individual processing steps were shown for the corresponding software (Riegl RiSCAN PRO, Metashape Pro, Laserdata SAGA LIS, ArcGIS Pro).

Since it was not possible to detect CPs on the steep rock faces, we used stable areas to calculate the level of detection. The standard deviations of differences between two DTMs can be used for the calculation of the error for the resulting DoD using a simple Gaussian error propagation (i.e. Lane et al. 2003)

$$\delta_{diff} = \sqrt{\delta_1^2 + \delta_2^2} \quad (1)$$

with δ_{diff} representing the standard deviation of the stable areas. Under the assumption that errors are statistically independent, the *t*-value of each DoD-cell can be calculated with

$$t = \frac{z_1 - z_2}{\delta_{diff}} \quad (2)$$

and be compared to a critical *t*-value (*tcrit*). Here, we used a confidence interval of 87%, corresponding to a *tcrit* of |1.5|. All |t|>1.5 to be considered statistically significant surface changes. The resulting LoD (Table 7) is then calculated according to Lane et al. (2003)

$$LoD = tcrit \sqrt{\delta_1^2 + \delta_2^2} \quad (3)$$

Due to the different acquisition configurations the individual DTMs are subject to uncertainties of different magnitudes. To exclude the areas erroneously declared as process areas, a clump filter was used (Olaya 2004, SAGA LIS). The clump filter detects the neighbourhood pixels with similar values and groups them. Depending on the settings of the threshold values, the clumps are then formed and all other pixels (lone pixels and small pixel clumps) can be changed to no-data (eliminated). The further analyses are only based on clumps of a specific defined extend (minimum number of cells, defined as a clump: 120).

After these steps, volume changes of rockfall areas can be determined by subtracting the individual DTMs from each other. For the calculation of surface changes, all grid cells with negative values within the rock fall areas were first summed up and then multiplied by the square cell size.

$$V = \sum DoD * L^2 \quad (4)$$

Using the sum of the negative cell values $\sum DoD$ the net volumetric sediment change *V* can be calculated with the raster cell size *L*.

3.3.2 Mapping of shadows and topographic changes in terrestrial historical photomosaics

The individual terrestrial historical datasets differ greatly in terms of radiometric and spatial resolution but also in

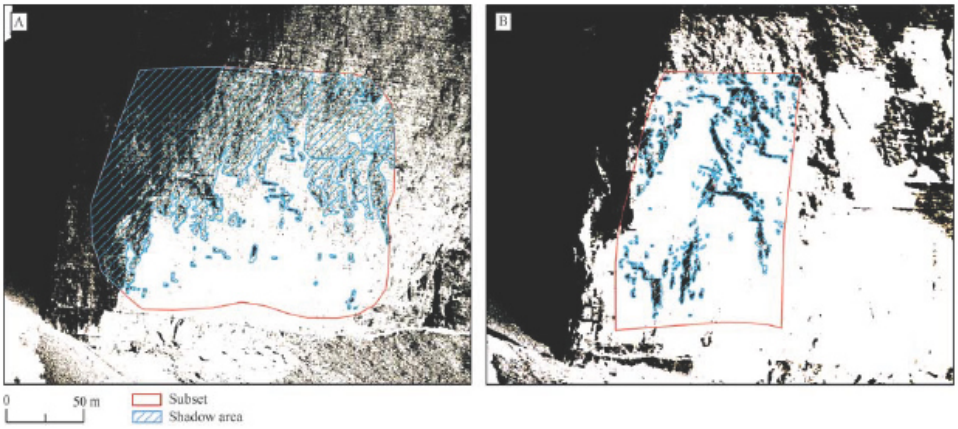

Fig. 5. Masked shadow areas of the historical images for the *Cima Grande* **(A)** and *Cima Ovest* **(B)**. The contrast value of the historical images was set to 100%. The two areas "subset", highlighted with red polygons, were investigated in more detail.

terms of entropy (exposure, contrast, etc.) and quality (physical degradation of images). As SfM is very sensitive to contrast changes in adjacent pixels, shadows can produce errors in the derived DTMs (especially in *z*-dimension). To exclude all shadowed areas from the DoD analysis, the contrast value for the historical photos was set to the maximum value (ArcGIS Pro). This facilitated the identification of shadow areas and their exclusion (reclassification tool in SAGA LIS) (Fig. 5).

To verify the derived surface changes, we tried to map major structures e.g. ridges or rock shelters in every single epoch. Figure 6 shows an exemplary mapping of these structures on the rock face. The 2D mapping was carried out in ArcGIS Pro for changes in the rock face in all epochs.

4 Results

The following chapter shows the results of TLS data processing before chapter 4.2 focuses on the results of the DTM generation from the historical photo data. The results of the change detection analysis are shown in chapter 4.3.

4.1 DTM generation from TLS data

The single scans from eight different scan positions resulted in a final 3D point cloud with approx. 56 million points with an average point density of 20.16 points/m². The co-registration of the single scans yielded a mean StD of 0.022 m (range: 0.015–0.038 m).

4.2 SfM-MVS processing of historical images

Table 6 shows the main parameters of SfM processing of the historical images for both AOIs (*Cima Grande, Cima Ovest*). The point densities, the number of points and the resulting photomosaic resolution for the year 1970 are remarkable. Rectified photomosaics were calculated for the historical data of 1970 and also for 1914 as well as for the high-resolution data of 2018 (Fig. 7). Due to low photo quality the calculation of tie-points was not possible for the years 1902 and 1930 and no DTM or rectified photomosaic could be created for this period. Although point clouds could be calculated for the 1914 data, they were excluded from further analysis because of extreme distortions, which could not be minimized despite various camera parameter settings. For this data, only 2D analysis on the photomosaics was conducted. Although the 1964/65 and 1979 photographs allowed the calculation of photomosaics, we refrained from further use of these data (change detection analysis) due to the extreme distortions that could not be corrected even by additional georeferencing operations.

4.3 Change detection analysis

4.3.1 2D-mapping of rock wall structures

Based on generated photomosaics, Figure 8 shows examples of rock areas where major changes could be mapped for the respective time periods. Looking at the 2018 mapping, it is noticeable that many of the structures that were visible in 1914 and 1970 (Fig. 8), such as outcrops,

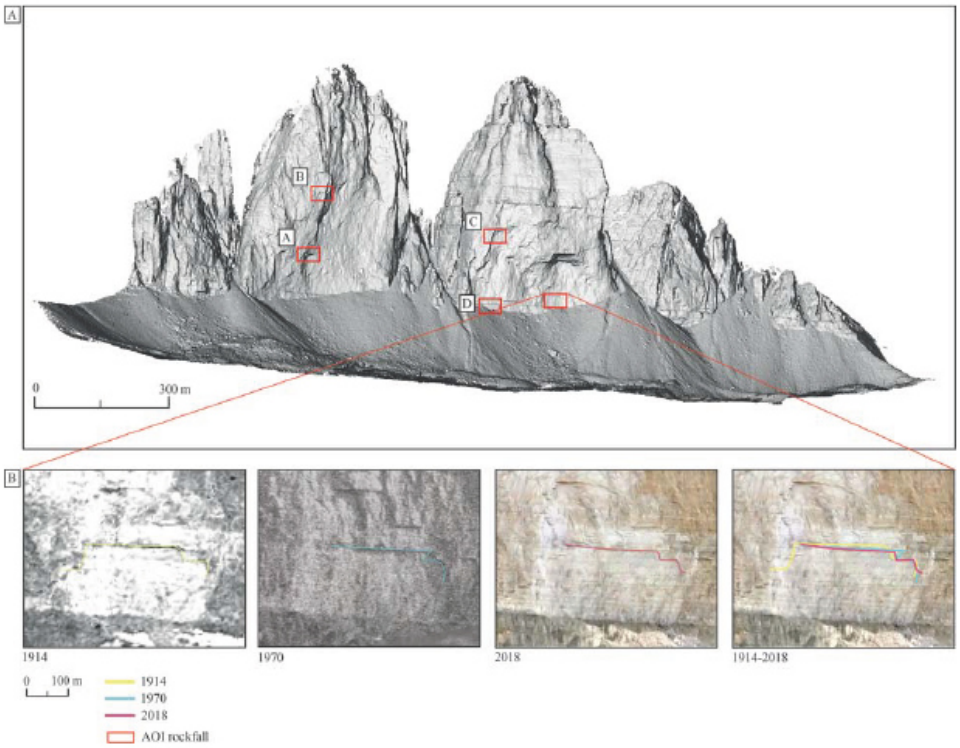

Fig. 6. (A). Hillshade of the entire *Tre Cime di Lavaredo*. The red squares A, B, C and D show the locations of the rockfall AOIs (discussed and shown in more detail later on in Chapter 4.3.1. and Fig. 8). For the areas in **(A)** and **(C)**, a further change detection analysis was carried out (see Chapter 4.3.2). **(B)**. Exemplary mapping of the structures in the rock face for all time slices used. View in south direction.

ridges, etc., mostly along the stratigraphy of the banked limestones, have changed, in some cases significantly, or were no longer present (Fig. 8A, C). The mapped area on the rock face of *Cima Ovest* (based on the 2018 photo) in Figure 8C, where there is a change in the rock face based on the photo verification, has an area of 21,870.51 m². The second mapped area on its rock face has an area of 64,269.12 m² (Fig. 8D). Based on the two-dimensional mapping of visible changes, DoD analysis were then used to quantify these changes (see Chapter 4.3.2).

4.3.2 Surface changes between 1970–2018 (DoD analysis)

The generated CPs from the TLS point cloud were successfully used to register the entire rock faces and the selected process areas. Due to the previously mentioned limitations regarding the quality of certain historical image sets, it was not possible to calculate DoD for all areas. Therefore, the change detection analysis was conducted on two specific process areas (see Fig. 8A and C in Chapter 4.3.1) for the observation period 1970–2018. The accuracies of the point cloud co-registrations and corresponding LoDs are summarised in Table 7 for both rock faces.

Despite the exclusion of the shadows (see Fig. 5) and areas with cell-changes below the respective LoD, we recognized some small fragmented zones of surface changes, which could not be verified by visual inspections (comparison of the respective orthomosaics) (Fig. 9). Although the areas of the individual changes are very small, they risk distorting the change values and therefore were excluded with the clump filter.

The filtered DoD for the *Cima Grande* clearly shows that a compact rock area broke out of the rock face

Table 6. Results of archival (1914, 1970) and 2018 image data processing.

Data	1914	1970		2018
	Cima Grande and *Cima Ovest* combined	*Cima Grande*	*Cima Ovest*	*Cima Grande* and *Cima Ovest* combined
Number of images	2	42	42	118
Mean sensor-object distance	2,700 m	1,520 m	1,690 m	1,610 m
Number of CPs	8	7	8	12
Control points RMSE (*x*, *y*, *z*)	4.6 m	0.32 m	0.47 m	0.19 m
Tie-points unfiltered [count]	187	18,330	18,424	87,293
Tie-points filtered [count]	–	14,997	15,314	67,686
RMS reprojection error	0.08 m	0.28 m	0.33 m	0.21 m
Max. reprojection error	0.19 m	0.87 m	1.10 m	0.62 m
Point cloud [count]	213,286	655,885	2,941,098	26,965,809
Mean point cloud density	0.2 p/m²	1.2 p/m²	3.9 p/m²	7.43 p/m²
Photomosaic resolution	51 cm	29.3 cm	14.3 cm	18.2 cm

Table 7. Results of the ICP adjustment between the LiDAR (2018) and archival image data (1970) as well as the DoD analysis for the stable areas. The LoD was set to a confidence interval of 87%. "Subset" refers to the area shown in Figures 5 and 9.

DTM	ICPRMSE [m]		Stable area DoD [m]			
	Rockface	Subset	Min	Max	StD	LoD
Cima Grande	0.89	0.4263	–1.9160	2.5654	0.6106	0.9159
Cima Ovest	1.08	0.5153	–2.5259	2.1147	0.5752	0.8628

(Fig. 10A). This can be verified by a visual comparison of the photomosaics from 1970 and 2018 (Fig. 10C and D) as well as by the swath profile (bandwidth 2 m) shown in Figure 10B. Some horizontal overhangs are clearly visible in the 1970 historical image (Fig. 10C), while the 2018 photomosaics no longer show this structure. Our assumption that major geomorphological changes occurred between 1970 and 2018 in this area of the rock face could be confirmed by quantitative analysis of the DoD 1970–2018 which yielded a volumetric change of -101.28 m³ and an overall process area of 34.42 m².

Figure 11 shows the filtered DoD of the AOI on the rock face *Cima Ovest*. It is clearly visible that a large contiguous area broke out of the rock face. A comparison between the 1970 and the 2018 images confirmed the results of the DoD analysis. The outcropping area becomes evident by the brighter colour of the rock (Fig. 11C) which points towards a lower stage of weathering due to lower/shorter exposure to rain and solar radiation. Compared to the previously described process area, the area of *Cima Ovest* shows a much wider extent of 474.74 m² and higher negative volume change of -1,872.87 m³.

5 Discussion

5.1 Data collection, photo quality and data processing

Overall, our expectation that a large number of photos could be collected from such a well-known mountain massif as the *Tre Cime di Lavaredo* was confirmed with a total of 270 photos from 1902. Despite the large number of historical photos, only a small portion of 42 photos (15.56%) could be used for quantitative 3D-analysis (change detection). We see the main reasons for this in (i) the lack of image pairs (stereo-images), (ii) poor image quality or varying image qualities in stereo-pairs and (iii) difficulties in determining the exact recording date (year). Figure 12 shows some examples of collected historical photos which could not be used for processing and further analysis due to the previously mentioned requirements.

Some image sets (e.g. 1914) enabled a SfM-MVS based surface reconstruction, but the respective DEMs could not be used for quantitative analysis. Reasons therefore are large geometric distortions which cause high errors in the *z*-dimension of the point clouds and

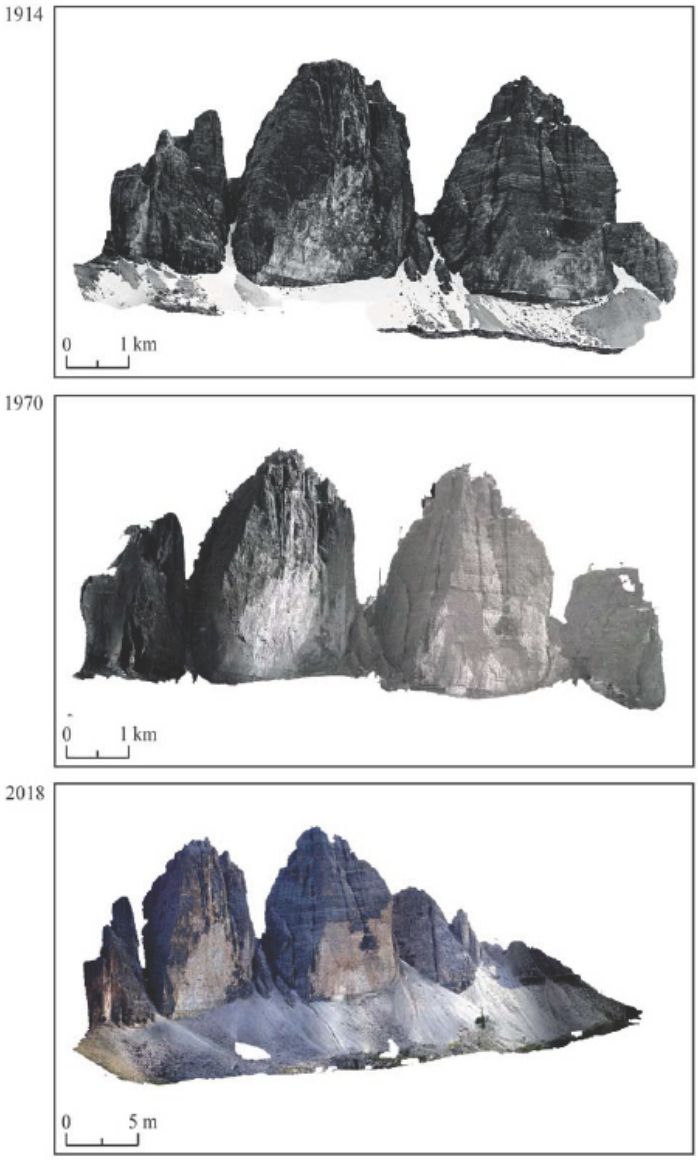

Fig. 7. Rectified photomosaics of the respective time slices 1914, 1970 and 2018. View in south direction.

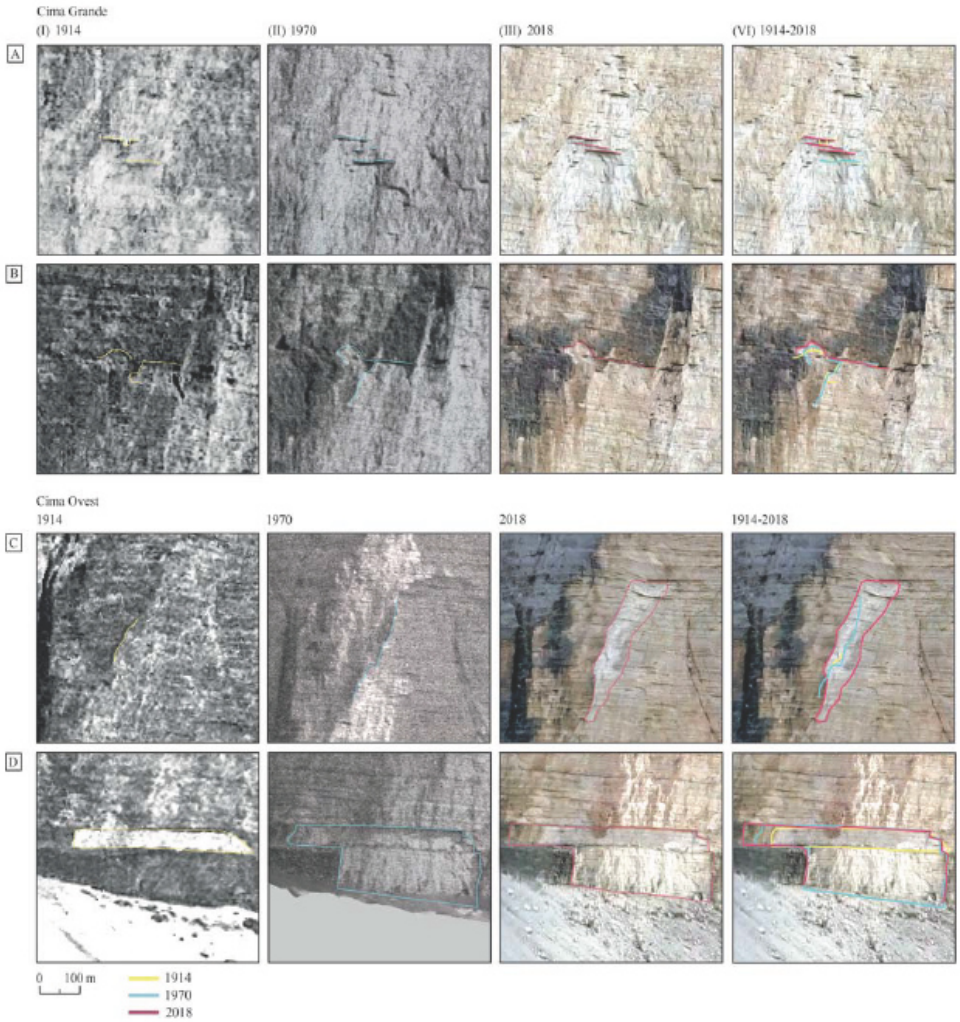

Fig. 8. 2D mapping of structures in the rock walls based on the historic images for the years 1914 (I), 1970 (II), the current dataset from 2018 (III) and surface changes (IV). **(A)–(D)** represent the areas shown in Figure 6 A. For the areas in **(A)** and **(C)**, a further change detection analysis was carried out (see Chapter 4.3.2).

respective DEMs. Despite the implementation of various processing strategies and parameters (SfM-MVS), these errors could not be minimized further. Therefore, we refrained from the use of the 3D point cloud (and DEM) of this data set and only used the photomosaic for two-dimensional analysis (mapping of structures and process areas, see Chapter 4.3.1).

Other data, such as the 1965 images showed unsuitable camera poses, overlaps or overexposure. Consequently, no tie-points can be found on the bright unweathered rock

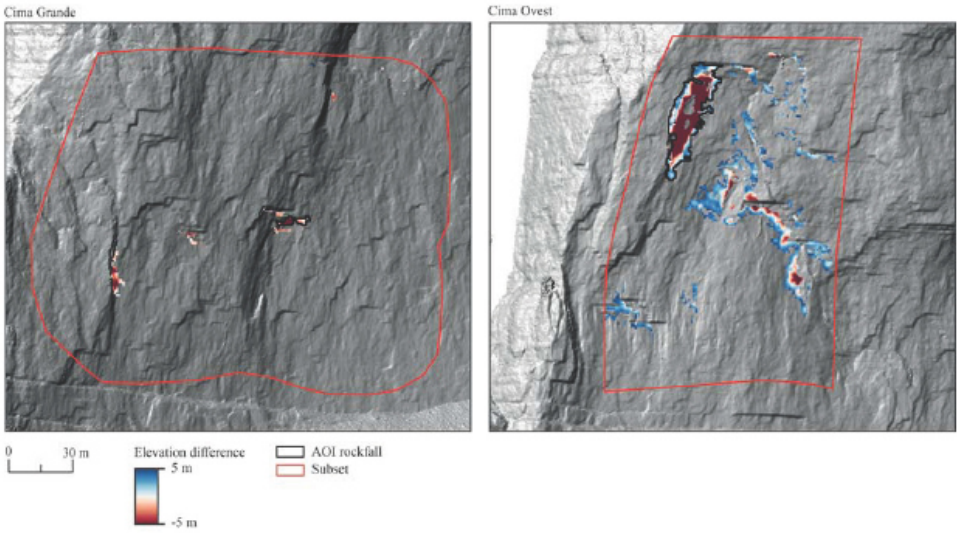

Fig. 9. DoD with applied LoD (see Table 7) and excluded shadow areas of the corresponding time epoch (1970–2018) for the two areas of the rock faces *Cima Grande* and *Cima Ovest*. The two "AOI rockfall" areas are the same as those shown in Figure 8 A and C. "Subset" represents the area that is also marked as a red polygon in Figure 5. View in south direction.

areas, as for the period of 1902–1930. The 1964/1965 and 1979 images could be processed into point clouds but the DEMs showed large geometric distortions which can be attributed to insufficient camera angles and low input quality of the images. This led to only a few tie-points as the software was not able to reconstruct the respective lens distortion parameters correctly and to calculate the appropriate camera model. This is consistent with Gomez et al. (2015) and Bakker & Lane (2017) who both point out the importance of image texture (entropy) for the bundle adjustment and feature extractions (tie-points) in the SfM processing. Aguilar et al. (2013) showed that the differences in the accuracy of a photogrammetric DTM depend significantly on the quality of bundle adjustment performances (generation of tie-points and reconstruction of camera positions based on the cameras exterior orientation parameters) and is therefore ultimately determined by the calculated camera model (e.g. Brown's 8-parameter model; Brown 1971). Relatively low image counts and image overlaps (such as in the historical data of 1902–1930, 1964/65 and 1979) can be accounted as major characteristics which contribute to difficulties in the SfM-based reconstruction of surfaces (Haas et al. 2016) and camera positions.

Image quality, especially resolution, plays another important role in image-based surface reconstruction as it determines the ability to detect terrain structures and to accurately define the location of CPs. This influences the accuracy and resolution of the final SfM-MVS product (Chirico et al. 2020). In addition to the general ability to accurately extract tie-points for feature matching, Mosbrucker et al. (2017) identified resolution or "ground sample distance" (GSD) as one of the most important factors in the quality of SfM-MVS derived products which is confirmed by the present study (photomosaic resolutions: 1914: 51 cm; 1964/65: 29.3 cm; 1970: 14.3 cm; 2018: 18.2 cm).

The discrepancies between the RMSE of the first (0.89 m for *Cima Grande* and 1.08 m for *Cima Ovest)* and the second registration steps (0.4263 m for *Cima Grande* and 0.5153 m for *Cima Ovest)* show the importance of further local co-registration processes (ICP adjustments) to minimize systematic errors in the respective DTMs. This consequently minimizes change detection thresholds and reduces noise in the DoD which leads to a more reliable detection of surface changes. This is in concordance with Stark et al. (2022) who have shown that a subsequent co-registration process of point clouds, first carried out on a wider area (e.g. rock face or catchment area) and second on a smaller process area (e.g. rockfall area, specific slope), minimizes systematic errors significantly.

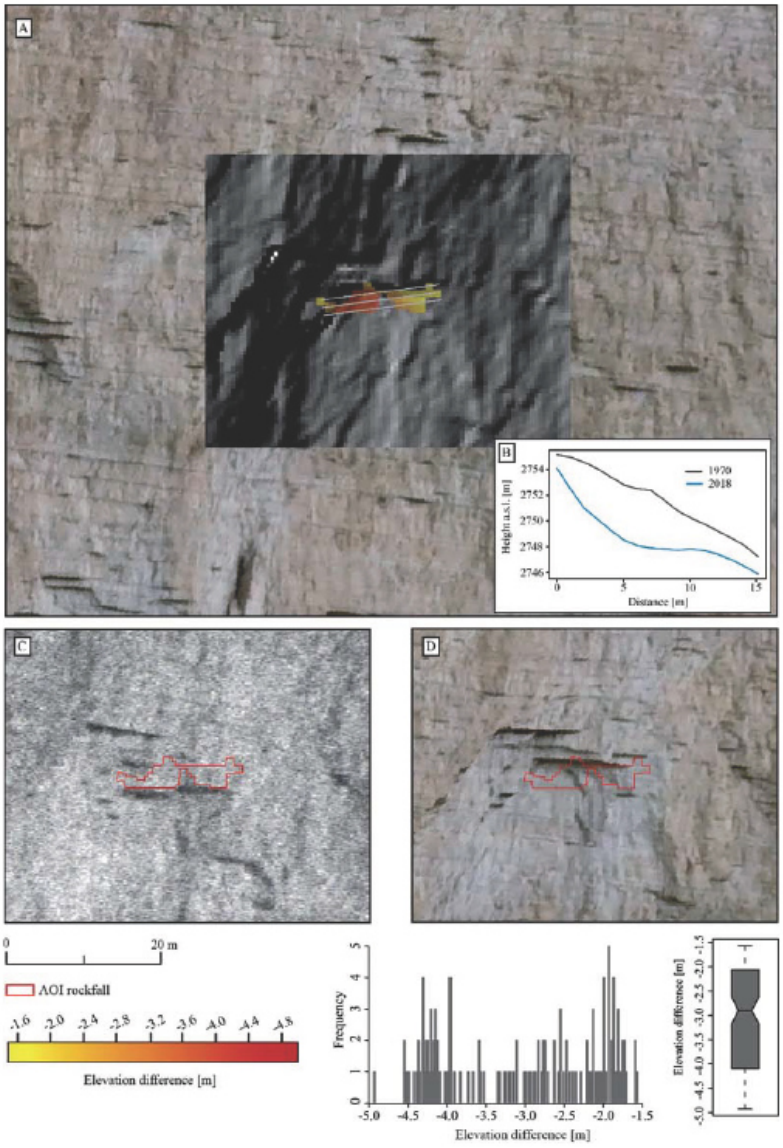

Fig. 10. Filtered DoD for the observation period 1970 to 2018 for the *Cima Grande* with a terrestrial digital image of 2018 and a hillshade **(A)**. This area is marked with the black polygon (AOI rockfall) in Figure 9 and correspond to the AOI **(A)** in Fig. 6. **(B)** shows a swath profile (2 m) for the respective data set. **(C)** and **(D)** show the erosion area based on the historical photo and the terrestrial digital image taken in 2018. View in south direction.

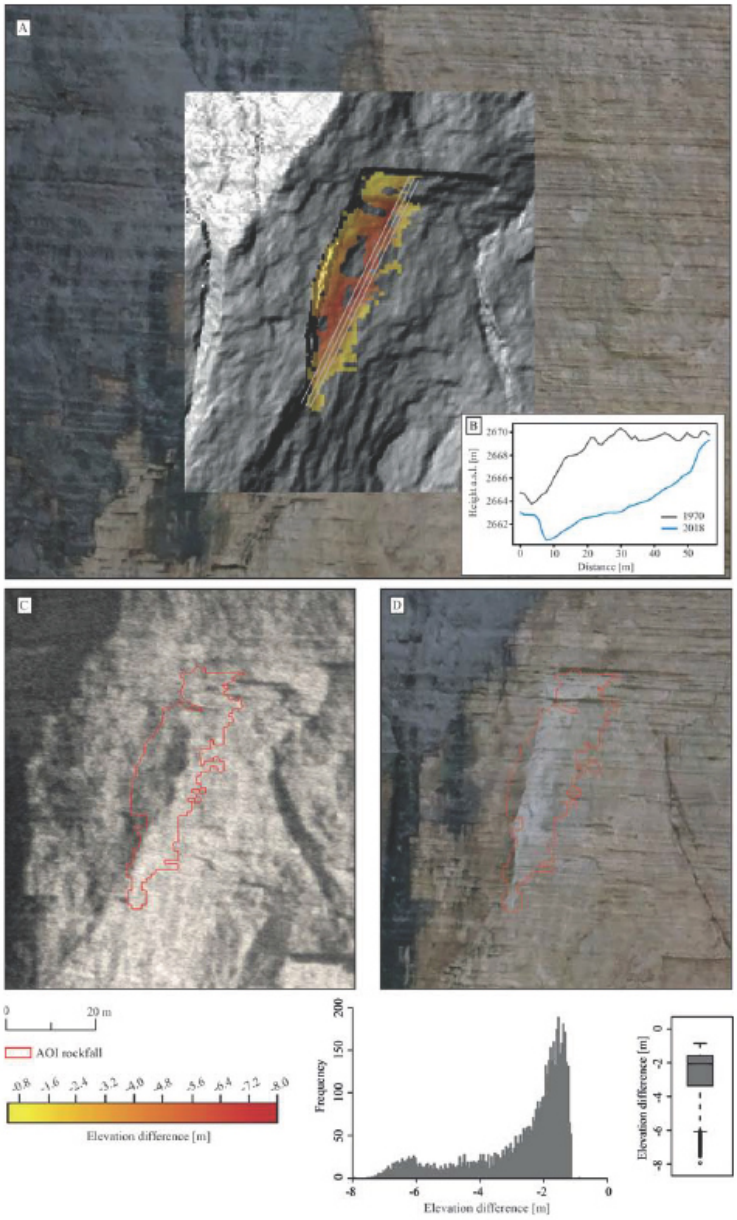

Fig. 11. Filtered DoD for the observation period 1970 to 2018 for the *Cima Ovest* with a terrestrial digital image of 2018 and a hillshade **(A)**. This area is marked with the black polygon (AOI rockfall) in Figure 9 and correspond to the AOI **(C)** in Figure 6. **(B)** shows a swath profile (2 m) for the respective data set. **(C)** and **(D)** show the erosion area based on the historical photo and the terrestrial digital image taken in 2018. View in south direction.

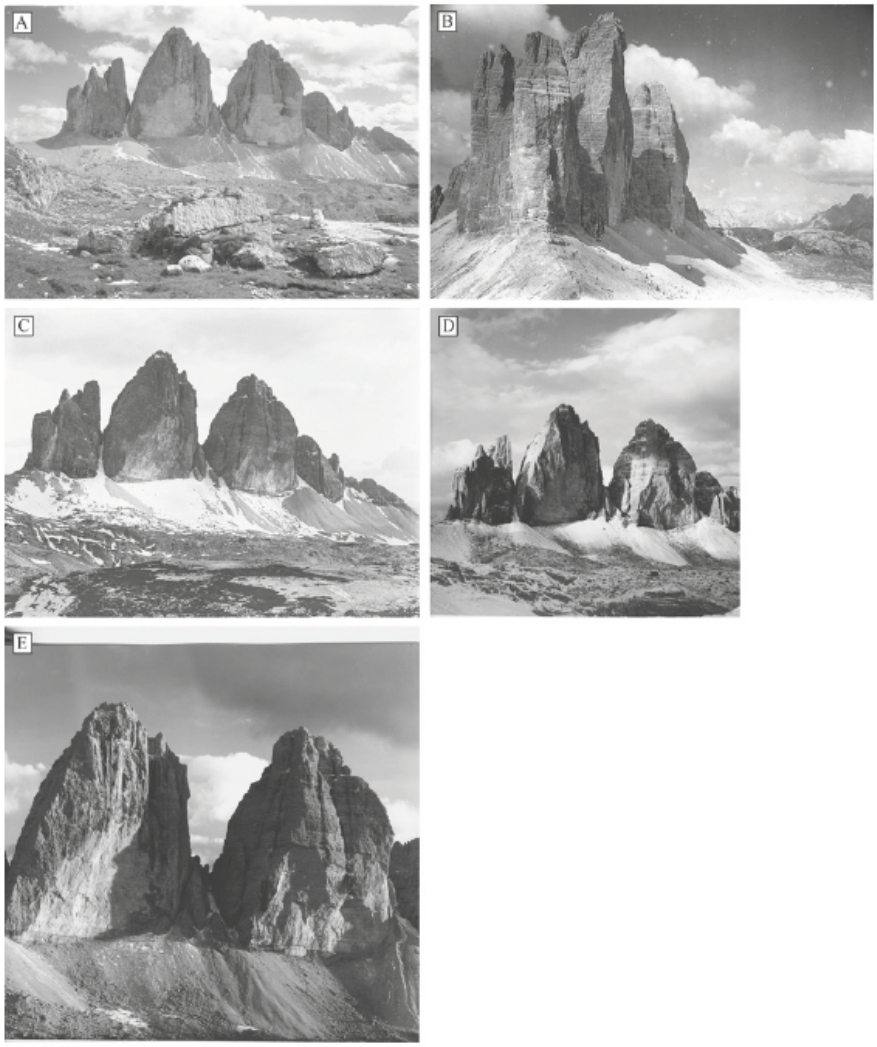

Fig. 12. An overview of the images those are not suitable for SfM-MVS processing due to different quality insufficiencies. **(A)**: The photo cannot be used for further processing due to its perspective. The other images from this data set have a comparable perspective. The date of the photo is between 1902–1930. Information about the exact date of taking the photo is not available (source: Amt für Film und Medien, Bozen, Südtirol, Italy). **(B)**: Due to contamination of the photo, it is also not processable. The perspective does not allow this either. The date when the photo was taken is between 1902 and 1939. More precise information about the exact date when the photo was taken is not available (source: Amt für Film und Medien, Bozen, Südtirol, Italy). **(C)**: This image has a different perspective between camera and object. It consists of a second photo. The photo was taken in 1914 (source: Universalarchiv der Deutschen Fotothek für Kunst- und Kulturgeschichte, Dresden, Germany). **(D)** and **(E)**: The rock faces of the two images have too many shadow areas which make point cloud processing impossible. The photo in **(D)** was taken in 1964 and the photo in **(E)** in 1979 (source: both Fotohaus Heimhuber (private archive)).

Unfortunately, the question of whether historical images are suitable for surface reconstruction of steep rock faces cannot be answered in general on the basis of specific parameters such as resolution, number of exposures or object-sensor-distance. Due to the varying qualities of the individual data sets, careful examination and preparation of the data is essential to answer the question of suitability. This includes, above all, constant controls within the individual processing steps.

5.2 Change detection

Based on the present workflow, the volume changes for the period 1970–2018 were successfully quantified. However, visual validations of the DoD revealed some outliers and incorrectly calculated surfaces due to differently pronounced shadows in the single images. This problem had been expected in the north walls of the *Tre Cime di Lavaredo*, as light and shadow in the area of the north walls change extremely depending on the time of the year and day. This led to variable lighting conditions in the images and problems in the SfM-MVS based surface reconstruction of certain data. The automatic filtering of the shadow areas led to an exclusion of these areas from the DoD and prevented erroneously reconstructed surfaces due to shadows from being included in the quantification of the volume changes. Unfortunately, this also led to an exclusion of shadow-affected areas for which smaller surface changes could be visually validated. Furthermore, the LoD led to the exclusion of additional areas for which surface changes could be verified on basis of the 2D-analysis (mapping of rock structures).

Finally, our analysis revealed two bigger rockfalls which caused extensive volumetric changes of -101.28 m³ for *Cima Grande* and -1,872.87 m³ for *Cima Ovest* between 1970 and 2018. Due to the filtering and the consideration of the LoD these volumes must be seen as minimum values. For example, the 1970–2018 DoD for the *Cima Ovest* shows a rockfall area of 474.74 m² (Fig. 11), whereas the respective 2D mapped measures 21,870.51 m². From the ratio, the filtered DoD corresponds to an area of 2.17% of the total process area.

Apart from the methodological limitations and possible options for further studies, our work has shown that the *Tre Cime di Lavaredo* represent an area characterized by the occurrence of large rockfalls. This fits well with reported rockfalls on these rock walls, but also to other studies from the Dolomites. Up to now almost all studies analysed rockfalls by means of TLS and SfM-MVS (high-resolution digital images or aerial images), but they did not use historical terrestrial images. Viero et al. (2013) investigated e.g. a bigger rockfall at the *Cima Uno* from 2007, which is also located in the Sesto Dolomites near *Tre Cime di Lavaredo*, where 40,000 m³ of dolomitic rock collapsed. Also Haas et al. (2012) quantified the volume of a rockfall in the Dolomites (Val di Funes) in 2003 with 10,373 m³ and an area of 577 m². This area of detachment fits also well with that of *Cime Ovest* with 474.74 m².

6 Conclusion

Apart from the present study, no other study has used historical terrestrial photographs to reconstruct rockwall surface. The recent state of research provided a good database for short- to mid-term analysis, but long-term analyses (several decades) are lacking. We aimed to bridge this gap with the present study and to provide more insights in the opportunities and challenges of SfM-based surface reconstruction on historical terrestrial images.

Based on the useable historical terrestrial images and recent TLS data we were able to show that point clouds and high-resolution DTMs can be generated and that the detection and quantification of surface changes of rockfalls are possible over a larger period (1970–2018). But our work also showed that processing historical terrestrial photos requires a lot of effort to reduce inaccuracies as best as possible and that despite the great effort in processing uncertainties remain. These relatively high inaccuracies and the low data availability, which is suitable for 3D reconstructions, limit the validity of the study concerning the change of rockfall dynamics in alpine areas due to climate change. For the analysis of e.g. changing frequency-magnitude relations, photos back to the early 20th century with a high temporal resolution would be necessary. Nevertheless, the present study showed that changes in the rock faces can also be recorded based on two-dimensional mappings and those changes in rockfall activity could be analysed. Unfortunately, to derive a rectified orthomosaic a photogrammetric workflow has to be applied, which limits the 2D-approach to historical data with a minimum of two overlapping images from different perspectives.

The present study also showed, that the use of historical terrestrial images is challenging in many ways. The search for historical terrestrial photographs shows that public and private archives can provide a large number of images, but that this search is time-consuming. Surprisingly, the photos were available in very different qualities and only a small fraction of the images were available as at least stereo-pairs. Therefore, we recommend extending the investigations to private photo archives to increase the number of images that can be used for 3D surface reconstructions and quantitative analysis. Searches in private collections should additionally be publicized through public appeals (on television or in print media), and data should be supplemented, e.g., through citizen science approaches.

Future research should evaluate the potential of monoplotting tools which allow two-dimensional mapping of visible process areas. The mapped changes could then be used to estimate volumes based on current high-resolution elevation models (LiDAR), as shown for example by Guerin et al. (2020b) in the Mont Blanc Massif for historical mapping. This would then enable an in-depth analysis of system changes over larger periods (e.g., due to climate change). But initially, errors in the DTMs must be reduced to optimise the spatial resolution. For monoplotting tools, inaccuracies must be minimised. This would result in an improvement of temporal resolution.

Data availability: The data used in this study are accessible upon request by contacting Kerstin Wegner (kwegner@ku.de).

Author contributions: KW, MS, FH and MB conceptualized the idea of the study. KW and MS collected the terrestrial laser scanning data of the *Tre Cime di Lavaredo*. KW conducted the archival research. KW and MS processed the data. KW analysed the data. MS, FH and MB supervised the analyses. KW wrote the draft of the manuscript with discussions and improvements from all co-authors.

Competing interests: The authors declare that they have no conflict of interest.

Acknowledgements: We greatly thank the archives (Universalarchiv der Deutschen Fotothek für Kunst- und Kulturgeschichte, Dresden, Germany, Amt für Film und Medien in Bozen, Südtirol, Italy) and Fotohaus Heimhuber (private archive) for providing the historical data sets. We also acknowledge the help during field work by the student assistant Daniel Fischer.

Financial support: The open access publication of this article was funded by the Deutsche Forschungsgemeinschaft (DFG, German Research Foundation) – Projektnummer 512640851. This research received no other external funding.

References

Abellán, A., Vilaplana, J. M., Calvet, J., García-Sellés, D., & Asensio, E. (2011). Rockfall monitoring by Terrestrial Laser Scanning – case study of the basaltic rock face at Castellfollit de la Roca (Catalonia, Spain). *Natural Hazards and Earth System Sciences, 11*(3), 829–841. https://doi.org/10.5194/nhess-11-829-2011

Aber, J. S., Marzolff, I., Ries, J. B., & Aber, S. E. W. (2019). *Small-Format Aerial Photography and UAS imagery. Principles, Techniques, and Geoscience Applications*. Amsterdam: Elsevier; https://doi.org/10.1016/C2016-0-03506-4

Agisoft LLC (2019). *Agisoft metashape user manuals, Professional edition*. Retrieved from https://www.agisoft.com/downloads/user-manuals/

Agüera-Vega, F., Carvajal-Ramírez, F., & Martínez-Carricondo, P. (2017). Assessment of photogrammetric mapping accuracy based on variation ground control points number using unmanned aerial vehicle. *Measurement, 98*, 221–227. https://doi.org/10.1016/j.measurement.2016.12.002

Aguilar, M. A., Aguilar, F. J., Fernández, I., & Mills, J. P. (2013). Accuracy assessment of commercial self-calibrating bundle adjustment routines applied to archival aerial photography. *The Photogrammetric Record, 28*(141), 96–114. https://doi.org/10.1111/j.1477-9730.2012.00704.x

Altmann, M., Piermattei, L., Haas, F., Heckmann, T., Fleischer, F., Rom, J., … Becht, M. (2020). Long-term changes of morphodynamics on Little Ice Age lateral moraines and the resulting sediment transfer into mountain streams in the Upper Kauner Valley, Austria. *Water (Basel), 12*(12), 3375. https://doi.org/10.3390/w12123375

Autonome Provinz Bozen-Südtirol (2008). *Natura 2000 Managementplan. Naturpark Drei Zinnen*. Retrieved from http://www.provinz.bz.it/natur-umwelt/natur-raum/downloads/Bericht_MP_NP-DZ_dt.pdf

Bakker, M., & Lane, S. N. (2017). Archival photogrammetric analysis of river-floodplain systems using Structure from Motion (SfM) methods. *Earth Surface Processes and Landforms, 42*(8), 1274–1286. https://doi.org/10.1002/esp.4085

Benjamin, J., Rosser, N. J., & Brain, M. J. (2020). Emergent characteristics of rockfall inventories captured at a regional scale. *Earth Surface Processes and Landforms, 45*(12), 2773–2787. https://doi.org/10.1002/esp.4929

Bennett, G. L., Molnar, P., Eisenbeiss, H., & McArdell, B. W. (2012). Erosional power in the Swiss Alps: Characterization of slope failure in the Illgraben. *Earth Surface Processes and Landforms, 37*(15), 1627–1640. https://doi.org/10.1002/esp.3263

Betz, S., Croce, V., & Becht, M. (2019). Investigating morphodynamics on Little Ice Age lateral moraines in the Italian Alps using archival aerial photogrammetry and airborne LiDAR data. *Zeitschrift für Geomorphologie, 62*(3), 231–247. https://doi.org/10.1127/zfg/2019/0629

Brasington, J., Langham, J., & Rumsby, B. (2003). Methodological sensitivity of morphometric estimates of coarse fluvial sediment transport. *Geomorphology, 53*(3-4), 299–316. https://doi.org/10.1016/S0169-555X(02)00320-3

Brown, D. C. (1971). Close-range camera calibration. *Photogrammetric Engineering, 37*, 855–866.

Cabo, C., Sanz-Ablanedo, E., Roca-Pardiñas, J., & Ordóñez, C. (2021). Influence of the number and spatial distribution of ground control points in the accuracy of UAV-SfM DEMs: An approach based on generalized additive models. *IEEE Transactions on Geoscience and Remote Sensing, 59*(12), 10618–10627. https://doi.org/10.1109/TGRS.2021.3050693

Carrivick, J. L., Smith, M. W., & Quincey, D. J. (2016). *Structure from Motion in the Geosciences*. Chichester: Wiley. https://doi.org/10.1002/9781118895818

Casagli, N., Frodella, W., Morelli, S., Tofani, V., Ciampalini, A., Intrieri, E., … Lu, P. (2017). Spaceborne, UAV and ground-

based remote sensing techniques for landslide mapping, monitoring and early warning. *Geoenvironmental Disasters, 4*(1), 9. https://doi.org/10.1186/s40677-017-0073-1

Chirico, P., DeWitt, J., & Bergstresser, S. (2020). Evaluating elevation change thresholds between structure-from-motion DEMs derived from historical aerial photos and 3DEP LiDAR data. *Remote Sensing (Basel), 12*(10), 1625. https://doi.org/10.3390/rs12101625

Conrad, O., Bechtel, B., Bock, M., Dietrich, H., Fischer, E., Gerlitz, L., … Böhner, J. (2015). System for Automated Geoscientific Analyses (SAGA) v. 2.1.4. *Geoscientific Model Development, 8*(7), 1991–2007. https://doi.org/10.5194/gmd-8-1991-2015

Derrien, A., Peltier, A., Villeneuve, N., & Staudacher, T. (2020). The 2007 caldera collapse at Piton de la Fournaise: new insights from multi-temporal structure-from-motion. *Volcanica, 3*(1), 55–65. https://doi.org/10.30909/vol.03.01.5565

Eker, R., Aydın, A., & Hübl, J. (2018). Unmanned aerial vehicle (UAV)-based monitoring of a landslide: Gallenzerkogel landslide (Ybbs-Lower Austria) case study. *Environmental Monitoring and Assessment, 190*(1), 28. https://doi.org/10.1007/s10661-017-6402-8

Eltner, A., Kaiser, A., Castillo, C., Rock, G., Neugirg, F., & Abellán, A. (2016). Image-based surface reconstruction in geomorphometry – merits, limits and developments. *Earth Surface Dynamics, 4*(2), 359–389. https://doi.org/10.5194/esurf-4-359-2016

Fey, C., & Wichmann, V. (2017). Long-range terrestrial laser scanning for geomorphological change detection in alpine terrain – handling uncertainties. *Earth Surface Processes and Landforms, 42*(5), 789–802. https://doi.org/10.1002/esp.4022

Fleischer, F., Haas, F., Piermattei, L., Pfeiffer, M., Heckmann, T., Altmann, M., … Becht, M. (2021). Multi-decadal (1953–2017) rock glacier kinematics analysed by high-resolution topographic data in the upper Kaunertal, Austria. *The Cryosphere, 15*(12), 5345–5369. https://doi.org/10.5194/tc-15-5345-2021

Frattini, P., Crosta, G. B., & Agliardi, F. (2012). Rockfall characterization and modeling. In J. J. Clague & D. Stead (Eds.), *Landslides, Types, Mechanisms and Modeling* (pp. 267–281). Cambridge, UK: Cambridge University Press. https://doi.org/10.1017/CBO9780511740367.023

Gallach, X., Carcaillet, J., Ravanel, L., Deline, P., Ogier, C., Rossi, M., … Garcia-Sellés, D. (2020). Climatic and structural controls on Late-glacial and Holocene rockfall occurrence in high-elevated rock walls of the Mont Blanc massif (Western Alps). *Earth Surface Processes and Landforms, 45*(13), 3071–3091. https://doi.org/10.1002/esp.4952

Gallo, I. G., Martínez-Corbella, M., Sarro, R., Iovine, G., López-Vinielles, J., Hérnandez, M., … Garcia-Davalillo, J. C. (2021). An integration of UAV-based photogrammetry and 3D modelling for rockfall hazard assessment: The Cárcavos case in 2018 (Spain). *Remote Sensing (Basel), 13*(17), 3450. https://doi.org/10.3390/rs13173450

Geissler, J., Mayer, C., Jubanski, J., Münzer, U., & Siegert, F. (2021). Analyzing glacier retreat and mass balances using aerial and UAV photogrammetry in the Ötztal Alps, Austria. *The Cryosphere, 15*(8), 3699–3717. https://doi.org/10.5194/tc-15-3699-2021

Gomez, C., Hayakawa, Y., & Obanawa, H. (2015). A study of Japanese landscapes using structure from motion derived DSMs and DEMs based on historical aerial photographs: New opportunities for vegetation monitoring and diachronic geomorphology. *Geomorphology, 242*, 11–20. https://doi.org/10.1016/j.geomorph.2015.02.021

Guerin, A., Stock, G. M., Radue, M. J., Jaboyedoff, M., Collins, B. D., Matasci, B., … Derron, M.-H. (2020a). Quantifying 40 years of rockfall activity in Yosemite Valley with historical Structure-from-Motion photogrammetry and terrestrial laser scanning. *Geomorphology, 356*, 107069. https://doi.org/10.1016/j.geomorph.2020.107069

Guerin, A., Ravanel, L., Matasci, B., Jaboyedoff, M., & Deline, P. (2020b). The three-stage rock failure dynamics of the Drus (Mont Blanc massif, France) since the June 2005 large event. *Scientific Reports, 10*(1), 17330. https://doi.org/10.1038/s41598-020-74162-1

Haas, F., Heckmann, T., Wichmann, V., & Becht, M. (2012). Runout analysis of a large rockfall in the Dolomites/Italian Alps using LIDAR derived particle sizes and shapes. *Earth Surface Processes and Landforms, 37*(13), 1444–1455. https://doi.org/10.1002/esp.3295

Haas, F., Hilger, L., Neugirg, F., Umstädter, K., Breitung, C., Fischer, P., … Becht, M. (2016). Quantification and analysis of geomorphic processes on a recultivated iron ore mine on the Italian island of Elba using long-term ground-based lidar and photogrammetric SfM data by a UAV. *Natural Hazards and Earth System Sciences, 16*(5), 1269–1288. https://doi.org/10.5194/nhess-16-1269-2016

Heckmann, T., Bimböse, M., Krautblatter, M., Haas, F., Becht, M., & Morche, D. (2012). From geotechnical analysis to quantification and modeling using LiDAR data: A study on rockfall in the Reintal catchment, Bavarian Alps, Germany. *Earth Surface Processes and Landforms, 37*(1), 119–133. https://doi.org/10.1002/esp.2250

Heiser, M., Scheidl, C., & Kaitna, R. (2017). Evaluation concepts to compare observed and simulated deposition areas of mass movements. *Computational Geosciences, 21*(3), 335–343. https://doi.org/10.1007/s10596-016-9609-9

Hemmelder, S., Marra, W., Markies, H., & De Jong, S. M. (2018). Monitoring river morphology & bank erosion using UAV imagery – A case study of the river Buëch, Hautes-Alpes, France. *International Journal of Applied Earth Observation and Geoinformation, 73*, 428–437. https://doi.org/10.1016/j.jag.2018.07.016

Hungr, O., & Evans, S. G. (1988). Engineering evaluation of fragmental rockfall hazards. *Proceedings of the 5th International Symposium on Landslides in Lausanne* (p. 685–690). Rotterdam: Balkema.

IPCC (2021). Climate Change 2021: The Physical Science Basis. Contribution of Working Group I to the Sixth Assessment Report of the Intergovernmental Panel on Climate Change. In V. Masson-Delmotte, A. Pirani, S. L. Connors, C. Péan, S. Berger, N. Caud, & B. Zhou (Eds.), Cambridge, UK: Cambridge University Press.

James, M. R., Robson, S., d'Oleire-Oltmanns, S., & Niethammer, U. (2017a). Optimising UAV topographic surveys pro-

cessed with structure-from-motion: Ground control quality, quantity and bundle adjustment. *Geomorphology, 280*, 51–66. https://doi.org/10.1016/j.geomorph.2016.11.021

James, M. R., Robson, S., & Smith, M. W. (2017b). 3-D uncertainty-based topographic change detection with structure-from-motion photogrammetry: Precision maps for ground control and directly georeferenced surveys. *Earth Surface Processes and Landforms, 42*(12), 1769–1788. https://doi.org/10.1002/esp.4125

James, M. R., Antoniazza, G., Robson, S., & Lane, S. N. (2020). Mitigating systematic error in topographic models for geomorphic change detection: Accuracy, precision and considerations beyond off-nadir imagery. *Earth Surface Processes and Landforms, 45*(10), 2251–2271. https://doi.org/10.1002/esp.4878

Jaud, M., Letortu, P., Théry, C., Grandjean, P., Costa, S., Maquaire, O., … Le Dantec, N. (2019). UAV survey of a coastal cliff face – selection of the best imaging angle. *Measurement, 139*, 10–20. https://doi.org/10.1016/j.measurement.2019.02.024

Krautblatter, M., & Dikau, R. (2007). Towards a uniform concept for the comparison and extrapolation of rockwall retreat and rockfall supply. *Geografiska Annaler: Series A. Physical Geography, 89*(1), 21–40. https://doi.org/10.1111/j.1468-0459.2007.00305.x

Lane, S. N., Westaway, R. M., & Hicks, D. M. (2003). Estimation of erosion and deposition volumes in a large, gravel-bed, braided river using synoptic remote sensing. *Earth Surface Processes and Landforms, 28*(3), 249–271. https://doi.org/10.1002/esp.483

Laporte-Fauret, Q., Marieu, V., Castelle, B., Michalet, R., Bujan, S., & Rosebery, D. (2019). Low-cost UAV for high-resolution and large-scale coastal dune change monitoring using photogrammetry. *Journal of Marine Science and Engineering, 7*(3), 63. https://doi.org/10.3390/jmse7030063

Legay, A., Magnin, F., & Ravanel, L. (2021). Rock temperature prior to failure: Analysis of 209 rockfall events in the Mont Blanc massif (Western European Alps). *Permafrost and Periglacial Processes, 32*(3), 520–536. https://doi.org/10.1002/ppp.2110

Linder, W. (2016). *Digital photogrammetry: a practical course*. Berlin: Springer; https://doi.org/10.1007/978-3-662-50463-5

Magnin, F., Josnin, J.-Y., Ravanel, L., Pergaud, J., Pohl, B., & Deline, P. (2017). Modelling rock wall permafrost degradation in the Mont Blanc massif from the LIA to the end of the 21st century. *The Cryosphere, 11*(4), 1813–1834. https://doi.org/10.5194/tc-11-1813-2017

Mayer, C., Gomes Pereira, L. M., & Kersten, T. P. (2018). A comprehensive workflow to process UAV images for the efficient production of accurate geo-information. *IX. National Conference on Cartography and Geodesy*, 1–8.

Mertes, J. R., Gulley, J. D., Benn, D. I., Thompson, S. S., & Nicholson, L. I. (2017). Using structure-from-motion to create glacier DEMs and orthoimagery from historical terrestrial and oblique aerial imagery. *Earth Surface Processes and Landforms, 42*(14), 2350–2364. https://doi.org/10.1002/esp.4188

Micheletti, N., Chandler, J. H., & Lane, S. N. (2015). Investigating the geomorphological potential of freely available and accessible structure-from-motion photogrammetry using a smartphone. *Earth Surface Processes and Landforms, 40*(4), 473–486. https://doi.org/10.1002/esp.3648

Mosbrucker, A. R., Major, J. J., Spicer, K. R., & Pitlick, J. (2017). Camera system considerations for geomorphic applications of SfM photogrammetry. *Earth Surface Processes and Landforms, 42*(6), 969–986. https://doi.org/10.1002/esp.4066

Müller, J., Gärtner-Roer, I., Thee, P., & Ginzler, C. (2014). Accuracy assessment of airborne photogrammetrically derived high-resolution digital elevation models in a high mountain environment. *ISPRS Journal of Photogrammetry and Remote Sensing, 98*, 58–69. https://doi.org/10.1016/j.isprsjprs.2014.09.015

Neugirg, F., Stark, M., Kaiser, A., Vlácilová, M., Della Seta, M., Vergari, F., … Haas, F. (2016). Erosion processes in calanchi in the Upper Orcia Valley, Southern Tuscany, Italy based on multitemporal high-resolution terrestrial LiDAR and UAV surveys. *Geomorphology, 269*, 8–22. https://doi.org/10.1016/j.geomorph.2016.06.027

Obanawa, H., & Hayakawa, Y. S. (2018). Variations in volumetric erosion rates of bedrock cliffs on a small inaccessible coastal island determined using measurements by an unmanned aerial vehicle with structure-from-motion and terrestrial laser scanning. *Progress in Earth and Planetary Science, 5*(1), 33. https://doi.org/10.1186/s40645-018-0191-8

Olaya, V. (2014). *Module filter clumps*. Retrieved from https://libguides.library.usyd.edu.au/c.php?g=508212&p=3476096

Paranunzio, R., Laio, F., Chiarle, M., Nigrelli, G., & Guzzetti, F. (2016). Climate anomalies associated with the occurrence of rockfalls at high-elevation in the Italian Alps. *Natural Hazards and Earth System Sciences, 16*(9), 2085–2106. https://doi.org/10.5194/nhess-16-2085-2016

Pfeiffer, T. J., & Bowen, T. D. (1989). Computer simulations of rockfalls. *Environmental & Engineering Geoscience, xxvi* (1), 135–146. https://doi.org/10.2113/gseegeosci.xxvi.1.135

Ravanel, L., & Deline, P. (2008). The West Face of Les Drus (Mont-Blanc massif): slope instability in a high-Alpine steep rock wall since the end of the Little Ice Age. *Géomorphologie: Relief, Processus. Environnement, 4*, 261–272.

Ravanel, L., & Deline, P. (2010). Climate influence on rockfalls in high-Alpine steep rockwalls: The north side of the Aiguilles de Chamonix (Mont Blanc massif) since the end of the 'Little Ice Age'. *The Holocene, 21*(2), 357–365. https://doi.org/10.1177/0959683610374887

Ravanel, L., Allignol, F., Deline, P., Gruber, S., & Ravello, M. (2010). Rock falls in the Mont Blanc massif in 2007 and 2008. *Landslides, 7*(4), 493–501. https://doi.org/10.1007/s10346-010-0206-z

RIEGL Laser Measurement Systems GmbH (2020). *RIEGL VZ-4000*. Retrieved from http://www.riegl.com/uploads/tx_pxpriegldownloads/RIEGL_VZ-4000_Datasheet_2020-09-14.pdf

Royán, M. J., Abellán, A., Jaboyedoff, M., Vilaplana, J. M., & Calvet, J. (2014). Spatio-temporal analysis of rockfall pre-

failure deformation using Terrestrial LiDAR. *Landslides, 11*(4), 697–709. https://doi.org/10.1007/s10346-013-0442-0

Sala, Z., Hutchinson, D. J., & Harrap, R. (2019). Simulation of fragmental rockfalls detected using terrestrial laser scans from rockslopes in south-central British Columbia, Canada. *Natural Hazards and Earth System Sciences, 19*(11), 2385–2404. https://doi.org/10.5194/nhess-19-2385-2019

Salvini, R., Francioni, M., Riccucci, S., Bonciani, F., & Callegari, I. (2013). Photogrammetry and laser scanning for analyzing slope stability and rock fall runout along the Domodossola-Iselle railway, the Italian Alps. *Geomorphology, 185*, 110–122. https://doi.org/10.1016/j.geomorph.2012.12.020

Sanz-Ablanedo, E., Chandler, J. H., Rodríguez-Pérez, J. R., & Ordóñez, C. (2018). Accuracy of Unmanned Aerial Vehicle (UAV) and SfM photogrammetry survey as a function of the number and location of ground control points used. *Remote Sensing (Basel), 10*(10), 1606. https://doi.org/10.3390/rs10101606

Stark, M., Rom, J., Haas, F., Piermattei, L., Fleischer, F., Altmann, M., & Becht, M. (2022). Long-term assessment of terrain changes and calculation of erosion rates in an alpine catchment based on SfM-MVS processing of historical aerial images. How camera information and processing strategy affect quantitative analysis. *Journal of Geomorphology, 1*(1), 43–77. https://doi.org/10.1127/jgeomorphology/2022/0755

Strunden, J., Ehlers, T. A., Brehm, D., & Nettesheim, M. (2015). Spatial and temporal variations in rockfall determined from TLS measurements in a deglaciated valley, Switzerland. *Journal of Geophysical Research. Earth Surface, 120*(7), 1251–1273. https://doi.org/10.1002/2014JF003274

Stumpf, A., Malet, J.-P., Allemand, P., Pierrot-Deseilligny, M., & Skupinski, G. (2015). Ground-based multi-view photogrammetry for the monitoring of landslide deformation and erosion. *Geomorphology, 231*, 130–145. https://doi.org/10.1016/j.geomorph.2014.10.039

Tonkin, T. N., & Midgley, N. G. (2016). Ground-control networks for image based surface reconstruction: An investigation of optimum survey designs using UAV derived imagery and structure-from-motion photogrammetry. *Remote Sensing (Basel), 8*(9), 786. https://doi.org/10.3390/rs8090786

Torres-Sánchez, J., López-Granados, F., Borra-Serrano, I., & Peña, J. M. (2018). Assessing UAV-collected image overlap influence on computation time and digital surface model accuracy in olive orchards. *Precision Agriculture, 19*(1), 115–133. https://doi.org/10.1007/s11119-017-9502-0

Ullman, S. (1979). The interpretation of structure from motion. *Proceedings of the Royal Society of London. Series B, Biological Sciences, 203*(1153), 405–426. https://doi.org/10.1098/rspb.1979.0006

Vanneschi, C., Di Camillo, M., Aiello, E., Bonciani, F., & Salvini, R. (2019). SfM-MVS photogrammetry for rockfall analysis and hazard assessment along the ancient Roman Via Flaminia road at the Furlo Gorge (Italy). *ISPRS International Journal of Geo-Information, 8*(8), 325. https://doi.org/10.3390/ijgi8080325

Verma, A. K., & Bourke, M. C. (2019). A method based on structure-from-motion photogrammetry to generate sub-millimetre-resolution digital elevation models for investigating rock breakdown features. *Earth Surface Dynamics, 7*(1), 45–66. https://doi.org/10.5194/esurf-7-45-2019

Viero, A., Furlanis, S., Squarzoni, C., Teza, G., Galgaro, A., & Gianolla, P. (2013). Dynamics and mass balance of the 2007 Cima Una rockfall (Eastern Alps, Italy). *Landslides, 10*(4), 393–408. https://doi.org/10.1007/s10346-012-0338-4

Vivero, S., & Lambiel, C. (2019). Monitoring the crisis of a rock glacier with repeated UAV surveys. *Geographica Helvetica, 74*(1), 59–69. https://doi.org/10.5194/gh-74-59-2019

Volkwein, A., Schellenberg, K., Labiouse, V., Agliardi, F., Berger, F., Bourrier, F., … Jaboyedoff, M. (2011). Rockfall characterisation and structural protection – a review. *Natural Hazards and Earth System Sciences, 11*(9), 2617–2651. https://doi.org/10.5194/nhess-11-2617-2011

Warrick, J. A., Ritchie, A. C., Adelman, G., Adelman, K., & Limber, P. W. (2017). New techniques to measure cliff change from historical oblique aerial photographs and structure-from-motion photogrammetry. *Journal of Coastal Research, 33*(1), 39–55. https://doi.org/10.2112/JCOASTRES-D-16-00095.1

Westoby, M. J., Brasington, J., Glasser, N. F., Hambrey, M. J., & Reynolds, J. M. (2012). 'Structure-from-Motion' photogrammetry: A low-cost, effective tool for geoscience applications. *Geomorphology, 179*, 300–314. https://doi.org/10.1016/j.geomorph.2012.08.021

Zhang, Z. (1994). Iterative point matching for registration of free-form curves and surfaces. *International Journal of Computer Vision, 13*(2), 119–152. https://doi.org/10.1007/BF01427149

Manuscript received: October 21, 2022
Revisions requested: March 28, 2023
Revised version received: May 19, 2023
Accepted: May 19, 2023

7.2 Assessing the effect of lithological setting, block characteristics and slope topography on the runout length of rockfalls in the Alps and on the island of La Réunion

Nat. Hazards Earth Syst. Sci., 21, 1159–1177, 2021
https://doi.org/10.5194/nhess-21-1159-2021

Natural Hazards and Earth System Sciences
Open Access
EGU

Assessing the effect of lithological setting, block characteristics and slope topography on the runout length of rockfalls in the Alps and on the island of La Réunion

Kerstin Wegner[1], Florian Haas[1], Tobias Heckmann[1], Anne Mangeney[2], Virginie Durand[2,a], Nicolas Villeneuve[2,3], Philippe Kowalski[2,4], Aline Peltier[2,4], and Michael Becht[1]

[1]Chair of Physical Geography, Catholic University of Eichstätt-Ingolstadt, 85072 Eichstätt, Germany
[2]Institut de Physique du Globe de Paris, Université de Paris, CNRS, 75005 Paris, France
[3]Laboratoire GéoSciences Réunion, Université de La Réunion, 97744 Saint-Denis, France
[4]Observatoire Volcanologique du Piton de la Fournaise, Institut de Physique du Globe de Paris, 97418 La Plaine des Cafres, France
[a]now at: Helmholtz Centre Potsdam – German Research Centre for Geosciences, GFZ, 14473 Potsdam, Germany

Correspondence: Kerstin Wegner (kwegner@ku.de) and Florian Haas (florian.haas@ku.de)

Received: 30 September 2020 – Discussion started: 6 October 2020
Revised: 16 February 2021 – Accepted: 25 February 2021 – Published: 31 March 2021

Abstract. In four study areas within different lithological settings and rockfall activity, lidar data were applied for a morphometric analysis of block sizes, block shapes and talus cone characteristics. This information was used to investigate the dependencies between block size, block shape and lithology on the one hand and runout distances on the other hand. In our study, we were able to show that lithology seems to have an influence on block size and shape and that gravitational sorting did not occur on all of the studied debris cones but that other parameters apparently control the runout length of boulders. Such a parameter seems to be the block shape, as it plays the role of a moderating parameter in two of the four study sites, while we could not confirm this for our other study sites. We also investigated the influence of terrain parameters such as slope inclination, profile curvature and roughness. The derived roughness values show a clear difference between the four study sites and seem to be a good proxy for block size distribution on the talus cones and thus could be used in further studies to analyse a larger sample of block size distribution on talus cones with different lithologies.

1 Introduction

Rockfall is an important geomorphic process on steep rock slopes and thus plays a significant role in geomorphic dynamics especially in high mountainous regions (e.g. Hungr and Evans, 1988; Krautblatter and Dikau, 2007; Bennett, et al., 2012; Frattini et al., 2012). Rock fragments are detached from cliff faces (primary rockfall) or remobilized from sediment stores (secondary rockfall) downslope (e.g. Rapp, 1960; Krautblatter and Dikau, 2007); move in a combination of falling, bouncing, rolling or sliding (e.g. Luckman, 2013a; Crosta et al., 2015); and are subsequently deposited on storage landforms such as talus cones. Even though rockfalls often take place in remote areas, they can still pose a potential natural hazard and can cause damage to human lives and local infrastructure facilities (e.g. Pfeiffer and Bowen, 1989; Dorren, 2003; Ravanel et al., 2010; Volkwein et al., 2011; Frattini et al., 2012; Heiser et al., 2017).

The occurrence and magnitude of rockfalls depend on the preconditioning and the preparatory factors (e.g. Meißl, 1998; Dorren, 2003; Dietze et al., 2017a) as well as on triggering events. The preconditioning and preparatory factors are mainly lithology, topography of the slope (aspect, steepness, altitude), vegetation (e.g. Meißl, 1998; Jaboyedoff and Derron, 2005), rainfall and weathering, frequency of freeze–thaw cycles, sun exposure, and root growth (e.g. Meißl, 1998;

Published by Copernicus Publications on behalf of the European Geosciences Union.

Jaboyedoff and Derron, 2005; Krautblatter and Dikau, 2007; Frattini et al., 2012; Crosta et al., 2015). Triggering events include volcanic or seismic forcing (Hibert et al., 2017; Durand et al., 2018).

Not only due to the change in the settlement structure in mountain regions but also in the context of global climate change, many studies exist about rockfall processes, focusing on the modelling of runout trajectories and the prediction of rockfall events (e.g. Kirkby and Statham, 1975; Meißl, 1998; Agliardi and Crosta, 2003; Dorren, 2003; Copons et al., 2009; Jaboyedoff and Labiouse, 2011; Frattini et al., 2012; Nappi et al., 2013; Wichmann, 2017; Volkwein et al., 2018; Caviezel et al., 2019), as well as on the measurement of rockfall activity by seismic monitoring (e.g. Vilajosana et al., 2008; Hibert et al., 2011; Farin et al., 2015; Dietze et al., 2017a, b; Durand et al., 2018; Feng et al., 2019). Most of these studies use lidar (light detection and ranging) techniques such as airborne laser scanning (ALS) as well as terrestrial laser scanning (TLS) to improve the understanding of this geomorphic process (e.g. Jaboyedoff et al., 2007; Abellán et al., 2011; Haas et al., 2012; Heckmann et al., 2012; Royán et al., 2014; Strunden et al., 2015; Sala et al., 2019). In recent times structure from motion (SfM) has also been increasingly used for such kinds of studies (e.g. Kromer et al., 2019; Vanneschi et al., 2019; Guerin et al., 2020).

In the context of hazard assessment and also for geomorphological models, not only the transported volumes but also the analysis of the maximum runout distance of blocks play an important role especially in populated mountain regions (e.g. Jaboyedoff and Labiouse, 2011; Volkwein et al., 2011; Lambert et al., 2013; Caviezel et al., 2019). Factors influencing the runout distance and the trajectory of blocks include topographic conditions, like the slope inclination, height of the fall, and curvature conditions (e.g. Meißl, 1998; Frattini et al., 2012; Leine et al., 2014). Other parameters are the surface properties including protection measures and the roughness of the slope (e.g. Meißl, 1998; Leine et al., 2014; Gratchev and Saeidi, 2019). Some studies show the influence of the properties of the rockfall itself, like the volume, geology, and size and shape of the blocks, on the runout distances (e.g. Kirkby and Statham, 1975; Meißl, 1998; Leine et al., 2014). In addition, the kinematical properties of the blocks and the restitution parameter influence the depositioning (e.g. Azzoni and de Freitas, 1995; Jaboyedoff and Labiouse, 2011; Ji et al., 2019; Sandeep et al., 2020). The size and shape of blocks and their interaction with slope properties are considered to comprise an important factor for the travel distance (e.g. Pfeiffer and Bowen, 1989; Meißl, 1998; Frattini et al., 2012; Leine et al., 2014).

The influence of block shape, block size and slope topography on the runout distance has been investigated only by a small number of studies (Azzoni and de Freitas, 1995; Haas et al., 2012; Fityus et al., 2013) and mainly in case studies or tests under laboratory conditions (Okura et al., 2000; Glover et al., 2015, Cui et al., 2017; Wang et al., 2018; Gratchev and Saeidi, 2019). Haas et al. (2012) already stated in their case study that the influence of the lithology on block shape and block size must be investigated with a broader view. This could be done e.g. in areas with different lithological settings, as the size and shape of rock fragments are determined by their lithological properties, among other influencing factors (Haas et al., 2012; Fityus et al., 2013). Some studies have described the deposition of boulders on the talus cone as gravitational sorting, where larger blocks are deposited in the distal part and smaller blocks on the upper part of the talus slope (e.g. Statham, 1973; White, 1981; Whitehouse and McSaveney, 1983; Kotarba and Strömquist, 1984; Jomelli and Francou, 2000; Sanders et al., 2009; Messenzehl and Dikau, 2017; Popescu et al., 2017; Kenner, 2019). The gravitational sorting of the blocks on the slope is a key factor for the roughness component of talus slopes and thus for the runout length of following rockfall events (Hungr and Evans, 1988), indicating a potential feedback loop in the formation of talus landforms.

The aim of this study is to carry out a comparative investigation of the morphometric properties and runout distances of rockfall fragments in mountain regions within different lithological settings. For our analysis we selected four sites with different lithological conditions, different rockfall activity and existing data with a very high quality. Due to lithological differences in the cliffs, we expected different statistical distributions of block sizes and block shapes on the talus slopes. The study is conducted using high-resolution digital terrain models (DTMs) and point clouds created from TLS surveys. Based on the research of Haas et al. (2012), we determined different block properties, sizes and shapes and analysed them in the context of runout distances and talus morphology.

2 Study sites

Four areas in high mountainous regions were selected for this investigation. Three of these areas are situated in the Alps; one area is located on the island of La Réunion (Fig. 1). The areas differ mainly with regard to the lithological conditions.

All areas are characterized by recent rockfall activity and a clearly distinguishable rock face with an associated scree slope. The selected study sites represent different processes such as rock topples and block fall. For Gampenalm (GA) and Dreitorspitze (DTS), the blocks are assigned to one rockfall event. For Piton de la Fournaise (PF) and the Zwieselbach valley (ZBT), the slope is characterized by deposited material from continuous rockfall processes, but also major events cannot be excluded. A further criterion for the selection of the area was that both the rock faces and the talus cones were clearly and completely visible to ensure complete and dense lidar acquisition.

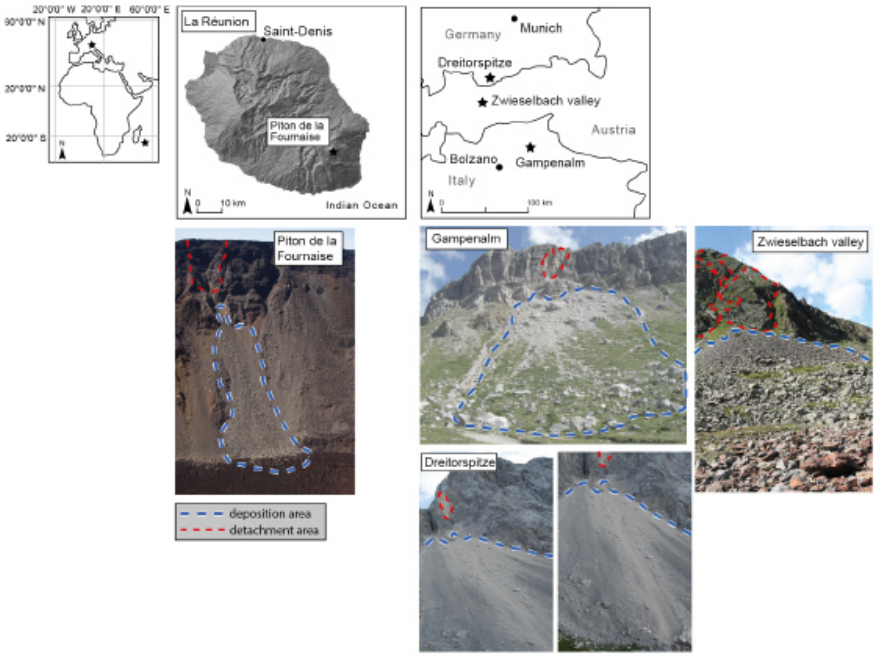

Figure 1. Geographical location of the study sites located on La Réunion and in the European Alps. The stars locate the location of the study sites. The dashed red lines limit the detachment areas of the rockfall events. The dashed blue and white lines represent the deposition area. (Source of the overview base map: ESRI, HERE, Garmin, OpenStreetMap contributors and the GIS user community.)

The GA and DTS areas are located in the southern and the northern Alps, respectively, and consist of sedimentary rocks specifically of different limestone formations (Table 1). The GA area is located in the Dolomites and is dominated by the thickly banked Rosengarten massif (cf. Haas et al., 2012). DTS is dominated by the thickly banked Wetterstein limestone. In both areas, major rockfall events occurred in recent years.

The ZBT in the Stubai Alps is located in the area of the crystalline Central Alps and is characterized by slated gneiss and metamorphic granites. There are not known to have been major rockfall events during the last few years, but the deposits on the talus cone indicate recent rockfall activity also including bigger blocks. For GA, DTS and the ZBT the precondition and preparatory factors cannot be determined exactly, but thawing of mountain permafrost can be excluded due to the altitude and exposure. As we do not have temperature and precipitation data, we cannot give any information about this.

The PF test site (Dolomieu crater) on La Réunion is the only area outside the Alps and is located in the Indian Ocean, east of Africa, but politically it belongs to France as an overseas department. PF is one of the most active volcanoes in the world (e.g. Peltier et al., 2009a). For the period from 1950 to 2013, 93 eruptions have been documented (Staudacher et al., 2016). Due to a summit collapse during an eruption in 2007 (e.g. Peltier et al., 2009b) a 340 m deep caldera was formed (e.g. Staudacher et al., 2016) in an area of 1100 × 800 m (e.g. Urai et al., 2007). On this volcano, the composition of the lava is mainly bimodal with a combination of aphyric basalts and olivine-rich basalts (e.g. Peltier et al., 2009a; Lénat et al., 2012). Due to the high tectonic stress (e.g. Merle et al., 2010; Staudacher et al., 2016), the high volcanic activity that generates deformation and seismic activity (e.g. Sens-Schönfelder et al., 2014; Peltier et al., 2018), and the layering of different lava flows, the rim is very unstable and thus prone to high rockfall activity (Hibert et al., 2017; Durand et al., 2018). This area certainly differs most clearly from all the other studied areas. Besides the volcanic rocks, both the cliff and the talus cones are very young landforms, as the geomorphic forming started directly after the emergence of the caldera in 2007. Further differences are the high deformation and seismic activity and the extremely high precipitation. Seismicity and rainfall have been show to play a role in rockfall trigger-

Table 1. Morphological and lithological characteristics of all investigated talus slopes.

Study area	PF	ZBT	GA	DTS
Altitude [m a.s.l.]	2632	2278	2450	2682
Lithology	Basalt	Gneisses, glimmers, metamorphic granites	Triassic dolomites, limestone, psephite	Triassic limestone, dolomite
Mean slope inclination [°]				
Talus cone	36	29	32	32
Cliff	55	50	59	66
Length [m]				
Talus cone	250	55	250	300
Cliff	150	60	150	100
Mean annual precipitation [mm yr^{-1}]	3000–4250	1000	862.2	1500
Mean annual temperature [°C]	13.8	0.9	7.8	6.7
Density [g cm^{-3}]	2.99	gneiss: 2.80 granite: 2.64	limestone: 2.55 dolomite: 2.70	limestone: 2.55 dolomite: 2.70
Friction angle φ [°]	35–38	gneiss: 26–29	limestone: 31–37	limestone: 31–37
Tensile strength [MPa]	10–30	gneiss: 5–20 granite: 7–25	limestone: 5–25 dolomite: 14	limestone: 5–25 dolomite: 14

ing (Hibert et al., 2017; Durand et al., 2018) but should not have any influence on the runout lengths of single blocks, so for the present investigations primarily the differences in lithology and in the case of PF the age have to be considered.

3 Materials and methods

3.1 Data acquisition and processing (TLS)

The data of all study sites have been acquired with a terrestrial 3D long-range laser scanner. Two systems were used: the Riegl LMS-Z420i and the Riegl VZ-4000. Each scanner works on the same principle of time of flight, but due to laser configurations, the scanning distance of the VZ-4000 is 4 times longer with 4000 m compared to 1000 m. Both systems provide colour information due to integrated camera systems in order to colorize the point clouds. The RGB values of the pictures allow the filtering of vegetation in the pre-processing of the data and simplify the visualization of e.g. individual blocks. All important technical information of both devices is listed in Table 2.

Due to the long distance between scanner and target and the poor reflectance of the volcanic material in the Dolomieu crater, we used the VZ-4000 for this study site. All other test sites were surveyed using the LMS-Z420i. To minimize shadowing effects, several scan positions were necessary at each site, which had to be referenced using manual adjustment and ICP algorithms (Table 3). Both tools are implemented in the software RiSCAN PRO (v2.2.1, http://www.riegl.com, last access date: 8 February 2021).

After the referencing, the data were exported as ASCII files containing x, y and z coordinates as well as RGB values for further analysis in SAGA GIS LIS (Conrad et al., 2015; Laserdata Information System, LIS: https://www.laserdata.at, last access: 8 February 2021). We worked on the vegetation-filtered and homogeneously thinned point clouds and created digital terrain models (DTMs) for all test sites with a raster resolution of 0.75 m using the lowest z value. Table 3 provides information about each study site including the vertical and horizontal scan resolution, the referencing precision, number of points in the raw data set, and the point density (points m^{-2}).

Table 2. Technical data of the two terrestrial laser scanning systems Riegl LMS-Z420i and VZ-4000 (RIEGL Laser Measurement Systems GmbH, 2010, 2020). The values of the VZ-4000 refer to measurements at a rate of 30 kHz.

	LMS-Z420i	VZ-4000
Max measurement range	1000 m	4000 m
Measurement rate	8000 points s^{-1}	23 000 points s^{-1}
Accuracy	10 mm	15 mm
Precision	4–8 mm	10 mm
Laser wavelength	Near infrared	Near infrared
Laser beam divergence	0.25 mrad	0.15 mrad

3.2 Determination of block size, block shape and runout length

As the block size and shape have a great influence on the runout distance of the falling rock material, we measured according to the workflow of Haas et al. (2012) the dimensions of the three axes (a, b and c) of single boulders for every study area (PF $n = 255$; GA $n = 618$; ZBT $n = 65$; DTS $n = 182$). We selected blocks that were deposited on the talus surface beginning from the upper and going to the lower parts

Table 3. Information about the TLS surveys for each study area.

	TLS system	Scan resolution	Referencing precision	Number of points in raw data set	Point density (points m^{-2})
PF	VZ-4000	0.02°	0.007–0.013 m	$> 60 \times 10^6$ points	55 points m^{-2}
ZBT	LMS-Z420i	0.05–0.1°	0.018–0.060 m	1.5×10^6 points	50 points m^{-2}
GA	LMS-Z420i	0.05–0.1°	0.012–0.058 m	8×10^6 points	54 points m^{-2}
DTS	LMS-Z420i	0.05–0.2°	0.015–0.065 m	3×10^6 points	54 points m^{-2}

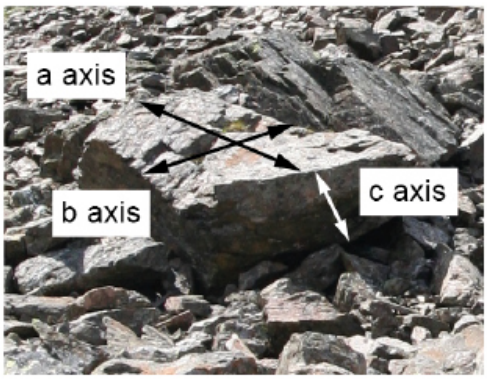

Figure 2. Deposited block on the ZBT talus cone with the three measured dimensions of the axes a, b and c.

of the talus cones. Based on the coloured lidar point clouds every block larger than approximately ~ 0.5 m was manually measured in the software RiSCAN PRO. Figure 2 shows an idealized sketch of a boulder with the three measured axes.

We followed the work of Haas et al. (2012), which used the formula of Valeton (1955) as an indicator of the block shape. By using the measured three axes, the volume (Eq. 1) and the axial ratio (Eq. 2) were approximated. The derived axial ratio of the measured blocks describes their block shape. For the calculation of the axial ratio, the parameter of the b axis must be set to 1 (cf. Valeton, 1955). With this method, blocks with an axial ratio of 1 can be described as a cuboid or as equant, but the method does not reflect the roundness of blocks. In the following we will also use the term of a small or low axial ratio. The larger the value of the axial ratio, the more elongated or irregularly shaped the blocks are. Here we will refer to a high axial ratio. The different lithology of the study areas determines the shape of the deposited blocks to a certain degree as predisposition (Glover et al., 2015).

$$\text{Block volume} = a \times b \times c \quad (1)$$

$$\text{Axial ratio} = a/b/c \quad (2)$$

Since a 3D approach to measure the blocks would be too time-consuming for this number of blocks, we decided to use the lengths of the axes of the blocks for all study sites. In order to be able to make an assessment about the overestimation of the calculated block volume, we selected a sample of 10 blocks with different sizes for each study area (Fig. 3). Using the TLS point clouds, the block volume was derived in RiSCAN PRO. The comparison between volume estimation via the three measured axes and the 3D volume calculation in RiSCAN PRO in all four areas shows that the volumes of the blocks are constantly overestimated. It is also visible that this overestimation appears relatively small in the ZBT area, which can be explained by the rather angular structure of the blocks (see Fig. 2). This provides an indication that the overestimation can be explained primarily by the fact that the axis calculation assumes rectangular edges for the volume calculation, which is certainly not true for all blocks of the other areas. However, in view of the uniform use of the axis method and the systematic overestimation in all areas, it seems permissible to us to calculate the volume via this simple method and to use it for the further analyses.

For the study areas of DTS and GA we determined the Euclidean distance from their detachment zones to each measured boulder to obtain the runout length. Since the exact detachment zone could not be determined at PF and the ZBT, we measured the Euclidean distance from the beginning of the transition between cliff and talus cone to each boulder instead. In order to be able to compare the runout distances between the slopes of the study areas and as they differ greatly in length, we normalized the runout lengths for each talus cone to the interval [0, 1]. We have assumed that a value of 0 stands for the detachment area or the area between the rock face and the slope. The value of 1 stands for the maximum runout length of a block.

3.3 Morphometric slope properties

3.3.1 Slope inclination and curvature

Based on the high-resolution DTMs of the study sites we performed a spatial analysis of the talus cones including morphometric properties with a presumed influence on the deposition (e.g. Wang and Lee, 2010; Frattini et al., 2012; Crosta et al., 2015) and runout distances of rockfall boulders (e.g. Glover et al., 2015): slope inclination and profile curvature. The slope inclination was derived based on the DTMs according to Zevenbergen and Thorne (1987).

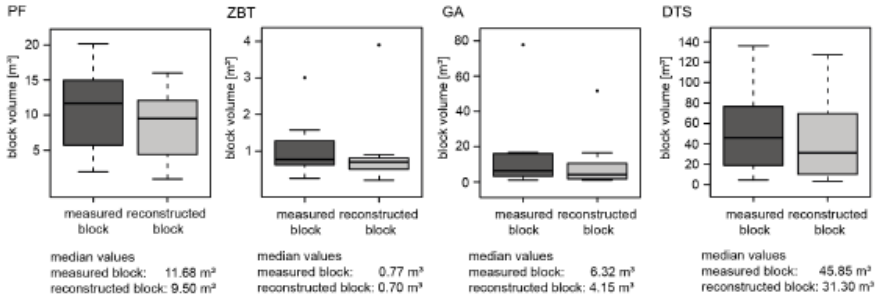

Figure 3. Boxplots of measured and reconstructed block volume. The thick black lines within the boxes show the median bounded by the first quartile (25th percentile) and the third quartile (75th percentile). The boxes show the interquartile range (IQR). The whiskers of the boxplots mark the minima and maxima of the data. The circles represent data which exceed the 1.5-fold IQR.

Additionally, we created three longitudinal profiles with a swath width of 10 m from the highest part of the cone to the distal boundary in order to characterize slope morphology of all four test sites to show changes in slope inclination and profile concavity (cf. Hergarten et al., 2014). We applied a kernel density estimation (cf. Cox, 2007) to compare the distributions of slope inclination between rock faces and talus cones and between the study sites.

3.3.2 Surface roughness

The roughness of the slope can serve as a proxy for the particle size distribution on the talus cone. This parameter could give more information regarding the gravitational sorting pattern where it indicates a coarsening towards the foot of the slope and/or a concentration of coarse material at the foot of the rock wall. This is to determine and analyse the sorting of particle sizes beyond the measured block sizes of the single debris cones. For this purpose, we calculated the roughness based on the high-resolution TLS point clouds. The algorithm used fits a plane for each point of the point cloud in its local neighbourhood with a search radius of 3 m (SAGA surface roughness module (PC); Laserdata Information System, LIS, 2010; https://www.laserdata.at, last access: 8 February 2021). Using the plane, the standard deviation of the distance to the fitted plane for each point was derived. To obtain the spatial distribution and the change in roughness along the slope for each study site, we classified the elevation values of the talus cones (z value) into 10 m classes. In order to be able to establish comparability between the study areas, we normalized the height values of the point clouds. Furthermore, we classified the block volumes to check whether they correspond to the spatially distributed roughness of the deposited blocks on the talus cone.

4 Results and discussion

4.1 Morphometric analyses

4.1.1 Block size and block shapes

In Table 4 we have listed mean and median values for block size and shape for the four study sites. To show the distribution of the block properties, size and shape, we have visualized the measured blocks with the longest axis greater than ~ 0.5 m in Fig. 4 using boxplots. With regard to the block volumes, the four investigated sites differ, in some cases very significantly. The smallest block sizes (Table 4) can be found in the ZBT area with a median value of 0.08 m^3, and the largest block sizes can be found in the DTS area with a median value of 13.16 m^3. The median is below 4 m^3 in the three areas of PF (3.38m^3), the ZBT (0.08 m^3) and GA (1.63 m^3). The data show a very homogeneous distribution and only small maximum values in PF and the ZBT, whereas in GA and DTS a very large dispersion and high maximum values (Table 4) are obvious. This indicates that a correlation between the lithological conditions and the block sizes involved in rockfall processes is very likely, as the largest blocks are mainly found in areas with banked limestones. This is clearly shown in the Wetterstein limestone and to a lesser degree in the Dolomite area. The extremely small block sizes are particularly striking in the ZBT area, which consists of metamorphic rocks. This can be explained by the rather slated and thus platy rock structure of the gneisses and by the long tectonic history of these rocks (see Fig. 2).

In contrast to the block sizes, the block shapes (Fig. 4) in all four areas show a high dispersion between equant and rather elongated or irregularly shaped blocks. The most elongated blocks can be found in the ZBT area with a median value of 2.63 (Table 4), which again can be explained by the slated structure of the gneisses. The limestones of the GA and DTS areas are very similar in the median, mean block shape and the dispersion of the data (Table 4, Fig. 4). The

Table 4. Mean and median values for the parameters block size and block shape for each study site. The values for block size and shape (axial ratio) were calculated using Eqs. (1) and (2) with $b = 1$.

	Block size		Block shape	
	Mean [m^3]	Median [m^3]	Mean	Median
PF	5.07	3.38	2.00	1.73
ZBT	0.29	0.08	2.87	2.63
GA	11.86	1.63	2.58	2.33
DTS	70.19	13.16	2.78	2.40

lowest values and therefore the most cuboid shaped blocks, consisting of volcanic rocks, were found in the PF area with a median value of 1.73. Whether this is due to lithology or to tectonic stresses caused by the high seismic activity and the resulting fissures and cracks cannot be finally clarified with the data of this study.

With regard to the block shapes and block size distributions in the areas, however, it can be concluded that the investigated areas show sufficient differences in both block sizes and shapes, and that this is very likely a consequence of the lithological setting. This allows for a more detailed investigation of the relationships between block shape, block size and runout distance. We will also analyse how the different process activities affect the deposition and runout distance.

4.1.2 Slopes of the talus cones

In addition to the block shape and block size, the topography of the talus cones also plays an important role and has to be considered for a runout analysis. Thus, we analysed the following form parameters: slope inclination and slope profiles (curvature) (Figs. 5 and 6).

The average slope inclinations of the talus cones lie between 28 and 36° and thus within the range for such landforms (e.g. Pérez, 1989, 1998; Francou and Manté, 1990; Jomelli and Francou, 2000; Sanders et al., 2009; Luckman, 2013b, Popescu et al., 2017; Volkwein et al., 2018). The mean slope inclination values for the talus cones of our study sites are for PF, the ZBT, GA and DTS 29, 32, 36 and 32°, respectively. This can provide an indication of the dependence between rock material and slope inclination of gravel or blocky material and thus supports the findings of other studies.

ZBT

Kenner (2019) reported in their study on amphibolite sediments slope angles of 35°, and Messenzehl and Dikau (2017) described in their survey on metamorphic rocks slope angles of 34–36° and 33–34°. Additionally, Gerber (1974) showed in his study a slope inclination of 33° for gneisses and metamorphic granites. For the ZBT we found only 28.9° for the metamorphic rocks, which is significantly lower than in the cited studies. It must be noted that especially in the ZBT the talus cone can be divided into two sectors, which differ very clearly in terms of slope (Fig. 5d). Thus, in the left area we find significantly higher slope inclinations with 43°, which are higher than the values from the literature, whereas in the right area rather significantly lower slope inclinations are found.

PF

The highest slope inclinations can be found on PF with 36.0° and its basaltic lava material. Yamamoto et al. (2005) conclude that basaltic material cannot be deposited on slopes of more than 33°. However, the higher average slope inclination at PF compared to the findings of Yamamoto et al. (2005) can be explained by the rock surface conditions, which also play an important role, since fresh volcanic rocks in particular are characterized by a high micro-roughness, especially where the lava could cool very quickly. Thus the slope seems to be controlled by the friction coefficient of the deposited material. In particular, for PF, analysis of seismic data for rockfalls suggests a friction coefficient of 35° for the talus slope (Hibert et al., 2011). This is supported by the distributions of the slope inclinations (see Figs. 5c and 6c), where the data scatter is lowest in the PF area. Here the distribution is very peaked and differs clearly from the distributions of the other three areas. The shape of the slope profiles (Figs. 5a and 6a) also points in a similar direction. The talus cone of PF follows a straight line over the entire length of the slope, whereas the other cones show a slight convexity in the upper and middle slope and a basal concavity at the end of the slope, which is in good agreement with the works of Kotarba and Strömquist (1984), Luckman (2013b), and Popescu et al. (2017). Nevertheless, it is very likely that the talus cone of PF represents a pure talus cone and has been reshaped since the summit collapse in 2007 by persistent rockfalls, whereas the talus cones of the other areas represent much older forms where different types of geomorphic processes occur (e.g. debris flows, avalanche deposits).

DTS and GA

The DTS and GA talus cones show quite similar values with 31.9 and 31.6°. Gerber (1974) measured 32° for talus cones consisting of limestone material, which corresponds to the study sites of GA and DTS. Serrano et al. (2019) described in their study slope inclinations for limestone formations of 32–36°, and Knoblich (1975) gives values of 28–43°. The two slopes are also similar regarding the longitudinal profiles (Fig. 6a). GA has a slightly basal concave talus cone downslope, while that of DTS is straighter.

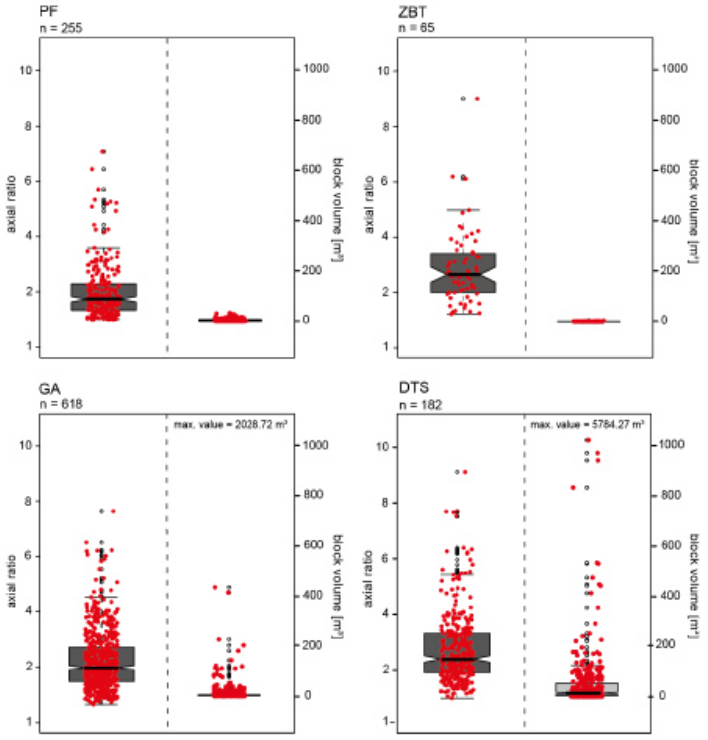

Figure 4. Boxplots of volume and shapes for the measured blocks. The red-coloured points correspond to each measured block. The thick black lines within the boxes show the median bounded by the first quartile (25th percentile) and the third quartile (75th percentile). The boxes show the interquartile range (IQR). The whiskers of the boxplots mark the minima and maxima of the data. The circles represent data which exceed the 1.5-fold IQR.

Table 5. Analysis of the relationship of block volume and axial ratio against runout length by means of Spearman's rank correlation for each study site.

	PF	ZBT	GA	DTS
Block volume ρ	0.15	0.33	−0.04	−0.29
Block volume p value	0.02	0.007111	0.39	$\ll 0.001$
Axial ratio ρ	0.06	0.27	−0.35	−0.42
Axial ratio p value	0.36	0.03	$\ll 0.001$	$\ll 0.001$

4.2 Relationship between block size, block shape and runout length

4.2.1 Analysis of individual boulders

In order to analyse the relationship between block volume, block shape and runout length, we calculated Spearman's rank correlation (Table 5). The results show only weak correlations between block volume and runout distance as well as weak correlations between runout length and block shape for the four test sites, which indicate no monocausal relationship.

These results are in contrast to other studies, which state that longitudinal sorting of talus cones shows an increase in block sizes downslope (Jomelli and Francou, 2000). Popescu et al. (2017) conclude that there is a gradual increase in boulder size towards the slope base, which is also stated by Co-

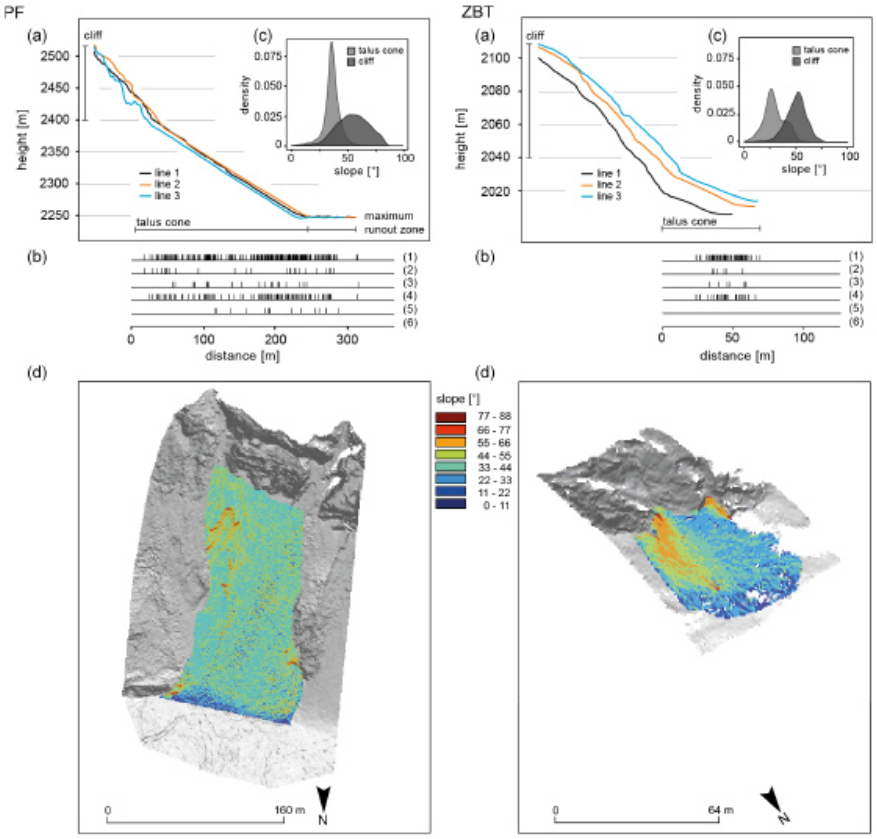

Figure 5. Slope characteristics for the PF and ZBT study sites. Three swath longitudinal profiles from the cliff to the maximum runout distance (**a**). Statistical distribution of all measured blocks regarding their shapes and volumes on the talus cone. Every single line represents a measured block, and thus the deposition on the slope can be illustrated. For this purpose, we have presented all blocks (1) and the most (2) and least (3) spheroidal blocks, and we have classified the block volume according to $10\,m^3$ (4), $10^2\,m^3$ (5) and $10^3\,m^3$ (6) (**b**). Kernel density estimation of slope inclination distinguished according to the cliff and the talus cone (**c**). Maps of slope inclination with different classes (**d**).

pons et al. (2009), determining a dependency of rock volume and runout distance. Serrano et al. (2019) showed that the distal part of a slope is characterized by the accumulation of large blocks. In contrast to these studies Caine (1967) found a decrease in blocks sizes with distance downslope, but his results are statistically insignificant. Messenzehl and Dikau (2017) showed that there is a distinct downslope increase in block size and sphericity, which indicates a combination of these block characteristics govern the runout length. These contradictory statements are supported by the work of Meißl (1998), who described in her analysis that the shape and size of the blocks mainly influence the width and height of the jumping parabolas, the rolling speed, and the timing of the change between jumping and rolling. Meißl (1998) has also observed that larger blocks do not always reach the longest runout distances. A possible cause could be that the blocks tend to sink, depending on the slope properties, but also interactions between the blocks cannot be excluded. Moreover, the fracturing of larger blocks can additionally lead to a loss of kinetic energy, which influences the disposition of blocks (Meißl, 1998).

In order to obtain a broader view on the data and in accordance with Haas et al. (2012), we plotted the relative distance against $\log_{10}$ block volume to show the relationship for

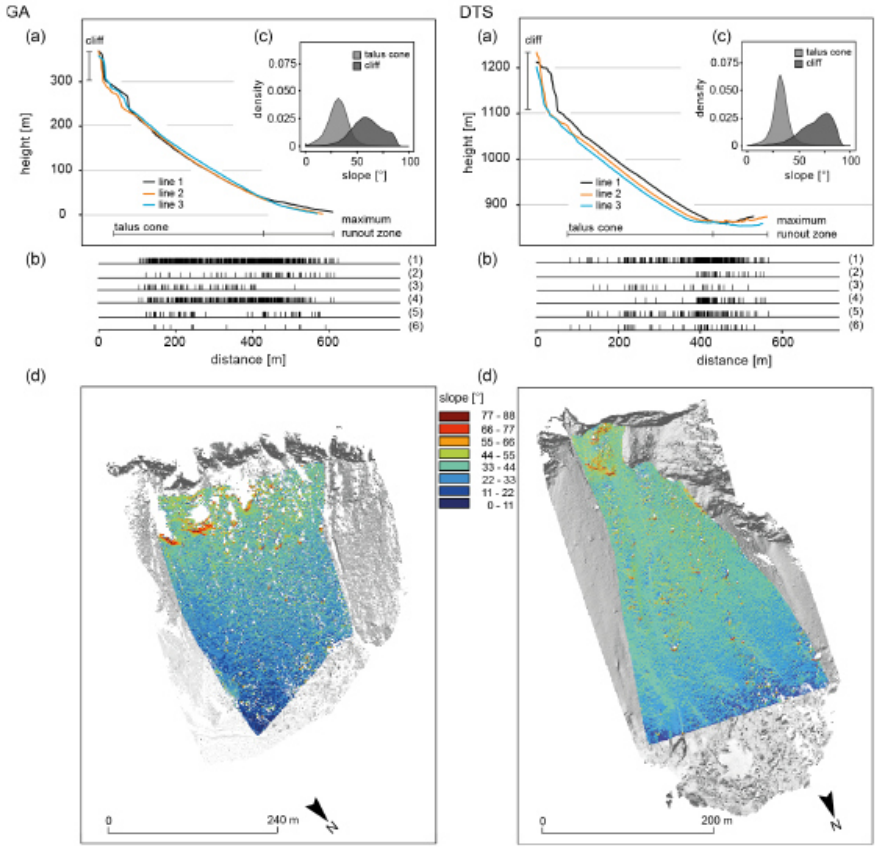

Figure 6. Slope characteristics for the GA and DTS study sites. Three swath longitudinal profiles from the cliff to the maximum runout distance (**a**). Statistical distribution of all measured blocks regarding their shapes and volumes on the talus cone. Every single line represents a measured block, and thus the deposition on the slope can be illustrated. For this purpose, we have presented all blocks (1) and the most (2) and least (3) spheroidal blocks, and we have classified the block volume according to $10\,m^3$ (4), $10^2\,m^3$ (5) and $10^3\,m^3$ (6) (**b**). Kernel density estimation of slope inclination distinguished according to the cliff and the talus cone (**c**). Maps of slope inclination with different classes (**d**).

every single talus cone in more detail (Figs. 7 and 8). We combined this analysis with the axial ratio of the boulders. Figures 7a and 8a show boxplots with six different quantile classes (< q10, q10–q25, q25–q50, q50–q75, q75–q90, > q90), which correspond to the 10 %, 25 %, 50 %, 75 % and 90 % quantiles of the $\log_{10}$ block volume and $\log_{10}$ axial ratio. To analyse the relationship of the parameters in more detail, we highlighted the 10 % and the 90 % quantile classes, which indicate blocks with a low (10 %) and high (90 %) axial ratio. These different classes are visualized with different symbols and colours in Figs. 7b and 8b.

Figures 7 and 8 show that we can subdivide our study sites into two classes, regarding the runout length and block size and shape. The first class represents the study sites where the blocks can be reliably assigned to one bigger rockfall event (GA and DTS). The second class consists of the PF and ZBT sites, where we cannot reliably assign the boulders to one event and therefore have to assume continuous rockfall activity.

In the ZBT and PF areas the block sizes seem to have a recognizable influence on the runout length. Although the dispersion of the data and Spearman's rank correlation show that this correlation is not significant (Table 5), large blocks above

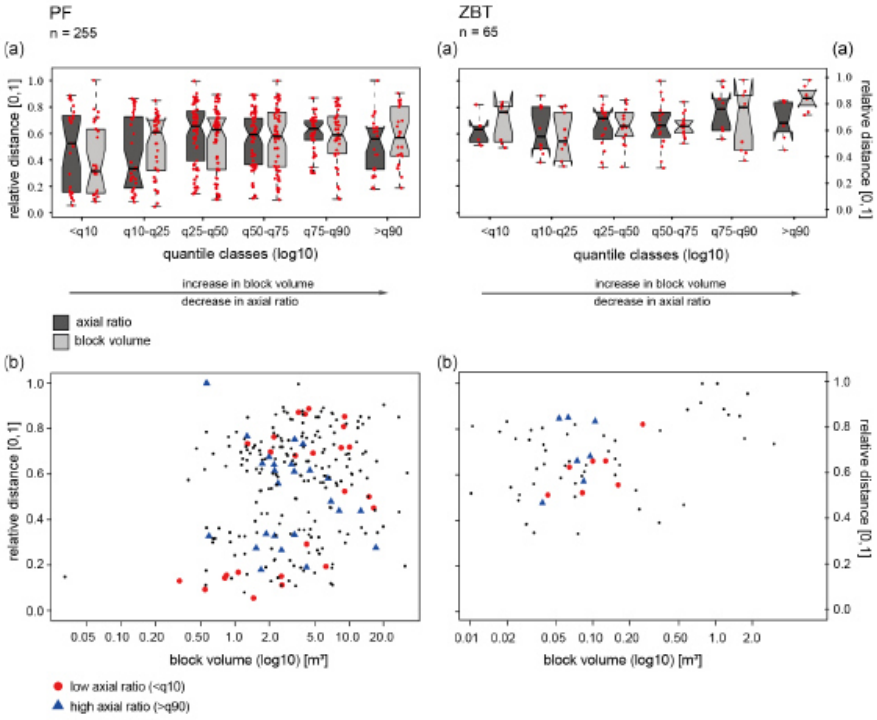

Figure 7. Boxplots of relative distance versus $\log_{10}$ block volume and $\log_{10}$ block shapes of the measured rocks for the PF and ZBT study sites (**a**). The red-coloured points correspond to each measured individual block. The thick black lines within the boxes show the median bounded by the first quartile (25th percentile) and the third quartile (75th percentile). The boxes show the interquartile range (IQR). The whiskers of the boxplots mark the minima and maxima of the data. The circles represent data that exceed the 1.5-fold IQR (**a**). Scatterplot of relative distance versus $\log_{10}$ block volume for all study sites. Blocks with a low axial ratio (< q10) and a high axial ratio (> q90) are highlighted with different colours and symbols (**b**).

a certain size are not present in the short runout lengths. However, Fig. 7b also shows that for PF, smaller and larger blocks are deposited in all areas of the slope. At the same time the block shape does not seem to play a major role in the runout distance, which is also indicated by Spearman's rank correlation: PF $r = 0.06$ and ZBT $r = 0.27$. Cuboid-shaped and elongated blocks can actually be found over the entire talus cone without any visible clustering (Fig. 7b).

GA and DTS show that the size of the blocks obviously does not play a major role in the runout length on the talus cones, as the median values do not show a significant trend, but the dispersion of the runout distances clearly increases with increasing block size. This is visible in both areas but is more pronounced at DTS. Beside this, it is also visible that blocks with larger volumes also have smaller runout distances (Figs. 7b and 8b). The scatterplots show that the block size is scattered strongly over the entire talus cone. The block size can therefore not be used as an explanation for the runout distance alone, which is in agreement with Spearman's rank correlation and supports our thesis above that there is no monocausal relationship.

The situation is different regarding the block shapes in the areas of GA and DTS. Here it is clearly visible that with an increase in axial ratio, the runout distance decreases. This is also quite consistent with the results of Spearman's rank correlation, because in these two areas a slight correlation between axial ratio and range can be stated (Table 5). This is also visible in Figs. 7b and 8b, which show the cuboid-shaped and longest blocks combined with the ranges: blocks with a low axial ratio (< q10) reach larger distances than elongated blocks (> q90) (e.g. Pérez, 1998). This can be seen in both areas from a relative distance of about 0.7 on the talus cone. We observed that the parameter axial ratio acts like a moderating parameter with regard to the deposition of

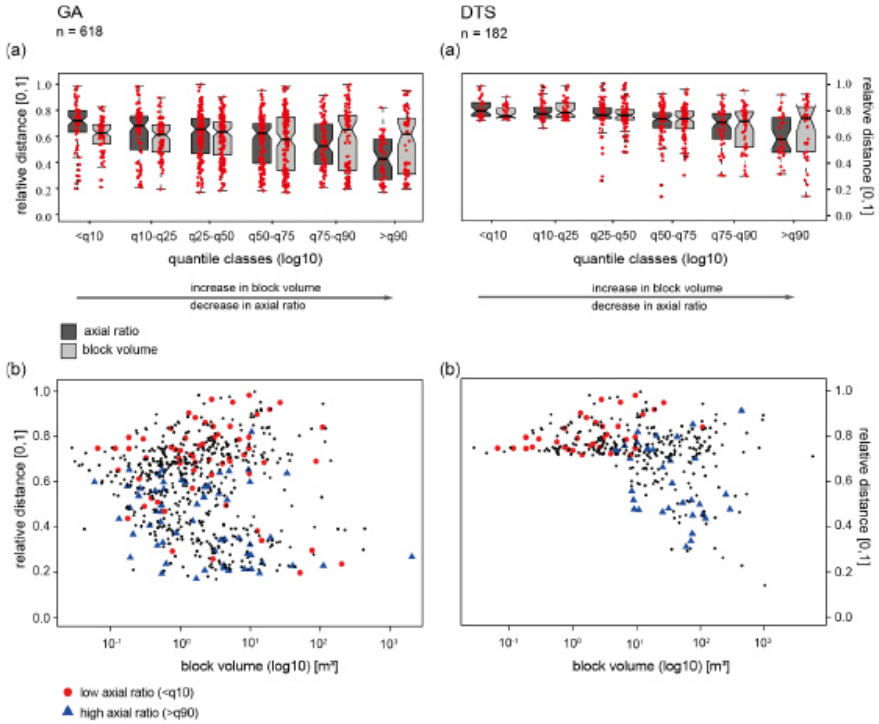

Figure 8. Boxplots of relative distance versus $\log_{10}$ block volume and $\log_{10}$ block shapes of the measured rocks for the GA and DTS study sites (**a**). The red-coloured points correspond to each measured individual block. The thick black lines within the boxes show the median bounded by the first quartile (25th percentile) and the third quartile (75th percentile). The boxes show the interquartile range (IQR). The whiskers of the boxplots mark the minima and maxima of the data. The circles represent data that exceed the 1.5-fold IQR (**a**). Scatterplot of relative distance versus $\log_{10}$ block volume for all study sites. Blocks with a low axial ratio (< q10) and a high axial ratio (> q90) are highlighted with different colours and symbols (**b**).

blocks. Pérez (1998) and Messenzehl and Dikau (2017) conclude in their studies that equant blocks are deposited predominantly at the talus toe. As already shown by Glover et al. (2015) in their rockfall simulation, uniformly shaped blocks followed by elongated blocks achieve the largest runout distances. Platy blocks, on the other hand, are known to tend to achieve long ranges only if they manage to place themselves on the shortest axis as the axis of rotation, which will probably not be the case for all blocks. This probably explains why such blocks tend to have shorter runout distances (Glover et al., 2015). It is particularly noticeable, however, that in the DTS area all blocks (< q10) with a low axial ratio achieve very high distances and are not found at all at the shorter distances (Fig. 8b). This supports the thesis above that platy blocks only achieve high runout distances when they are placed on the short axis (wheel effect). This is different in the GA area. Here the majority of the cuboid-shaped blocks can be found not only at the end of the slope but also on the upper slope (Fig. 8b). This could be explained by the fact that the blocks collide with each other during a large rockfall event, thereby dissipating their energy, or perhaps split into smaller blocks, resulting in the different block shapes being deposited in both the lower and the upper area of the talus cone (Ruiz-Carulla and Corominas, 2020). Although this cannot be definitively confirmed with the present study, eyewitness reports speak in favour of the fact that such a collision of blocks did indeed take place at least at GA.

4.2.2 Roughness as indicator for block size distribution

To put the sampling analysis into a broader context and to verify if our single-block analysis is representative for all talus cones, we attempted to use our high-resolution data to calculate roughness on an area-wide scale for all de-

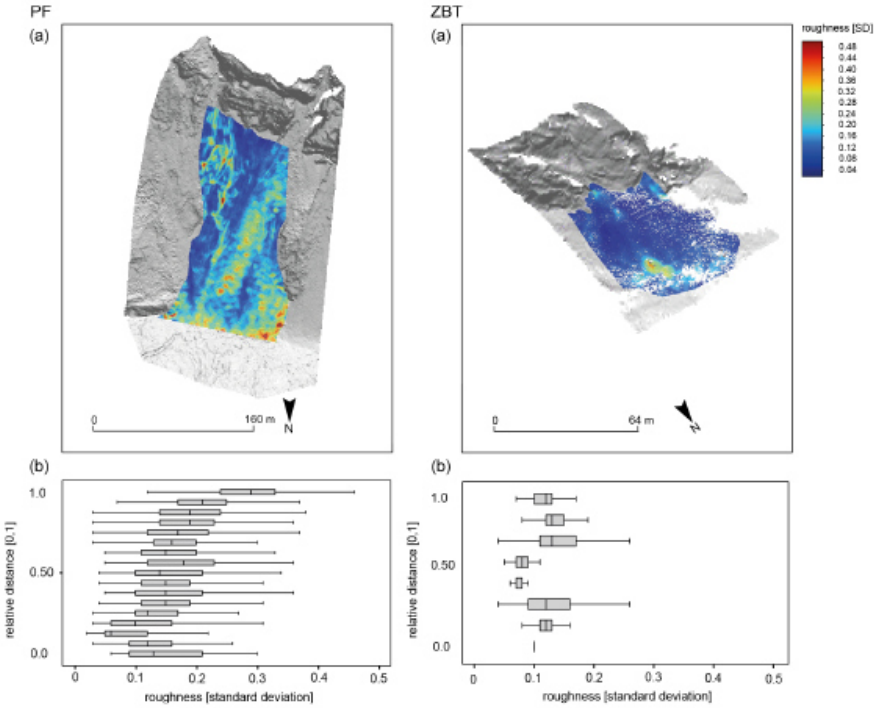

Figure 9. Maps of classified slope inclination for the PF and ZBT talus cones (**a**). Calculated roughness (standard deviation) based on the TLS point clouds which are classified into 10 m classes of the runout distance. To compare these values, we normalized the runout length to [0, 1] (**b**).

bris cones. Here, we understand roughness as an indicator of block size, with high roughness corresponding to large blocks and low roughness corresponding to smaller blocks.

The derived roughness based on the TLS point clouds shows a clear difference between the study sites (Figs. 9 and 10), which we also found in our single-block analysis in Sect. 4.2.1. The highest roughness values on the GA and DTS talus cones can be found on the upper slope – this pattern is somewhat less pronounced in the ZBT – and then fall off and rise again towards the end of the slope. This is in good agreement with our single-block analysis, where bigger blocks tend to have longer runout distances, but some of the bigger blocks show shorter runout distances (Figs. 7 and 8). In contrast to the other talus cones the roughness in PF and the ZBT seems to be continuously increasing in the downslope direction with the lowest roughness on the upper slope and the highest roughness at the end of the slope (Fig. 9a and b). This is also in good agreement with our results of the single-block analysis in Sect. 4.2.1, where we found a recognizable influence of the runout distance by the block volume (Fig. 7). It is also visible that the ZBT shows the lowest roughness values, which fits very well with the platy structure of the gneisses, since these blocks are mostly deposited with the shortest axis perpendicular to the talus cone. Wang and Lee (2010) and Mikoš et al. (2006) simulate in their studies that the roughness of the slope has an influence on the trajectory of the blocks and accordingly influences the deposition. In their laboratory experiment, Gratchev and Saeidi (2019) also come to the conclusion that the surface properties influence the rebound angle and, accordingly, the trajectory of rockfall material.

As our data show the talus cones only for one time step and we do not have information about the pre-event roughness, we cannot draw any conclusion about how the roughness of the talus cone acts as a moderating factor for the runout distances of our single blocks. But regarding Statham (1976) it is very likely that the roughness can play a major role and thus has influenced the runout distance of blocks in the past and will also do so in the future. However, it must be taken into account that the influence of roughness is also likely to

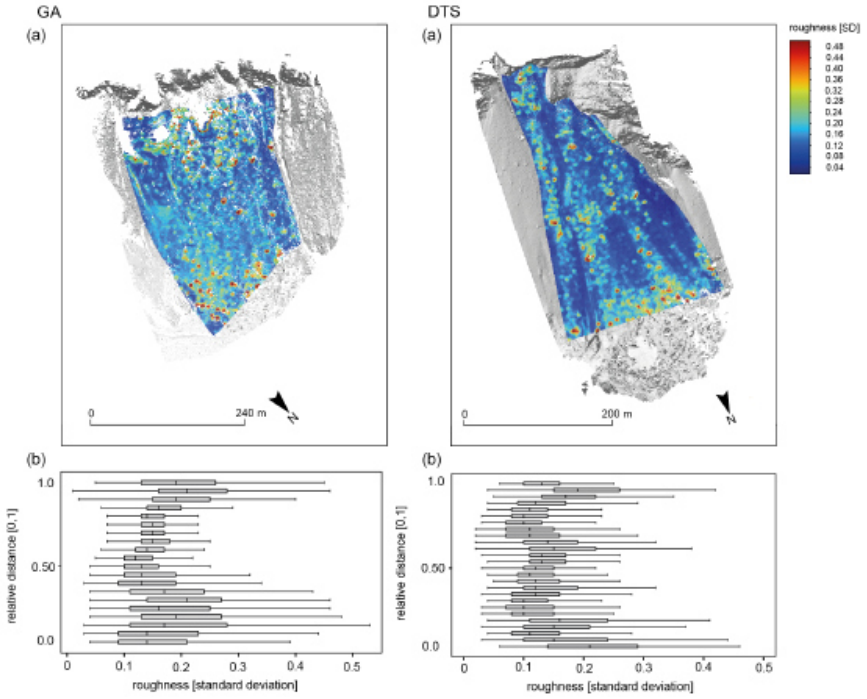

Figure 10. Maps of classified slope inclination for the GA and DTS talus cones (**a**). Calculated roughness (standard deviation) based on the TLS point clouds which are classified into 10 m classes of the runout distance. To compare these values, we normalized the runout length to [0, 1] (**b**).

depend on the block size of the rockfall material. It must be considered that the influence of roughness for smaller particles on the slope is more decisive than for larger particles that are not stopped by coarser material (Statham, 1976).

5 Conclusion

Our investigations show a discernible relationship between the lithology and the characteristics of the rockfall material within the four test sites. We found larger blocks on the talus cones of GA and DTS with their thickly banked limestones and dolomites. In contrast smaller blocks were found in areas with slated and platy gneisses (ZBT) as well as in thinly layered basaltic lava material (PF).

In addition to block size, lithology also seems to have a significant effect on block shape. Thus, the highest axial ratios were found in the ZBT area with platy gneisses. The limestones of DTS and GA show similar mean values and a similar scatter of data, indicating that dolomites and Wetterstein limestones produce similar block sizes and block shapes to thick-bedded reef limestones. Just the scatter of the data and the block size force the block volume and the block shape to not only be controlled by the banking, which indeed tends to lead to large block sizes. An additional controlling variable seems to be the clefting of the material. The combination of irregular clefting and thick banks apparently results in blocks with large volumes but different axial ratios. In contrast to the other test sites, the material of PF with its small block sizes and low axial ratios differs clearly. Here, the thin stratification of the lava material in connection with the strong tectonic stress due to frequent earthquakes and the resulting numerous fractures in the material certainly play a significant role in block size and block shape, resulting in smaller volumes and regularly shaped boulders.

Our analyses reveal a complex relation between block size and block shape with respect to the runout distance of deposited blocks with divergences between different lithological settings. Compared to other studies (Whitehouse and McSaveney, 1983; Jomelli and Francou, 2000; Sanders et al., 2009; Luckman, 2013a; Messenzehl and Dikau, 2017; Popescu et al., 2017) and with respect to our results we can

neither confirm nor reject the theory of gravitational sorting (Figs. 7b and 8b) as we did not find a clear relationship between block size and runout distance.

But for PF, GA and DTS we can confirm a tendency towards gravitational sorting to varying degrees, since blocks with a higher block volume tend to have longer runout distances. But we also find larger blocks with shorter runout distances as well as smaller blocks with longer runout distances. In contrast, almost no gravitational sorting could be detected for the ZBT area.

Thus and in agreement with other studies (e.g. Meißl, 1998; Haas et al., 2012; Glover et al., 2015; Messenzehl and Dikau, 2017) we can assume that the block size does not seem to be the only controlling variable.

According to our findings, the axial ratio of boulders for GA and DTS seems to influence the deposition of rock fragments on the talus cone such that blocks with increasing axial ratios have decreasing runout distances (Pérez, 1998; Glover et al., 2015; Messenzehl and Dikau, 2017; Volkwein et al., 2018). It seems that boulders with a low axial ratio roll over any axis and do not lose momentum, while boulders with a high axial ratio seem to either not always place themselves on the favourable axis of rotation or lose energy by tumbling due to their unfavourable axial ratio. In our study, blocks of the DTS study site with a low axial ratio achieve large runout distances. For the GA study site, blocks with a low axial ratio are found on the upper and on the lower part of the slope. But in the case of PF and the ZBT we cannot confirm the hypothesis of a moderating role of the axial ratio. For both study sites cuboid-shaped blocks as well as elongated blocks are deposited over all the slopes. Whether this is due to the different lithological setting or the fact that GA as well as DTS primarily includes blocks of one rockfall event, while the blocks in PF and the ZBT represent several individual and presumably temporally unrelated block falls, cannot finally be clarified. For this reason, singular rockfalls in different lithologies should be investigated in further studies.

The spatial roughness analysis based on the TLS point clouds shows a good agreement with single-block analysis regarding the dependencies between runout distance and block volume. Thus we can conclude that roughness can be used for such analysis instead of time-consuming single-block measurements. By using roughness as a proxy for block size, it would therefore be possible to investigate a larger number of test areas with this method and thus to investigate the implied relationships between lithology and block size in more depth in future studies. Such studies could perhaps be supplemented by a sample analysis of block shapes. Furthermore, due to the increasing number of available lidar data sets, it seems possible to include roughness as an additional influencing factor in a runout distance analysis, since information about the relief before an event would already be available for future rockfall events. We are quite sure that such a study can be carried out on the basis of ALS data or photogrammetric elevation models based on aerial photographs, where point densities are high enough to resolve blocks of a certain size, which are nowadays available for the whole of the Alps and mountain ranges worldwide.

Data availability. The data used in this study are accessible upon request by contacting Kerstin Wegner (KWegner@ku.de).

Author contributions. KW, FH and TH designed the conceptual idea of the manuscript. KW and FH collected the terrestrial laser scanning data on La Réunion. FH collected the TLS data of DTS, the ZBT and GA. TH contributed to statistical analysis of data. VD, NV and PK acquired the dGPS data on La Réunion. NV, PK and AP contributed to fieldwork on La Réunion. AM contributed to the financial support of the travel costs to La Réunion and gave feedback on the analysis of data, references, results and interpretation. MB contributed to the acquisition of the terrestrial laser scanner. KW wrote the manuscript with discussions and improvements from all co-authors.

Competing interests. The authors declare that they have no conflict of interest.

Acknowledgements. Florian Haas kindly provided the photographs used for Fig. 1, in particular of La Réunion, Dreitorspitze and Zwieselbach valley. The photo of Gampenalm was taken by an installed camera as part of the ERC SLIDEQUAKES project. We greatly appreciate the constructive comments and detailed feedback by the three anonymous referees that helped to improve the quality of this paper.

Financial support. Financial support for the fieldwork on La Réunion was provided by ERC-CG-2013-PE10-617472SLIDEQUAKES. This is IPGP contribution no. 4204. The open-access publication of this article was supported by the Open Access Fund of the Catholic University Eichstätt-Ingolstadt.

Review statement. This paper was edited by Yves Bühler and reviewed by three anonymous referees.

References

Abellán, A., Vilaplana, J. M., Calvet, J., García-Sellés, D., and Asensio, E.: Rockfall monitoring by Terrestrial Laser Scanning – case study of the basaltic rock face at Castellfollit de la Roca (Catalonia, Spain), Nat. Hazards Earth Syst. Sci., 11, 829–841, https://doi.org/10.5194/nhess-11-829-2011, 2011.

Agliardi, F. and Crosta, G. B.: High resolution three-dimensional numerical modelling of rockfalls, Int. J. Rock Mech. Min., 40, 455–471, https://doi.org/10.1016/S1365-1609(03)00021-2, 2003.

Azzoni, A. and de Freitas, M. H.: Experimentally gained parameters, decisive for rock fall analysis, Rock Mech. Rock Eng., 28, 111–124, https://doi.org/10.1007/BF01020064, 1995.

Bennett, G. L., Molnar, P., Eisenbeiss, H., and McArdell, B. W.: Erosional power in the Swiss Alps: Characterization of slope failure in the Illgraben, Earth Surf. Proc. Land., 37, 1627–1640, https://doi.org/10.1002/esp.3263, 2012.

Caine, N.: The texture of talus in Tasmania, J. Sediment. Res., 37, 796–803, https://doi.org/10.1306/74D717A3-2B21-11D7-8648000102C1865D, 1967.

Caviezel, A., Demmel, S. E., Ringenbach, A., Bühler, Y., Lu, G., Christen, M., Dinneen, C. E., Eberhard, L. A., von Rickenbach, D., and Bartelt, P.: Reconstruction of four-dimensional rockfall trajectories using remote sensing and rock-based accelerometers and gyroscopes, Earth Surf. Dynam., 7, 199–210, https://doi.org/10.5194/esurf-7-199-2019, 2019.

Conrad, O., Bechtel, B., Bock, M., Dietrich, H., Fischer, E., Gerlitz, L., Wehberg, J., Wichmann, V., and Böhner, J.: System for Automated Geoscientific Analyses (SAGA) v. 2.1.4, Geosci. Model Dev., 8, 1991–2007, https://doi.org/10.5194/gmd-8-1991-2015, 2015.

Copons, R., Vilaplana, J. M., and Linares, R.: Rockfall travel distance analysis by using empirical models (Solà d'Andorra la Vella, Central Pyrenees), Nat. Hazards Earth Syst. Sci., 9, 2107–2118, https://doi.org/10.5194/nhess-9-2107-2009, 2009.

Cox, N. J.: Kernel estimation as a basic tool for geomorphological data analysis, Earth Surf. Proc. Land., 32, 1902–1912, https://doi.org/10.1002/esp.1518, 2007.

Crosta, G. B., Agliardi, F., Frattini, P., and Lari, S.: Key issues in rock fall modeling, hazard and risk assessment for rockfall protection, in: Engineering Geology for Society and Territory, 2, Landslide Processes, eds.: Lollino, G., Giordan, D., Crosta, G., Corominas, J., Azzam, R., Wasowski, J., and Sciarra, N., Springer, International Publishing, Cham, Heidelberg, New York, Dordrecht, London, Switzerland, 43–58, https://doi.org/10.1007/978-3-319-09057-3_4, 2015.

Cui, Sh., Pei, Xj., and Huang, Rq.: Rolling motion behavior of rockfall on gentle slope: an experimental approach, J. Mt. Sci., 14, 1550–1562, https://doi.org/10.1007/s11629-016-4144-7, 2017.

Dietze, M., Mohadjer, S., Turowski, J. M., Ehlers, T. A., and Hovius, N.: Seismic monitoring of small alpine rockfalls – validity, precision and limitations, Earth Surf. Dynam., 5, 653–668, https://doi.org/10.5194/esurf-5-653-2017, 2017.

Dietze, M., Turowski, J. M., Cook, K. L., and Hovius, N.: Spatiotemporal patterns, triggers and anatomies of seismically detected rockfalls, Earth Surf. Dynam., 5, 757–779, https://doi.org/10.5194/esurf-5-757-2017, 2017.

Dorren, L. K. A.: A review of rockfall mechanics and modelling approaches, Prog. Phys. Geog., 27, 69–87, https://doi.org/10.1191/0309133303pp359ra, 2003.

Durand, V., Mangeney, A., Haas, F., Jia, X., Peltier, A., Hibert, C., Ferrazzini, V., Kowalski, P., Lauret, F., Brunet, C., Satriano, C., Wegner, K., Delorme, A., Bonilla, F., and Villeneuve, N.: On the link between external forcings and slope instabilities in the Piton de la Fournaise summit crater, Reunion Island, J Geophys Res: Earth Surface, 123, 2422–2442, https://doi.org/10.1029/2017JF004507, 2018.

Farin, M., Mangeney, A., Toussaint, R., de Rosny, J., Shapiro, N., Dewez, T., Hibert, C., Mathon, C., Sedan, O., and Berger, F.: Characterization of rockfalls from seismic signal: Insights from laboratory experiments, J. Geophys. Res.-Sol. Ea., 120, 7102–7137, https://doi.org/10.1002/2015JB012331, 2015.

Feng, L., Pazzi, V., Intrieri, E., Gracchi, T., and Gigli, G.: Rockfall seismic features analysis based on in situ tests: frequency, amplitude, and duration, J. Mt. Sci., 16, 955–970, https://doi.org/10.1007/s11629-018-5286-6, 2019.

Fityus, S. G., Giacomini, A., and Buzzi, O.: The significance of geology for the morphology of potentially unstable rocks, Eng. Geol., 162, 43–52, https://doi.org/10.1016/j.enggeo.2013.05.007, 2013.

Francou, B. and Manté, C.: Analysis of the segmentation in the profile of alpine talus slopes, Permafrost Periglac., 1, 53–60, https://doi.org/10.1002/ppp.3430010107, 1990.

Frattini, P., Crosta, G. B., and Agliardi, F.: Rockfall characterization and modeling, in: Landslides, Types, Mechanisms and Modeling, eds.: Clague, J. J. and Stead, D., Cambridge University Press, Cambridge, United Kingdom, 267–281, https://doi.org/10.1017/CBO9780511740367.023, 2012.

Gerber, E.: Klassifikation von Schutthalden, Geogr. Helv., 29, 73–82, https://doi.org/10.5194/gh-29-73-1974, 1974.

Glover, J., Bartelt, P., Christen, M., and Gerber, W.: Rockfall-simulation with irregular rock blocks, in: Engineering Geology for Society and Territory, Volume 2, eds.: Lollino, G., Giordan, D., Crosta, G. B., Corominas, J., Azzam, R., Wasowski, J., and Sciarra, N., Springer, International Publishing, Cham, Heidelberg, New York, Dordrecht, London, Switzerland, 1729–1733, https://doi.org/10.1007/978-3-319-09057-3_306, 2015.

Gratchev, I. and Saeidi, S.: The effect of surface irregularities on a falling rock motion, Geomechanics and Geoengineering, 14, 52–58, https://doi.org/10.1080/17486025.2018.1508857, 2019.

Guerin, A., Stock, G. M., Radue, M. J., Jaboyedoff, M., Collins, B. D., Matasci, B., Avdievitch, N., and Derron, M.-H.: Quantifying 40 years of rockfall activity in Yosemite Valley with historical Structure-from-Motion photogrammetry and terrestrial laser scanning, Geomorphology, 356, 1–18, https://doi.org/10.1016/j.geomorph.2020.107069, 2020.

Haas, F., Heckmann, T., Wichmann, V., and Becht, M.: Runout analysis of a large rockfall in the Dolomites/Italian Alps using LIDAR derived particle sizes and shapes, Earth Surf. Proc. Land., 37, 1444–1455, https://doi.org/10.1002/esp.3295, 2012.

Heckmann, T., Bimböse, M., Krautblatter, M., Haas, F., Becht, M., and Morche, D.: From geotechnical analysis to quantification and modeling using LiDAR data: A study on rockfall in the Reintal catchment, Bavarian Alps, Germany, Earth Surf. Proc. Land., 37, 119–133, https://doi.org/10.1002/esp.2250, 2012.

Heiser, M., Scheidl, C., and Kaitna, R.: Evaluation concepts to compare observed and simulated deposition areas of mass movements, Comput. Geosci., 21, 335–343, https://doi.org/10.1007/s10596-016-9609-9, 2017.

Hergarten, S., Robl, J., and Stüwe, K.: Extracting topographic swath profiles across curved geomorphic features, Earth Surf. Dynam., 2, 97–104, https://doi.org/10.5194/esurf-2-97-2014, 2014.

Hibert, C., Mangeney, A., Grandjean, G., and Shapiro, N. M.: Slope instabilities in Dolomieu crater, Réunion island: From seismic signals to rockfall characteristics, J. Geophys. Res., 116, 1–18, https://doi.org/10.1029/2011JF002038, 2011.

Hibert, C., Mangeney, A., Grandjean, G., Peltier, A., DiMuro, A., Shapiro, N. M., Ferrazzini, V., Boissier, P., Durand, V., and

Kowalski, P.: Spatio-temporal evolution of rockfall activity from 2007 to 2011 at the Piton de la Fournaise volcano inferred from seismic data, J. Volcanol. Geoth. Res., 333-334, 36–52, https://doi.org/10.1016/j.jvolgeores.2017.01.007, 2017.

Hungr, O. and Evans, S. G.: Engineering evaluation of fragmental rockfall hazards, in: Proceedings of the 5th International Symposium on Landslides, Lausanne, Switzerland, 10–15 July 1988, 894318, 685–690, 1988.

Jaboyedoff, M. and Derron, M.-H.: Hazard assessment within an Integrated Risk Assessment Process for Landslides (IRAPL), in: Proceedings of the International Conference on Landslide Risk Management, Vancouver, Canada, 31 May–3 June 2005, 2005.

Jaboyedoff M., Metzger R., Oppikofer T., Couture R., Derron M.-H., Locat J., and Turmel D.: New insight techniques to analyze rock-slope relief using DEM and 3D-imaging cloud points: COLTOP-3D software, in: Proceedings of the 1st Canada-US Rock Mechanics Symposium, Vancouver, Canada, 27–31 May 2007, ARMA-07-008, 61–68, 2007.

Jaboyedoff, M. and Labiouse, V.: Technical Note: Preliminary estimation of rockfall runout zones, Nat. Hazards Earth Syst. Sci., 11, 819–828, https://doi.org/10.5194/nhess-11-819-2011, 2011.

Ji, Z.-M., Chen, Z.-J., Niu, Q.-H., Wang, T.-J., Song, H., and Wang, T.-H.: Laboratory study on the influencing factors and their control for the coefficient of restitution during rockfall impacts, Landslides, 16, 1939–1963, https://doi.org/10.1007/s10346-019-01183-x, 2019.

Jomelli, V. and Francou, B.: Comparing the characteristics of rockfall talus and snow avalanche landforms in an Alpine environment using a new methodological approach: Massif des Ecrins, French Alps, Geomorphology, 35, 181–192, https://doi.org/10.1016/S0169-555X(00)00035-0, 2000.

Kenner, R.: Mass wasting processes affecting the surface of an alpine talus slope: Annual sediment budgets 2009–2018 at Flüelapass, eastern Swiss Alps, Land Degrad. Dev., 31, 451–462, https://doi.org/10.1002/ldr.3462, 2019.

Kirkby, M. J. and Statham, I.: Surface stone movement and scree formation, J. Geol., 83, 349–362, https://www.jstor.org/stable/30059027 (last access: 8 February 2021), 1975.

Knoblich, K.: Über den Böschungswinkel von Schutthalden, Catena, 2, 1–10, https://doi.org/10.1016/S0341-8162(75)80001-4, 1975.

Kotarba, A. and Strömquist, L.: Transport, sorting and deposition processes of Alpine debris slope deposits in the Polish Tatra mountains, Geogr. Ann. A, 66, 285–294, https://doi.org/10.1080/04353676.1984.11880116, 1984.

Krautblatter M. and Dikau R.: Towards a uniform concept for the comparison and extrapolation of rockwall retreat and rockfall supply, Geogr. Ann. A, 89, 21–40, https://doi.org/10.1111/j.1468-0459.2007.00305.x, 2007.

Kromer, R., Walton, G., Gray, B., Lata, M., and Group, R.: Development and optimization of an automated fixed-location time lapse photogrammetric rock slope monitoring system, Remote Sens., 11, 1–18, https://doi.org/10.3390/rs11161890, 2019.

Lambert, S., Bourrier, F., and Toe, D.: Improving three-dimensional rockfall trajectory simulation codes for assessing the efficiency of protective embankments, Int. J. Rock Mech. Min., 60, 26–36, https://doi.org/10.1016/j.ijrmms.2012.12.029, 2013.

Leine, R. I., Schweizer, A., Christen, M., Glover, J., Bartelt, P., and Gerber, W.: Simulation of rockfall trajectories with consideration of rock shape, Multibody Syst. Dyn., 32, 241–271, https://doi.org/10.1007/s11044-013-9393-4, 2014.

Lénat, J.-F., Bachèlery, P., and Merle, O.: Anatomy of Piton de la Fournaise volcano (La Réunion, Indian Ocean), Bull. Volcanol., 74, 1945–1961, https://doi.org/10.1007/s00445-012-0640-y, 2012.

Luckman, B. H.: Processes, transport, deposition, and landforms: rockfall, in: Mountain and Hillslope Geomorphology, Treatise on Geomorphology, edited by: Shroder, J. F., Stoffel, M., and Marston, R. A., Reference Module in Earth Systems and Environmental Sciences, 7, 174–182, https://doi.org/10.1016/B978-0-12-374739-6.00162-7, 2013a.

Luckman, B. H.: Talus slopes, ed.: Elias, S. A., The Encyclopedia of Quaternary Science, 3, 566–573, Elsevier, Amsterdam, 2013b.

Meißl, G.: Modellierung der Reichweite von Felsstürzen, Fallbeispiele zur GIS-gestützten Gefahrenbeurteilung aus dem Bayerischen und Tiroler Alpenraum, PhD thesis, Institute of Geography, University of Innsbruck, Austria, 249 pp., 1998.

Merle, O., Mairine, P., Michon, L., Bachèlery, P., and Smietana, M: Calderas, landslides and paleo-canyons on Piton de la Fournaise volcano (La Réunion Island, Indian Ocean), J. Volcanol. Geoth. Res., 189, 131–142, https://doi.org/10.1016/j.jvolgeores.2009.11.001, 2010.

Messenzehl, K. and Dikau, R.: Structural and thermal controls of rockfall frequency and magnitude within rockwall-talus systems (Swiss Alps), Earth Surf. Proc. Land., 42, 1963–1981, https://doi.org/10.1002/esp.4155, 2017.

Mikoš, M., Petje, U., and Ribičič, M.: Application of a rockfall simulation program in an Alpine valley in Slovenia, in Proceedings of the INTERPRAEVENT International Symposium Disaster Mitigation of Debris Flows, Slope Failures and Landslides, Niigata, Japan, 25–27 September 2006, 199–211, 2006.

Nappi, M., Budetta, P., Lombardi, G. and Minotta, C.: Rockfall run-out estimate comparing empirical and trajectographic approaches, in: Landslide Science and Practice Volume 6: Risk Assessment, Management and Mitigation, eds.: Margottini, C., Canuti, P., and Sassa, K., Springer, Berlin, Heidelberg, Germany, 177–182, https://doi.org/10.1007/978-3-642-31319-6_25, 2013.

Okura, Y., Kitahara, H., Sammori, T., and Kawanami, A.: The effects of rockfall volume on runout distance, Eng. Geol., 58, 109–124, https://doi.org/10.1016/S0013-7952(00)00049-1, 2000.

Peltier, A., Bachèlery, P., and Staudacher, T.: Magma transport and storage at Piton de la Fournaise (La Réunion) between 1972 and 2007: A Review of geophysical and geochemical data, J. Volcanol. Geoth. Res., 184, 93–108, https://doi.org/10.1016/j.jvolgeores.2008.12.008, 2009a.

Peltier, A., Staudacher, T., Bachèlery, P., and Cayol, V.: Formation of the April 2007 caldera collapse at Piton de la Fournaise volcano: Insights from GPS data, J. Volcanol. Geoth. Res., 184, 152–163, https://doi.org/10.1016/j.jvolgeores.2008.09.009, 2009b.

Peltier, A., Villeneuve, N., Ferrazzini, V., Testud, S., Hassen, T., Boissier, P., and Catherine, P.: Changes in the long-term geophysical eruptive precursors at Piton de la Fournaise: Implications for the response management, Front. Earth Sci., 6, https://doi.org/10.3389/feart.2018.00104, 2018.

Pérez, F. L.: Talus fabric and particle morphology on Lassen Peak, California, Geogr. Ann. A, 71, 43–57, https://doi.org/10.2307/521007, 1989.

Pérez, F. L.: Talus fabric, clast morphology, and botanical indicators of slope processes on the Chaos Crags (California Cascades), USA, Geogr. Phys. Quatern., 52, 1–22, https://doi.org/10.7202/004861ar, 1998.

Pfeiffer, T. J. and Bowen, T. D.: Computer simulations of rockfalls, Bulletin of the Association of Engineering Geologists, 26, 135–146, https://doi.org/10.2113/gseegeosci.xxvi.1.135, 1989.

Popescu, R., Vespremeanu-Stroe, A., Onaca, A., Vasile, M., Cruceru, N., and Pop, O.: Low-altitude permafrost research in an overcooled talus slope–rock glacier system in the Romanian Carpathians (Detunata Goală, Apuseni Mountains), Geomorphology, 295, 840–854, https://doi.org/10.1016/j.geomorph.2017.07.029, 2017.

Rapp, A.: Recent development of mountain slopes in Kärkevagge and surroundings, northern Scandinavia, Geogr. Ann., 42, 65–200, https://doi.org/10.1080/20014422.1960.11880942, 1960.

Ravanel, L., Allignol, F., Deline, P., Gruber, S., and Ravello, M.: Rock falls in the Mont Blanc Massif in 2007 and 2008, Landslides, 7, 493–501, https://doi.org/10.1007/s10346-010-0206-z, 2010.

RIEGL Laser Measurement Systems GmbH: Data Sheet, RIEGL LMS-Z420i, Horn, Austria, 2010.

RIEGL Laser Measurement Systems GmbH: Data Sheet, RIEGL VZ-4000, Horn, Austria, 2020.

Royán, M. J., Abellán, A., Jaboyedoff, M., Vilaplana, J. M., and Calvet, J.: Spatio-temporal analysis of rockfall pre-failure deformation using Terrestrial LiDAR, Landslides, 11, 697–709, https://doi.org/10.1007/s10346-013-0442-0, 2014.

Ruiz-Carulla, R. and Corominas, J.: Analysis of Rockfalls by Means of a Fractal Fragmentation Model, Rock Mech. Rock Eng., 53, 1433–1455, https://doi.org/10.1007/s00603-019-01987-2, 2020.

Sala, Z., Hutchinson, D. J., and Harrap, R.: Simulation of fragmental rockfalls detected using terrestrial laser scans from rock slopes in south-central British Columbia, Canada, Nat. Hazards Earth Syst. Sci., 19, 2385–2404, https://doi.org/10.5194/nhess-19-2385-2019, 2019.

Sandeep, C. S., Luo, L., and Senetakis, K.: Effect of Grain Size and Surface Roughness on the Normal Coefficient of Restitution of Single Grains, Materials, 13, 814, https://doi.org/10.3390/ma13040814, 2020.

Sanders, D., Ostermann, M., and Kramers, J.: Quaternary carbonate-rocky talus slope successions (Eastern Alps, Austria): sedimentary facies and facies architecture, Facies, 55, 345–373, https://doi.org/10.1007/s10347-008-0175-z, 2009.

Sens-Schönfelder, C., Pomponi, E., and Peltier, A.: Dynamics of Piton de la Fournaise volcano observed by passive image interferometry with multiple references, J. Volcanol. Geoth. Res., 276, 32–45, https://doi.org/10.1016/j.jvolgeores.2014.02.012, 2014.

Serrano, E. Sanjosé, J. J., Gómez-Gutiérrez, Á., and Gómez-Lende, M.: Surface movement and cascade processes on debris cones in temperate high mountain (Picos de Europa, northern Spain), Sci. Total Environ., 649, 1323–1337, https://doi.org/10.1016/j.scitotenv.2018.08.405, 2019.

Statham, I.: Scree slope development under conditions of surface particle movement, T. I. Brit. Geogr., 59, 41–53, https://doi.org/10.2307/621711, 1973.

Statham, I.: A scree slope rockfall model, Earth Surf. Proc., 1, 43–62, https://doi.org/10.1002/esp.3290010106, 1976.

Staudacher, T., Peltier, A., Ferrazzini, V., Di Muro, A., Boissier, P., Catherine, P., Kowalski, P., Lauret, F., and Lebreton, J.: Fifteen years of intense eruptive activity (1998–2013) at Piton de la Fournaise volcano: a review, in: Active Volcanoes of the Southwest Indian Ocean. Piton de la Fournaise and Karthala, eds.: Bachèlery, P., Lénat, J.-F., Di Muro, A., and Michon, L., Springer, Berlin, Heidelberg, Germany, 139–170, https://doi.org/10.1007/978-3-642-31395-0_9, 2016.

Strunden, J., Ehlers, T. A., Brehm, D., and Nettesheim, M.: Spatial and temporal variations in rockfall determined from TLS measurements in a deglaciated valley, Switzerland, J. Geophys. Res. Earth Surf., 120, 1251–1273, https://doi.org/10.1002/2014JF003274, 2015.

Urai, M., Geshi, N., and Staudacher, T.: Size and volume evaluation of the caldera collapse on Piton de la Fournaise volcano during the April 2007 eruption using ASTER stereo imagery, Geophys. Res. Lett., 34, 1944–8007, https://doi.org/10.1029/2007GL031551, 2007.

Valeton, I.: Beziehungen zwischen petrographischer Beschaffenheit, Gestalt und Rundungsgrad einiger Flussgerölle (Dependencies between petrographic conditions, shape and rounding of a few bedload gravel), Petermann Geogr. Mitt., 99, 13–17, 1955.

Vanneschi, C., Di Camillo, M., Aiello, E., Bonciani, F., and Salvini, R.: SfM-MVS photogrammetry for rockfall analysis and hazard assessment along the ancient Roman Via Flaminia road at the Furlo gorge (Italy), ISPRS Int. Geo-Inf., 8, 1–23, https://doi.org/10.3390/ijgi8080325, 2019.

Vilajosana, I., Suriñach, E., Abellán, A., Khazaradze, G., Garcia, D., and Llosa, J.: Rockfall induced seismic signals: case study in Montserrat, Catalonia, Nat. Hazards Earth Syst. Sci., 8, 805–812, https://doi.org/10.5194/nhess-8-805-2008, 2008.

Volkwein, A., Schellenberg, K., Labiouse, V., Agliardi, F., Berger, F., Bourrier, F., Dorren, L. K. A., Gerber, W., and Jaboyedoff, M.: Rockfall characterisation and structural protection – a review, Nat. Hazards Earth Syst. Sci., 11, 2617–2651, https://doi.org/10.5194/nhess-11-2617-2011, 2011.

Volkwein, A., Brügger, L., Gees, F., Gerber, W., Krummenacher, B., Kummer, P., Lardon, J., and Sutter, T.: Repetitive rockfall trajectory testing, Geosciences, 8, 1–27, https://doi.org/10.3390/geosciences8030088, 2018.

Wang, I.-T. and Lee, C.-Y.: Influence of slope shape and surface roughness on the moving paths of a single rockfall, World Academy of Science, Engineering and Technology, International Journal of Civil, Environmental, Structural, Construction and Architectural Engineering, 4, 122–128, 2010.

Wang, Y., Jiang, W., Cheng, S., Song, P., and Mao, C.: Effects of the impact angle on the coefficient of restitution in rockfall analysis based on a medium-scale laboratory test, Nat. Hazards Earth Syst. Sci., 18, 3045–3061, https://doi.org/10.5194/nhess-18-3045-2018, 2018.

White, S. E.: Alpine mass movement forms (noncatastrophic): Classification, description, and significance, Arctic Alpine Res., 13, 127–137, https://doi.org/10.2307/1551190, 1981.

Whitehouse, I. E. and McSaveney, M. J.: Diachronous talus surfaces in the Southern Alps, New Zealand, and their implications to talus accumulation, Arctic Alpine Res., 15, 53–64, https://doi.org/10.2307/1550981, 1983.

Wichmann, V.: The Gravitational Process Path (GPP) model (v1.0) – a GIS-based simulation framework for gravi-

tational processes, Geosci. Model Dev., 10, 3309–3327, https://doi.org/10.5194/gmd-10-3309-2017, 2017.

Yamamoto, T., Takada, A., Ishizuka, Y., Miyaji, N., and Tajima, Y.: Basaltic pyroclastic flows of Fuji volcano, Japan: characteristics of the deposits and their origin, Bull. Volcanol., 67, 622–633, https://doi.org/10.1007/s00445-004-0398-y, 2005.

Zevenbergen, L. W. and Thorne, C. R.: Quantitative analysis of land surface topography, Earth Surf. Proc. Land., 12, 47–56, https://doi.org/10.1002/esp.3290120107, 1987.

7.3 Multitemporal Quantification of the Geomorphodynamics on a Slope within the Cratère Dolomieu at the Piton de la Fournaise (La Réunion, Indian Ocean) Using Terrestrial LiDAR Data, Terrestrial Photographs, and Webcam Data

geosciences

MDPI

Article

Multitemporal Quantification of the Geomorphodynamics on a Slope within the Cratère Dolomieu at the Piton de la Fournaise (La Réunion, Indian Ocean) Using Terrestrial LiDAR Data, Terrestrial Photographs, and Webcam Data

Kerstin Wegner [1,*], Virginie Durand [2,3], Nicolas Villeneuve [3,4,5], Anne Mangeney [3], Philippe Kowalski [3,5], Aline Peltier [3,5], Manuel Stark [1], Michael Becht [1] and Florian Haas [1]

[1] Physical Geography, Catholic University of Eichstaett Ingolstadt, 85072 Eichstaett, Germany
[2] Geo Seismic—Cycles, Université Côte d'Azur, IRD, CNRS, Observatoire de la Côte d'Azur, Géoazur, 06560 Sophia-Antipolis, France
[3] Institut de Physique du Globe de Paris, Université Paris Cité, CNRS, 75005 Paris, France; nicolas.villeneuve@univ-reunion.fr (N.V.); anne.mangeney@gmail.com (A.M.)
[4] Laboratoire GéoSciences Réunion, Université de La Réunion, 97744 Saint Denis, France
[5] Observatoire Volcanologique du Piton de la Fournaise, Institut de Physique du Globe de Paris, 97418 La Plaine des Cafres, France
* Correspondence: kwegner@ku.de

Abstract: In this study, the geomorphological evolution of an inner flank of the Cratère Dolomieu at Piton de La Fournaise/La Réunion was investigated with the help of terrestrial laser scanning (TLS) data, terrestrial photogrammetric images, and historical webcam photographs. While TLS data and the terrestrial images were recorded during three field surveys, the study was also able to use historical webcam images that were installed for the monitoring of the volcanic activity inside the crater. Although the webcams were originally intended to be used only for visual monitoring of the area, at certain times they captured image pairs that could be analyzed using structure from motion (SfM) and subsequently processed to create digital terrain models (DTMs). With the help of all the data, the geomorphological evolution of selected areas of the crater was investigated in high temporal and spatial resolution. Surface changes were detected and quantified on scree slopes in the upper area of the crater as well as on scree slopes at the transition from the slope to the crater floor. In addition to their quantification, these changes could be assigned to individual geomorphological processes over time. The webcam photographs were a very important additional source of information here, as they allowed the observation period to be extended further into the past. Besides this, the webcam images made it possible to determine the exact dates at which geomorphological processes were active.

Keywords: terrestrial images; webcam data; LiDAR; TLS; photogrammetry; structure from motion; rockfalls; multitemporal change detection

Citation: Wegner, K.; Durand, V.; Villeneuve, N.; Mangeney, A.; Kowalski, P.; Peltier, A.; Stark, M.; Becht, M.; Haas, F. Multitemporal Quantification of the Geomorphodynamics on a Slope within the Cratère Dolomieu at the Piton de la Fournaise (La Réunion, Indian Ocean) Using Terrestrial LiDAR Data, Terrestrial Photographs, and Webcam Data. *Geosciences* **2024**, *14*, 259. https://doi.org/10.3390/geosciences14100259

Received: 8 August 2024
Revised: 11 September 2024
Accepted: 24 September 2024
Published: 28 September 2024

1. Introduction

Slopes in high mountain and volcanic regions are formed by a variety of geomorphological processes and their interaction. Forming and evolving craters and calderas are important geomorphic processes in volcanic regions. Gravitational instabilities can be induced by ongoing deformation and other processes affecting volcanic surfaces [1–3]. Observations have shown that calderas form mainly by subsidence, caused by magma draining from an underlying reservoir causing the overlying rock to collapse [4–7]. This collapse creates steep slopes susceptible to continuous rockfall and debris flows, for example, leading to deposits within the caldera [7]. In general, two main types of processes, depending on their occurrence and amplitude, govern the construction and evolution of high mountain slopes. There are high-frequency, low-amplitude phenomena that are

constantly monitored, measured, and quantified [8]. However, there are also low-frequency, high-amplitude events that are measured only sporadically [9–12]. For example, fluvial erosion contrasts with landslides and other debris avalanches. Infrequent processes such as debris flows or rockfalls can affect a high proportion of the sediment balance. Both the magnitude and frequency of these events are of great scientific interest, and this is why they are quantified in numerous studies, whereby different approaches are used [13].

It is possible to identify and map individual events of high magnitude using archival data such as historical aerial photographs, historical airborne laser scanning (ALS) data, photographs, or written records, e.g., [3,14–18]. Quantities of transported material can be derived from diachronic digital terrain models (DTMs) obtained by LiDAR (light detection and raging) acquisitions and/or stereophotogrammetric (SfM: structure from motion) analyses. However, the exact localization of the event can be used to determine the transported quantities at least approximately with current 3D surveys, e.g., [16]. In addition, it is necessary to consider the importance of the timing of the event's occurrence. It is essential that this is defined as accurately as possible. Due to this difficulty, it is important to note that temporal precision hinges on the temporal resolution of the input data. Depending on the region, time series of high-resolution aerial photographs can be available with an interval of several decades [13,16], whereas newer ALS data have intervals of up to a decade. This makes it difficult to determine the recurrence probability of such larger events accurately.

In addition to the fact that the frequency is not precisely recordable, there is a further problem in high mountain regions due to the usually very high geomorphodynamics. On steep and vegetation-free slopes, such as those of the Cratère Dolomieu of Piton de la Fournaise (PLF), individual processes may occur in succession, making it difficult to differentiate them. This problem is even more significant when the frequency of event occurrence is much higher than that of data acquisition. Consequently, this leads to inaccuracies regarding the frequency and magnitude of recorded events and, accordingly, in the data processing [19]. The probability of multiple events occurring between two measurement campaigns (especially several small ones that are not identified at the time of their occurrence and are later obscured by a larger one) is very high. This directly increases the error in calculating the frequency of occurrence [19].

Seismometers are therefore increasingly being used to monitor the frequency and magnitude of gravitational mass movements, e.g., [20–23]. These measurements make it possible to localize such events (starting zone, process area) precisely and to quantify them accurately using the seismic signals [24]. In addition to seismometers, InSAR (Interferometric Synthetic Aperture Radar) data can be used to monitor calderas [25,26].

Terrestrial photographs are another possibility to record changes on steep slopes, e.g., [16,18,27,28], but often have low temporal resolution, even for well-known locations like, e.g., famous alpine peaks [18]. While these images can extend observation series into the past, they cannot provide high temporal densification. In contrast, webcams (automatic cameras) used over the past 30 years offer a solution [29–32]. The prerequisites for the use of such data are (i) the longest possible period of time over which a webcam was operated at a fixed location and (ii) that the data were appropriately saved over this period. If these conditions are fulfilled, single images can be used for detailed spatial mapping and identification of single events, e.g., by visual inspection with a very high temporal resolution. This allows precise determination of event frequency in time and magnitude through subsequent quantification via, e.g., SfM or LiDAR. If such webcam images are available in pairs, direct quantitative analyses can be performed on the overlapping areas using a more or less 4D approach. In most cases, such image pairs are not installed according to stereophotogrammetric principles. Instead, they are captured to represent a slope from different angles or to view larger slope sections, which can result in overlaps that can in turn be used (with restrictions) for stereophotogrammetric processing.

Although there are some studies that use fixed webcams for volcano monitoring, these are not for the purpose of multitemporal analysis and quantification of geomorphological

processes [33–36]. For this reason, this study used two webcams in combination with additional data such as terrestrial LiDAR and terrestrial photography within the Cratère Dolomieu at PLF. The aim was to determine the geomorphodynamics of a slope over a period of approximately six years (2010–2016). In addition, the study aimed to investigate whether these photographs can help to analyze geomorphodynamics at a higher temporal resolution.

2. Study Area

La Réunion is a tropical island located in the Indian Ocean east of Madagascar (Figure 1). It forms an oceanic shield volcano with a spatial extent of nearly 240 km in diameter and a height of seven km measured from the seafloor [37,38]. The island has an age of around five Ma [39], beginning with the growth of the adjacent volcanoes Piton des Neiges (PDN) and Les Alizés (LA). While LA is now completely dismantled [37], PDN has remained inactive since its last eruption 27 ka years ago [40] but still forms the highest peak of La Réunion with about 3070 m a.s.l. All eruptions during the last 27 ka took place at PLF, which is situated on the flanks of LA and PDN and has a height of 2632 m a.s.l. PLF is among the most active shield volcanoes of the world [41] with a high eruptive frequency of one eruption every eight months on average [21]. The Cratère Dolomieu of PLF in its present shape (Figure 1) was partly formed by a collapse during an eruption in April 2007 and has partially begun to fill up due to lava flows of following eruptions [42]. The collapse of the crater floor created steep rock faces up to 320 m high, which are prone to continuous rockfall activity, varying widely in volume [22].

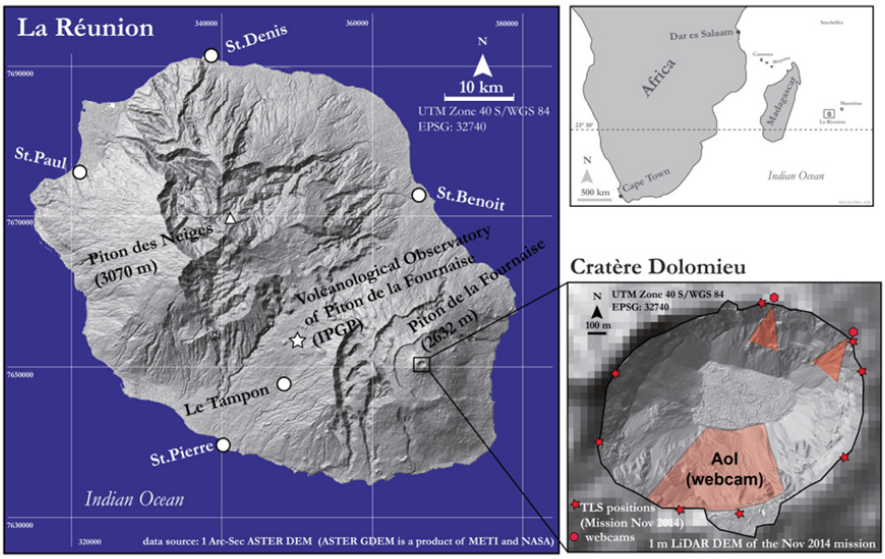

Figure 1. Location of the study area Cratère Dolomieu of the PLF. (Source of the overview base map: ASTER DEM. Source of the overview map of the Cratère Dolomieu is a 1 m DEM based on terrestrial laser scanning data acquired in 2014).

In addition to the volcanic filling of the caldera, geomorphic processes are involved in reshaping the "fresh" landscape inside the crater, characterized by high magnitudes and short frequencies. The very high geomorphic activity, resulting in massive slope failures and corresponding talus cones, is due to seismicity combined with the lithological and topographical conditions, as well as the extremely high amounts of rainfall [21,22]. The average annual precipitation ranges between 3000 and 4250 mm/year (for a watershed

of the PLF catchment area, [43]) with particularly intense precipitation during the rainy season. Reference [44] measured a mean annual rainfall of 6200 mm. The climate station on the southern rim of the Cratère Dolomieu (Figure 1) recorded an annual mean precipitation of 7469 mm for the period 2010 until 2016 with a maximum of 9890 mm in 2015.

3. Materials and Methods

3.1. Acquisition and Registration of Ground-Based LiDAR Data

During a two-day mission in November 2014, the Cratère Dolomieu was captured by the terrestrial laser scanner (TLS) Riegl VZ4000 with a maximum scanning distance up to 4000 m. Stable, precipitation-free weather conditions had to prevail during the entire data acquisition period. The position of the sun also had to be taken into account in order to avoid excessive shading. Both the TLS data and the terrestrial photographs were taken by climbing up to the crater.

To provide a high-resolution point cloud of the whole crater and to minimize shadowing effects (c.f. [45]), the scanning was conducted from eight different scan positions, which were all located close to the crater rim (Figures 1 and 2). The TLS specifications and survey parameters are listed in Tables 1 and 2. The horizontal and vertical scan resolution was set to a 0.02° step width and included overlapping areas between the single scans and also areas in the backside of every scan position. The backside scans were captured in order to scan tie points (Riegl reflectors). Those exact positions of the reflectors were measured externally during the mission by using a dGNSS system (Figure 2) and thus provide information about the global coordinate system (UTM40S/WGS84; EPSG: 32740) after postprocessing. The acquired TLS raw data had to pass several postprocessing steps (c.f. [45]), beginning with the registration/referencing of every single scan position by using an iterative closest point (ICP) algorithm (Multi Station Adjustment tool) in the software RiScan Pro (Version 2.4, riegl.com) [46,47]. The referencing accuracies show values between 0.007 m and 0.013 m.

Figure 2. Riegl VZ4000 laser scanner located on the crater rim and dGNSS measurement of tie points (Riegl reflector) (own photographs captured during fieldwork in 2014).

After the registration and the merging of all scan positions, the resulting raw point cloud was linked with global coordinates by using dGNSS measured reflectors of four backside scans. After the processing procedure, the data were ASCII formatted (x, y, z, RGB values) and exported as global coordinates. The LiDAR point clouds had to be rotated in order to receive a z coordinate that is perpendicular to the rock face [49]. Ground control points (GCPs) were extracted from the LiDAR point cloud for georeferencing and scaling of the rock faces. These selected GCPs were also used for further SfM processing. All further processing steps (e.g., thinning, filtering, DEM generation) were performed using LIS Desktop/SAGA GIS (c.f. 3.5).

Table 1. Specifications of the TLS Riegl VZ-4000 [48]. The values given are based on measurements taken at a rate of 30 kHz (* = milliradian).

Parameter	Riegl VZ-4000
Max. measurement range	4000 m
Min. measurement range	5 m
Field of view	60° (vertical) × 360° (horizontal)
Measurement rate	Max. 230,000 pts./s
Accuracy	15 mm
Precision	10 mm
Laser wavelength	Near-infrared
Laser beam divergence	0.15 mrad *

Table 2. Survey parameters of TLS.

Survey Parameter	
No. of scan positions	8
No. of backside scans	8
Humidity	30%
Temperature	28 °C
Year	2014

3.2. Acquisition of Terrestrial Photographs

During missions in 2014 (at the same time as the TLS mission), 2015, and 2016 (additional missions without TLS acquisition) terrestrial photographs were captured around the crater rim, including all scan positions but also locations between them. Three different uncalibrated cameras were used for these images (Table 3). For this work, only pictures of the east-facing slope (2014 and 2016) as well as of the north-facing slope (same section as the webcams, 2010–2016, c.f. 3.3) were used for the following processing steps, which all pictures had to pass in order to produce SfM-based point clouds (c.f. 3.4).

Table 3. Three different camera systems used to capture the terrestrial photographs.

Parameters	Webcam	Webcam	Camera System 3	Camera System 4	Camera System 5
Type	Pentax	Canon	Pentax	Canon	Nikon
Name	K200D	EOS350D	Kx	EOS 1DS Mark III	D610
Resolution	10.2 MP	8 MP	12.2 MP	21.1 MP	24.3 MP
Focal length	18 mm	20 mm	28 mm	35 mm	32 mm
Exposure	1/200	1/40	1/200	1/100	1/400
Responsivity	100	100	200	100	100
Aperture	F/8	F/16	F/11	F/8	F/4.5
Amount of pictures	390	485	496	92	133
Amount of pictures used for data processing	2 pairs	4 pairs	4 pieces	4 pieces	4 pieces
Year	10/2009–07/2010	12/2010–12/2011	2014	2015	2016

3.3. Acquisition of Webcam Photographs

Between 2009 and 2012, a large number of photographs (875) were captured by two webcams located at the northern rim of the Cratère Dolomieu, focusing on the northern exposed slopes (Figure 1). During this period, different types of non-calibrated SLR cameras were used (Table 3). Parameters of the webcam-based camera systems are given in Table 3. Both camera setups were configured as time-lapse cameras with a fixed interval but without synchronization. Since the cameras were not originally intended for photogrammetric imaging, but rather to observe different zones of the southwestern crater, they did not operate in parallel for the entire period. This was compounded by data outages. On

most days of both years, two pictures were available from each camera. However, due to the rapidly changing weather conditions on PLF, shadowing effects, and the lack of synchronization (resulting in different lightning conditions), only a few photographs were suitable for processing with SfM (4D analysis) (Table 3). Even though only a few photos could be used for the 4D analysis, individual photos still proved to be very helpful. They allowed for better visual classification of events over time, even if only partially.

3.4. SfM and Global Registration of the Point Clouds

To produce 3D point clouds from both the terrestrial and the webcam photographs, the following processing steps were performed using Agisoft Metashape Professional (AMP; Agisoft/Vers. 1.2.3-64bit). The overall data processing workflow for this study is shown in Figure 3.

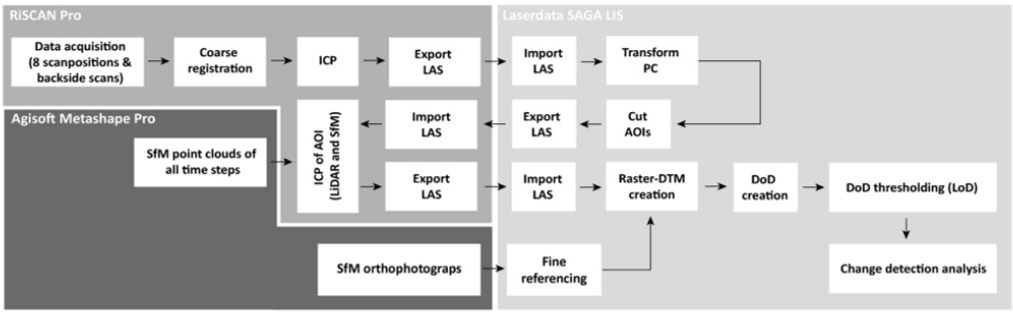

Figure 3. The entire workflow for processing TLS data, digital terrestrial, and webcam photographs is illustrated. The particular processing steps are demonstrated for each relevant software (RiSCAN PRO (Version 2.4), Agisoft Metashape Pro (Version 1.5.5), Laserdata SAGA LIS (Version 3.0.7, 3.1.0)).

- Pictures from each time step were aligned, and tie points were automatically derived by AMP, resulting in a first sparse point cloud, but still without a global referencing.
- GCPs were set on every single picture. Since it is not allowed to enter the crater, there are no markers available inside it. Thus, GCPs were first selected using concise objects in the 2014 TLS point cloud. The GCPs derived from the TLS point cloud were employed for scene triangulation and reconstruction [50], as well as for defining and adjusting the external orientation parameters (scale, rotation, translation) of the image sets [51]. The coordinates of the GCPs were obtained for structures that were clearly visible in both the TLS point cloud and the terrestrial photographs and had remained unchanged throughout the observation period. The criterion for the selection was the visibility of the concise objects/formations (e.g., big boulders, structures in the rock face, which are more stable than others) in both the 2014 TLS and the 2014 terrestrial photographs. A total of 39 GCPs were selected to ensure sufficient reference points in all terrestrial and webcam photographs, considering the geomorphologic changes between 2009 and 2016, and thus the appearance or disappearance of concise objects, especially in the earlier picture pairs (2009–2013). The 2014 terrestrial photographs serve, then, for localization of GCPs in the photographs from other time steps.
- Based on the sparse point cloud and using the available GCPs, the dense cloud of the 2014 terrestrial photographs was derived.
- After referencing the 2014 terrestrial photographs, the dense point cloud was exported as an LAS file and imported into RiSCAN Pro for an ICP adjustment. This was carried out between the 2014 LiDAR point cloud and the 2014 SfM point cloud, with the 2014 LiDAR point cloud serving as the "Master".
- The final referenced 2014 SfM point cloud and the corresponding orthophotographs were used to identify and extract GCPs for referencing the webcam photographs. After

the final adjustment of the sparse cloud in AMP, a dense point cloud for each image pair of the webcam photographs was derived and exported as an LAS file.

- These LAS files were imported into RiSCAN Pro and an ICP adjustment was performed on the base of stable areas (Figure 4). This adjustment was necessary because uplift and subsidence had occurred in the area of the crater over the years due to active volcanism, making coordinates alone unreliable for fitting the individual point clouds. By using stable areas within the Areas of Interest (AoIs), these inconsistencies were avoided, assuming that these uplifts and subsidence did not occur at specific points but had approximately constant values in these areas.

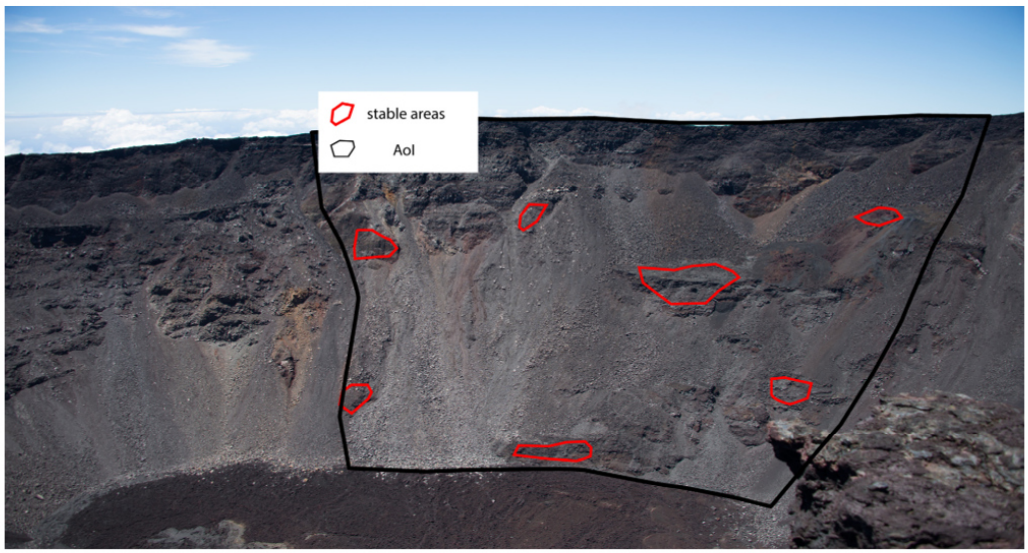

Figure 4. Investigated slope and stable areas for ICP adjustment. The location of the AoI can be seen in Figure 1 on the overview map of the crater.

At the end of this workflow, adjusted point clouds and orthophotographs are available for the different time steps. The point clouds were created as LAS files. The additional orthoimages were exported as referenced tiff files. All further processing steps (e.g., thinning, filtering, DEM generation) were performed similarly to the TLS and LiDAR data by using SAGA LIS.

3.5. Two-Step SfM and LiDAR Point Cloud Referencing

Given the significant differences in resolution, accuracy, and coverage among the various photogrammetric point clouds due to varying data quality [52,53], the goal was to reduce these discrepancies using the ICP algorithm (see Section 3.1). It was ensured that the co-registration was performed on data with similar point densities. To achieve this, the TLS point density was adjusted ("point cloud thinning") to match the density of the corresponding SfM point clouds. Even after the first co-registration, the DTMs may still have some minor systematic errors. These were reduced by focusing on the stable surfaces in the vicinity of the respective process areas in a second co-registration step. Finally, all point clouds were exported as individual LAS files for further analysis.

3.6. Quantification of Surface Changes

The LAS files for all time steps, including TLS and SfM data, were imported to SAGA LIS Desktop (Vers. 3.0.7-64bit)/SAGA GIS (Vers. 3.1.0-64bit) by producing a SAGA point

cloud. To eliminate flying points or artefacts, the "isolated point filter" and the "flying point filter" were applied (c.f. [45]). Deriving surface changes or the corresponding volumes by using a normal GIS system is challenging due to the poor representation of vertical areas. However, GIS systems provide many additional tools for spatial data analysis. LIS Desktop provides both 3D as well as 2.5D data formats and tools. Consequently, all surface changes and the corresponding volumes were derived in LIS by using the 3D point cloud data format. This was achieved by using the tool "distance between point clouds", which derives the 3D differences between corresponding points. These are defined using the point normal information. This normal information is in turn provided by a robust plane fitting approach, which is described in detail by [54]. Based on the 3D distances between corresponding points, areas with changes were mapped and DEMs of these areas for the single time steps were derived. Using these DEMs, the volume of each area was calculated by using the SAGA tool Cut & Fill [55] and by considering a Level of Detection (LoD).

3.7. Error Propagation

Since all point clouds contain inaccuracies due to measurement errors and registration inaccuracies, a LoD must be defined to differentiate measurement errors from actual topographic changes [54,56–58]. For calculating an LoD for the surface change calculation (point to point distances) of every single time step, a statistical approach of [57] using stable areas [59,60] was applied. The workflow, which is described in detail by [45] and [21] for the Cratère Dolomieu, uses the derived combined normal distribution error from the formula,

$$\delta_{point\ distance} = \sqrt{\sigma^2_{point\ distance} + \sigma^2_{point\ distance}}$$

where σ is the standard deviation of the derived point to point distances of assumed stable areas between two-time steps.

Following [60], the absolute value of each point to point distance (DP1 DP2) was divided by $\delta_{point\ distance}$ in order to calculate a t score:

$$t = \frac{|D_{P1} - D_{P2}|}{\delta_{point\ distance}}$$

Using a simple t-test ($t$crit at the 95% confidence interval with $t > 1.96$), the point to point distances can then be classified as probably real surface changes or probably measurement errors, and thus, an LoD can be derived for every single time step (Table 4). Point to point distances below the certain LoD were not used for the volume calculation.

Table 4. LoD derived from stable areas with corresponding used data sets.

Period	Data Set	LoD on Stable Areas
2010–2011	Webcam–webcam	0.59 m
2011–2012	Webcam–webcam	0.60 m
2012–2014	Webcam–TLS	0.69 m
2014–2015	TLS–terrestrial photographs	0.26 m
2015–2016	TLS–terrestrial photographs	0.45 m
2010–2016	Webcam–TLS	0.80 m

4. Results and Discussion

4.1. Useable Photographs for 4D Analysis

A total of 875 photos from the webcams were available between fall 2009 and 2012 to record changes in the southern crater area. In total, 485 of the photos are from the eastern camera and 390 from the western camera (Table 3). The data were carefully sifted and, unfortunately, most of the photos had to be discarded for the 4D analysis. For certain time periods, image pairs were not available due to memory issues, power supply failure, or incorrect time synchronization. Numerous photos were taken under bad weather

conditions, like it is shown in Figure 5. As a result, no tie points can be found on the crater slopes during data processing.

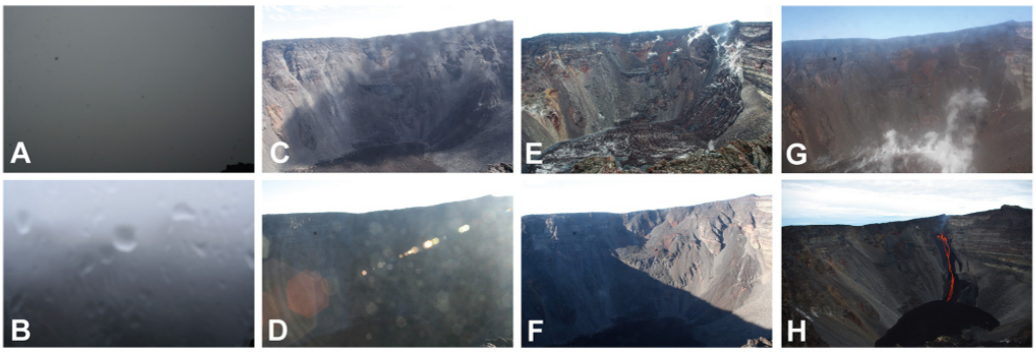

Figure 5. Different examples of photographs that were not usable for further SfM processing due to insufficiencies regarding differences in the quality. (**A**) Investigated slope was either completely or partially in clouds. (**B**) Camera lens was fogged. (**C**) Contamination on the camera lens. (**D**) Light reflections lead to a poor contrast. (**E**) Existing ground fog does not allow data processing. (**F**) Strong shadows especially during summer in the southern hemisphere led to contrast differences. (**G**) Existing fog in the crater. (**H**) Volcanic eruption occurred on 4 January 2010, moving lava prevented use of this image pair.

At the end of this review, 35 image pairs remained available for further 4D processing. For all these image pairs, a first alignment was calculated in AMP. After this first attempt, another 20 image pairs had to be discarded. In these image pairs, contrast and illumination differences, which at first glance were considered unproblematic, caused problems with the alignment. As a result, the software was unable to correctly reconstruct the respective lens distortion parameters and compute the appropriate camera model, which resulted in only a few tie points. This aligns with the findings of [61,62], who emphasize the critical role of image texture (entropy) in bundle adjustment and feature extraction (tie points) during SfM processing.

At the end of the process, it was decided to include photographs from January 2010, January 2011, and January 2012 for this study. With the TLS photos taken in November 2014, the photos taken in fall 2015, and the photos taken in fall 2016, this allowed similar periods to be processed in the analysis.

4.2. Achieved Accuracies

Based on the stable areas, an LoD could be calculated for the individual periods. The values of this LoD depend on the data used and it turns out that the point clouds calculated from webcam images in particular show higher values (Table 4). This applies, for example, to the periods 2010 to 2011 and 2011 to 2012, which were determined solely based on point clouds calculated from webcam images. The combination of webcam images and TLS data also shows a high LoD. In contrast, the combination of TLS data and the manually taken photographs provides the lowest values, with the period 2014 to 2015 showing the lowest LoD at 0.29 m, and 2015 to 2016 the second lowest with 0.45 m. Due to data gaps and the use of varying methods, different LoD values are to be expected. This indicates that the magnitudes observed differ across individual years. Small events cannot be detected in these data, which is, for example, not possible with the used webcam data sets. Due to the annual data, it is not clear whether the events were single or overlapping. However, the photographs provide some information that suggests that some of the events were single.

Nevertheless, it cannot be excluded that additional events occurred later. In this case, a higher temporal resolution of the data sets would be needed.

4.3. Mapping of Surface Changes Based on Webcam Photographs

To detect surface changes, the first step involved reviewing the photos of 2010 and 2016 to identify areas where major surface changes had occurred within the investigated period. These areas were then compared with the overlapping areas of the photographs to ensure that these active areas were within the derivable DTMs. At the end, four zones with visible major surface changes were identified. Although a large zone in the northern area with deposits is clearly visible in Figure 6, no surface changes could be quantified there. The areas were then mapped as polygons based on the SfM-derived orthophotos of the single time steps. These polygons were subsequently used as AoIs for the quantitative evaluations based on a DEM of differences (DoDs). Figure 6 shows these zones for 2010 and 2016. The perspectives of these photographs differ slightly because the photograph of 2010 was captured by the webcams, while the 2016 photograph was taken manually during a field survey. Consequently, the camera systems have different exposure angles. Nevertheless, surface changes between 2010 and 2016 are clearly visible. The most pronounced changes can be found at rockfall zone I.

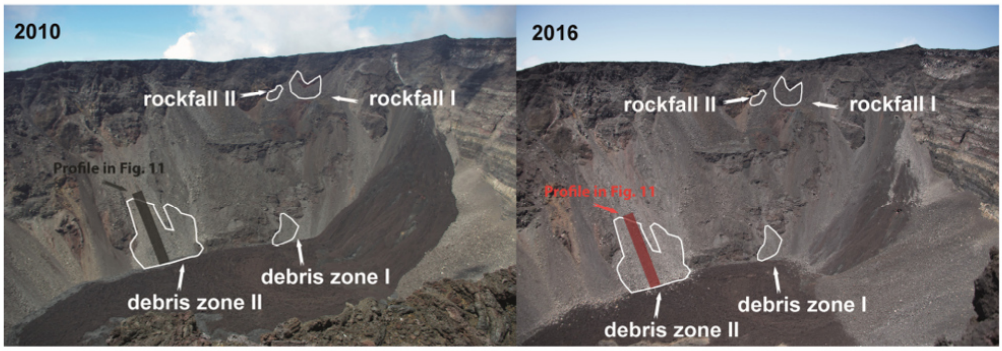

Figure 6. Mapped areas with visible surface changes within the different time steps between 2010 and 2016 that lie inside the derivable DTM. Both highlighted profile lines (grey, red) for the years 2010 and 2016 are analyzed in Figure 11.

4.4. Calculation of Surface Changes on the Mapped AoIs

4.4.1. Rockfall Zones

In the two rockfall zones (zones I and II), bigger deposits were observed below the bedrock areas (Figure 7). Due to the marginal position of the rock faces in the photographs and the limitations caused by the single overlap, surface changes in the rock faces could only be determined for the lower areas. For the adjacent scree slopes, however, we were able to quantify the deposits.

Throughout the study period, it is clearly visible that rockfall activity in rockfall zone I increased from 2010 to 2014 and decreased between 2014 and 2016. The accumulated material between 2010 and 2012 amounted to 1748 m^3 with a mean thickness of 20 cm between 2010 and 2011 and 11 cm between 2011 and 2012. From 2012 to 2014, the activity was an order of magnitude higher than during the previous period, totaling 16,799 m^3 with a mean thickness of nearly 3 m. This represents an annual deposition of almost 8400 m^3 and a mean annual thickness of almost 1.5 m.

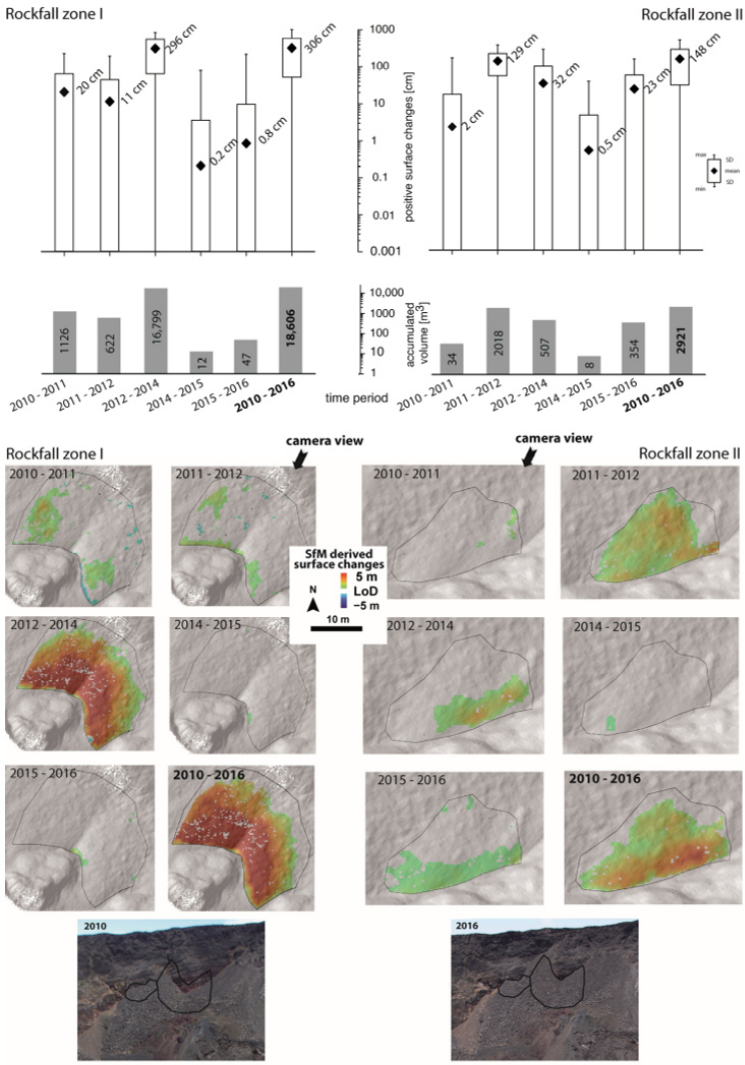

Figure 7. Derived surface changes (digital terrain model of differences: DoDs) for the two rockfall hotspots 1 and 2 between 2010 and 2016 (shaded relief in the background is derived on the base of the 2016 DTM). Also shown are the positive surface changes [cm] and the accumulated volume [m^3] of the two areas for the corresponding periods.

In addition to the quantification of the surface changes, the difference models reveal that accumulation on this scree slope is spatially very limited between 2010 and 2011, and between 2011 and 2012, likely due to smaller single events. This is also the conclusion reached by [21]. In their studies, they describe a decrease in activity in the years 2010 to 2011, which can be considered as a stable phase [21]. Between 2012 and 2014, a large-scale accumulation on the slope occurred, which can possibly be the consequence of a larger individual event. Even though no seismic activity could be detected for this period, one

possible explanation for the destabilization is the combination of rainfall and strong winds caused by two tropical cyclones in early 2013 [22]. From 2014 onwards, only small surface changes are visible directly at the foot of the rock face, so that this area of the crater has apparently come to a temporal rest. While the activity of rockfalls is decreasing in this area of the crater, an increase can be observed in the northwestern area, also due to higher volcanic activity [21,22].

In rockfall zone II, no surface changes are visible between 2010 and 2011. Starting from 2011, an active phase begins, marked by a first large-scale accumulation with a volume of 2018 m^3 between 2011 and 2012, followed by a slightly lower accumulation of 507 m^3 between 2012 and 2014. After one year (2014 to 2015) with almost no activity, accumulation volumes of 354 m^3 were recorded between 2015 and 2016. The average surface changes between 2012 and 2014 and 2015 and 2016 were 32 cm and 23 cm, respectively. From 2011 until 2012, a mean accumulation height of 129 cm was detectable. The difference models of rockfall zone II clearly show that the accumulation is spatially very limited to areas close to the rock face between 2012 and 2014, and between 2015 and 2016, likely due to smaller single events with accumulation zones close to the rock face. The large-scale accumulation between 2011 and 2012 is probably the consequence of a larger individual event, which led to almost the entire rockfall zone II becoming an accumulation area.

For an area northwest of the Cratère Dolomieu, the authors of [21] were able to detect rockfalls with a volume of 80,000 m^3 during the study period from November 2014 to January 2016 in their survey based on TLS and terrestrial photogrammetry, among other methods. Increasing eruptive activity was detected in this period [22]. However, this area is not covered by the webcams, although if more permanent camera systems were to be installed on the crater rim, using photogrammetric principles, the entire slope and its processes could be captured. In a study on Volcán de Colima (Mexico) by [63], rockfall volumes were derived from high-resolution photographs. However, a conventional change detection study was not conducted. Instead, they categorized the rockfalls into several classes and calculated mean volumes for each. Their results showed mean volumes of 56.6 m^3, 43 m^3, and 146.7 m^3 [63], which are significantly lower than the values we calculated. In contrast, [1] measured significantly larger surface changes than ours over a comparable period (2011–2017) in their study of the Telica volcano in Nicaragua using an unmanned aerial vehicle (UAV). They recorded surface changes of 8400–140,000 m^3. It should be mentioned here that no process areas were detected, as we did. However, they do not provide a contextual classification of what triggered the observed surface changes, either.

4.4.2. Debris Zones

Within the investigated debris zones, surface changes are observable from 2010 to 2016 (Figure 8), with some exceeding one meter in height. Both zones are again located in the marginal area of the photos and at the transition between the debris cone and the crater floor. The photographs clearly indicate that the debris cones have expanded considerably to the crater floor, suggesting substantial accumulation in these areas.

In debris zone I, the activity was notably high between 2010 and 2014. During this period, 1821 m^3 of material accumulated between 2010 and 2011, followed by a slight accumulation of 107 m^3 between 2011 and 2012, and a higher accumulation of 1039 m^3 between 2012 and 2014. In total, 2967 m^3 of material was deposited during this period. The results up to 2012 are in good agreement with the investigations of [22], as the large surface changes in this phase of high seismic activity can be explained either by this or by rain. Even though a period of eruptive activity can be observed again from 2014 onwards [22], there was almost no accumulation in this area between 2014 and 2016. The average surface changes range between 10 cm and 110 cm between 2010 and 2014. After 2014, surface changes were minimal, and the deposition patterns do not clearly indicate whether the accumulation was due to landslide processes or fluvial deposits from sediment sources in their upper slope areas.

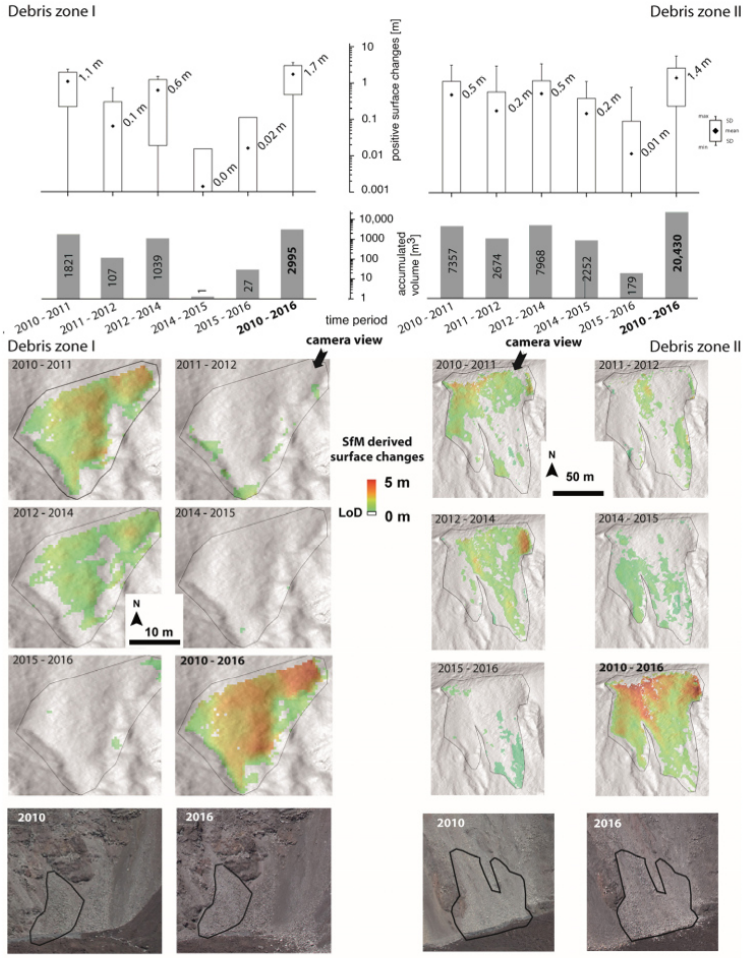

Figure 8. Derived surface changes (DoDs) on two selected debris cones between 2010 and 2016 (shaded relief in the background is derived on the base of the 2016 DTM). Also shown are the positive surface changes [cm] and the accumulated volume [m^3] of the two areas for the corresponding periods.

Debris zone II exhibits distinct linear depositional patterns, which indicate that the depositional area was formed by debris flows or fluvial processes. The high accumulation for the period 2012 to 2014 is presumably due to precipitation, since, as already mentioned, two cyclones occurred in 2013 [22]. However, larger individual boulders at the foot of the slope appear to have been deposited due to gravitational processes (falling stones) [64]. It is likely that different single processes formed the deposits. During fieldwork, gravitational processes (such as individual rockfall events or smaller rockfalls) were observed, and individual webcam images reveal linear structures that may indicate smaller debris flows (Figure 9).

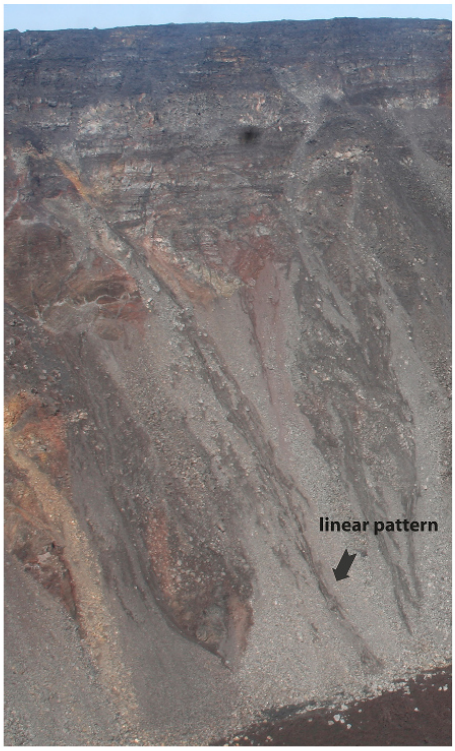

Figure 9. Clearly visible linear patterns on the debris zone II.

Overall, debris zone II is significantly larger than debris zone I and includes additional areas of loose material in the upper area, which transitions into rock areas in the uppermost area. According to the visual inspection, the upper areas have also changed over the observation period, but these zones lie outside the overlapping areas, so no DTMs could be calculated for them using SfM.

Due to increased eruptive activity, zone II like zone I shows increased accumulation in the first phase of the observation period [22]. The highest deposit volumes were recorded between 2010 and 2011 (7357 m^3), between 2011 and 2012 (2674 m^3), and between 2012 and 2014 (7968 m^3). In the period from 2012 to 2014, precipitation must be assumed to be the trigger [22]. After 2015, the activity decreases significantly to 179 m^3. The maximum value of the average surface change is 50 cm. Reference [15] calculated surface changes of 47.8 $\pm$ 3.6 $\times$ 10^3 m^3 in another area of the Cratère Dolomieu using airborne SfM in their studies conducted from December 2014 to May 2015. It should be noted, however, that even if eruptive activity resumed during this period [22], this deposition occurred in the highly active northwestern area of the crater. Their analyses indicate that this large landslide occurred in mid-May 2015. For the whole period of their investigations from April 2008 to May 2015, they calculated a cumulative volume of 1.8 $\pm$ 0.1 $\times$ 10 m^3 surface changes [15]. However, only processes larger than 1000 m^3 were quantified and the resolution of the data did not allow any conclusions to be drawn about possible triggering. Additionally, their investigations did not distinguish between different types of processes. The only event identified as a landslide was the one that occurred in April 2015. The investigations conducted by [65], who used TLS to collect data from various areas of a slope of the Vesuvius crater in 2005, 2006, and 2009, quantified surface changes amounting to a

total volume of 20,300 m^3 across three areas. Their findings align closely with our results for debris zone II, which totaled 20,430 m^3. Another study, conducted with UAV-based photogrammetry on the slopes of Stromboli volcano, calculated surface changes of 21.5 m^3 for the period from December 2018 to June 2019 [17]. There is no differentiation by process type in their study either. Reference [66] shows volume changes of 210.08 m^3 in their studies at the active Lascar volcano in Chile with the use of a UAV for a period from 2017 to 2020. Appending the data, they were able to determine that a collapse occurred first, followed by rockfalls, and then the material was deposited as a landslide.

4.5. Temporal Specification of the Single Events

Since large events with strong surface changes should be visually recognizable in individual photographs, webcam photographs unsuitable for SfM processing were not used. With this approach of visual inspection of the photographs, a better temporal resolution of the process dynamics can be obtained. Existing studies have also successfully used single automatic cameras to detect single rockfall events (cf. [67]). All available webcam images were used and transformed into short films, zooming to the different zones to visualize surface changes (Figure 10). Only those photos with fog or wet lenses were excluded. Even if photographs are not suitable for SfM processing, the aim of this method was the identification of events and their confinement to a period between two photographs. For rockfall zone I, the major surface changes occurred after 2013, a period for which no webcam images were available. Consequently, the smaller surface changes between 2010 and 2012 could not be identified as single events.

Figure 10. The white arrows show visually detectable surface changes (DoDs) in rock zone II between 13 June 2011 and 19 June 2011.

In rockfall zone II, the highest surface changes occurred between 2011 and 2012. After reviewing the photographs, these changes were attributed to the period between 13 June 2011 and 19 June 2011 (Figure 10). Since no changes were visible before and after this period, it seems likely that the surface changes resulted from one major single event. Even though the photos provide evidence that individual processes occurred, it cannot be ruled out that other events took place at a later time. A higher temporal resolution of the data sets would be necessary in this case.

In the debris zones, most of the surface changes are within the period for which webcam images were available. For debris zone I, it could be determined that the lower scree slope was apparently built up successively by smaller single events, partly by individual rocks that were presumably transported gravitationally and deposited at the foot of

the slope. Besides this successive deposition, however, a larger event occurred between 3 March 2010 and 16 March 2010, where material was transported linearly (fluvially or as a smaller debris flow) and then deposited as small cones at the base of the slope. Following this event, additional material was deposited, but no larger events were identified in the subsequent webcam photographs.

Continuous monitoring using webcam images is more difficult for the smaller debris zone II. However, the quantification results indicate a major surface change occurred between January 2010 and January 2011, as observed by [22] in their studies. Visual inspection of the webcam images indicated this change happened between 13 July 2010 and 2 December 2010. Unfortunately, no webcam images exist for the period between July and December 2010, preventing a more precise determination of the exact timing.

4.6. Geomorphic Perspective

The surface changes determined for the investigated slope show the high level of activity generally present within the crater, a finding consistent with other studies [15,21,22]. This high activity is largely attributable to the combination of high tectonic/seismic stress and the very high rainfall amounts on La Réunion. Reference [22] showed that rockfall activity, occurring about 2.5 years after the crater collapse, can be triggered by volcano tectonic seismicity and, to a lesser extent, rainfall. The sensitivity to seismic activity depends on the stability state of the crater walls. The observations of [21] show that even low seismicity ($M < 3$) at PLF can lead to increased rockfall activity. During the first 2.5 years post-collapse, the walls are so unstable that they fall without the need for external forcing. In the period without eruptive activity (2012–2014) and consequently with low seismic activity, it can be assumed that the main trigger is rain [22]. However, the high activity recorded in some areas between 2010 and 2016 is likely also due to the recent formation of the crater, indicating that the system remains in an unstable state. Following the crater collapse in 2007, steep slopes with unconsolidated material formed and were subsequently shaped by gravitational processes. While PLF is characterized by different eruptive phases during the observation period, the situation is different for the Telica volcano. It is constantly active and it can be assumed that the processes taking place are due to eruptive activity [1]. Unlike other mountainous areas, the debris cones are extremely young and the first webcam images from early 2010 capture the state of development after three years of geomorphological formation. Using the webcam images, the period of geomorphological development of the scree slopes can be extended from two years (2014 to 2016) to six years (2010 to 2016).

Figure 11A illustrates the slope development as a profile line (swath profile with a width of 25 m) from 2010 to 2016 (with only two profile lines shown here for better visibility). This indicates a slight flattening of the slope gradient over these six years. Figure 11B demonstrates that this flattening occurred successively and averaged around 1° slope inclination over these years. The statistical scattering range of the slope inclination has also decreased, an indicator that the slope is gradually stabilizing to a certain slope inclination and thus possibly to the slope angle of the prevailing substrate. The 35° slope inclination is in the upper range of the slope angles to be expected for scree slopes and is within the expected range as studies by [68–70] show. Reference [3] determined an average slope inclination of 33°. It is assumed that other process dynamics are responsible for this. In fact, lab experiments on granular layers submitted to high-frequency low-amplitude acoustic waves show that such waves may reduce by a few degree the avalanche angle (the maximum stability angle) of the granular layer by weakening intergranular friction [71]. Small-amplitude, high-frequency volcano tectonic seismicity may have a similar effect on the granular deposits on the slopes (see discussion in [22]). This could also be an indication that the investigated scree slope could be further flattened in the future and that the geomorphological development in this area was not yet complete in 2016.

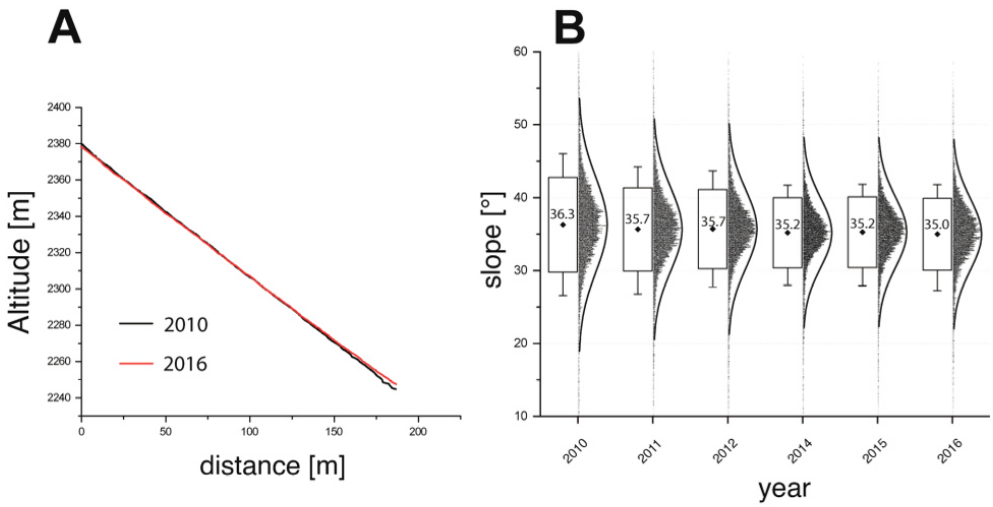

Figure 11. (**A**) The two lines are showing the slope development as a swath profile of debris zone II between 2010 and 2016. The location of the profile lines can be found in Figure 6. (**B**) Statistical range of the slope inclination for the years 2010 until 2016 showing a flattening of approximately 1°.

5. Conclusions

5.1. Methodological Aspect

From a methodological perspective, it can be asserted that using webcams for 4D analyses is only suitable in exceptional cases, when they are specifically installed for photogrammetric purposes at the time of installation. Despite the proximity of the webcams used in this study, the data processing was extremely complex. It required integrating LiDAR data in conjunction with photogrammetrically generated point clouds created from photos taken in parallel to the LiDAR mission. This integration allowed for the extraction of GCPs and fine referencing via ICP before converting the webcam images into 3D models and refining for quantitative investigations. Since the webcams were not initially intended for photogrammetric analysis, this meant that the camera positions were not ideal. Additionally, studies, particularly from the use of drone images for the creation of photogrammetric point clouds, show that overlap is crucial for minimizing errors in point cloud creation (c.f. [13]). In addition to the overlap values, the criteria specified for this include recommendations regarding the overlap directions (front- and sidelap). Due to using only two cameras, this study was limited to the sidelap, which limited the evaluable area of the slope to the central overlapping areas, and therefore, only slope sections (debris areas) that did not have complex 3D structures could be analyzed. Consequently, rock faces within the crater have a complex 3D surface and are additionally located at the marginal areas of the photographs, so those zones could not be analyzed. It therefore makes sense for future studies to extend the spatial resolution of the investigations for a process area by installing several webcams.

Nevertheless, the results indicate that webcam images can provide valuable information on geomorphological process dynamics by extending observation periods into the past and compressing them over time. Although not all photo pairs could be used for the 3D analysis in this case study, it was still possible to quantitatively assess individual periods. In addition, visual identification of process dynamics based on individual images allowed for some evaluation of the temporal development of the surface changes.

In the future, incorporating monoplotting tools alongside 3D evaluation could enhance the ability to make quantitative statements about process sequences, complementing visual

inspection. In particular, since webcam recordings are rarely available as image pairs, focusing on monoplotting tools for retrospective analysis is advisable. Future studies should also consider integrating webcams/automatic cameras into monitoring studies to enable quantitative investigations. However, it is crucial that photogrammetric principles, such as overlap rates or overlap directions, be considered [13,18,72]. If photogrammetric principles are followed, webcam-based photographs provide significant potential for data recording, particularly in highly active geomorphological areas. This approach enables the differentiation and quantification of individual processes. Drawing from drone studies, using additional cameras with effective distribution (front- and sidelap) should significantly reduce processing effort and improve evaluation results.

5.2. Geomorphological Aspects

The slope section considered in this study represents a very young geomorphological form that has developed over a few years through a combination of gravitational mass movements (such as landslide processes and debris flows) and fluvial processes. This allows tracing the development of these slopes, which in the Alps typically takes centuries or even millennia after the glaciers melted, over an exceptionally short period. Although the first available data are only available from 2010, just three years after the original formation of the crater collapse, historical webcam images combined with LiDAR and terrestrial manual images enable the reconstruction of slope development over nearly six years.

The results indicate that the slope development begins with an initial formation phase that occurs rapidly within the first few years. Following this, the slope undergoes a more gradual progression from 2010 to 2016. This development leads to the slope eventually reaching an angle determined by the substrate. Even though it is not possible to distinguish between individual geomorphological processes, there is a demonstration of clear progression from the initial rapid formation to a more stable slope configuration over time. This adjustment of the slope inclination from 36.3° on average in 2010 to 35° on average in 2016 is still very rapid and clearly visible, possibly due to the decrease in the maximum stability angle of the granular material due to the cumulative effect of low-amplitude and high-frequency local seismicity [22,71]. As [3] describes the average slope angles as being 33°, it can be assumed that this adjustment process was not yet complete in 2016. Thus, a new survey of this slope area should be carried out in the future to check the extent to which the slope inclinations have developed since 2016.

The rate of adaption in this area is certainly influenced by the unique conditions at PLF. This region is volcanically very active, which causes surface movements, e.g., due to magma in the subsurface and seismic influences. Additionally, the volcanic material in the area of the rock faces has a very clear stratification, which was built up from basaltic lava and pyroclastics. These layers have varying degrees of stability, and combined with tectonic/seismic stress, this certainly enhances rock fall activity [73]. In some cases, the crater rim also features extensive deep crack formations, which further increases the instability of the rock faces. For example, Ref. [15] shows a rockfall with large magnitudes in the area of the eastern exposure of the crater, starting from such a crack. From a geomorphological perspective, the crater is ideally well-suited for current geomorphological process research, as these processes here occur at both very high frequency and, in some cases, with very high magnitudes. The spatially contained area (with a crater diameter of about 1 km) and the ideal observation perspective from the crater rim make it well-suited for observing with LiDAR or terrestrial photogrammetry. Therefore, it would also be beneficial to install similar fixed camera systems in other accessible craters. The only obstacle is the inability to enter the crater, which hampers the installation of stable survey points. Despite this, the area presents a promising opportunity for future research into geomorphological process dynamics using ground-based remote sensing techniques.

Author Contributions: Conceptualization, K.W. and F.H.; data curation, K.W. and F.H.; formal analysis, K.W. and F.H.; funding acquisition, A.M.; investigation, K.W., V.D., N.V., A.M., P.K., A.P., M.S. and F.H.; methodology, K.W. and F.H.; project administration, A.M., M.B. and F.H.; resources, N.V., A.M., P.K. and A.P.; software, K.W. and F.H.; supervision, F.H., A.M., M.S. and M.B.; validation, K.W., V.D., M.S. and F.H.; visualization, K.W.; writing—original draft preparation, K.W. and F.H.; writing—review and editing, K.W., V.D., N.V., A.M., A.P., M.S., M.B. and F.H. All authors have read and agreed to the published version of the manuscript.

Funding: This research received no external funding. The field trip for data acquisition on La Réunion and some discussions on the results were financed by ERC Contract No. ERC-CG-2013-PE10-617472 SLIDEQUAKES.

Data Availability Statement: The webcam-based data from the installed camera system and the climate station data was provided by the Volcanological Observatory of Piton de la Fournaise (Observatoire Volcanologique du Piton de la Fournaise, Institut de Physique du Globe de Paris (OVPF-IPGP, doi:10.18715/REUNION.OVPF). We thank the Service National d'Observation en Volcanologie (SNOV-CNRS-INSU) for the use of the database. The raw data supporting the conclusions of this article will be made available by the authors on request.

Acknowledgments: We would like to thank our colleagues at the Piton de la Fournaise Volcanological Observatory for their great support during the field work and data acquisition. In addition, we want to thank the four anonymous reviewers for their help to improve our manuscript.

Conflicts of Interest: The authors declare no conflicts of interest.

References

1. Hanagan, C.; La Femina, P.C.; Rodgers, M. Changes in Crater Morphology Associated With Volcanic Activity at Telica Volcano, Nicaragua. *Geochem. Geophys. Geosyst.* **2020**, *21*, e2019GC008889. [CrossRef]
2. Civico, R.; Ricci, T.; Scarlato, P.; Andronico, D.; Cantarero, M.; Carr, B.B.; De Beni, E.; Del Bello, E.; Johnson, J.B.; Kueppers, U.; et al. Unoccupied Aircraft Systems (UASs) Reveal the Morphological Changes at Stromboli Volcano (Italy) before, between, and after the 3 July and 28 August 2019 Paroxysmal Eruptions. *Remote Sens.* **2021**, *13*, 2870. [CrossRef]
3. Tournigand, P.-Y.; Smets, B.; Laxton, K.; Dille, A.; France, L.; Chazot, G.; Ho, C.; Wauthier, C.; Nicholson, E.J.; Kasanzu, H.C.; et al. Remote volcano monitoring using crowd-sourced imagery and Structure-from-Motion photogrammetry: A case study of Oldoinyo Lengai's active pit crater since the 2007–08 paroxysm. *J. Volcanol. Geotherm. Res.* **2023**, *443*, 107918. [CrossRef]
4. Geshi, N.; Shimano, T.; Chiba, T.; Nakada, S. Caldera collapse during the 2000 eruption of Miyakejima Volcano, Japan. *Bull. Volcanol.* **2002**, *64*, 55–68. [CrossRef]
5. Michon, L.; Staudacher, T.; Ferrazzini, V.; Bachèlery, P.; Marti, J. April 2007 collapse of Piton de la Fournaise: A new example of caldera formation. *Geophys. Res. Lett.* **2007**, *34*, 104. [CrossRef]
6. Duputel, Z.; Rivera, L. Show more The 2007 caldera collapse of Piton de la Fournaise volcano: Source process from very-long-period seismic signals. *Geoplanet-Earth Plan. Lett.* **2019**, *527*, 115786. [CrossRef]
7. Harnett, C.E.; Watson, R.A.; Holohan, E.P.; Schöpfer, M.P.J. Collapse caldera walls: Mechanical controls on slope failure and morphology. *J. Volcanol. Geotherm. Res.* **2023**, *442*, 107893. [CrossRef]
8. Klotz, S.; Le Bouteiller, C.; Mathys, N.; Fontaine, F.; Ravanat, X.; Olivier, J.-E.; Liébault, F.; Jantzi, H.; Coulmeau, P.; Richard, D.; et al. A high-frequency, long-term data set of hydrology and sediment yield: The alpine badland catchments of Draix-Bléone Observatory. *Earth Syst. Sci. Data* **2023**, *15*, 4371–4388. [CrossRef]
9. Barbarella, M.; Fiani, M.; Lugli, A. Landslide monitoring using multitemporal terrestrial laser scanning for ground displacement analysis. *Geomat. Nat. Hazards Risk* **2015**, *6*, 398–418. [CrossRef]
10. Pfeiffer, J.; Zieher, T.; Rutzinger, M.; Bremer, M.; Wichmann, V. Comparison and time series analysis of landslide displacement mapped by airborne, terrestrial and unmanned aerial vehicle based platforms. In Proceedings of the ISPRS Annals of the Photogrammetry, Remote Sensing and Spatial Information Sciences, ISPRS Geospatial Week, Enschede, The Netherlands, 10–14 June 2019.
11. Saito, H.; Uchiyama, S.; Hayakawa, Y.S.; Obanawa, H. Landslides triggered by an earthquake and heavy rainfalls at Aso volcano, Japan, detected by UAS and SfM-MVS photogrammetry. *Prog. Earth Planet Sci.* **2018**, *5*, 15. [CrossRef]
12. Carr, B.B.; Lev, E.; Vanderkluysen, L.; Moyer, D.; Marliyani, G.I.; Clarke, A.B. The Stability and Collapse of Lava Domes: Insight From Photogrammetry and Slope Stability Models Applied to Sinabung Volcano (Indonesia). *Front. Earth Sci.* **2022**, *10*, 813813. [CrossRef]
13. Stark, M.; Rom, J.; Haas, F.; Piermattei, L.; Fleischer, F.; Altmann, M.; Becht, M. Long-term assessment of terrain changes and calculation of erosion rates in an alpine catchment based on SfM-MVS processing of historical aerial images. How camera information and processing strategy affect quantitative analysis. *J. Geomorphol.* **2022**, *1*, 43–77. [CrossRef]
14. Ravanel, L.; Deline, P. Climate influence on rock-falls in high-Alpine steep rockwalls: The north side of the Aiguilles de Chamonix (Mont Blanc massif) since the end of the 'Little Ice Age'. *Holocene* **2010**, *21*, 357–365. [CrossRef]

15. Derrien, A.; Villeneuve, N.; Peltier, A.; Michon, L. Multi-temporal airborne structure-from-motion on caldera rim: Hazard, visitor exposure and origins of instabilities at Piton de la Fournaise. *Prog. Phys. Geogr. Earth Environ.* **2018**, *43*, 193–214. [CrossRef]
16. Guerin, A.; Stock, G.M.; Radue, M.J.; Jaboyedoff, M.; Collins, B.D.; Matasci, B.; Avdievitch, N.; Derron, M.-H. Quantifying 40 years of rockfall activity in Yosemite Valley with historical Structure-from-Motion photogrammetry and terrestrial laser scanning. *Geomorphology* **2020**, *356*, 107069. [CrossRef]
17. Gracchi, T.; Stefanelli, C.T.; Rossi, G.; Di Traglia, F.; Nolesini, T.; Tanteri, L.; Casagli, N. UAV-Based Multitemporal Remote Sensing Surveys of Volcano Unstable Flanks: A Case Study from Stromboli. *Remote Sens.* **2022**, *14*, 2489. [CrossRef]
18. Wegner, K.; Stark, M.; Haas, F.; Becht, M. Suitability of terrestrial archival imagery for SfM-MVS based surface reconstruction of steep rock walls for the detection of rockfalls. *J. Geomorphol.* **2023**. [CrossRef]
19. Rom, J.; Haas, F.; Hofmeister, F.; Fleischer, F.; Altmann, M.; Pfeiffer, M.; Heckmann, T.; Becht, M. Analysing the Large-Scale Debris Flow Event in July 2022 in Horlachtal, Austria Using Remote Sensing and Measurement Data. *Geosciences* **2023**, *13*, 100. [CrossRef]
20. Fontaine, F.R.; Roult, G.; Michon, L.; Barruol, G.; Di Muro, A. The 2007 eruptions and caldera collapse of the Piton de la Fournaise volcano (La Réunion Island) from tilt analysis at a single very broadband seismic station. *Geophys. Res. Lett.* **2014**, *41*, 2803–2811. [CrossRef]
21. Durand, V.; Mangeney, A.; Haas, F.; Jia, X.; Peltier, A.; Hibert, C.; Ferrazzini, V.; Kowalski, P.; Lauret, F.; Brunet, C.; et al. On the link between external forcings and slope instabilities in the Piton de la Fournaise summit crater, Reunion Island. *J. Geophys. Rev. Earth Surf.* **2018**, *123*, 2422–2442. [CrossRef]
22. Durand, V.; Mangeney, A.; Bernard, P.; Jia, X.; Bonilla, F.; Satriano, C.; Saurel, J.-M.; Aissaoui, E.M.; Peltier, A.; Ferrazzini, V.; et al. Repetitive small seismicity coupled with rainfall can trigger large slope instabilities on metastable volcanic edifices. *Commun. Earth Environ.* **2023**, *4*, 383. [CrossRef]
23. Suriñach, E.; Vilajosana, I.; Khazaradze, G.; Biescas, B.; Furdada, G.; Vilaplana, J.M. Seismic detection and characterization of landslides and other mass movements. *Nat. Hazards Earth Syst. Sci.* **2005**, *5*, 791–798. [CrossRef]
24. Walter, M.; Schwaderer, U.; Joswig, M. Seismic monitoring of precursory fracture signals from a destructive rockfall in the Vorarlberg Alps, Austria. *Nat. Hazards Earth Syst. Sci.* **2012**, *12*, 3545–3555. [CrossRef]
25. Nobile, A.; Acocella, V.; Ruch, J.; Aoki, Y.; Borgstrom, S.; Siniscalchi, V.; Geshi, N. Steady subsidence of a repeatedly erupting caldera through InSAR observations: Aso, Japan. *Bull. Volcanol.* **2017**, *79*, 32. [CrossRef]
26. Richter, N.; Froger, J.-L. The role of Interferometric Synthetic Aperture Radar in Detecting, Mapping, Monitoring, and Modelling the Volcanic Activity of Piton de la Fournaise, La Réunion: A Review. *Remote Sens.* **2020**, *12*, 1019. [CrossRef]
27. Vanneschi, C.; Di Camillo, M.; Aiello, E.; Bonciani, F.; Salvini, R. SfM-MVS photogrammetry for rock-fall analysis and hazard assessment along the ancient Roman Via Flaminia road at the Furlo Gorge (Italy). *ISPRS Int. J. Geo-Inf.* **2019**, *8*, 325. [CrossRef]
28. Gallo, I.G.; Martínez-Corbella, M.; Sarro, R.; Iovine, G.; López-Vinielles, J.; Hérnandez, M.; Robustelli, G.; Mateos, R.M.; García-Davalillo, J.C. An integration of UAV-based photogramme-try and 3D modelling for rockfall hazard assessment: The Cárcavos case in 2018 (Spain). *Remote Sens.* **2021**, *13*, 3450. [CrossRef]
29. Roncella, R.; Forlani, G.; Fornari, M.; Diotri, F. Landslide monitoring by fixed-base terrestrial stereo-photogrammetry. In Proceedings of the ISPRS Annals of the Photogrammetry, Remote Sensing and Spatial Information Sciences, ISPRS Technical Commission V Symposium, Riva del Garda, Italy, 23–25 June 2014.
30. Eltner, A.; Kaiser, A.; Abellan, A.; Schindewolf, M. Time lapse structure-from-motion photogrammetry for continuous geomorphic monitoring. *Earth Surf. Proc. Landf.* **2017**, *42*, 2240–2253. [CrossRef]
31. Kromer, R.; Walton, G.; Gray, B.; Lato, M.; Group, R. Development and Optimization of an Automated Fixed-Location Time Lapse Photogrammetric Rock Slope Monitoring System. *Remote Sens.* **2019**, *11*, 1890. [CrossRef]
32. Blanch, X.; Guinau, M.; Eltner, A.; Abellan, A. Fixed photogrammetric systems for natural hazard monitoring with high spatio-temporal resolution. *Nat. Hazards Earth Syst. Sci.* **2023**, *23*, 3285–3303. [CrossRef]
33. Falsaperla, S.; Neri, M.; Pecora, E.; Spampinato, S. Multidisciplinary study of flank instability phenomena at Stromboli volcano, Italy. *Geophys. Res. Lett.* **2006**, *33*, 15. [CrossRef]
34. Calvari, S.; Intrieri, E.; Di Traglia, F.; Bonaccorso, A.; Casagli, N.; Cristaldi, A. Monitoring crater-wall collapse at active volcanoes: A study of the 12 January 2013 event at Stromboli. *Bull. Volcanol.* **2016**, *78*, 39. [CrossRef]
35. Coltelli, M.; d'Aranno, P.J.V.; de Bonis, R.; Tello, J.F.G.; Marsella, M.; Nardinocchi, C.; Pecora, E.; Proietti, C.; Scifoni, S.; Scutti, M.; et al. The Use of Surveillance Cameras for the Rapid Mapping of Lava Flows: An Application to Mount Etna Volcano. *Remote Sens.* **2017**, *9*, 192. [CrossRef]
36. Barnie, T.; Hjörvar, T.; Titos, M.; Sigurðsson, E.M.; Pálsson, S.K.; Bergsson, B.; Ingvarsson, Þ.; Pfeffer, M.A.; Barsotti, S.; Arason, Þ.; et al. Volcanic plume height monitoring using calibrated web cameras at the Icelandic Meteorological Office: System overview and first application during the 2021 Fagradalsfjall eruption. *J. Appl. Volcanol.* **2023**, *12*, 4. [CrossRef]
37. Michon, L.; Saint-Age, F. Morphology of Piton de la Fournaise basaltic shield volcano (La Réunion Island): Characterization and implication in the volcano evolution. *J. Geophys. Res.* **2008**, *113*, 2156–2202. [CrossRef]
38. Le Friant, A.; Lebas, E.; Clément, V.; Boudon, G.; Deplus, C.; De Voogd, B.; Bachèlery, P. A new model for the evolution of La Réunion volcanic complex from complete marine geophysical surveys. *Geophys. Res. Lett.* **2011**, *38*, 39. [CrossRef]
39. Gillot, P.-Y.; Lefèvre, J.-C.; Nativel, P.E. Model for the structural evolution of the volcanoes of Réunion island. *Earth Planet. Sci. Lett.* **1994**, *122*, 291–302. [CrossRef]

40. Famin, V.; Paquez, C.; Danišík, M.; Gardiner, N.J.; Michon, L.; Kirkland, C.L.; Berthod, C.; Friedrichs, B.; Schmitt, A.K.; Monié, P. Multitechnique geochronology of intrusive and explosive activity on Piton des Neiges Volcano, Réunion Island. *Geochem. Geophys. Geosyst.* **2022**, *23*, e2021GC010214. [CrossRef]
41. Lénat, J.-F.; Bachèlery, P. Dynamics of magma transfer at Piton de la Fournaise volcano (Réunion Island, Indian Ocean). In *Modeling of Volcanic Processes. Earth Evolution Sciences*; King, C.-Y., Scarpa, R., Eds.; Vieweg+Teubner Verlag: Wiesbaden, Germany, 1988; pp. 57–72.
42. Staudacher, T.; Ferrazzini, V.; Peltier, A.; Kowalski, P.; Boissier, P.; Catherine, P.; Lauret, F.; Massin, F. The April 2007 eruption and the Dolomieu crater collapse, two major events at Piton de la Fournaise (La Réunion Island, Indian Ocean). *J. Volcanol. Geotherm. Res.* **2009**, *184*, 126–137. [CrossRef]
43. Garcin, M.; Poisson, B.; Pouget, R. High rates of geomorphological processes in a tropical area: The Remparts river case study (Réunion Island, Indian Ocean). *Geomorphology* **2005**, *67*, 335–350. [CrossRef]
44. Join, J.-L.; Folio, J.-L.; Bourhane, A.; Comte, J.-C. Groundwater Resources on Active Basaltic Volcanoes: Conceptual Models from La Réunion Island and Grande Comore. In *Active Volcanoes of the Southwest Indian Ocean Piton de la Fournaise and Karthala*; Bachèlery, P., Lénat, J.-F., Di Muro, A., Michon, L., Eds.; Springer: Berlin/Heidelberg, Germany, 2016; pp. 61–70.
45. Haas, F.; Hilger, L.; Neugirg, F.; Umstädter, K.; Breitung, C.; Fischer, P.; Hilger, P.; Heckmann, T.; Dusik, J.; Kaiser, A.; et al. Quantification and analysis of geomorphic processes on a recultivated iron ore mine on the Italian island Elba using long-time ground-based LIDAR and photogrammetric data by an UAV. *Nat. Hazards Earth Syst. Sci.* **2016**, *16*, 1269–1288. [CrossRef]
46. Zhang, Z. Iterative point matching for registration of free-form curves and surfaces. *Int. J. Comput. Vis.* **1994**, *13*, 119–152. [CrossRef]
47. Micheletti, N.; Chandler, J.H.; Lane, S.N. Investigating the geomorphological potential of freely available and accessible structure-from-motion photo-grammetry using a smartphone. *Earth Surf. Proc. Landf.* **2015**, *40*, 473–486. [CrossRef]
48. Riegl VZ-4000. Available online: http://www.riegl.com/uploads/tx_pxpriegldownloads/RIEGL_VZ-4000_Datasheet_2020-09-14.pdf (accessed on 10 September 2024).
49. Conrad, O.; Bechtel, B.; Bock, M.; Dietrich, H.; Fischer, E.; Gerlitz, L.; Wehber, J.; Wichmann, V.; Böhner, J. System for Automated Geoscientific Analyses (SAGA) v. 2.1.4. *Geosci. Model Dev.* **2015**, *8*, 1991–2007. [CrossRef]
50. Westoby, M.J.; Brasington, J.; Glasser, N.F.; Hambrey, M.J.; Reynolds, J.M. 'Structure-from-Motion' photogrammetry: A low-cost, effective tool for geoscience applications. *Geomorphology* **2012**, *179*, 300–314. [CrossRef]
51. James, M.R.; Robson, S.; d'Oleire-Oltmanns, S.; Niethammer, U. Optimising UAV topographic surveys with structure-from-motion: Ground control quality, quantity and bundle adjustment. *Geomorphology* **2017**, *280*, 51–66. [CrossRef]
52. James, M.R.; Robson, S.; Smith, M.W. 3-D uncertainty-based topographic change detection with structure-from-motion photogrammetry: Precision maps for ground control and directly georeferenced surveys. *Earth Surf. Proc. Landf.* **2017**, *42*, 1769–1788. [CrossRef]
53. James, M.R.; Antoniazza, G.; Robson, S.; Lane, S.N. Mitigating systematic error in topographic models for geomorphic change detection: Accuracy, precision and considerations beyond off-nadir imagery. *Earth Surf. Proc. Landf.* **2020**, *45*, 2251–2271. [CrossRef]
54. Fey, C.; Wichmann, V. Long-range terrestrial laser scanning forgeomorphological change detection in alpineterrain—Handling uncertainties. *Earth Surf. Proc. Landf.* **2017**, *42*, 789–802. [CrossRef]
55. Heckmann, T. Cut & Fill module for SAGA GIS 2.2.0. 2006.
56. Brasington, J.; Langham, J.; Rumsby, B. Methodological sensitivity of morphometric estimates of coarse fluvial sediment transport. *Geomorphology* **2003**, *53*, 299–316. [CrossRef]
57. Lane, S.N.; Westaway, R.M.; Murray, H.D. Estimation of erosion and deposition volumes in a large, gravel-bed, braided river using synoptic remote sensing. *Earth Surf. Proc. Landf.* **2003**, *28*, 249–271. [CrossRef]
58. Bennett, G.L.; Molnar, P.; Eisenbeiss, H.; McArdell, B.W. Erosiononal power in the Swiss Alps: Characterization of slope failure in the Illgraben. *Earth Surf. Proc. Landf.* **2012**, *37*, 1627–1640. [CrossRef]
59. Brasington, J.; Rumsby, B.T.; McVey, R.A. Monitoring and modelling morphological change in a braided gravel-bed river using high resolution GPS-based survey. *Earth Surf. Proc. Landf.* **2000**, *25*, 973–990. [CrossRef]
60. Westaway, R.M.; Lane, S.N.; Hicks, D.M. The development of an automated correction procedure for digital photogrammetry for the study of wide, shallow, gravel bed rivers. *Earth Surf. Proc. Landf.* **2000**, *25*, 209–226. [CrossRef]
61. Gomez, C.; Hayakawa, Y.; Obanawa, H. A study of Japanese landscapes using structure from motion derived DSMs and DEMs based on historical aerial photographs: New opportunities for vegetation monitoring and diachronic geomorphology. *Geomorphology* **2015**, *242*, 11–20. [CrossRef]
62. Bakker, M.; Lane, S.N. Archival photogrammetric analysis of river-floodplain systems using Structure from Motion (SfM) methods. *Earth Surf. Proc. Landf.* **2017**, *42*, 1274–1286. [CrossRef]
63. Mueller, S.B.; Varley, N.R.; Kueppers, U.; Lesage, P.; Reyes Davila, G.A.; Dingwell, D.B. Quantification of magma ascent rate through rockfall monitoring at the growing/collapsing lava dome of Volc'an de Colima, Mexico. *Solid Earth* **2013**, *4*, 201–213. [CrossRef]
64. Kuehnert, J.; Mangeney, A.; Capdeville, Y.; Vilotte, J.P.; Stutzmann, E.; Chaljub, E.; Aissaoui, M.; Boissier, P.; Brunet, C.; Kowalski, P.; et al. Rockfall localization based on inter-station ratios of seismic energy. *J. Geophys. Res.—Earth Surface* **2021**, *126*. [CrossRef]

65. Pesci, A.; Teza, G.; Casula, G.; Fabris, M.; Bonforte, A. Remote Sensing and Geodetic Measurements for Volcanic Slope Monitoring: Surface Variations Measured at Northern Flank of La Fossa Cone (Vulcano Island, Italy). *Remote Sens.* **2011**, *5*, 2238–2256. [CrossRef]
66. Ai, L.; Walter, T.R.; Aguilera, F.; Layana, S.; Mania, R.; Kujawa, C.; Zimmer, M.; Inostroza, M. Crater morphology, nested ring structures, and temperature anomalies studied by unoccupied aircraft system data at Lascar volcano, northern Chile. *J. Volcanol. Geotherm. Res.* **2023**, *439*, 107840. [CrossRef]
67. Mourey, J.; Lacroix, P.; Duvillard, P.A.; Marsy, G.; Marcer, M.; Malet, E.; Ravanel, L. Multi method monitoring of rockfall activityalong the classic route up Mont Blanc (4809 m a.s.l.) to encourage adaption by mountaineers. *Nat. Hazards Earth Syst. Sci.* **2022**, *22*, 445–460. [CrossRef]
68. Chandler, R.J. The Inclination of Talus, Arctic Talus Terraces, and Other Slopes Composed of Granular Materials. *J. Geol.* **1973**, *81*, 1–14. [CrossRef]
69. Carson, M.A. Angles of Repose, Angles of Shearing Resistance and Angles of Talus Slopes. *Earth Surface Process.* **1977**, *2*, 363–380. [CrossRef]
70. van Steijna, H.; Boelhouwers, J.; Harris, S.; Hétu, B. Recent research on the nature, origin and climatic relations of blocky and stratified slope deposits. *Prog. Phys. Geogr.* **2002**, *26*, 551–575. [CrossRef]
71. Léopoldès, J.; Jia, X.; Tourin, A.; Mangeney, A. Triggering granular avalanches with ultrasound. *Phys. Rev. E* **2020**, *102*, 042901. [CrossRef]
72. Eltner, A.; Kaiser, A.; Castillo, C.; Rock, G.; Neugirg, F.; Abellán, A. Image-based surface reconstruction in geomorphometry—Merits, limits and developments. *Earth Surf. Dyn.* **2016**, *4*, 359–389. [CrossRef]
73. Chen, Y.; Remy, D.; Froger, L.J.; Peltier, A.; Villeneuve, N.; Darrozes, J.; Perfettini, H.; Bonvalot, S. Long term ground displacement using InSAR and GNSS at Piton de la Fournaise volcano between 2009 and 2014. *Remote Sens. Environ.* **2017**, *194*, 230–247. [CrossRef]

7.4 On the Link Between External Forcings and Slope Instabilities in the Piton de la Fournaise Summit Crater, Reunion Island

AGU100 ADVANCING EARTH AND SPACE SCIENCE

JGR

Journal of Geophysical Research: Earth Surface

RESEARCH ARTICLE
10.1029/2017JF004507

On the Link Between External Forcings and Slope Instabilities in the Piton de la Fournaise Summit Crater, Reunion Island

Virginie Durand[1], Anne Mangeney[1], Florian Haas[2], Xiaoping Jia[3], Fabian Bonilla[1,4], Aline Peltier[5], Clément Hibert[6], Valérie Ferrazzini[5], Philippe Kowalski[5], Frédéric Lauret[5], Christophe Brunet[5], Claudio Satriano[1], Kerstin Wegner[2], Arthur Delorme[1], and Nicolas Villeneuve[5]

[1]Institut de Physique du Globe de Paris, CNRS UMR 7154, Université Paris Diderot-Paris 7, Paris, France, [2]Catholic University of Eichstaett-Ingolstadt, Eichstätt, Germany, [3]Institut Langevin, ESPCI Paris Tech, CNRS UMR 7587, Paris, France, [4]IFSTTAR, Université Paris-Est, Paris, France, [5]Observatoire Volcanologique du Piton de la Fournaise/Institut de Physique du Globe de Paris, Sorbonne Paris Cité, La Plaine des Cafres, Réunion Island, France, [6]Institut de Physique du Globe de Strasbourg, EOST, UMR 7516 CNRS, Strasbourg, France

Key Points:
- We investigate the link between external forcings and rockfall volume in a volcanic environment
- We highlight delayed triggering of large rockfalls by small repetitive seismic events
- We compare the rockfall volume estimated using seismic and photogrammetric data

Supporting Information:
- Supporting Information S1

Correspondence to:
V. Durand,
vdurand@ipgp.fr

Citation:
Durand, V., Mangeney, A., Haas, F., Jia, X., Bonilla, F., Peltier, A., et al. (2018). On the link between external forcings and slope instabilities in the Piton de la Fournaise summit crater, Reunion Island. *Journal of Geophysical Research: Earth Surface*, *123*, 2422–2442. https://doi.org/10.1029/2017JF004507

Received 9 OCT 2017
Accepted 3 SEP 2018
Accepted article online 17 SEP 2018
Published online 10 OCT 2018

Abstract We have analyzed the impact of different forcings, such as rain and seismicity, on slope instabilites on an active volcano. For this, we compiled a catalog of the locations and volumes of rockfalls in the Piton de la Fournaise crater using seismic records. We validated it by comparing the locations and volumes to those deduced from photogrammetric data. We analyzed 10,477 rockfalls, spanning the period 2014 to 2016. This period corresponds to the renewal of volcanic activity after a 41-month rest. Our analysis reveals that renewed eruptive activity has unsettled the crater edges. External forcings such as rain and seismicity are shown to potentially increase the number and the volume of rockfalls, with a stronger impact on the volume. Preeruptive seismicity seems to be the main triggering factor for the largest volumes, with a delay of one to several days. Rain alone does not seem to trigger especially large rockfalls. We infer that repetitive vibrations from the many seismic events, combined with the action of rain, induce crack (or slip) growth in highly fractured (or granular) materials, leading to the collapse of large volumes. Regarding their spatial distribution before an eruption, the largest rockfalls seem to migrate toward the location of magma extrusion.

1. Introduction

Rockfalls (RFs) form one of the main geomorphic processes involved in the reshaping of landscapes in mountainous areas (De Blasio, 2011). Because of their sudden and often unpredictable occurrences, they represent an important natural hazard. RFs are mainly controlled by different external factors, such as climate (D'Amato et al., 2016; Delonca et al., 2014; Dietze, Mohadjer, et al., 2017; Helmstetter & Garambois, 2010; Krautblatter et al., 2012), seismicity (Keefer, 2002; Lin et al., 2008; Tatard et al., 2010), and volcanic activity (Calder et al., 2002; Hibert, Mangeney, et al., 2017; Voight et al., 2000). However, the influence of these factors and the way they trigger RFs are not yet well understood (D'Amato et al., 2016; Dietze, Turowski, et al., 2017; Hibert, Mangeney, et al., 2017; Stock et al., 2013). Indeed, it is difficult to clearly link these different forcings to RF occurrences. One reason is that these different forcings can overlap or have additive effects. Another is that time-accurate data are needed to better constrain the relationship between the triggers and the RFs. Until recently, RFs were only identified and classified using field observations or aerial/satellite images (Krautblatter et al., 2012; Lacroix, 2016). This leads to high uncertainty in their times of occurrence. New monitoring techniques, with regular photography and lidar campaigns or satellite data, can provide more complete catalogs of RFs in a given region (among others, Abellan et al., 2011; D'Amato et al., 2016; Lacroix, 2016). However, they do not provide accurate occurrence times, with time precision of tens of minutes in the case of continuous monitoring, and sometimes give access only to the cumulative volume of several RFs. Over the last few years, in order to obtain more accurate RF catalogs, new methods have been developed to compute the volumes of RFs from seismic signals, in addition to detecting and locating them accurately (Dammeier et al., 2011; Deparis et al., 2008; Dietze, Mohadjer, et al., 2017; Helmstetter & Garambois, 2010; Hibert et al., 2011, 2014; Lacroix & Helmstetter, 2011; Norris, 1994; Zimmer & Sitar, 2015). These new catalogs, with precise occurrence times (precision on the order of seconds) and location and volume of each individual event, allow more detailed studies

on the links between RFs and external forcings like climate and seismic or volcanic activity (Dietze, Turowski, et al., 2017; Helmstetter & Garambois, 2010; Hibert, Mangeney, et al., 2017; Lacroix & Helmstetter, 2011).

It is well known that rain can trigger RFs through several possible mechanisms. It can increase the pore pressure (Dietze, Turowski, et al., 2017), or it can produce chemical weathering, dissolving rock compounds (D'Amato et al., 2016; Dietze, Turowski, et al., 2017; Krautblatter et al., 2012). Whatever the process involved, RF activity has been shown to generally begin 1 hr to 2 days after the triggering rain episode (D'Amato et al., 2016; Delonca et al., 2014; Dietze, Turowski, et al., 2017; Helmstetter & Garambois, 2010; Krautblatter et al., 2012). Helmstetter and Garambois (2010) also point out that rain can have a long-lasting effect, with RF activity continuing several days after the rain has stopped. Earthquakes are a second important triggering factor. Existing studies on the influence of earthquakes on slope instabilities mainly concern landslides or a mix of RFs and landslide events. They show that earthquakes can produce a permanent decrease in bulk ground strength leading to a slope collapse (Ambraseys & Bilham, 2012; Marc et al., 2015). This mechanism can explain why high landslide rates are observed for several months to years after an earthquake (Lin et al., 2008; Marc et al., 2015). The combination of seismic shaking and elevated pore pressure can lead to slope destabilization several days after ground shaking has stopped (Keefer, 2002). It is commonly assumed that earthquakes with magnitude $M < 4$ are not potential triggers for slope instabilities (Keefer, 1984; Tatard et al., 2010). However, some observations suggest that sequences of small seismic events ($M < 3.6$), because of repetitive shaking, may contribute to the triggering of a rockslide (Del Gaudio et al., 2000). Although it is difficult to clearly discriminate rain and earthquake effects in some regions (Lin et al., 2008; Tatard et al., 2010), during dry periods of the year, seismicity appears to be the most important triggering factor (Koukouvelas et al., 2015). A third important triggering factor is volcanic activity. It has been shown in several studies that volcanic seismicity, explosions due to eruptive activity, and local surface deformations due to magmatic intrusion and extrusion trigger RFs on volcanic edifices (Calder et al., 2002; Hibert, Mangeney, et al., 2017; Voight et al., 2000).

These studies highlight the need for systematic data to improve the understanding of the role of external forcings, especially the influence of small seismicity, in slope destabilization. Here we apply the method developed by Hibert et al.(2011, 2014) to investigate the spatiotemporal evolution of the number and volume of RFs in the crater of the Piton de la Fournaise volcano (Reunion Island). These RFs are subjected to rain, volcanic seismicity, and deformation. We first explain how we create a catalog of RFs, comprising their occurrence dates, locations, and volumes, using the seismic signals they generate. We then validate these locations and volumes with those obtained from photogrammetric data. Next, we use our RF catalog to analyze the spatiotemporal evolution of RFs. We correlate them with external forcings such as seismic and eruptive activity and rainfall. In the last section, we discuss the links between the changes in RF activity and external forcings, in particular the influence of seismic activity and rainfall on the size of RFs.

2. Study Site

The Piton de la Fournaise volcano is a unique site to study RFs. The first reason is that the Dolomieu crater floor collapsed during the major April 2007 eruption (Michon et al., 2007; Peltier, Staudacher, et al.,2009; Staudacher et al., 2009), exposing mostly vertical rockwalls prone to a continuous RF activity. The second reason is that the summit of the volcano is densely instrumented, with seismic and geodetic networks (Figure 1), cameras, and regular photogrammetric campaigns. It thus offers an unparalleled combination of data to study RF activity. Finally, Piton de la Fournaise is located in a tropical region and is one of the most active basaltic volcanoes in the world, with an eruption every 8 months on average (Peltier, Bachèlery, et al. 2009; Roult et al., 2012; Staudacher et al., 2009). This setting makes it possible to investigate the influence of different kinds of forcings on RF activity, such as rainfall and seismic and volcanic activities.

Hibert et al., (2011, 2014, 2017) used the seismic network to analyze the RF activity that followed the 2007 Dolomieu summit crater collapse. They show that the highest RF activity lasted for 2 months after the collapse. This 2-month strong relaxation phase was followed by a smoother and longer phase exhibiting a constant rate of RFs but with a decrease in their volume. This phase lasted at least 3 years, until 2010 (Hibert et al., 2017), suggesting a long-term evolution of RF activity related to crater stability. They also analyzed the spatiotemporal evolution of RFs in the Dolomieu crater during this particularly active period, between 2007 and 2011. They observed an increase in the number and volume of RFs before some eruptions and the migration of the RFs toward the location of the next eruption, sometimes occurring 1 or 2 years later. This migration pattern is in agreement with the location of seismic noise changes observed before some eruptions

Journal of Geophysical Research: Earth Surface 10.1029/2017JF004507

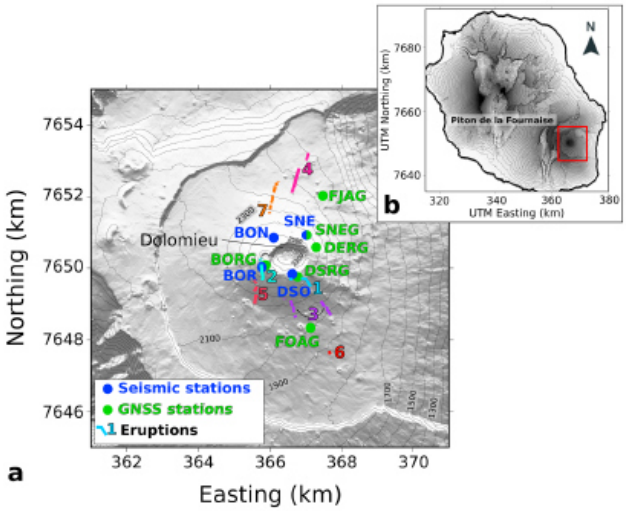

Figure 1. (a) Digital elevation model of the Piton de la Fournaise volcano and location of the seismic and Global Navigation Satellite System (GNSS) stations used in this study and of the eruptions that occurred from 2014 to 2016. (1) 20 and 21 June 2014, (2) 4–15 February 2015, (3) 17–30 May 2015, (4) 30 July to 2 August 2015, (5) 24 August to 31 October 2015, (6) 26 and 27 May 2016, and (7) 11–18 September 2016. The lines next to the eruption numbers show the location of the eruptive fissures. (b) Piton de la Fournaise on Reunion island. The red box denotes the area shown in (a).

(Obermann et al., 2013). These changes highlight the existence of a mechanical forcing at depth linked to magma intrusion that may explain the observed migration of the RFs. However, because the 2007–2010 period was dominated by RF activity related to the crater collapse relaxation, it is difficult to clearly link RF activity with different external forcings such as rainfall and eruptive activity. To better assess the impact of the different forcings without the dominant influence of the postcollapse relaxation of the crater slopes, we analyze here the RF activity over a period long after the collapse, between 2014 and 2016. During this period, seven eruptions occurred, after a break that lasted 41 months. Looking at a period long after the crater collapse allows us to both confirm some results of Hibert et al. (2017) and highlight new links with the forcings (coupled action of seismicity and rain) that were hidden during the postcollapse relaxation period.

3. Materials and Methods

3.1. Data

The Piton de la Fournaise volcano is very well instrumented, with 39 seismic and 24 Global Navigation Satellite System (GNSS) stations. During the 2014–2016 study period, we consider only the four summit seismic stations and the six GNSS stations indicated in Figure 1. We use the seismic signals generated by RFs (see examples in Figure 2) at these four stations to locate the RFs. To compute their volumes, we use only three stations (BOR, DSO, and SNE) because of the presence of strong site effects at BON station. BOR and DSO stations present a gap in the data from 17 February 2014 to 4 March 2014, leading to no volume estimation during this short period. GNSS stations are used to quantify the deformation of the cone. GNSS data are postprocessed with the GAMIT/GLOBK software package (Herring et al., 2010). GAMIT uses (i) the precise ephemerides of the international GNSS Service (IGS); (ii) a stable support network of 20 IGS stations not located on Reunion Island but scattered elsewhere in the Indian Ocean; (iii) a tested parameterization of the troposphere; and (iv) models of ocean loading, Earth, and lunar tides. Plate motion used to correct data is deduced from the REUN IGS station located 15 km to the west of the summit and assumed not to be affected by any volcanic deformation. The final daily precision of the measurements is on the order of millimeters. Daily rain data are obtained from a rain gauge located at SNE station, at the summit of the cone.

Journal of Geophysical Research: Earth Surface 10.1029/2017JF004507

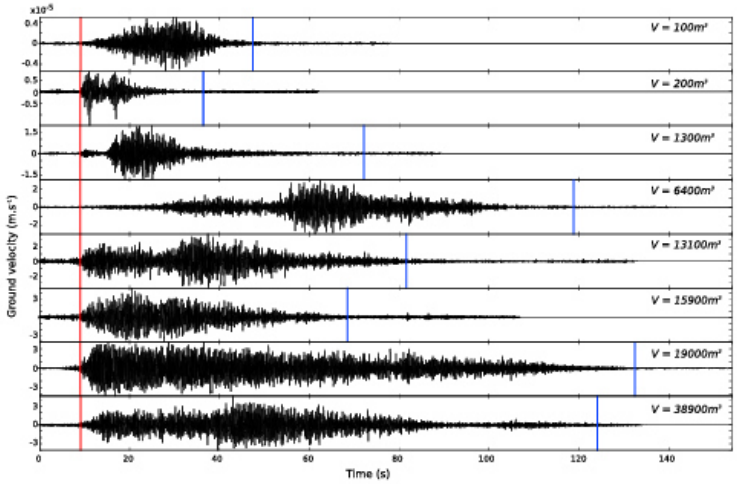

Figure 2. Examples of seismic signals generated by rockfalls of different volumes. The red and blue vertical bars show the beginning and end of the rockfall signals, respectively, detected using the method proposed by Hibert et al. (2014). These signals were all recorded at DSO station.

Two lidar/photogrammetric campaigns were conducted at Piton de la Fournaise volcano. The first one was done in November 2014 and the second in January 2016. These measurements allow us to directly estimate the cumulative RF volume during this period and to compare it with the one computed from seismic data.

3.2. Detection, Classification, and Location of RFs Using Seismic Data

To extract the seismic signals corresponding to RFs at the four summit seismic stations (Figure 1), we use the RF catalog provided by the Observatoire Volcanologique du Piton de la Fournaise (OVPF). In the OVPF catalog, events are classified manually, based on the knowledge and expertise of the operators. Thus, we apply the classification code developed by Hibert et al. (2014) on the extracted signals to remove potential signals that are not generated by RFs. The next step consists in picking the onset of the signal, using a kurtosis-based method (Baillard et al., 2014; Hibert et al., 2014). Then, we apply a locating method based on propagation models built using the Fast Marching Method (Hibert et al., 2014, Sethian, 1996a, 1996b, 1996c). For each pair of stations, it produces a hyperbola corresponding to the most probable source location based on the difference between picked arrival times. For each event, all the hyperbola are stacked, their crossing point giving the optimal location of the source. The uncertainties in picking the signal onset and in the locating process are taken into account (supporting information Text S1), providing an estimation of the spatial location error. We keep only RFs with a location error of less than 500 m, which corresponds to the radius of the crater.

3.3. Volume Estimation Using Seismic Data

We compute the RF volume (Figure 3a) using the formula proposed by Hibert et al. (2011):

$$V = \frac{3E_S}{R_{S/P}\rho g L(\tan\delta\cos\theta - \sin\theta)}, \quad (1)$$

where $\rho = c_0\rho_i$ is the density of the granular mass, with the density of intact rock ρ_i = 2,000 kg/m^3 and the solid volume fraction of the granular material $c_0 = 0.6$. The length of the slope over which RFs occur L and the slope angle θ being fairly uniform all around the crater, we use fixed values: We choose L = 500 m as the average length and $\theta = 35°$ as the mean slope angle. The $\delta = 0°$ is the repose angle of the deposit on the slope (the deposit is very flat, almost parallel to the slope), and $R_{S/P}$ is the mean ratio between seismic energy and potential energy lost by RFs.

We compute the seismic energy E_S using a formula proposed by Vilajosana et al. (2008):

$$E_S = \int_{t_1}^{t_2} 2\pi r\rho hcu_{env}(t)^2 e^{ar}\,dt, \quad (2)$$

Journal of Geophysical Research: Earth Surface 10.1029/2017JF004507

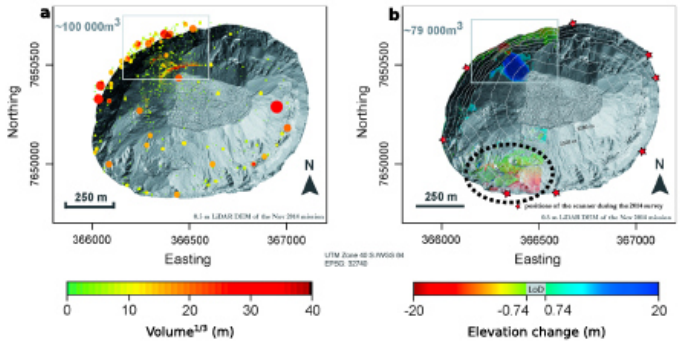

Figure 3. (a) Volumes of the RFs ($V^{1/3}$ is represented) that occurred from October 2014 to January 2016, computed using seismic signals. Each round dot represents a RF, and its radius and color are proportional to the cubic root of the RF volume. The white square defines the area where the total volume (100,000 m^3) is computed. (b) Same as (a) but using photogrammetric data and method. The dotted ellipse highlights the inferred subsiding zone. RF = rockfall.

where t_1 and t_2 are, respectively, the picked onset and final times of the seismic signal, r is the distance between the event and the recording station, $h = 160$ m the thickness of the layer through which surface waves propagate, and $\rho = 2{,}000$ kg/m^3 the density of the ground. The $\alpha = f\pi/Qc$ is a damping factor that accounts for anelastic attenuation of the waves (Aki & Richards, 1980), where $f = 5$ Hz is the frequency, $Q = 50$ the quality factor, and c the group velocity of surface waves, being the optimal velocity given by the locating method, ranging from 480 to 1,200 m/s. The $u_{env}(t)$ is the amplitude envelope of the seismic signal (here the ground velocity). See Hibert et al. (2011) for details concerning the values assigned to each parameter.

Equation (1) is based on the fact that similar power laws are obtained when relating the potential energy to the flow duration on one hand and the seismic energy to the seismic duration on the other hand (Hibert et al., 2011; Levy et al., 2015). Indeed, by coupling seismic analysis with numerical simulation to calculate the potential energy lost by granular flows, the following relations have been found for RFs in different contexts (Deparis et al., 2008; Hibert et al., 2011; Levy et al., 2015):

$$E_i = A_i t_i^{B_i}, \tag{3}$$

where $i = P$ for the potential energy lost E_P and for the granular flow duration t_P, and $i = S$ for the seismic energy E_S and for the duration of the seismic signal t_S. A_i is a constant. The exponent of the power law B has been shown to be related in particular to the characteristics of the topography on which the granular mass is flowing (Hibert et al., 2011; Levy et al., 2015). In this study, we force $B_S = B_P$. Given the similarity in the power laws and field observations showing that $t_S \simeq t_P$, it is possible to calculate the ratio $R_{S/P}$ between the seismic energy and the potential energy: $R_{S/P} = A_S/A_P$. In this study, we choose to use the potential energies calculated by Hibert et al. (2011) for granular flows on the Dolomieu crater topography. Even though the seismic energies we obtain are smaller than those calculated during the period investigated in Hibert et al. (2011), they seem to follow the same power law (Figure 4). We compute the ratio $R_{S/P}$ for each month and each station (BOR, DSO, and SNE). We fit the data in a log-log scale and use a least squares regression. The fitting process and results are shown in Figure 4. We obtain the following ratio for each station, averaged over the study period:

- BOR: $R_{S/P} = 4.12 \times 10^{-7}$
- DSO: $R_{S/P} = 1.49 \times 10^{-6}$
- SNE: $R_{S/P} = 9.69 \times 10^{-7}$

To compute the RF volumes, we use the averaged seismic energy and $R_{S/P}$ ratio over the three stations, with the arithmetic average $R_{S/Pav} = 5.1 \times 10^{-7}$.

For some events, we found inconsistencies between the energies computed at each station. Therefore, we selected only the consistent energies to compute the volume (see Text S2 for more details). Then, a visual

Journal of Geophysical Research: Earth Surface 10.1029/2017JF004507

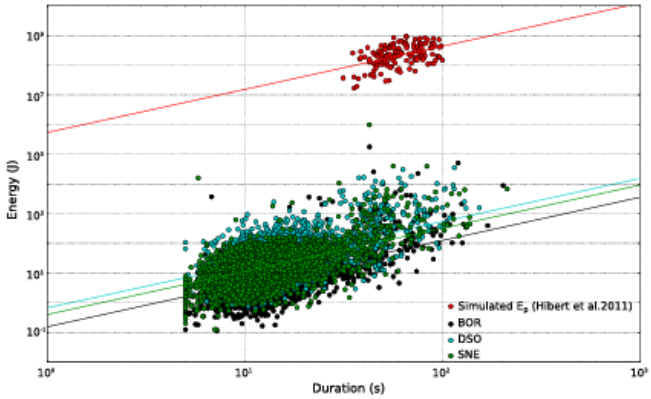

Figure 4. Simulated potential energy (from ; Hibert et al., 2011) as a function of rockfall duration (in red) and observed seismic energy as a function of seismic signal duration, along with the corresponding best fit regression lines, for the seismic stations BOR, DSO, and SNE (in black, blue, and green, respectively). We constrain the regression lines for the seismic energy to have the same slope as the one fitting the potential energy ($B = 1.45$). See Figure 1 for the locations of the seismic stations.

check of the seismic signals of all the events was performed, to remove potentially ambiguous events (e.g., multiple events, including volcano-tectonic ones). Because we focused on the analysis of large events in this study, we chose to check only the largest volumes ($V > 3{,}000$ m^3), thus removing six (out of 63) of them (see examples in Figures S4 and S5).

Given the complexity of the system, it is difficult to determine accurate error in the RF volume computed using seismic data. However, for a particular RF, Hibert et al. (2011) compared the volume computed using seismic data and the volume estimated from photogrammetric data. The comparison showed that the volume is overestimated by 30% using seismic data. To check the validity of the volumes we computed using seismic data, we compared them with lidar and photogrammetric data (see following section).

3.4. Volume Estimations Using Ground-Based Lidar and Photogrammetric Data

3.4.1. Acquisition and Processing of Ground-Based Lidar Data

Lidar data were acquired during a 2-day field campaign in November 2014 using a Terrestrial Laserscanner (TLS) Riegl VZ4000 with a maximum scanning distance up to 4,000 m. To provide high-resolution point data of the crater and minimize shadowing effects (Haas et al., 2016), the scanning was done from eight different scan positions around the crater rim (e.g., Figure 3b). Global positions of the scan sites were provided by externally measured reflectors (dGNSS system). After several postprocessing steps (Haas et al., 2016), including registration/referencing of every single scan position (iterative closest point [ICP]-based algorithm; precision of the referencing: 0.007 to 0.013 m), thinning, and filtering (e.g., flying points in the Riscan Pro software, riegl.com), total number of points sums up to 60.10^6 (mean point density: 55 points per square meter). Point clouds of all single scan positions were merged and exported as ASCII files. All subsequent processing steps were performed using LIS Desktop/SAGA GIS.

3.4.2. Acquisition and Processing of Terrestrial Photographs

During two field campaigns, in 2014 (during the TLS acquisition) and 2016 (without TLS acquisition), terrestrial photographs were captured around the crater rim using two different camera systems (2014: Pentax K-x, 28 mm; 2016: Nikon D610, 28 mm). To increase the quality of the photogrammetric model, we used the scanning positions but also added some camera positions in between. Standard processing steps were performed with Photoscan Professional (Agisoft/Vers. 1.2.3-64bit) to produce 3-D point clouds of the terrestrial photographs:

- Pictures of every time step were aligned, and tie points (reflector targets) were automatically derived by Photoscan Professional, resulting in an initial sparse point cloud.

- To provide global coordinates, ground control points (GCPs) were set on every single picture. Given the absence of available markers inside the crater, GCPs were chosen using concise objects in the 2014 TLS point cloud. In this manner, a sum of 39 GCPs were selected, taking into account probable surface changes between 2014 and 2016, resulting in the appearance or disappearance of concise objects in the earlier or later picture.
- Using the sparse point cloud and the available GCPs, dense clouds were derived for the 2016 photographs. The total number of points was 10.10^6 for the western part (50%) of the crater (mean point density: 10 points per square meter). After the processing procedure, the point cloud data were ASCII formatted (*x*,*y*,*z*, and RGB values) and exported as global coordinates. All subsequent processing steps were done using LIS Desktop/SAGA GIS in the same way as for the ground-based lidar data .

3.4.3. Quantification of Surface Changes

The ASCII files of all time steps, including TLS (2014) and Structure from Motion (2016) data, were imported to LIS Desktop/SAGA GIS (Vers. 3.0.7-64bit)/SAGA GIS (Vers. 3.1.0-64bit) by producing a SAGA point cloud. To check the orientation of both data sets, point clouds were fine-adjusted by applying the ICP adjustment (e.g., Besl & McKay, 1992) in LIS Desktop and by using only stable areas for the fine adjustment. The fine adjustment of the 2014 point cloud (slave) to the 2014 point cloud (master) was carried out successfully with a value of 0.36 m (standard deviation for all points used for the ICP). After this, point clouds were segmentized by plane fitting (SAGA LIS tool segmentation by planes) in order to produce normal vectors for these single planes (and thus for all points belonging to a certain plane). This step was necessary for the following point-to-point distance calculation using the tool distance between point clouds (e.g., Fey & Wichman, 2017). Based on this information, 3-D surface changes were obtained from the measured elevation changes (Figure 3b), and the volumes for certain areas in the western part of the crater were calculated.

3.4.4. Calculation of the Measurement Error

As each method and their combination contain measurement errors leading to uncertainties in the volume calculation, a statistical approach was used for the assessment of the error. This approach assumes that (i) the errors can be calculated using stable areas (e.g., solid rocks, Westaway et al., 2000), (ii) the errors will follow a normal distribution for these stable areas with a mean of 0 (Brasington et al., 2000), and (iii) the uncertainties are independent. The approach of Lane et al. (2003) for the estimation of the level of detection for derived differences of digital elevation models was used to calculate the error in the point-to-point distances. Therefore, the combined normal distributed error $\delta_{pointdistance}$ can be derived using the formula

$$\delta_{pointdistance} = \sqrt{\sigma^2_{pointdistance} + \sigma^2_{pointdistance}}, \tag{4}$$

where $\sigma = 0.32$ m is the standard deviations for the point-to-point distances for the stable area for the two field campaigns, resulting in a $\delta_{pointdistance}$ of 0.45 m. The absolute value of each point-to-point distance ($D_{P1} - D_{P2}$) is then divided by $\delta_{pointdistance}$ to calculate a *t* score (Bennett et al., 2012):

$$t = \frac{|D_{P1} - D_{P2}|}{\delta_{pointdistance}}. \tag{5}$$

A simple *t* test is then conducted for each point to decide whether the change on this point is significant or not. We apply a simple probabilistic threshold (t_{crit}) at the 90% confidence interval ($t > 1.645$) to classify surface changes as probably representing real change or measurement error (e.g., Haas et al., 2016). Thus, only point-to-point distances with real changes over 0.74 m ($> t_{crit}$) are used for the calculation of the elevation changes (e.g., Lane et al., 2003), subtracting the single time steps, which result in positive (accumulation) or negative surface changes (erosion).

4. Results

4.1. Comparison of Seismic and Photogrammetric Method Results

We compare the volume of RFs computed using the two methods over the period from November 2014 to January 2016 (corresponding to the period of photogrammetric measurements). The RF locations provided by the two methods (Figures 3a and 3b) are consistent (both methods show the most active zone to be north northwest of the crater). The most active zone presents steep slopes and large cracks, prone to generate big RFs (OVPF database, Figure S6). This could explain the larger volumes of the RFs observed in this area. The seismic data (Figure 3a) show that the southwestern part of the crater is not very active, despite the presence of

Journal of Geophysical Research: Earth Surface 10.1029/2017JF004507

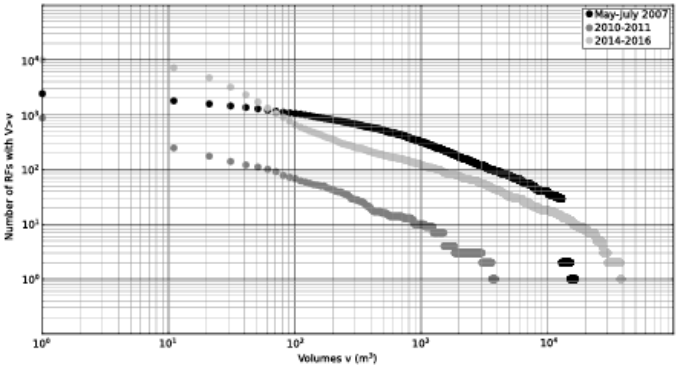

Figure 5. Comparison of the distribution of the RF volume over the periods May–July 2007 (black), 2010–2011 (dark gray), and 2014–2016 (light gray). The *y* axis represents the number of RFs with volume greater than the corresponding volume on the *x* axis. This distribution shows that the catalog of RFs is reliable for volumes greater than 100 m^3. RF = rockfall.

large cracks. This observation appears to be inconsistent with the photogrammetric data (Figure 3b) that show large detached volumes but with few or no visible deposits. The discrepancy between the two data sets and the absence of deposits suggest that a different mechanism is involved here. It is inferred that subsidence is occurring on the southern edge of the crater. This assumption is consistent with the absence of seismic activity in this zone, since subsidence is seismically silent. It is also consistent with the negative surface changes and the lack of corresponding deposits shown by photogrammetric data. This limited case analysis shows the value of coupling two different methods to interpret the mechanism controlling the deformation of the crater edges.

Using the photogrammetric data, we extracted the precise volume of the largest deposits in the northwestern zone of the crater, obtaining a total volume of ~80,000 m^3. We found a volume of the same order of magnitude using the seismic method, with a total of ~100,000 m^3 when adding up the volumes of RFs with $V > 100$ m^3. The frequency-volume distribution shown in Figure 5 follows a power law for $V > 100$ m^3 (Figure S7). For the 2014–2016 period, the observed excess of small events is likely due to a wrong classification of small volcano-tectonic (VT) events into RFs. In the following analysis, we will consider only RFs with $V > 100$ m^3, for which our catalog is reliable. To determine the impact of neglecting the small events, we estimate their total volume using the power law (which we believe to be more accurate that the observed count of small events). From this approach, the total volume of small RFs ($V < 100 m^3$, Figure S7) is ~8,500m^3, which is a small percentage (8.5%) of the total volume of RFs. The lack of larger events compared to the power law prediction may be due to the existence of a maximal volume of RFs that cannot be exceeded in the crater. The volume overestimation when using seismic data vs. photogrammetric data may be due to errors in RF location and duration and/or to the underestimation of the slope angle. It may also be related to the use of numerical simulations of granular flows, whereas at least the first part of the RFs we observe exhibits free fall. Part of the difference between the two methods may also be due to the removal of the smallest deposits (height < 0.74 m) by the photogrammetric method. However, the 26% discrepancy observed here is similar to that found by Hibert et al. (2011) for a single RF event and supports the use of the seismic method to estimate the volume and location of RFs. In the following analysis, we will use these volumes and locations to analyze the spatiotemporal distribution of the RFs.

4.2. RF Catalog Description

Using seismic signals, we located and computed the volume of 10,477 RFs occurring between January 2014 and December 2016. The average error in the event locations is 200 m (Text S1). In Figure 6a, we do not observe the expected increase in RF number or volume just before (1 day) or during all the eruptions. On the contrary, we note a decrease in RF activity. This is the result of missing events, drowned in the noise generated by the high number of volcano-tectonic events just before the eruptions and by the volcanic tremor during the eruptions. Some RFs are large enough to be detected (see during eruptions 2 and 3, Figure 6a). We used them in

Journal of Geophysical Research: Earth Surface 10.1029/2017JF004507

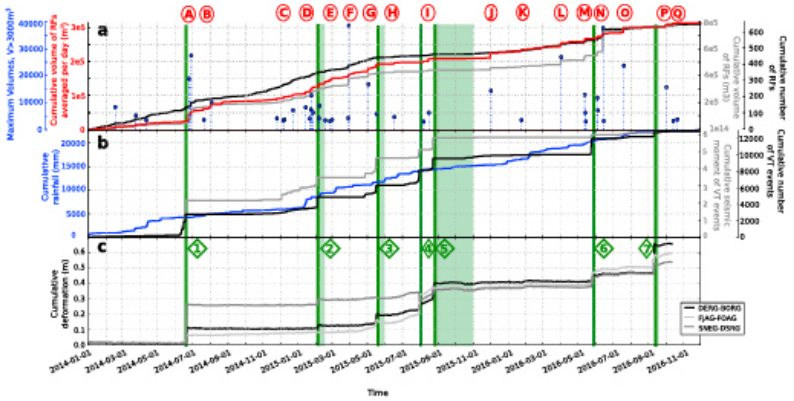

Figure 6. (a) Temporal evolution of the RFs: cumulative number (black), cumulative volume (gray), cumulative volume averaged per day (red), and maximum volumes of individual events per day when greater than 3,000 m^3 (blue dots). (b) Temporal evolution of rainfall (blue) and shallow volcano-tectonic (VT) events plotted as cumulative number (black) and cumulative seismic moment (gray). (c) Cumulative deformation of the base (light gray) and of the summit (dark gray and black) of the terminal cone. The locations of Global Navigation Satellite System stations are indicated in Figure 1. The letters denote significant increases in RF volume (steps in red and gray curves, blue dots). The green vertical lines and rectangles show the start times and durations of eruptions. RF = rockfall.

the comparison with the photogrammetric volume, but they are not considered in the following spatiotemporal analysis because of the incompleteness of the catalog during eruptions. Outside of these periods, 122 of the located RFs have volumes greater than 1,000 m^3, while 57 have volumes greater than 3,000 m^3 (Figure 5). The two largest RFs have volumes close to 40,000 m^3 (Figure 3a).

Figure 5 presents the comparison of the volume distributions for the periods studied by Hibert et al., (2011, 2017) and for the 2014–2016 period. It shows that RF activity in 2014–2016 is lower than during the first 2-month phase of the postcollapse relaxation from May to July 2007. However, this activity is higher than during the more stable period of 2010–2011. We infer that even if more stable than during the postcollapse relaxation phase, the crater edges have been unsettled by the recovery of the eruptive activity after a 4-year break, leading to larger volumes than those at the end of the relaxation period.

4.3. Temporal Evolution of RF Activity

Figure 6 represents the cumulative number of RFs over the 2014–2016 period along with the cumulative volume of RFs (the RF number and volume per day are represented on Figure S8). We compare the total cumulative volume to the cumulative volume averaged per day. To compute the averaged volume per day, we divide the total volume by the number of RFs:

$$V_{av}(t) = \frac{\sum_{i=1}^{n(t)} V_i(t)}{n(t)}, \quad (6)$$

where $V_i(t)$ is the individual volume of each RF, and $n(t)$ the total number of RFs occurring during day t. Plotting the averaged volume per day highlights the importance of the larger volumes compared to the smaller ones. We observe variations on the three curves, with stronger variations of the volume than of the number of RFs. The steps indicated by letters on Figure 6 have an averaged volume per day greater than 1,500 m^3 and include individual events with volumes greater than 3,000 m^3 (Table 1 and blue dots in Figure 6a). In the following, we will use the term *RF swarm* to name these steps. The beginning and ending dates of the RF swarms are selected manually to capture the periods of volume increase.

Most of these RF swarms last 2 to 15 days, except the third one (C) that lasts 1 month. This RF swarm is actually made of three distinct episodes of volume increases separated by less than 15 days. We compare the temporal evolution of RFs with the number and seismic moment of volcano-tectonic events and with rainfall recorded at

Journal of Geophysical Research: Earth Surface 10.1029/2017JF004507

Table 1
Description of the RF Swarms Shown in Figure 6

RF swarm	Number of events	V_{max} (m^3)	V_{av} (m^3)	Number of events $V > 3{,}000\ m^3$	Number of events $V > 1{,}000\ m^3$	First day of the swarm	Duration (days)
A	115	27,700	946	5	16	2014/06/23	13.8
B	150	10,400	156	2	3	2014/07/16	18.4
C	657	7,300	77	4	6	2014/11/24	34.9
D	72	12,800	707	5	9	2015/01/13	14.5
E	243	3,700	94	3	8	2015/02/15	15.2
F	143	38,900	387	2	4	2015/03/27	6.9
G	232	17,000	118	1	3	2015/05/01	13.5
H	22	4,800	307	1	2	2015/06/15	2.7
I	94	6,400	131	2	2	2015/08/05	12.8
J	43	14,500	356	1	1	2015/11/30	2.9
K	27	3,600	189	1	1	2016/01/22	4.9
L	27	27,100	1,154	1	3	2016/03/31	2.9
M	36	13,000	899	4	5	2016/05/12	4.9
N	144	37,900	1,275	14	19	2016/06/04	11.9
O	8	23,900	3,549	1	3	2016/07/14	6.3
P	27	15,900	738	1	2	2016/09/29	6.1
Q	14	3,300	261	1	1	2016/10/12	3.6

Note. Dates are formatted as year/month/day. RF = rockfall.

a summit station on the volcano (Figure 6b). Most of the increases in RF activity seem to be related to increases in volcano-tectonic seismicity. Figure 6c presents the distance changes between pairs of GNSS stations located at the cone summit and base (Figure 1), representing the evolution of the cone deformation. It is difficult to link the deformation observed on these curves with the changes in RF volume.

To quantify the link between volcano-tectonic events, rainfall, and RF swarms, we compute the cross correlation between pairs of time series X and Y using the common formula:

$$C(X,Y) = \frac{X * Y}{N \times \sigma_X \times \sigma_Y}, \tag{7}$$

where N is the length of the time series and σ_X and σ_Y their respective standard deviations. The cross correlation between two time series is calculated several times, shifting one of the time series by 1 day. This allows us to identify the time lag that gives the best correlation. In order to obtain correlation coefficients comprised between −1 and 1, we divide them by the corresponding autocorrelations:

$$\frac{C(X,Y)}{C(X,X)C(Y,Y)}. \tag{8}$$

For each RF swarm (A to Q, Figure 6), we compute the cross correlation between the time series of the number of volcano-tectonic events and of the RF volume, ranging from 30 days before to 1 day after the first day of the RF swarm. We show an example of the result obtained for swarm G in Figure 7a. In the same way, we compute the cross correlations and time lags between the time series of volcano-tectonic seismic moment and the time series of the RF volume and number (swarm G, Figures 7b and 7d). We apply the same strategy to look at the cross correlation between rainfall and RF volume but using a period ranging from 8 days before to 1 day after the first day of the RF swarm (swarm G, Figure 7c).

We observe a clear correlation between the daily seismic moment of volcano-tectonic events per day and RF volume (see, e.g., swarm G in Figure 7a and Tables S1 and S2), with associated time lags ranging from 3 to 30 days (Figure 7e): 59% of the RF swarms show a correlation with the daily seismic moment of volcano-tectonic events exceeding 0.6 and 23% exceeding 0.8. The correlation between the number of volcano-tectonic events per day and RF volume is weaker: 41% of the RF swarms show a correlation with the number of volcano-tectonic events exceeding 0.6 and 12% exceeding 0.8. The correlation of seismicity with

Journal of Geophysical Research: Earth Surface 10.1029/2017JF004507

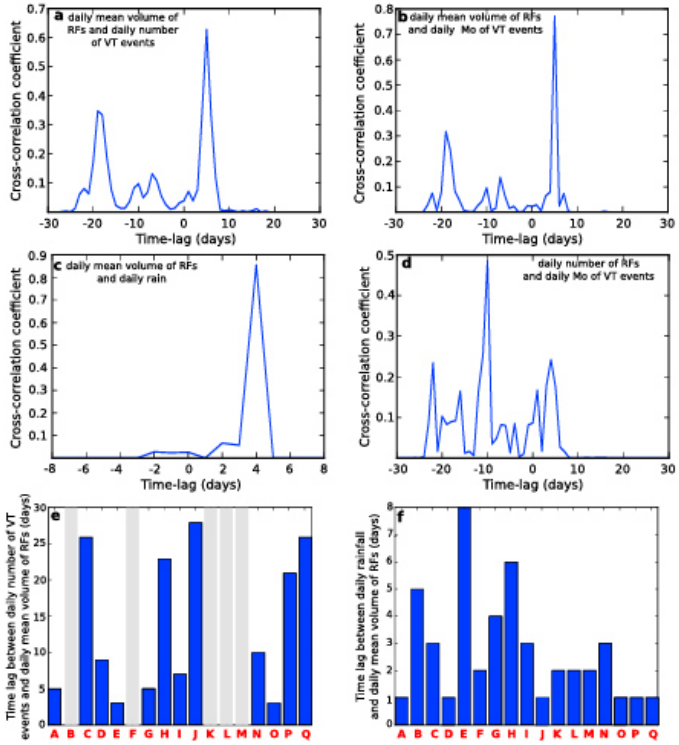

Figure 7. Examples of cross correlation between daily mean volume of RFs and (a) daily number of volcano-tectonic (VT) events, (b) daily seismic moment of VT events, (c) daily amount of rainfall, and (d) between daily number of RFs and daily maximum magnitude of VT events. (e) Time lags corresponding to the maximum cross-correlation coefficient between daily mean volume of RFs and daily number of VT events for each RF swarm (A–Q in Figure 6). (f) As for (e), for cross correlation between daily mean volume of RFs and daily amount of rainfall. RF = rockfall.

the daily number of RFs is poor (Figure 7d and Tables S1 and S2). From the time lag distribution shown in Figure 7e, we use an average time lag of 14 days for the following analysis. No corresponding time lag for episodes B, F, K, L, and M means that there was no seismicity during the 30 days before these RF swarms.

In the same way, we compute the cross correlation between daily rainfall and RF volume. The correlation is also good (see, e.g., swarm G in Figure 7c and Tables S1 and S2): 48% of the correlations significantly exceed 0.6 and 29% exceed 0.8, for correlation times up to 8 days. From the time lag distribution shown in Figure 7f, we use an averaged time lag of 3 days for the following analysis. This offset is in agreement with other studies (Delonca et al., 2014; Helmstetter & Garambois, 2010; Hibert, Mangeney, et al., 2017).

According to these results and to better highlight the links between the RF swarms and external forcings, we compare the daily average volume of RFs to the number of volcano-tectonic events summed over the 14 previous days and to the rainfall summed over the three previous days (Figure 8a). We also compare the volume of RFs with the deformation at the summit of the volcano (Figure 8b). The increases in seismic activity often match a cone deformation episode, because both are triggered by the dike intrusion (Peltier et al., 2016; Segall et al., 2013; Staudacher et al., 2016). Since the two are linked, we chose to sum the absolute deformation velocity of the summit of the volcano (SNEG-DSRG pair of stations) over the same period of 14 days as seismicity. Note, however, that we do not capture RFs occurring during the eruptions. Consequently, the response time of RFs to seismicity or deformation may be shorter than 1 day at the time of the eruptions.

Journal of Geophysical Research: Earth Surface 10.1029/2017JF004507

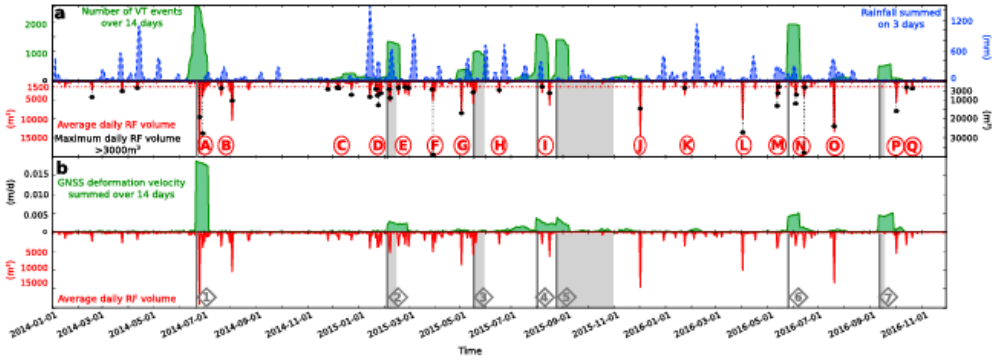

Figure 8. Comparison of the temporal evolution of the external forcings with the volume of RFs averaged per day. (a, top) Number of volcano-tectonic events summed over the prior 14 days, from day $j-14$ to day j (green), and rainfall summed over the prior 3 days, from day $j-3$ to day j (blue). (a, bottom) Averaged volume of RFs per day (red) and maximum volume per day, when it exceeds 3,000 m^3 (black). Note that the y axis limits are different for the averaged and maximum volumes. The letters denote significant increases in RF volume ($V_{av} > 1,500\ m^3$ and $V_{max} > 3,000\ m^3$, limit indicated by the red-dotted line). The gray vertical lines and rectangles show the start times and durations of the eruptions. (b, top) Absolute velocity of the cone deformation represented by the SNEG-DSRG baseline variations, summed over the prior 14 days. (b, bottom) Same as (a). RF = rockfall; GNSS = Global Navigation Satellite System; VT = volcano-tectonic.

We observe clearly in Figure 8a that all the bursts of volcano-tectonic events are related to RF swarms in the following 14 days (swarms A, C, D, G, I, N, O, and P). In the same way, most of the cone deformation episodes are also followed or concomitant with a RF swarm (Figure 8b). Most of the RF swarms are also preceded by rainfall (48% of the RF swarms show a significant correlation with rainfall during the eight previous days). However, large rainfalls does not necessarily trigger a RF swarm (e.g., the rain episode of February 2016 in Figure 8a).

4.4. Spatiotemporal Evolution of RF Activity

Figures 9, 10, and 11 show the spatiotemporal evolution of RFs during swarms A to Q. The first RF swarm occurs after the first eruption following the 4-year break. The slopes of the crater are homogeneously destabilized during swarm A, with small and large RFs. This first swarm is remarkable owing to the high number of volumes greater than 1,000 m^3 (16, Table 1 and Figure 9a). The RF distribution is still homogeneous during swarms B and C. During swarm C, the activity begins to concentrate in the northwestern part of the crater. The most active north northwestern zone shows more small RFs, smaller than 1,000 m^3. Most of the small RFs will indeed occur in this zone over the whole period. Note that this zone corresponds to the steepest and most fractured slopes of the crater. Five months after eruption 1, swarms C and D activate this area with large volumes, greater than 3,000 m^3 (Figures 9c and 9d). This zone is very active until May 2015 (Figures 9c, 9d, 9f, and 10a), showing a long-term relaxation of about 6 months. Then, after swarm G and during 1 year, this area shows very little activity, with only small RFs, even during the different swarms (Figures 10b–10f). In May 2016, events larger than 10,000 m^3 reactivate this northwestern zone, before swarm N, when the second largest volume (37,900 m^3) of the studied period occurs (Figures 11a and 11b). Then the RF activity seems to quiet down again until the end of 2016 (Figures 11c–11e). From November 2014, most of the large events that are preceded by a seismic crisis (C, D, E, G, N, O, and P) are located in the active northwestern part of the crater. On the other hand, the largest volumes of swarms not directly explained by seismicity (B, F, H, J, K, and L) occur on the other slopes. This is the case of the largest event of the period ($V = 38,800\ m^3$, Figure 9f).

In order to look at the impact of eruptive activity on the RF distribution, we plot the spatiotemporal evolution of the RFs between the eruptions (Figures 12 and 13). The first observation we can make is that RFs are larger after the first eruption than before (Figures 12a and 12b). In both cases (before and after eruption 1), they are homogeneously distributed around the crater even if they are slightly more concentrated in the north northwestern zone. After the second eruption, they tend to concentrate in the north northwestern part, with smaller volumes. The volumes increase again before the sixth eruption, in the north northwestern active area, but also on the side of the crater closest to the eruption (Figure 13b). This eruption is followed by one of the largest RFs of the 2014–2016 period. This RF is located in the most active zone of the crater and closer to the seventh eruption location.

Journal of Geophysical Research: Earth Surface 10.1029/2017JF004507

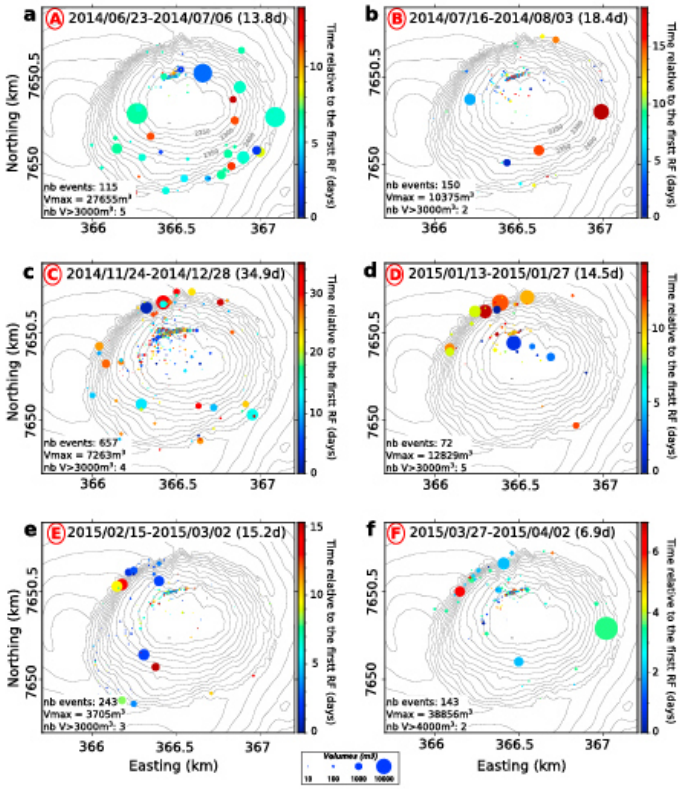

Figure 9. (a–f) Spatial distribution of the RFs making up the A–F swarms shown in Figure 6. For each swarm, the time span corresponds to its duration. Each round dot represents a RF, and its radius is proportional to the RF volume. The colors of the round dots indicate the time from the first RF of the swarm. RF = rockfall.

Looking at the spatial distribution of the RFs during the days preceding all the eruptions, the unstable north northwestern zone is almost always destabilized, but we also note a tendency of the largest RFs to concentrate on the crater edge closest to the next eruption location, a few days before. This is observed for summital eruptions (numbers 1 and 2 in Figure 12) and for most of the distal ones (numbers 3, 4, 6, and 7 in Figures 12 and 13). Eruptions 2, 4, and 7 occur on the northwestern side of the crater, close to the most destabilized zone. It is thus difficult to link them to RF activity occurring in this area. As for eruptions 1, 3, and 6, they occur on the opposite side, much less active in terms of RFs (Figures 3a, 9, 10, and 11). However, events of average to large volumes occur in this zone a few days before these eruptions (Figures 12, 13, and 14). Furthermore, a more detailed investigation of what is happening during the four RF swarms preceding eruptions (swarms D, G, I, and M, occurring during the 20 days preceding eruptions 2, 3, 5, and 6, respectively) shows that the largest RFs tend to migrate toward the next eruption location (Figure 14).

5. Discussion

5.1. Evolution of the RF Activity Compared to the Postcollapse Period

The period we analyze is far enough from the 2007 crater floor collapse to be less affected by the postcollapse relaxation of the crater slopes. Furthermore, it corresponds to the renewal of eruptive activity of the volcano after a break of 41 months. This resurgence in volcanic activity was accompanied by a high activity

Journal of Geophysical Research: Earth Surface 10.1029/2017JF004507

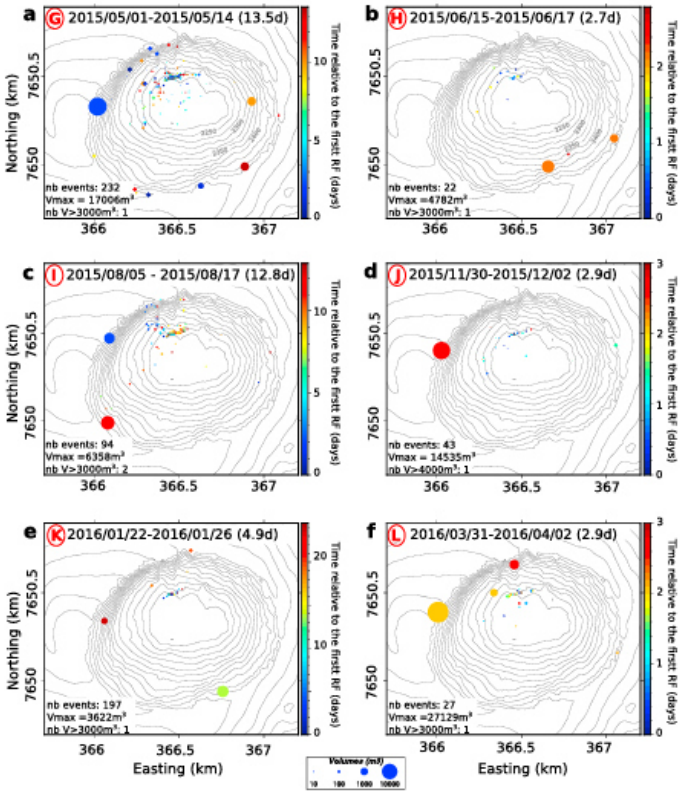

Figure 10. Same caption as Figure 9 for rockfall swarms G–L.

of volcano-tectonic events: more than 2,000 seismic events occurred during the 2 weeks preceding the June 2014 eruption (Lengliné et al., 2016). The RF activity during the 2014–2016 period is higher than that at the end of the relaxation period, from 2010 to 2011 (Figure 5). We infer that the increase in the RF activity compared to the 2010–2011 period is the signature of crater slope destabilization due to the renewal of volcanic activity, accompanied by the resumption of volcano-tectonic seismicity and deformation. The RFs constituting the first RF swarm (A) of the period are located homogeneously around the crater (Figure 9a). They are subsequently preferably located in the most active zone, northwest of the crater (Figure 3). However, before most of the eruptions (85%), the largest RFs tend to migrate toward the eruption location in the days leading up to the eruption (Figures 12 and 13). This corroborates Hibert, Mangeney, et al.'s (2017) observations on RF migration before eruptions. Another interesting observation over the 2014–2016 period is that eruption number 6, like eruption number 1, seems to reactivate slope instability at different places in the crater (Figures 13b and 13c). One common feature of eruptions 1 and 6 is that they both occur after a quiet period of more than 1 year. This may explain the similarities observed in the RF response to these eruptions. During the period of quiescence, the RFs are subjected to a long-term forcing caused by gravity and rainfall episodes. We infer that this long forcing initiates the destabilization of the slopes, while the sudden high seismicity associated with the renewal of volcanic activity triggers the simultaneous fall of all the unsettled slopes.

The $R_{S/P}$ ratio we calculate for the 2014–2016 period is smaller than the one obtained by Hibert et al. (2011) for the 2007–2008 period but similar to that observed for RFs in Montserrat (Levy et al., 2015). Measurements of

Journal of Geophysical Research: Earth Surface 10.1029/2017JF004507

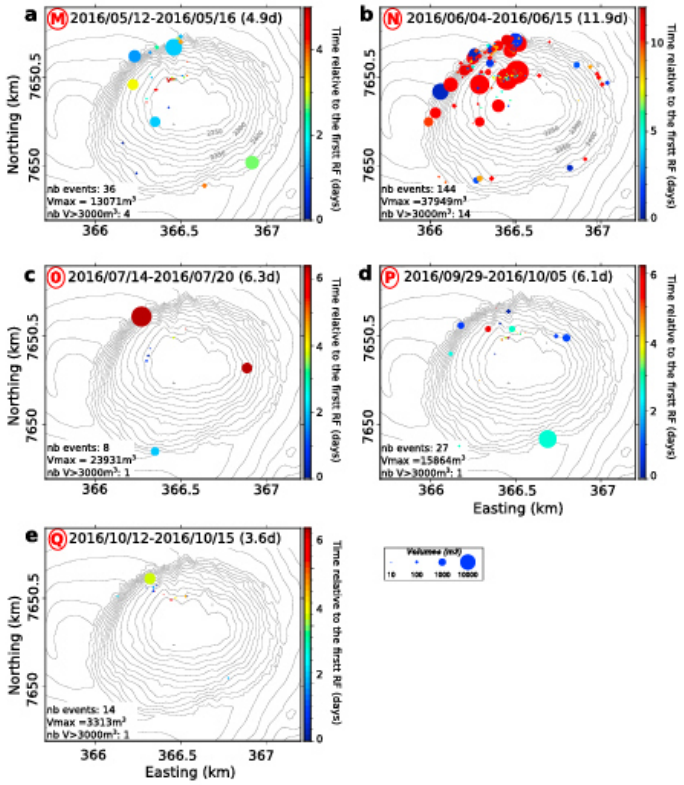

Figure 11. Same caption as Figure 9 for rockfall swarms M–Q.

seismic efficiency $R_{S/P}$ are a key issue. Different values have been found in different environments: $R_{S/P}$ values ranging from 10^{-5} to 10^{-3} have been found by Hibert et al. (2011) for the Piton de la Fournaise volcano over the 2007–2011 period and by Deparis et al. (2008) for RFs in the French Alps. On the other hand, smaller $R_{S/P}$ values ranging from 10^{-6} to 10^{-5} have been found by Levy et al. (2015) for granular flows in Montserrat valleys and by Berrocal et al. (1978) for a landslide in Peru. Free-fall laboratory experiments of beads and grains have shown that the seismic energy dissipated during an impact depends on the grain size and velocity, on the nature of the receiving plate, and on the slope angle (Farin et al., 2016, 2018), as confirmed by field measurements (Hibert, Malet, et al., 2017). Furthermore, Bachelet et al., (2016, 2018) have shown that the presence of an erodible bed can decrease the seismic energy transmitted to the ground for free-fall grains, in agreement with field observations of rock impact (Farin et al., 2015). The reason is that part of the acoustic energy is dissipated in the erodible bed by inelastic collision and agitation of grains. We can thus possibly explain the smaller ratio (i.e., seismic energies) obtained here compared to those of Hibert et al. (2011) by the smaller size of the 2014–2016 RFs and by the presence of an erodible bed due to the accumulation of RF deposits after the crater collapse.

5.2. Link Between RFs and External Forcings

Looking at the temporal evolution of the RFs (Figure 6), we observe small changes in their rate of occurrence, related to eruption times and rainfall amounts. We notice an interaction between seismic events and RFs, with a response time of several days (Figure 8a). This vibration-induced destabilization of crater slopes could be compared to the delayed dynamic triggering of earthquakes, where the impingement of remote or local seis-

Journal of Geophysical Research: Earth Surface 10.1029/2017JF004507

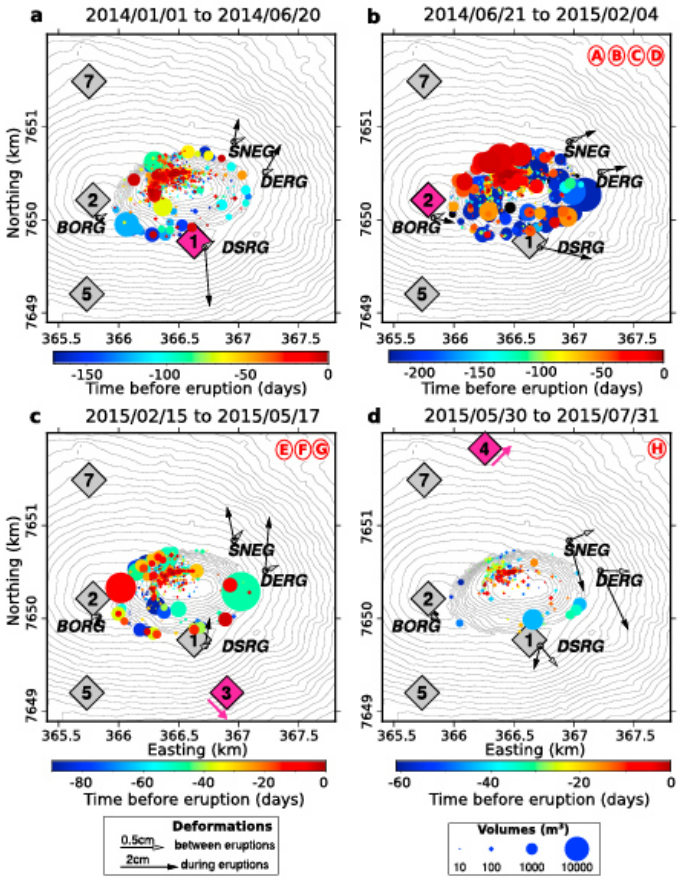

Figure 12. Spatiotemporal evolution of RFs during intereruption periods (eruptions 1 to 4). The pink diamond denotes the upcoming eruption. Each round dot represents a RF, and its radius is proportional to the RF volume. The colors of the round dots denote the time to the upcoming eruption. The gray and black arrows represent the horizontal displacements at the summit during the intereruption period and the first day of the eruption, respectively. The red letters indicate the RF swarm present in each plotted period. (a) Eruption 1: 20 and 21 June 2014, (b) Eruption 2: 4–15 February 2015, (c) Eruption 3: 17–30 May 2015, and (d) Eruption 4: 30 July to 2 August 2015. RF = rockfall.

mic waves on a granular fault gouge drives it to failure or slip (Gomberg & Johnson, 2005; Hill & Prejean, 2006). Several laboratory investigations on sliding of a frictional interface (Bureau et al., 2001; Capozza et al., 2009; Léopoldès et al., 2013) and dynamics of a granular medium (Johnson & Jia, 2005; Johnson et al., 2008; Lastakowski et al., 2015) subjected to external vibrations provide clues to the role of seismic waves in fault instability. Jia et al. (2011) and Léopoldès et al. (2013) have shown that ultrasounds can lubricate the grain contact bonding via vibration-induced growth of microslips or cracks, decreasing the elastic modulus and the static threshold of granular media and consequently triggering the failure. Similar to the destabilization process studied here, Jaeger et al. (1989) have also found that the angle of repose of a vibrated sandpile relaxes quasi-logarithmically in the course of time. They showed that such relaxation phenomena could be explained by an activation process in which mechanical vibration could play a role of effective temperature T_{eff} in dense

Journal of Geophysical Research: Earth Surface 10.1029/2017JF004507

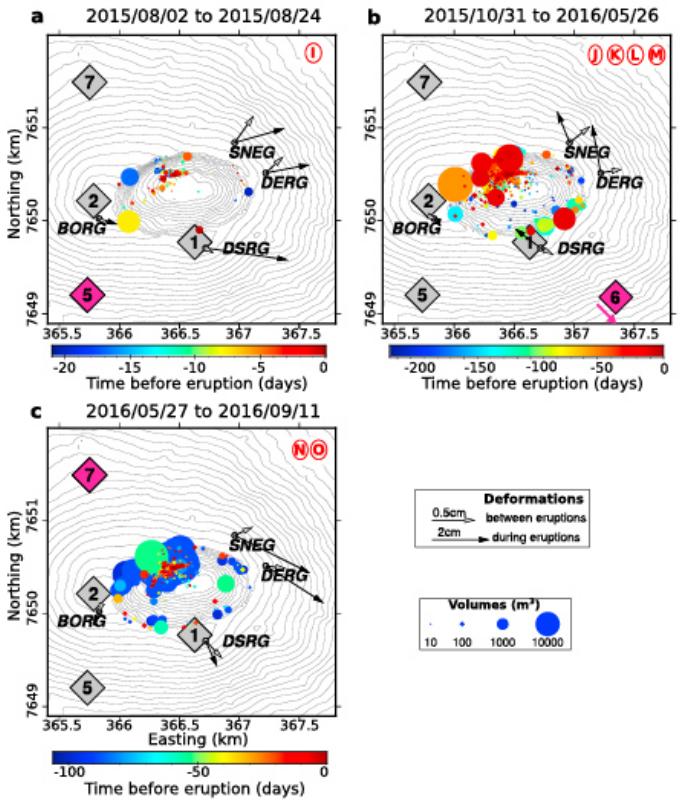

Figure 13. Same as Figure 12 for eruptions 5 to 7. (a) Eruption 5: 24 August to 31 October 2015, (b) Eruption 6: 26 and 27 May 2016, and (c) Eruption 7: 11–18 September 2016.

granular media (Liu & Nagel, 1998), being proportional to the vibration energy (Léopoldès et al., 2013). This may describe the transition from jammed solid to flowing liquid states.

Such an activation mechanism is reminiscent of thermal activation involved in crack nucleation (Das & Scholz, 1981) or the rate-and-state-dependent friction process (Baumberger & Caroli, 2006; Di Toro et al., 2011). The latter has been invoked to explain earthquake nucleation (Dieterich, 1979; Rice & Ruina, 1983; Scholz, 2002) where the characteristic time to failure may be estimated from the critical slip distance (Campillo & Ionescu, 1997; Dieterich, 1992) and the slow rupture velocity, ranging from a few microseconds to a few minutes or a few days for different systems (Latour et al., 2013). A nucleation process may thus explain the observed time delay of a few days for RF triggering, where the number or repetitions of seismic events plays a more important role than their maximum magnitude, possibly due to the effect of vibration energy (i.e., T_{eff}) rather than a pulsed stress, in the phenomena leading to rupture.

We estimate the dynamic strain required in laboratory experiments and field observations to trigger the instability. In the case of model granular media, an ultrasound of $f \sim 10–100$ kHz induces a displacement of $u \sim 1–10$ nm. With a wave velocity of $c \sim 100–500$ m/s (Jia et al., 2011; Johnson & Jia, 2005), the dynamic strain $\epsilon_d = 2\pi u/\lambda$ is of the order of $\sim 10^{-6}$ (with wavelength $\lambda = c/f$). At the Piton de la Fournaise volcano, the displacement at the summit of the volcano triggered by the *S* wave of volcano-tectonic events of $M \sim 3$ (maximum magnitude of these events) is of the order of 10^{-7} m for a vibration velocity of around 10^{-5} m/s at a

Journal of Geophysical Research: Earth Surface 10.1029/2017JF004507

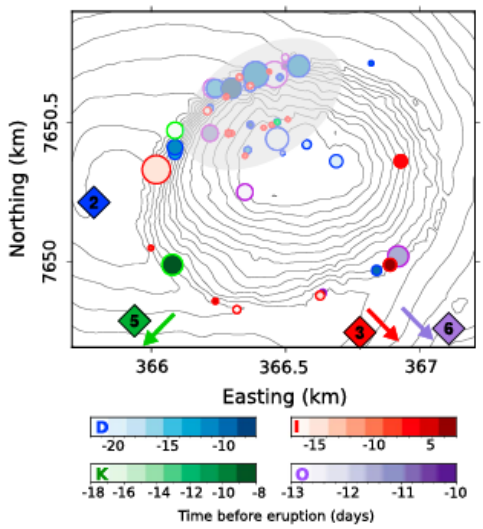

Figure 14. Zoom on the four RF swarms (D, G, I, and M) preceding eruptions number 2, 3, 5, and 6. Each round dot represents a RF, and its radius is proportional to the RF volume. The colors of the periphery of the round dots correspond to the related eruption (colored diamonds). The intensity of the round dot colors shows the time to the eruption. The letters in the colored bars correspond to the RF swarms shown in Figure 8a. (2) 4–15 February 2015, (3) 17–30 May 2015, (5) 24 August to 31 October 2015, and (6) 26 and 27 May 2016. RF = rockfall.

frequency of about 10 Hz. The *S* wave velocity in a highly fractured basaltic media is about 500 m/s, producing a dynamic strain on the order of 10^{-8}, which is smaller than the values found in the above laboratoryexperiments and in some cases of dynamic triggering of earthquakes (Gomberg & Johnson, 2005). The extrapolation of laboratory experiments to natural conditions needs further investigation. This is especially the case for the Piton de la Fournaise volcano, given that the effect of the cone deformation and rainfall must be taken into account in addition to seismic activity.

Even if we assume that the effect of the postcollapse relaxation of the crater slopes is no longer dominant, it is still difficult to discriminate between the influences of the different factors on RF activity. Indeed, there are intricate relations between volcanic seismicity, cone deformation, rainfall, and RFs. First, volcano-tectonic seismicity and deformation are linked and often simultaneous. They are both triggered by the pressurization at depth of the volcanic system and by the migration of the magma. Second, Piton de la Fournaise is exposed to a tropical climate with some of the highest rainfall intensities in the world (with an average of 7,000 mm/year). Because of the high activity of the volcano, rain is often coincident with seismicity and/or cone deformation. However, from the observations in Figure 8, volcano-tectonic events seem to play a predominant role. Indeed, all the increases in seismic activity are followed by a RF swarm, even if there is little deformation and little rainfall (e.g., the C swarm in Figure 8, with a maximum volume of 17,000 m^3, was preceded by relatively low rainfall, 129 mm over the 10 previous days). Nor is it obvious that rainfall is sufficient to trigger large RFs ($V > 15{,}000\ m^3$) in the Piton de la Fournaise crater (Figure 8a). In this context, it is thus difficult to determine the exact influence of rainfall on the increases in RF volume. From our observations, it seems that even small seismicity ($M < 3$) observed at the Piton de la Fournaise volcano can generate higher RF activity. However, in this volcanic context, it is likely that the combined action of seismicity and rain leads to the increase of RF activity we observe: Subcritical crack growth processes may be very efficient, triggered by seismicity (as described in the previous paragraph) and enhanced by infiltration of meteoric water in cracks interacting with volcanic gases (Atkinson & Meredith, 1987; Kilburn & Voight, 1998).

During our study period, seven RF swarms out of 17 (B, F, H, J, K, L, and M in Figure 8) are not directly explained by seismic activity, deformation, or rainfall. The largest volumes of swarm B occur on the southern and eastern slopes of the crater (Figure 9b), destabilized about 10 days before, during RF episode A. We infer that this corresponds to the relaxation of this area after the activity triggered 1 month earlier by the first eruptive activity since the 41-month break. Note that a small rainfall event occurred before swarm B. As for swarms F, H, J, K, and L, they consist of a few large events ($> 3{,}000\ m^3$) located outside of the northwestern zone and some small ones ($< 1{,}000\ m^3$) in the northwestern zone. They are not preceded by seismicity nor significant deformation during the previous days. Neither are any of these swarms, except K, preceded by significant rainfall. The observation of these five RF swarms (F, H, J, K, and L) suggests that the destabilization of large volumes outside of the steepest slopes seems to be a long-term process. We infer that the renewal of volcano-tectonic activity destabilized the whole crater on the short and long term with a delay of a few days for the steepest slopes until the end of their relaxation and several months for the more stable slopes. To confirm that the large volumes of swarms F, H, J, K, and L are linked to the renewal of volcano-tectonic activity, another study should be carried during a period with no significant seismicity. We highlight here a different behavior of the RFs, depending on the steepness of the slopes. The steepest slopes (NW of the crater) are prone to generate many RFs of various sizes and respond quickly (a few days) to seismic activity. On the other hand, the smoothest slopes exhibit fewer RFs and mainly large ones. They generally respond to the combined action of seismicity and rain with a delay of more than 1 month.

Finally, swarm M occurs mainly in the most active zone of the crater and consists of a few large events ($> 3{,}000\ m^3$) along with small events ($< 200\ m^3$, Figure 11a). It occurs during a small rainfall event, without seis-

micity nor significant deformation during the previous days (Figure 8). It is difficult to conclude that this limited rainfall event could be sufficient to trigger such a change in RF volumes. Another possibility could be that the destabilization of the area is a long-term process. Indeed, there was no large RF on the northwestern slope for 12 months (Figures 10b–10f, 12d, and 13a) after the relaxation of RF activity due to the renewed eruptive activity. However, there were seismic activity, deformation, and rainfall during this period that, together with the force of gravity, could have progressively destabilized the area. Subsequently, a small amount of rain and deformation could be sufficient to trigger large RFs. This hypothesis is consistent with the fact that swarm M marks the beginning of a second destabilization episode, lasting 2 months, with 14 RFs of volumes greater than 3,000 m^3.

The vertical slopes of the Dolomieu crater form a system at its limit of stability in relation to the permanent exposure to gravitation forces. For this reason, a small disturbance can be sufficient to unsettle these slopes. Thus, the initiation of a crack or small changes in material cohesion or pressure resulting from seismic activity, deformation, or rainfall may trigger larger RFs, after a time delay of several days in the case of the Piton de la Fournaise volcano. Numerical simulations and laboratory experiments taking into account the long-term effect of gravity could provide more information on what controls the time delays of subsequent large RFs. To better understand and discriminate between the influences of seismicity and rainfall on RF volume, further study should be carried out over the transition period, from 2010 to 2014, during which there were no eruptions and low seismic activity.

6. Conclusions

The Piton de la Fournaise volcano represents a unique site to study the response of unstable slopes to different forcings. The existence of a large seismic data set along with photogrammetric data allowed us to compare and show good agreement between the location and volume of the RFs estimated using these two types of data (Figure 3). Coupling these two different data sets also sheds light on the mechanisms controlling the deformation of the crater edges. Our study shows the complexity of the Piton de la Fournaise system, with intricate interactions between RFs, eruptive activity (deformation and seismicity), and rainfall. Despite this complexity, we were able to extract information on response times of RFs to the different external forcings. Hibert, Mangeney, et al. (2017) pointed out a two-step relaxation phase after the 2007 crater collapse: 2 months of strong RF activity, followed by a decrease of the rate of occurrence and volume of RFs, until reaching a constant frequency 3 years later. Our study throws some light on smaller-scale response times between external forcings and RF activity. Seismicity, deformation, and rainfall can trigger an increase in RF volume that can last for 10 days to 1 month. These RF swarms occur after certain delays: 3 days for rain and 3 to 20 days for seismicity and deformation. A longer-term response of RFs to seismic activity and deformation is observed on the sides of the crater presenting lower slopes. By comparing our observations with laboratory experiments performed on granular materials (Jia et al., 2011; Léopoldès et al., 2013), we suggest that seismic activity could lead to the collapse of large volumes after a delay of one to several days: the repetition of vibration decreases the yield stress via crack growth or slip propagation in highly fractured or granular materials. This subcritical crack growth process may be enhanced by fluid-crack interaction due to rainfall. We also extract information on the spatial distribution of RFs in response to a localized forcing such as eruptions. Like Hibert, Mangeney, et al. (2017), we highlight a tendency of RF activity to migrate, following the locations of the eruptions.

Acknowledgments

The permanent GNSS and seismic data used in this paper were collected by Observatoire Volcanologique du Piton de la Fournaise/Institut de Physique du Globe de Paris (OVPF/IPGP). GNSS and seismic data are accessible at the Volobsis website: http//volobsis.ipgp.fr/. This work was funded by ERC Slidequakes. We want to thank Pr Di Toro and two anonymous reviewers for their thoroughgoing reviews that helped us to greatly improve our manuscript, as well as the Editor and Associate Editor for their helpful comments.

References

Abellan, A., Vilaplana, J. M., Calvet, J., Garcia-Selles, D., & Asensio, E. (2011). Rockfall monitoring by Terrestrial Laser Scanning case study of the basaltic rock face at Castellfollit de la Roca (Catalonia, Spain). *Natural Hazards and Earth System Sciences, 11*, 829–841.

Aki, K., & Richards, P. G. (1980). *Quantative seismology: Theory and methods* (2nd ed., 645 pp.). Sausalito, CA: University Science Books.

Ambraseys, N., & Bilham, R. (2012). The Sarez-Pamir earthquake and landslide of 18 February 1911. *Seismological Research Letters*, 83(2), 294–314.

Atkinson, B. K., & Meredith, P. G. (1987). *The theory of subcritical crack growth with applications to minerals and rocks in fracture mechanics of rock Edited by* B. K. Atkinson. London: Academic. 11–166.

Bachelet, V., Mangeney, A., de Rosny, J., & Toussaint, R. (2016). *Effect of the surface roughness on the seismic signal generated by a single rock impact: Insight from laboratory experiments*. Vienna Austria: EGU abstract.

Bachelet, V., Mangeney, A, de Rosny, J., Toussaint, R., & Farin, M. (2018). Elastic wave generated by granular impact on rough and erodible surfaces. *Journal of Applied Physics, 123*(4), 44901.

Baillard, C., Crawford, W. C., Ballu, V., Hibert, C., & Mangeney, A. (2014). An automatic kurtosis-based P- and S-phase picker designed for local seismic networks. *Bulletin of the Seismological Society of America, 104*(1), 394409.

Baumberger, T., & Caroli, C. (2006). Solid friction from stickslip down to pinning and aging. *Advance Physics, 55*, 2794348.

Bennett, G. L., Molnar, P., Eisenbeiss, H., & McArdell, B. W. (2012). Erosiononal power in the Swiss Alps: Characterization of slope failure in the Illgraben. *Earth Surface Processes and Landforms, 37*(9), 1627–1640.

Berrocal, J., Espinosa, A., & Galdos, J. (1978). Seismological and geological aspects of the Mantaro landslide in Peru. *Nature*, *275*(5680), 533536.
Besl, P. J., & McKay, N. D. (1992). A method for registration of 3D-shapes. *IEEE Transactions on Pattern Analysis and Machine Intelligence*, *14*(2), 239–256.
Brasington, J., Rumsby, B. T., & McVey, R. A. (2000). Monitoring and modelling morphological change in a braided gravel-bed river using high resolution GPS-based survey. *Earth Surface Processes and Landforms*, *25*(9), 973–990.
Bureau, L., Baumberger, T., & Caroli, C. (2001). Jamming creep of a frictional interface. *Physical Review E*, *64*, 31502. 1–4.
Calder, E. S., Luckett, R., Sparks, R. S. J., & Voight, B. (2002). Mechanisms of lava dome instability and generation of rockfalls and pyroclastic flows at Soufriere Hills Volcano, Montserrat. *Geological Society, London, Memoirs*, *21*(1), 173–190.
Campillo, M., & Ionescu, I. (1997). Initiation of antiplane shear instability under slip dependent friction. *Journal of Geophysical Research*, *102*(B9), 20636–20371.
Capozza, R., Vanossi, A., Vezzani, A., & Zapperi, S. (2009). Suppression of friction by mechanical vibrations. *Physical Review Letters*, *103*, 8.
D'Amato, J., Hantz, D., Guerin, A., Jaboyedoff, M., Baillet, L., & Mariscal, A. (2016). Influence of meteorological factors on rockfall occurrence in a middle mountain limestone cliff. *Natural Hazards and Earth System Sciences*, *16*, 719–735.
Dammeier, F., Moore, J. R., Haslinger, F., & Loew, S. (2011). Characterization of alpine rockslides using statistical analysis of seismic signals. *Journal of Geophysical Research*, *116*, F04024. https://doi.org/10.1029/2011JF002037
Das, S., & Scholz, C. (1981). Theory of time-dependent rupture in the Earth. *Journal of Geophysical Research*, *86*, 6039–6051.
De Blasio, F. V. (2011). *Introduction to the physics of landslides: Lecture notes on the dynamics of mass wasting*, pp. 408. New York: Springer.
Del Gaudio, V., Trizzino, R., Calcagnile, G., Calvaruso, A., & Pierri, P. (2000). Landsliding in seismic areas: The case of the Acquara-Vadoncello landslide (southern Italy). *Bulletin of Engineering Geology and the Environment*, *59*, 23–37.
Delonca, A., Gunzburger, Y., & Verdel, T. (2014). Statistical correlation between meteorological and rockfall databases. *Natural Hazards and Earth System Sciences*, *14*(8), 1953–1964.
Deparis, J., Jongmans, D., Cotton, F., Baillet, L., Thouvenot, F., & Hantz, D. (2008). Analysis of rock-fall and rock-fall avalanche seismograms in the French Alps. *Bulletin of the Seismological Society of America*, *98*(4), 17811796.
Di Toro, G., Han, R., Hirose, T., De Paola, N., Nielsen, S., Mizoguchi, K., et al. (2011). Fault lubrication during earthquakes. *Nature*, *471*, 494–498. https://doi.org/10.1038/nature09838
Dieterich, J. (1979). Modeling of rock friction 1. Experimental results and constitutive equations. *Journal of Geophysical Research*, *84*(B5), 2161–2168.
Dieterich, J. (1992). Earthquake nucleation on faults with rate- and state-dependent strength. *Tectonophysics*, *211*, 115–134.
Dietze, M., Mohadjer, S., Turowski, J. M., Ehlers, T. A., & Hovius, N. (2017). Seismic monitoring of small alpine rockfalls—Validity, precision and limitations. *Earth Surface Dynamics*, *5*, 653–668.
Dietze, M., Turowski, J. M., Cook, K. L., & Hovius, N. (2017). Spatiotemporal patterns, triggers and anatomies of seismically detected rockfalls. *Earth Surface Dynamics*, *5*, 757–779.
Farin, M., Mangeney, A., De Rosny, J., Toussaint, R., Sainte-Marie, J., & Shapiro, N. (2016). Experimental validation of theoretical methods to estimate the energy radiated by elastic waves during an impact. *Journal of Sound and Vibration*, *362*, 176–202.
Farin, M., Mangeney, A., De Rosny, J., Toussaint, R., & Trinh, P. T. (2018). Link between the dynamics of granular flows and the generated seismic signal: Insights from laboratory experiments. *Journal of Geophysical Research: Earth Surface*, *123*, 1407–1429. https:doi.org/10.1029/2017JF004296
Farin, M., Mangeney, A., Toussaint, R., De Rosny, J., Shapiro, N., Dewez, T., et al. (2015). Characterization of rockfalls from seismic signal: Insights from laboratory experiments. *Journal of Geophysical Research: Solid Earth*, *120*, 7102–7137. https://doi.org/10.1002/2015JB012331
Fey, C., & Wichman, V. (2017). Long-range terrestrial laser scanning for geomorphological change detection in alpine terrain handling uncertainties. *Earth Surface Processes Landforms*, *42*, 789–802.
Gomberg, J., & Johnson, P. (2005). Seismology: Dynamic triggering of earthquakes. *Nature*, *437*(7060), 830–830.
Haas, F., Hilger, L., Neugirg, F., Umstdter, K., Breitung, C., Fischer, P., et al. (2016). Quantification and analysis of geomorphic processes on a recultivated iron ore mine on the Italian island Elba using long-time ground-based lidar and photogrammetric data by an UAV. *Natural Hazards and Earth System Sciences*, *16*, 1269–1288.
Helmstetter, A., & Garambois, S. (2010). Seismic monitoring of Séchilienne rockslide (French Alps): Analysis of seismic signals and their correlation with rainfalls. *Journal of Geophysical Research*, *115*, F03016. https://doi.org/10.1029/2009JF001532
Herring, T. A., King, R. W., & McClusky, S. C. (2010). GAMIT: GPS analysis at MIT. Release 10.4.Massachusetts Institute of Technology, Cambridge.
Hibert, C., Malet, J. P., Bourrier, F., Provost, F., Berger, F., Bornemann, P., & Mermin, E. (2017). Single-block rockfall dynamics inferred from seismic signal analysis. *Earth Surface Dynamics*, *5*(2), 283.
Hibert, C., Mangeney, A., Grandjean, G., Baillard, C., Rivet, D., Shapiro, N. M., et al. (2014). Automated identification, location, and volume estimation of rockfalls at Piton de la Fournaise volcano. *Journal of Geophysical Research: Earth Surface*, *119*, 1082–1105. https://doi.org/10.1002/2013JF002970
Hibert, C., Mangeney, A., Grandjean, G., Peltier, A., DiMuro, A., Shapiro, N. M., et al. (2017). Spatio-temporal evolution of rockfall activity from 2007 to 2011 at the Piton de la Fournaise volcano inferred from seismic data. *Journal of Volcanology and Geothermal Research*, *333–334*, 36–52. https://doi.org/10.1016/j.jvolgeores.2017.01.007
Hibert, C., Mangeney, A., Grandjean, G., & Shapiro, N. M. (2011). Slope instabilities in Dolomieu crater, Réunion Island: From seismic signals to rockfall characteristics. *Journal of Geophysical Research*, *116*, F04032. https://doi.org/10.1029/2011JF002038
Hill, D. P., & Prejean, S. G. (2006). Dynamic triggering. In G. Schubert, & H. Kanamori (Eds.), *Treatise on geophysics vol. 4*. Amsterdam: Elsevier, pp. 257–291. Earthquake Seismology.
Jaeger, H., Liu, C.-h., & Nagel, S. (1989). Relaxation at the angle of repose. *Physical Review Letters*, *62*, 40–43.
Jia, X., Brunet, T., & Laurent, J. (2011). Elastic weakening of a dense granular pack by acoustic fluidization: Slipping, compaction, and aging. *Physical Review E*, *84*, 2.
Johnson, P. A., & Jia, X. (2005). Nonlinear dynamics, granular media and dynamic earthquake triggering. *Nature*, *437*, 871–874.
Johnson, P. A., Savage, H., Knuth, M., Gomberg, J., & Marone, C. (2008). Effects of acoustic waves on stick–slip in granular media and implications for earthquakes. *Nature*, *451*(7174), 57–60.
Keefer, D. K. (1984). Landslides caused by earthquakes. *Geological Society of America Bulletin*, *95*, 406–421.
Keefer, D. K. (2002). Investigating landslides caused by earthquakes—A historical review. *Surveys in Geophysics*, *23*, 473–510.
Kilburn, C., & Voight, B. (1998). Slow rock fracture as eruption precursor at Soufriere Hills volcano, Montserrat. *Geophysical Research Letters*, *25*(19), 3665–3668.

Koukouvelas, I., Litoseliti, A., Nikolakopoulos, K., & Zygouri, V. (2015). Earthquake triggered rock falls and their role in the development of a rock slope: The case of Skolis Mountain, Greece. *Engineering Geology*, *191*, 71–85.
Krautblatter, M., Moser, M., Schrott, L., Wolf, J., & Morche, D. (2012). Significance of rockfall magnitude and carbonate dissolution for rock slope erosion and geomorphic work on Alpine limestone cliffs (Reintal, German Alps). *Geomorphology*, *167–168*, 21–34.
Lacroix, P. (2016). Landslides triggered by the Gorkha earthquake in the Langtang valley, volumes and initiation processes. *Earth, Planets and Space*, *68*, 46. https://doi.org/10.1186/s40623-016-0423-3
Lacroix, P., & Helmstetter, A. (2011). Location of seismic signals associated with microearthquakes and rockfalls on the Schilienne Landslide, French Alps. *Bulletin of the Seismological Society of America*, *101*(1), 341–353.
Lane, S. N., Westaway, R. M., & Murray, H. D. (2003). Estimation of erosion and deposition volumes in a large, gravel-bed, braided river using synoptic remote sensing. *Earth surface processes Landforms*, *28*(3), 249–271.
Lastakowski, H., Géminard, J.-C., & Vidal, V. (2015). Granular friction: Triggering large events with small vibrations. *Scientific reports*, *5*, 13455.
Latour, S., Schubnel, A., Nielson, S., Madarriaga, R., & Vinciguerra, S. (2013). Characterization of nucleation during laboratory earthquakes. *Geophysical Research Letters*, *40*, 5064–5069. https://doi.org/10.1002/grl.50974
Lengliné, O., Duputel, Z., & Ferrazzini, V. (2016). Uncovering the hidden signature of a magmatic recharge at Piton de la Fournaise volcano using small earthquakes. *Geophysical Research Letters*, *43*, 4255–4262. https://doi.org/10.1002/2016GL068383
Léopoldès, J., Conrad, G., & Jia, X. (2013). Onset of sliding in amorphous films triggered by high-frequency oscillatory shear. *Physical Review Letters*, *110*, 248301.
Levy, C., Mangeney, A., Bonilla, F., Hibert, C., Calder, E. S., & Smith, P. J. (2015). Friction weakening in granular flows deduced from seismic records at the Soufrire Hills Volcano, Montserrat. *Journal of Geophysical Research: Solid Earth*, *120*, 75367557. https://doi.org/10.1002/2015JB012151
Lin, G. W., Chen, H., Hovius, N., Horng, M. J., Dadson, S., Meunier, P., & Lines, M. (2008). Effects of earthquake and cyclone sequencing on landsliding and fluvial sediment transfer in a mountain catchment. *Earth Surface Processes and Landforms*, *33*(9), 1354–1373.
Liu, A., & Nagel, S. (1998). Jamming is not just cool any more. *Nature*, *396*, 21–22.
Marc, O., Hovius, N., Meunier, P., Uchida, T., & Hayashi, S. (2015). Transient changes of landslide rates after earthquakes. *Geology*, *43*(10), 883–886.
Michon, L., Staudacher, T., Ferrazzini, V., BachÀlery, P., & Marti, J. (2007). April 2007 collapse of Piton de la Fournaise: A new example of caldera formation. *Geophysical Research Letters*, *34*, L21301. https://doi.org/10.1029/2007GL031248
Norris, R. D. (1994). Seismicity of rockfalls and avalanches at three cascade range volcanoes: Implications for seismic detection of hazardous mass movements. *Bulletin of the Seismological Society of America*, *84-5*, 1925–1939.
Obermann, A., Planès, T., Larose, E., & Campillo, M. (2013). Imaging preeruptive and coeruptive structural and mechanical changes of a volcano with ambient seismic noise. *Journal of Geophysical Research: Solid Earth*, *118*, 6285–6294. https://doi.org/10.1002/2013JB010399
Peltier, A., Bachèlery, P., & Staudacher, T. (2009). Magma transport and storage at Piton de La Fournaise (La Réunion) between 1972 and 2007: A review of geophysical and geochemical data. *Journal of Volcanology and Geothermal Research*, *184*(1), 93–108.
Peltier, A., Beauducel, F., Staudacher, T., Catherine, P., & Kowalski, P. (2016). Contribution of tiltmeters and extensometers to monitor Piton de La Fournaise activity, *Active volcanoes of the Southwest Indian Ocean*. Springer: Berlin, Heidelberg, pp. 287–303.
Peltier, A., Staudacher, T., Bachèlery, P., & Cayol, V. (2009). Formation of the April 2007 caldera collapse at Piton de La Fournaise volcano: Insights from GPS data. *Journal of Volcanology and Geothermal Research*, *184*(1), 152–163.
Rice, J., & Ruina, A. (1983). Stability of steady frictional slipping. *Journal of Applied Mechanics*, *50*(2), 343–349.
Roult, G., Peltier, A., Taisne, B., Staudacher, T., Ferrazzini, V., Di Muro, A., et al. (2012). A new comprehensive classification of the Piton de la Fournaise activity spanning the 1985–2010 period. Search and analysis of short-term precursors from a broad-band seismological station. *Journal of Volcanology and Geothermal Research*, *241*, 78–104.
Scholz, C. (2002). *The mechanics of earthquakes and faulting* (2nd ed.). New York: Cambridge University Press.
Segall, P., Llenos, A. L., Yun, S.-H., Bradley, A. M., & Syracuse, E. M. (2013). Time-dependent dike propagation from joint inversion of seismicity and deformation data. *Journal of Geophysical Research: Solid Earth*, *118*, 5785–5804. https://doi.org/10.1002/2013JB010251
Sethian, J. A. (1996a). A fast marching level set method for monotonically advancing front. *Proceedings of the National Academy of Sciences*, *93*, 15911595.
Sethian, J. A. (1996b). Theory, algorithms, and applications of level set methods for propagating interfaces. *Acta Numerica*, *5*, 309395.
Sethian, J. A. (1996c). *Level set methods*: Cambridge University Press.
Staudacher, T., Ferrazzini, V., Peltier, A., Kowalski, P., Boissier, P., Catherine, P., et al. (2009). The April 2007 eruption and the Dolomieu crater collapse, two major events at Piton de la Fournaise (La Réunion Island, Indian Ocean). *Journal of Volcanology and Geothermal Research*, *184*(1), 126–137.
Staudacher, T., Peltier, A., Ferrazzini, V., Di Muro, A., Boissier, P., Catherine, P., et al. (2016). Fifteen years of intense eruptive activity (1998–2013) at Piton de La Fournaise Volcano: A review. In P. Bachélery et al. (Eds.), *Active volcanoes of the Southwest Indian Ocean* (pp. 139–170). Berlin Heidelberg: Springer-Verlag.
Stock, G., Collins, B., Santaniello, D., Zimmer, V., Wieczorek, G., & Snyder, J. (2013). Historical rock falls in Yosemite National Park. *U.S. Geological Survey Data Series*, *746*, 17.
Tatard, L., Grasso, J.-R., Helmstetter, A., & Garambois, S. (2010). Characterization and comparison of landslide triggering in different tectonic and climatic settings. *Journal of Geophysical Research*, *115*, F04040. https://doi.org/10.1029/2009JF001624
Vilajosana, I., Surinach, E., Abellán, A., Khazaradze, G., Garcia, D., & Llosa, J. (2008). Rockfall induced seismic signals: Case study in Montserrat, Catalonia. *Natural Hazards and Earth System Sciences*, *8*(4), 805–812.
Voight, B., Young, K. D., Hidayat, D., Subandrio, Purbawinata, Subandrio, Purbawinata, M. A., et al. (2000). Deformation and seismic precursors to dome-collapse and fountain-collapse nuees ardentes at Merapi Volcano, Java, Indonesia, 1994–1998. *Journal of Volcanology and Geothermal Research*, *100*, 261–287.
Westaway, R. M., Lane, S. N., & Hicks, D. M. (2000). The development of an automated correction procedure for digital photogrammetry for the study of wide, shallow, gravel bed rivers. *Earth Surface Processes and Landforms*, *25*(2), 209–226.
Zimmer, V. L., & Sitar, N. (2015). Detection and location of rock falls using seismic and infrasound sensors. *Engineering Geology*, *193*, 49–60.

8 Zusammenfassung und Diskussion der Ergebnisse

> "*Geomorphology, like the rest of geosciences, has always had two major themes: a quest to understand the Earth's history and 'products' – its landscapes and seascapes – and, in parallel, a quest to understand its formative processes.*"
>
> (Tucker, 2012)

Im Rahmen dieser Dissertation wurden zum einen methodische Aspekte der Oberflächenrekonstruktion untersucht, welche Gegenstand von Publikation I sind. Darüber hinaus erfolgte eine Betrachtung von Aspekten der Quantifizierung von Sturzprozessen, die ebenfalls in Publikation I dargestellt sind, sowie in den Publikationen III und IV. Publikation II beschäftigt sich mit der Analyse der reichweitenbeeinflussenden Parameter einzelner Felsblöcke von Sturzprozessen.

Grundlage der Analysen waren sowohl TLS als auch photogrammetrische Daten (terrestrische digitale und terrestrische historische Fotoaufnahmen, Webcam-Daten) mit anschließender Auswertung der daraus generierten Punktwolken, Gelände- und Höhenmodelle und weiteren abgeleiteten Reliefparameter.

Trotz unterschiedlicher Schwerpunktsetzungen in den einzelnen Studien konnten neue Erkenntnisse in der Datenerfassung, -verarbeitung und -anwendung photogrammetrischer Daten zur Analyse von Sturzprozessen an steilen Felswänden sowie zur kombinierten Nutzung von TLS und Photogrammetrie gewonnen und zentrale Fragestellungen beantwortet werden.

Obwohl die Ziele dieser Arbeit mit den angewandten Methoden erreicht wurden, sind einige Limitationen und Faktoren bei der Betrachtung der Ergebnisse zu beachten.

Auch wenn die wichtigsten Ergebnisse der Untersuchungen bereits Gegenstand der Diskussion in den entsprechenden Publikationen gewesen sind, sollen sie im Folgenden im Sinne einer untersuchungsübergreifenden Diskussion zusammengefasst werden.

8.1 Methodische Schwerpunkte

Sowohl der Stand der Forschung als auch die Ergebnisse der einzelnen Publikationen verdeutlichen, dass insbesondere Sturzprozesse an steilen Felshängen aufgrund der Aufnahmegeometrie besonders gut mit TLS erfasst werden können. Ein weiterer Vorteil von TLS ist die Generierung multitemporaler Datensätze mit frei festlegbaren Aufnahmeintervallen, die neben einer räumlichen auch eine zeitliche Differenzierung der Prozessdynamik ermöglichen (Carrivick, et al., 2013).

Für eine verlässliche Aussage über die Frequenz-Magnituden-Beziehung von Sturzprozessen und für die Rekonstruktion der Felsoberfläche sind Daten über mehrere Jahrzehnte erforderlich. Der Beobachtungszeitraum ist in der Regel zu kurz für eine vollständige Erfassung der Prozessdynamik alpiner Felshänge. Außerdem verwenden viele Studien zeitlich zu gering aufgelöste Datensätze (Abellán, et al., 2011; Strunden, et al., 2015; Kenner, 2019).

Werden Sturzereignisse in zu großen zeitlichen Abständen erfasst, besteht die Gefahr, dass mehrere kleinere Prozesse als ein einziges Ereignis interpretiert werden, was zu einer Verzerrung der Magnitude-Frequenz-Verteilung führt (Williams, et al., 2019). Dies beeinträchtigt insbesondere die realistische Einschätzung der häufigsten und größten zu erwartenden Ereignisse, da kleinvolumige Prozesse systematisch unterrepräsentiert bleiben (Williams, et al., 2019). Zudem ist zu berücksichtigen, dass Extremereignisse nicht erfasst werden können.

Eine direkte Messung von Sturzprozessen ist durch eigene Daten aufgrund der geringen Frequenz und Unvorhersehbarkeit in der Regel nicht möglich oder nur zufällig. Während TLS sowie aktuelle photogrammetrische Aufnahmen Oberflächenveränderungen lediglich über kurze Untersuchungszeiträume erfassen, ermöglichen historische Fotodatensätze, die ebenfalls auf den Prinzipien der Photogrammetrie ausgewertet werden, Oberflächenrekonstruktionen mit weitreichenden Zeitreihen.

Die Herausforderung bei historischen Fotografien besteht darin, dass der Zeitpunkt der Aufnahme bereits vorgegeben ist und nicht individuell nach eigenem Ermessen gewählt werden kann. Bei den historischen Fotos der Drei Zinnen stellte sich die Suche als herausfordernd dar. Zwar wurde eine Vielzahl von Fotos aus der Vergangenheit gefunden, doch ihre Qualität war häufig für die photogrammetrische Datenprozessierung ungeeignet, weshalb schließlich die Entscheidung auf einen einzigen Jahrgang fiel. Jedoch ist es nach intensiver Datenprozessierung erfolgreich gelungen, Oberflächenveränderungen für zwei Bereiche der Felswände von 1970 bis 2018 zu quantifizieren. Nach derzeitigem Kenntnisstand gibt es keine weiteren Arbeiten, die mit diesen Methoden historische terrestrische Fotografien zur Quantifizierung von Oberflächenveränderungen nutzen.

Eine Einschränkung bei der Analyse und dem Vergleich der Ergebnisse stellt die unterschiedliche Dauer der Beobachtungszeiträume dar. So umfasst diese für die Untersuchungen an den Drei Zinnen einen Zeitraum von 48 Jahren, während für La Réunion Beobachtungszeiträume von sechs beziehungsweise vier Jahren vorliegen (Tabelle 6).

Tabelle 6. Zusammenfassende Übersicht der Untersuchungsgebiete Drei Zinnen und La Réunion, einschließlich der angewandten Methoden, Zeiträume, Volumenveränderungen im Untersuchungszeitraum sowie der Genauigkeiten und der Datenprozessierung.

Paper	Untersuchungsgebiet	Methode	Zeitraum	Dauer [Jahre]	Volumina [m^3]	ICP [m]	LoD [m]
I	Drei Zinnen	TLS SfM: historische terrestrische Fotoaufnahmen & aktuelle terrestrische Fotoaufnahmen	1970-2018	48	-101,28 -1872,87	0,89 1,08	0,9159 0,8628
III	La Réunion	TLS SfM: Webcams & aktuelle terrestrische Fotoaufnahmen	2010-2016	6	18.606 2.921 2.955 20.430	0,007 0,013	0,8
IV	La Réunion	TLS SfM: aktuelle terrestrische Fotoaufnahmen	2014-2016	2	~80.000	0,007 0,013	0,74

Derrien et al. (2018) konnten mit terrestrischen SfM zwar Oberflächenveränderungen im Krater Dolomieu im Zeitraum von 2008 bis 2015 mit einem Volumen von 1,7–1,9 x 10^6 m^3 quantifizieren, jedoch keine einzelnen Prozesse identifizieren. Einzige Ausnahme war ein größerer Prozess mit einem Volumen von 44,2–51,4 x 10^3 m^3 innerhalb von fünf Monaten. Auch wenn sowohl die Untersuchungen in Publikation III und IV als auch die von Derrien et al. (2018) zeigen, dass auf La Réunion Oberflächenveränderungen von großer Magnitude messbar sind, besteht dennoch die Gefahr, dass solche großdimensionierten Prozesse kleinere überlagern und somit deren Erfassung erschwert oder verhindert wird.

Prozesse mit geringerer Frequenz konnten in den durchgeführten Analysen (Publikation I, III) nicht erfasst werden, was auf die unzureichende zeitliche Auflösung der Datensätze zurückzuführen ist. Trotzdem zeigen die beiden Publikationen, dass sowohl die Bearbeitung historischer terrestrischer Fotoaufnahmen als auch webcambasierte Datensätze mit einem signifikanten Aufwand verbunden ist, um Ungenauigkeiten so gut wie möglich zu reduzieren. Dennoch verbleiben bei der Verarbeitung stets gewisse Unsicherheiten und Fehler. Die LoD-Werte für die Drei Zinnen betragen 0,92 m und 0,86 m, während für La Réunion Werte von 0,8 m und 0,74 m ermittelt wurden (Tabelle 6). Damit befindet sich der LoD der webcambasierten Datensätze für den Zeitraum von 2010 bis 2016 in einem vergleichbaren Bereich wie jener der übrigen erhobenen Daten. Gleichzeitig wird jedoch deutlich, dass der LoD stark von der jeweils eingesetzten Datenquelle beeinflusst wird. So weisen die aus Webcamaufnahmen gewonnenen Daten signifikant höhere Unsicherheiten auf als terrestrische Fotografien und TLS-Daten (siehe Publikation III, Tabelle 4). Guerin et al. (2020) erhalten in ihren Untersuchungen geringere LoD-Werte von 0,18 und 0,34 m für den Zeitraum 1976 bis 2010.

Insbesondere in solchen Gebieten wie auf La Réunion ist die Installation stationärer Kamerasysteme, wie beispielsweise Webcams, sinnvoll, um die Dynamik der Prozesse in detaillierter Weise zu erfassen und um Überlagerungen in der Datenauswertung zu vermeiden. Dies gilt vor allem für geomorphologisch aktive Regionen mit hoher seismischer Aktität, wie sie für La Réunion charakteristisch ist. Durch die Verwendung von Webcam-Daten ist ebenfalls eine visuelle Suche nach Prozessen und eine Eingrenzung des Zeitraums möglich.

Für die Installation müssen jedoch bestimmte Voraussetzungen erfüllt sein, um eine spätere Datenauswertung zu gewährleisten:

- Kamerakalibrierung: Kalibrierungsparameter wie Brennweite, Verzerrungskoeffizienten und optische Achsen sollten bekannt sein. Dadurch kann eine Verzerrung aufgrund der Objektivgeometrie vermieden werden. Falls diese Parameter nicht bekannt sind, verfügt Metashape Pro über eine interne Autokalibrierungsfunktion.
- Stabile Positionierung: Eine stabile und feste Installation ist zu gewährleisten, um die Bildqualität nicht zu beeinträchtigen.
- Blickwinkel: Für eine photogrammetrische Auswertung sind mindestens zwei Kamerasysteme essenziell. Es wird jedoch eine höhere Anzahl von Fotos für die Prozessierung empfohlen (Smith, et al., 2016). Der Winkel der Kameras zueinander sollte > 25–30° sein. Andernfalls ist es nicht möglich, gemeinsame korrespondierende Bildpunkte zu finden. Außerdem ist darauf zu achten, dass die beiden Kameras über ausreichend Bildüberlappung (nicht < 40 %) verfügen (Eltner, et al., 2016; Smith, et al., 2016). Dies ist wichtig, um die entsprechenden Bildmerkmale in den Fotos zu identifizieren. So können die einzelnen Fotos später zugeordnet werden.
- Referenzpunkte: Um eine Georeferenzierung der Daten durchzuführen, werden Kontrollpunkte verwendet, die entweder festinstalliert im Untersuchungsgebiet vorhanden sind oder aus einem TLS-Datensatz extrahiert werden können. Da jedoch nicht in allen Untersuchungsgebieten die Installation von festen Kontrollpunkten möglich ist, sind zusätzlich beispielsweise TLS-Daten erforderlich.
- Kameraeigenschaften: Die eingesetzten Kamerasysteme sollten eine hohe Bildauflösung bieten. Zudem ist auf stabile Beleuchtungsverhältnisse zu achten, obwohl dies nicht immer garantiert werden kann, da es auf La Réunion beispielsweise aufgrund des Sonnenstandes zu extremen Schattenverhältnissen im Krater kommen kann. Des Weiteren müssen die Geräte gegen externe Umwelteinflüsse wie Feuchtigkeit oder starke Temperaturschwankungen geschützt sein. Für eine zuverlässige Datenauswertung ist zudem eine konstante Datenrate sowie eine sichere Speicherung der Daten unerlässlich.

Während TLS und photogrammetrische Verfahren eine präzise räumliche Erfassung von Oberflächenveränderungen ermöglichen, erweitern seismische Messungen das methodische Spektrum um eine zeitlich hochauflösende Detektion von Sturzprozessen. Auch wenn die quantifizierten Oberflächenveränderungen mit den beiden Verfahren nicht übereinstimmen, liefert die Interpretation der seismischen Aufzeichnungen geomorphologische Informationen, die eine differenzierte Erklärung der Prozessdynamik ermöglicht.

Die Ablagerung von Sturzprozessen und deren räumliche Verteilung dienen als Art Stellvertretergröße für eine Bewertung der Aktivität von Sturzprozessen. Durch aufwändige manuelle Vermessung der einzelnen abgelagerten Gesteinsblöcke in der Punktwolke, können Informationen über die Form und Größe der Blöcke gewonnen werden. Dies ist sehr zeitaufwendig, ermöglicht aber die Ableitung genauer Parameter. Voraussetzung dafür sind jedoch räumlich hochaufgelöste Daten, wie sie TLS bietet.

Es kann nur der aktuelle Zustand der einzelnen Blöcke gemessen werden. Informationen aus der Zeit vor dem Aufprall oder aus möglichen Kontaktreaktionen von davor sind nicht verfügbar.

Messenzehl & Dikau (2017) und Messenzehl et al. (2018) verwenden im Gegensatz zu der Blockvermessung in Publikation II ausgewählte Transekte in ihren Untersuchungshängen und vermessen die Blöcke vor Ort im Gelände. Der Vorteil der Verwendung von Punktwolken besteht darin, dass anschließend zusätzliche Reliefparameter wie beispielsweise die Rauigkeit abgeleitet und weitergehende Analysen durchgeführt werden können. Außerdem ist die Punktwolke jederzeit verfügbar.

Wie viele andere Studien analysieren auch Caviezel et al. (2019) die Trajektorien in einem einzigen Untersuchungsgebiet und verwenden in ihrer Arbeit dafür normierte Blöcke. Solche Analysen sollten auf andere Gebiete und vor allem auf unterschiedliche Blöcke bezüglich Größe und Form ausgeweitet werden.

8.2 Geomorphologische Schwerpunkte

Nach der Diskussion der methodischen Aspekte dieser Arbeit sollen im Folgenden die neuen Erkenntnisse und Möglichkeiten, die sich aus der geomorphologischen Prozessforschung hinsichtlich des Einsatzes von TLS und terrestrischer Photogrammetrie ergeben, aufgezeigt werden.

Neben der Quantifizierung und Rekonstruktion von Sturzprozessen sind Analysen der beteiligten Faktoren von entscheidender Bedeutung. Dafür wurden in vier Untersuchungsgebieten mit unterschiedlichen lithologischen Bedingungen eine morphometrische Analyse von Blockgröße und -form sowie Schuttkegeleigenschaften durchgeführt (Publikation II). Im Gegensatz zu den Fragestellungen in Publikation II sind diese nur in wenigen anderen Arbeiten Gegenstand der Analysen (Azzoni & de Freitas, 1995; Haas, et al., 2012; Fityus, et al., 2013) und beschränken sich in der Regel auf einzelne Untersuchungsflächen oder werden unter Laborbedingungen durchgeführt (Okura, et al., 2000; Glover, et al., 2015; Cui, et al., 2017; Wang, et al., 2018; Gratchev & Saeidi, 2019; Caviezel, et al., 2021).

Es ist jedoch anzumerken, dass die vermessenen Blöcke in den Gebieten der Gampenalm und der Dreitorspitze eindeutig spezifischen Sturzprozessen zugewiesen werden können, wohingegen eine derartige Zuordnung für die Standorte Piton de la Fournaise und Zwieselbachtal nicht möglich ist.

Die Untersuchungsergebnisse in Publikation II zeigen einen Zusammenhang zwischen der Lithologie und der Charakteristik der Gesteinsblöcke hinsichtlich ihrer Reichweite innerhalb der ausgewählten Testgebiete. Zudem verdeutlichen sie eine komplexe Wechselwirkung zwischen der Blockgröße und -form in Bezug auf die Reichweite der abgelagerten Blöcke (Abbildung 5, Abbildung 6). Unter den verschiedenen lithologischen Bedingungen lassen sich deutliche Unterschiede erkennen.

In den durch Dolomit und Wettersteinkalk charakteristischen Gebieten (Gampenalm und Dreitorspitze) finden sich größere Gesteinsblöcke, was auf die bankige Schichtung des Gesteins zurückzuführen ist. Im Gegensatz dazu wurde bei den metamorphen Gesteinen (Zwieselbachtal, Piton de la Fournaise), insbesondere dem Gneis, vor allem eine größere Häufigkeit kleinerer Gesteinsgrößen erfasst, was durch die plattige Struktur dieses Materials erklärbar ist.

Auch hinsichtlich der Blockform sind deutliche Unterschiede festzustellen. Die Untersuchungsgebiete zeigen eine große Variabilität an Blockformen, die von gleichförmig, eher länglichen (Zwieselbachtal) Gesteinsblöcken bis hin zu unregelmäßig geformten Blöcken reichen. Die meisten quaderförmigen Blöcke wurden am Piton de la Fournaise nachgewiesen. Ob diese Ausprägung auf die spezifische Lithologie oder auf tektonische Beanspruchungen infolge der ausgeprägten seismischen Aktivität und der damit verbundenen Kluft- und Spaltenbildung zurückzuführen ist, kann auf der Grundlage der in dieser Studie erhobenen Daten nicht abschließend beurteilt werden.

Im Vergleich zu anderen Studien (Whitehouse & McSaveney, 1983; Jomelli & Francou, 2000; Sanders et al., 2009; Luckman, 2013; Messenzehl & Dikau, 2017; Popescu et al., 2017) konnte die Theorie der gravitativen Sortierung weder bestätigt noch widerlegt werden, da kein eindeutiger Zusammenhang zwischen Blockgröße und Reichweite nachgewiesen werden konnte. Dennoch lässt sich in Übereinstimmung mit anderen Arbeiten (Meißl, 1998; Haas et al., 2012; Glover et al., 2015; Messenzehl & Dikau, 2017) die Annahme treffen, dass die Blockgröße nicht die einzige Variable ist, die die Reichweite der Blöcke beeinflusst. Vielmehr zeigt sich, dass das Achsenverhältnis der Blöcke einen entscheidenen Einfluss auf ihre Reichweite hat (Publikation II). Die Ergebnisse belegen, dass in zwei Untersuchungsgebieten die Ablagerung der Gesteinsblöcke vom Achsenverhältnis bestimmt wird (Gampenalm und Dreitorspitze). Mit abnehmender Spherizität nimmt dort die Reichweite ab. Gleichzeitig zeigen die Auswertungen auch, dass Blöcke mit größerem Achsenverhältnis kürzere Reichweiten aufweisen (Abbildung 6). Darüber hinaus wurde für das Untersuchungsgebiet Gampenalm festgestellt, dass Blöcke mit einem geringen Achsenverhältnis tendenziell eine größere Reichweite aufweisen und zugleich ein Anstieg des Blockvolumens zu beobachten ist (Abbildung 6).

Eine mögliche Erklärung hierfür kann sein, dass es bei großvolumigen Sturzprozessen zu Kollisionen zwischen einzelnen Blöcken kommt, wodurch Bewegungsenergie dissipiert wird oder eine Fragmentierung in kleinere Gesteinsblöcke erfolgt. In der Folge können unterschiedliche Blockformen sowohl im oberen als auch im unteren Bereich des Schuttkegels abgelagert werden (Ruiz-Carulla & Jordi, 2020).

Im Untersuchungsgebiet Dreitorspitze fällt auf, dass Blöcke mit einem geringen Achsenverhältnis größere Reichweiten erzielen und nicht im oberen, kürzeren Hangabschnitt zur Ablagerung kommen. Eine mögliche Erklärung hierfür bieten die Ergebnisse von Glover et al. (2015), die in ihren Untersuchungen darlegen, dass plattige Gesteinsblöcke nur dann weite Distanzen zurücklegen können, wenn sie sich um ihre kurze Achse rotieren und dadurch eine radähnliche Bewegungsform annehmen. Dieser Zusammenhang konnte jedoch nicht auf die beiden anderen Untersuchungsgebiete übertragen werden, in denen Blöcke mit allen Achsenverhältnissen über alle Bereiche der Schutthalden verteilt wurden (Abbildung 5). Abschließend bestätigen auch die Ergebnisse der Analysen von Messenzehl & Dikau (2017), dass die Spherizität der Gesteinsblöcke mit zunehmender Hangabwärtsrichtung zunimmt.

Ein weiterer möglicher Grund für das Ausbleiben der gravitativen Sortierung liegt in der komplexen Prozessinteraktion auf den Schutthalden. Insbesondere in den Untersuchungsgebieten Piton de la Fournaise und Zwieselbachtal, deren Ablagerungen keinem alleinigen Sturzprozess zugeordnet werden können, muss die Interaktion mit Murablagerungen und Schwemmakkumulationen berücksichtigt

werden. Da Murablagerungen eine grobblockige und ungeordnete Struktur aufweisen, erhöht das Auftreffen von Gesteinsblöcken auf solchen Ablagerungen die Wahrscheinlichkeit eines kinetischen Energieverlusts. Infolgedessen verkürzt sich die Reichweite der einzelnen Blöcke. Außerdem können Levees als natürliche Barrieren wirken, welche die Trajektorien der Gesteinsblöcke beeinflussen. Schwemmakkumulationen können den Reibungswiderstand der Halde vermindern. Durch die geringere Neigung im Vergleich zu Schutthalden, kann die reduzierte Hangabtriebskraft eine frühzeitigere Ablagerung begünstigen.

Über die lithologischen Parameter hinaus muss die Hangtopographie, insbesondere die Steilheit der Schutthalden, als weiterer Einflussfaktor für die Reichweitenanalyse berücksichtigt werden. Mit zunehmender Hangneigung verringert sich die der Bewegung entgegenwirkende Reibungskomponente, was an steilen Schutthalden wie am Piton de la Fournaise (36°) die Beibehaltung der kinetischen Energie und somit potenziell größeren Reichweiten begünstigt (Wegner, et al., 2021). Im Gegensatz dazu führen flachere Hangabschnitte wie die Gampenalm (32°) oder das Zwieselbachtal (29°) zu einem verstärkten Energieentzug durch Reibung und Kollisionen (Wegner, et al., 2021).

Die räumliche Rauigkeitsanalyse auf Basis der TLS-Punktwolken weist zudem eine gute Übereinstimmung mit der Einzelblockanalyse hinsichtlich der Abhängigkeiten zwischen Reichweite und Rauigkeit auf.

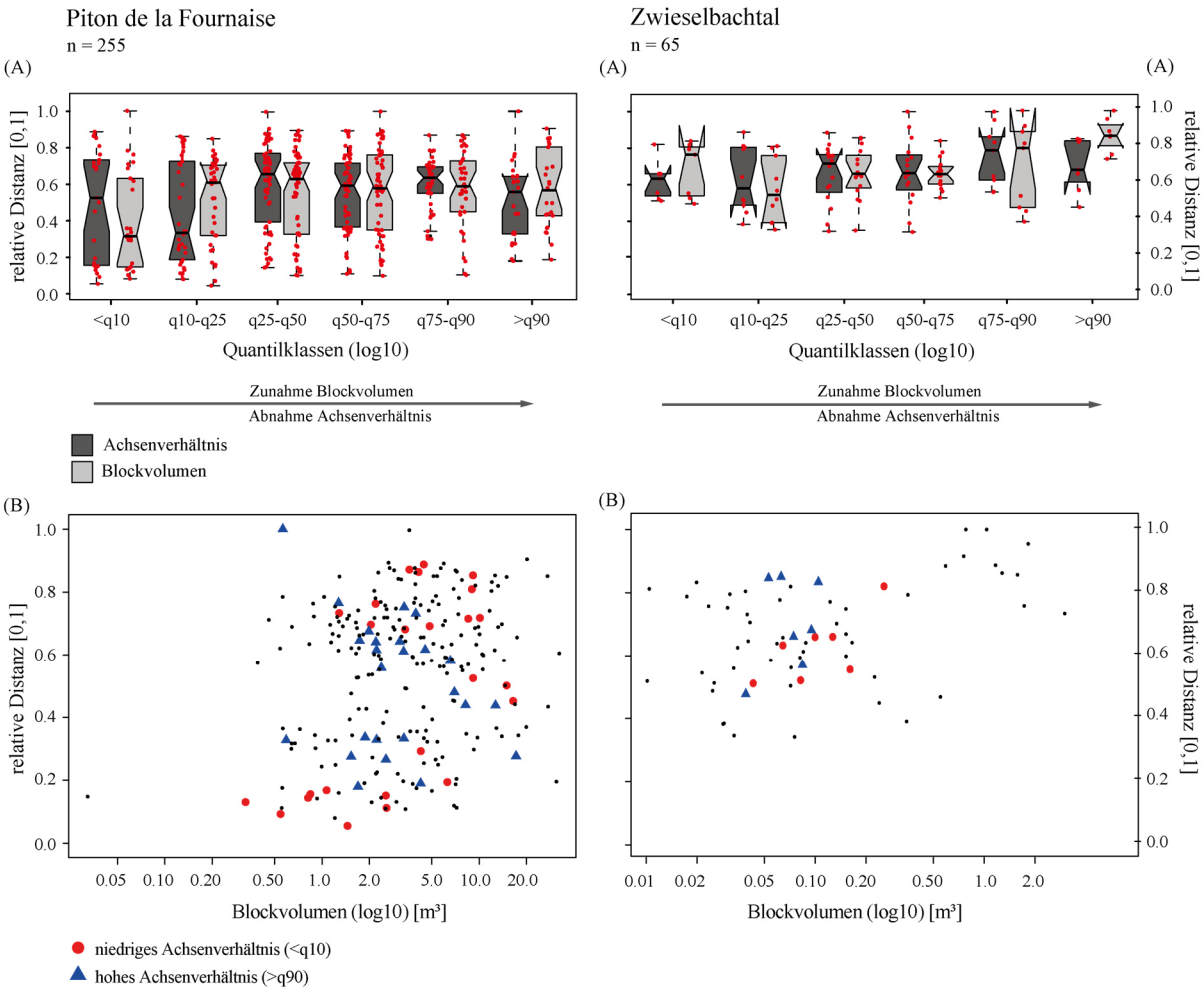

Abbildung 5. Die Boxplots zeigen den relativen Abstand der log10-Blockvolumina und log10-Blockformen der gemessenen Gesteinsblöcke für die beiden Untersuchungsflächen Piton de la Fournaise und Zwieselbachtal (A). Jeder rot eingefärbte Punkt entspricht einem einzelnen gemessenen Block (A). (B) zeigt jeweils das Streudiagramm der relativen Distanz in Abhängigkeit vom log10-Blockvolumen. Blöcke mit niedrigem (< q10) und hohem (> q90) Achsenverhältnis sind durch unterschiedliche Farben und Symbole gekennzeichnet (verändert nach Wegner, et al., 2021).

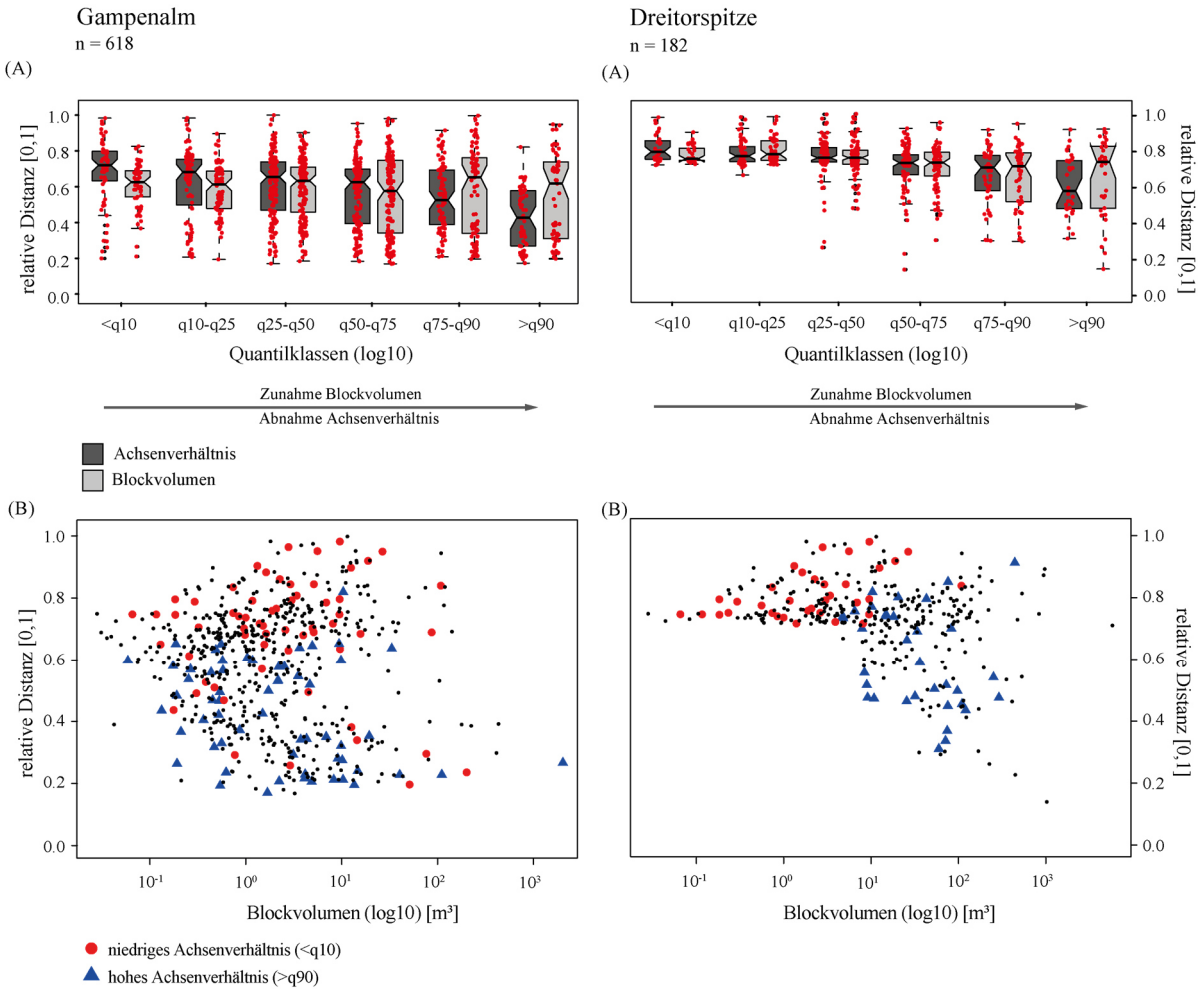

Abbildung 6. Die Boxplots zeigen den relativen Abstand der log10-Blockvolumina und log10-Blockformen der gemessenen Gesteinsblöcke für die beiden Untersuchungsflächen Gampenalm und Dreitorspitze (A). Jeder rot eingefärbte Punkt entspricht einem einzelnen gemessenen Block (A). (B) zeigt jeweils das Streudiagramm der relativen Distanz in Abhängigkeit vom log10-Blockvolumen. Blöcke mit niedrigem (< q10) und hohem (> q90) Achsenverhältnis sind durch unterschiedliche Farben und Symbole gekennzeichnet (verändert nach Wegner, et al., 2021).

Neben der Reichweitenanalyse (Publikation II), welche den Einsatz hochauflösender TLS-Daten für einen geeigneten Einsatz demonstriert, widmen sich Publikation I, III und IV dieser Dissertation hochauflösenden, multitemporalen Geländemodellen, die aus LiDAR und SfM Photogrammetrie generiert werden.

Anders als in anderen Studien, die sich ausschließlich auf Geländemodelle aus luftgestützten historischen Fotoaufnahmen zur Analyse langfristiger Veränderungen stützen (Ravanel & Deline, 2008; Ravanel & Deline, 2010; Guerin, et al., 2020), ermöglichte der hier verfolgte Ansatz die Einbeziehung weiterer historischer terrestrischer Fotodaten in die Auswertung.

Die in Publikation I durchgeführte Analyse dokumentierte zwei große Bereiche mit Oberflächenveränderungen an den Drei Zinnen mit Volumenänderungen von -101,28 m^3 an der Großen Zinne und -1.872,87 m^3 an der Westlichen Zinne im Zeitraum zwischen 1970 und 2018 (Abbildung 7 & Abbildung 8).

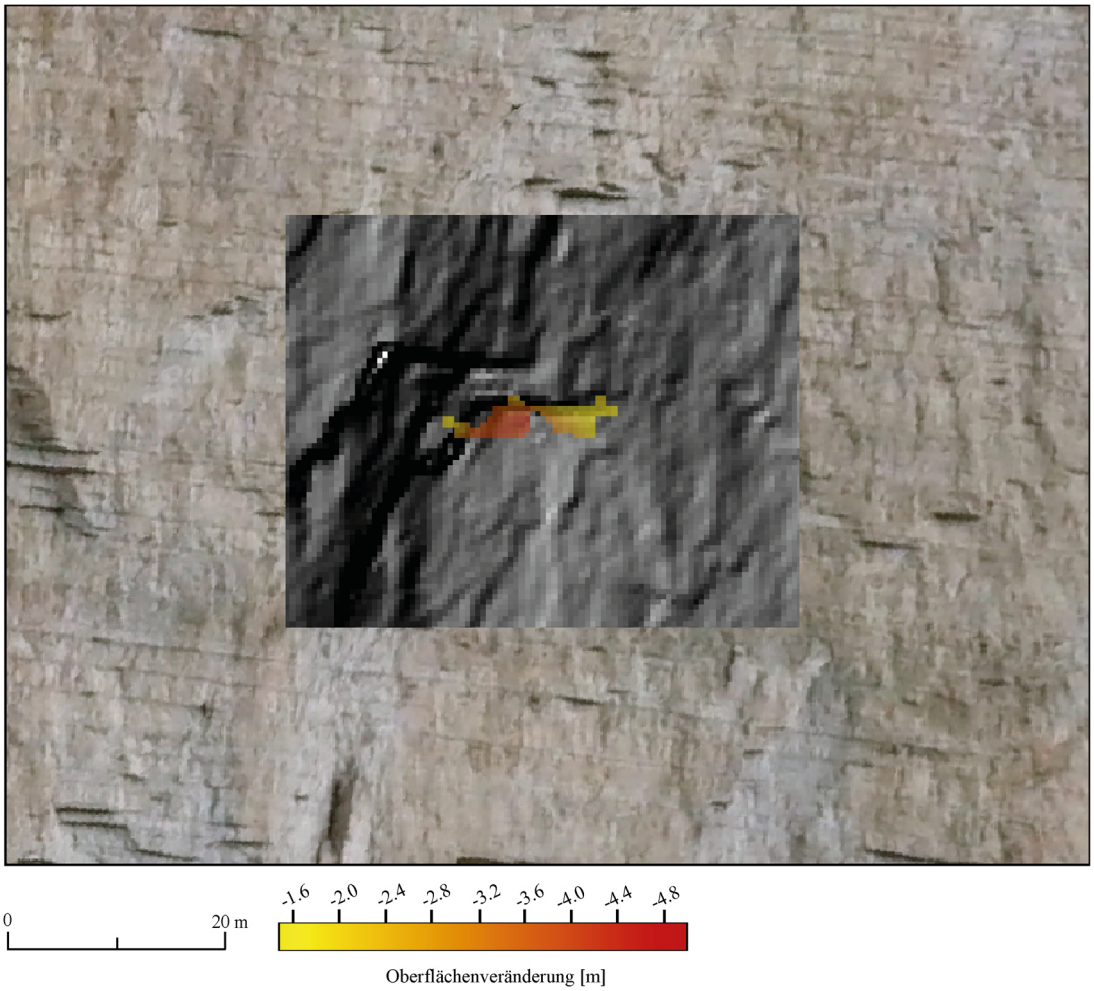

Abbildung 7. DoD für den Beobachtungszeitraum 1970–2018 der Großen Zinne (Drei Zinnen, Italien) mit einem terrestrischen digitalen Foto von 2018 und einem analytical hillshade. Blick nach Süden (verändert nach Wegner, et al., 2023).

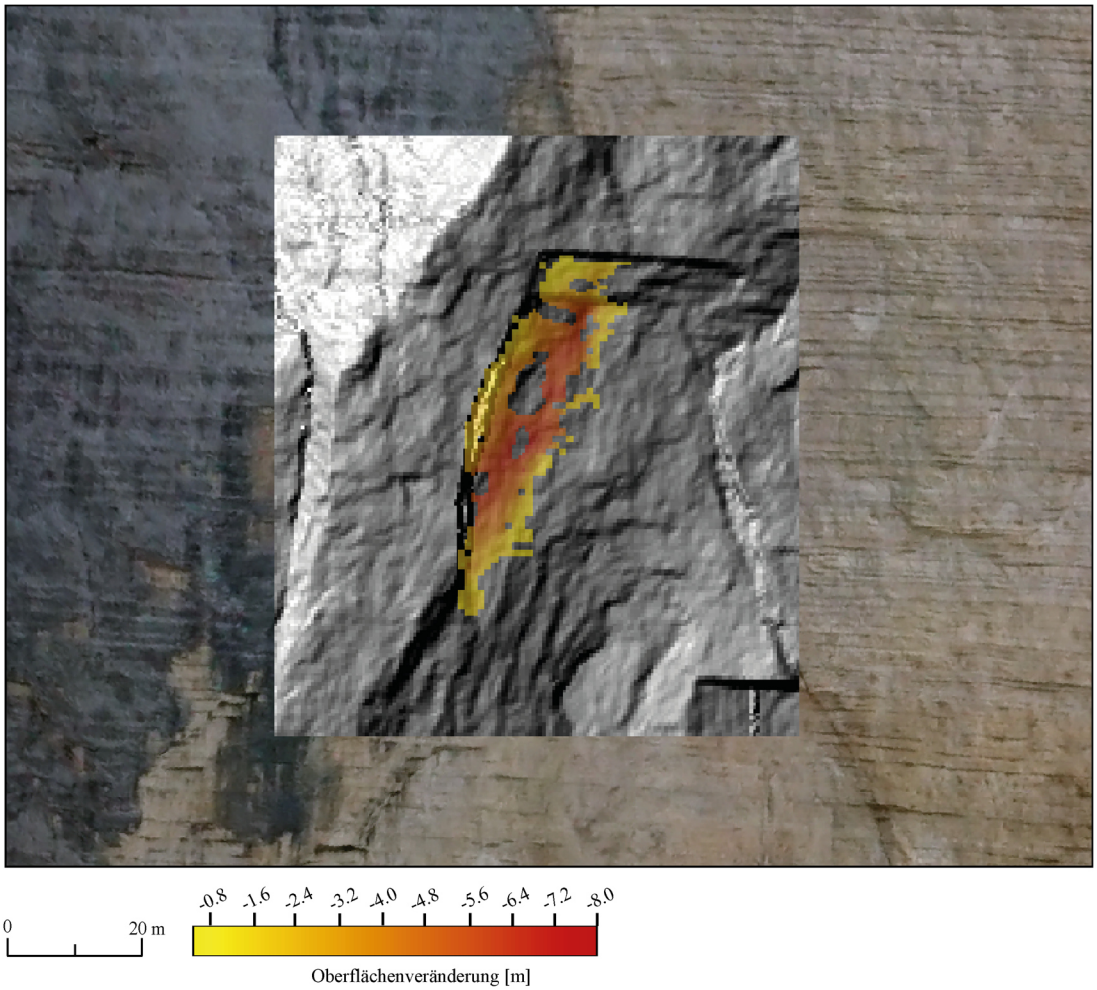

Abbildung 8. DoD für den Beobachtungszeitraum 1970–2018 der Westlichen Zinne (Drei Zinnen, Italien) mit einem terrestrischen digitalen Foto von 2018 und einem analytical hillshade. Blick nach Süden (verändert nach Wegner, et al., 2023).

In ihren Untersuchungen berechnen Guerin et al. (2020) mehrere Oberflächenveränderungen über einen Zeitraum von 41 Jahren mit Volumina, die von -93 m^3 bis -3.883 m^3 variieren. Auch an der zweiten Untersuchungsfläche reichen die Volumina von mindestens -31 m^3 bis maximal -20.193 m^3. Ihre Ergebnisse zeigen ebenfalls eine ähnlich große Streuung wie die der vorliegenden Arbeit. Bei der Betrachtung ihrer Ergebnisse fällt auf, dass vor allem historische Sturzereignisse größere Volumina an Oberflächenveränderungen aufweisen als jüngere Ereignisse, mit wenigen Ausnahmen (Guerin, et al., 2020). Dies lässt sich durch die geringe zeitliche Auflösung historischer fotografischer Datensätze erklären. Die Abstände zwischen den Aufnahmezeitpunkten betragen oft mehrere Jahre oder Jahrzehnte, wodurch die zeitliche Differenzierung einzelner Ereignisse nicht möglich ist (Williams, et al., 2019).

Für die Einordnung der Ergebnisse an den Drei Zinnen ist es daher empfehlenswert, weitere Untersuchungsgebiete in den Dolomiten auszuwählen, um eine lange Zeitreihe unter Verwendung historischer terrestrischer Fotografien einzubeziehen.

Im Vergleich zu den Ergebnissen auf La Réunion zeigen sich dort deutlich größere Volumenveränderungen. Dennoch ist bemerkenswert, dass die Sturzprozesse in diesem geomorphologisch hochaktiven Gebiet ein weites Größenspektrum aufweisen. Diese deutliche Volumenvariabilität kann mit den

verschiedenen Phasen der seismischen Aktivität des Vulkans Piton de la Fournaise in Verbindung gebracht werden. So wurden in den seismisch stabilen Jahren 2010–2011 und 2011–2012 nur geringe Oberflächenveränderungen festgestellt (Publikation IV), wohingegen die auffälligen Ablagerungen im Zeitraum 2012–2014 auf starke Niederschläge und die Einwirkung zweier Zyklone Anfang 2013 zurückgeführt werden konnten (Durand, et al., 2023). Diese linearen Strukturen, die auf fluviale Ablagerungsprozesse hindeuten, konnten auf der einen Untersuchungsfläche im Krater visuell festgestellt werden.

Obwohl die Oberflächenveränderungen der in Publikation IV untersuchten Flächen ab 2014 abnahmen, konnten auf einer Untersuchungsfläche eine Veränderung von ca. 80.000 m^3 quantifiziert werden. Dieses Gebiet wird allerdings nicht durch die Webcams erfasst. Auch Derrien et al. (2018) berechneten für diesen Bereich des Kraters zwischen 2015 und 2016 große Volumenänderungen von $47{,}8 \pm 3.6 \times 10^3$ m^3.

In anderen vulkanischen Untersuchungsgebieten wie dem Telica (Nicaragua) wurden für einen vergleichbaren Untersuchungszeitraum von sechs Jahren mittels UAV Oberflächenveränderungen von 8.400–140.000 m^3 quantifiziert (Hanagan, et al., 2020) , die deutlich über den gemessenen maximalen Volumenveränderungen in Publikation IV liegen. Im Gegensatz dazu zeigen UAV-basierte Ergebnisse am Vulkan Stromboli (Italien) für einen Zeitraum von nur sechs Monaten sehr geringe Oberflächenveränderungen von 9,7 m^3 und 21,5 m^3 (Gracchi, et al., 2022). Pesci et al. (2011) quantifizierten in ihren Untersuchungen am Krater des Vesuvs (Italien) mithilfe von TLS Oberflächenveränderungen von 20.300 m^3 über einen Zeitraum von vier Jahren. Ihre Volumenberechnungen sind mit den berechneten Werten für zwei Gebiete in Publikation III vergleichbar. Diese Unterschiede verdeutlichen, dass die gemessenen Oberflächenveränderungen stark von den jeweils dominierenden geomorphologischen Prozessen sowie von auslösenden Faktoren wie seismischer Aktivität oder intensiven Niederschlagsereignissen beeinflusst werden.

Obwohl die in Publikation IV dargestellten Ergebnisse der Photogrammetrie und Seismik hinsichtlich der Oberflächenveränderungen nicht übereinstimmen, lässt sich diese Diskrepanz durch eine Absenkung im betreffenden Kraterbereich erklären, die seismisch nicht erfassbar ist. Ein zusätzliches Indiz für diesen Prozess stellt das Fehlen eines zugehörigen Ablagerungsbereichs dar (Durand, et al., 2018).

Der Einfluss externer Faktoren wie Niederschlag zeigt sich darin, dass Regenereignisse sowohl die Häufigkeit als auch das Volumen von Sturzprozessen verstärken können. Dabei wirkt sich seismische Aktivität tendenziell stärker auf das Volumen der Ereignisse aus. Zudem begünstigt die Kombination aus seismischen Erschütterungen und Niederschlägen die Ausbildung von Rissen im stark zerklüfteten Gesteinsmaterial, was die Hangstabilität weiter reduziert, und großvolumige Sturzprozesse begünstigen kann.

Die Untersuchungen am Piton de la Fournaise sind besonders lohnend, da es sich im Vergleich zu anderen Vulkankratern oder vor allem den Alpen um eine sehr junge geomorphologische Formung handelt. Da der Einsturz des Kraters im Jahr 2007 stattfand, begann die Auswertung der verwendeten Daten erst vier Jahre später.

9 Fazit und Ausblick

> "*Creating a new theory is not like destroying an old barn and erecting a skyscraper in its place. It is rather like climbing a mountain, gaining new and wider views, discovering unexpected connections between our starting points and its rich environment. But the point from which we started out still exists and can be seen, although it appears smaller and forms a tiny part of our broad view gained by the mastery of the obstacles on our adventurous way up.*"
>
> (Einstein & Infeld, 1938)

Die vorangegangene Diskussion und die Darstellung der Ergebnisse innerhalb der verschiedenen Publikationen zeigen bereits, dass die Untersuchung der Instabilität von Felshängen mit spezifischen und praktischen Problemen verbunden ist. Diese können weder durch eine einzige Methode oder Technik noch durch einen einzigen Erklärungsansatz gelöst werden. Aus der Synthese der Ergebnisse der einzelnen Publikationen ergibt sich eine Vielzahl von einzelnen Ansatzpunkten für die weiteren Forschungsarbeiten, die sich sowohl auf methodische als auch auf prozessgeomorphologische Aspekte beziehen.

Wie eingangs bereits erläutert, ist das Verständnis in der geomorphologischen Prozessforschung unter anderem darauf ausgelegt, die einzelnen beeinflussenden Faktoren besser zu verstehen. Diese geomorphologischen Formen und die mit ihnen verbundenen Prozesse bilden sich in der Regel über lange Zeiträume und unter dem Einfluss einer Vielzahl von Faktoren. Außerdem unterliegen die räumlichen und zeitlichen Prozesse sowie ihre Intensität teilweise starken Schwankungen.

Mit dem eingesetzten und teilweise kombinierten Einsatz der Methoden des TLS und der digitalen Photogrammetrie auf Basis von zum Teil historischen terrestrischen Fotoaufnahmen und webcambasierten Daten wurden Sturzprozesse sowohl über längere als auch über kurze Zeiträume erfolgreich analysiert und quantifiziert.

Zukünftige Forschungsarbeiten sollten das Potenzial des Monoplottings evaluieren, das eine zweidimensionale Kartierung der Prozessareale ermöglicht (Altmann, et al., 2023). Die kartierten Veränderungen könnten in einem nächsten Schritt zur Abschätzung des Volumens auf der Grundlage aktueller hochauflösender Höhenmodelle (LiDAR) verwendet werden.

Es hat sich außerdem gezeigt, dass die Kombination verschiedener Fernerkundungsmethoden, wie beispielsweise TLS mit SfM-MVS, von Vorteil ist, um etwa Datenlücken oder komplexe Oberflächentopographien zu rekonstruieren. Diese Fusion ist auch hilfreich, um Sturzprozesse in geomorphologisch

hochaktiven Gebieten zu quantifizieren. Zudem ermöglichen hochfrequente Messungen eine bessere Unterscheidung zwischen einzelnen geomorphologischen Prozessen, die sich über längere Zeiträume hinweg überlagern.

Um für eine Gefahrenanalyse die Reichweite der einzelnen Blöcke zu analysieren, sollte für zukünftige Arbeiten die Rauigkeit als ein Proxy für die Blockgröße aus Punktwolkendaten ermittelt werden. Dies ermöglicht es, eine größere Anzahl von Untersuchungsflächen in unterschiedlichen lithologischen Bedingungen auszuwerten und den Zusammenhang von Reichweite und Eigenschaften der Felsblöcke weiter zu untersuchen.

Literaturverzeichnis

Abellán, A. et al., 2011. Rockfall monitoring by Terrestrial Laser Scanning – case study of the basaltic rock face at Castellfollit de la Roca (Catalonia, Spain). *Natural Hazards and Earth System Sciences*, 11(3), p. 829–841.

Aber, J. S., Marzolff, I., Ries, J. B. & Aber, S. E., 2019. *Small-Format Aerial Photography and UAS Imagery Principles, Techniques, and Geoscience Applications*. zweite Hrsg. Amsterdam, Oxford, Cambridge: Elsevier.

Agliardi, F. & Crosta, G. B., 2003. High resolution three-dimensional numerical modelling of rockfalls. *International Journal of Rock Mechanics and Mining Sciences,* 40(4), p. 455–471.

Altmann, M. et al., 2020. Long-Term Changes of Morphodynamics on Little Ice Age Lateral Moraines and the Resulting Sediment Transfer into Mountain Streams in the Upper Kauner Valley, Austria. *Water*, 12(12), p. 3375.

Altmann, M. et al., 2023. Quantitative Long-Term Monitoring (1890–2020) of Morphodynamic and Land-Cover Changes of a LIA Lateral Moraine Section. *Geosciences,* 13(4).

Azzoni, A. & de Freitas, M. H., 1995. Experimentally gained parameters, decisive for rock fall analysis. *Rock Mechanics and Rock Engineering*, Band 28, p. 111–124.

Bakker, M. & Stuart, N. L., 2017. Archival photogrammetric analysis of river–floodplain systems using Structure from Motion (SfM) methods. *Earth Surf. Process. Landforms*, 42(8), p. 1274–1286.

Baltsavias, E. P., 1999. A comparison between photogrammetry and laser scanning. *ISPRS Journal of Photogrammetry & Remote Sensing*, 54(2–3), p. 83–94.

Becht, M., 1995. *Untersuchungen zur aktuellen Reliefentwicklung in alpinen Einzugsgebieten*. München: Geobuch.

Benjamin, J., Rosser, N. J. & Brain, M. J., 2020. Emergent characteristics of rockfall inventories captured at a regional scale. 45(12), p. 2773–2787.

Bennett, G. L., Molnar, P. E. H. & McArdell, B. W., 2012. Erosional power in the Swiss Alps: Characterization of slope failure in the Illgraben. *Earth Surface Processes and Landforms*, 37(15), p. 1627–1640.

Betz, S., Croce, V. & Becht, M., 2019. Investigating morphodynamics on Little Ice Age lateral moraines in the Italian Alps using archival aerial photogrammetry and airborne LiDAR data. *Zeitschrift für Geomorphologie*, 62(3), p. 231–247.

Blanch, X. et al., 2024. A cost-effective image-based system for 3D geomorphic monitoring: An application to rockfalls. *Geomorphology,* Band 449.

Bonometti, F. N., Dattola, G., Frattini, P. & Crosta, G. B., 2025. Rockfall triggering and meteorological variables in the Dolomites (Italien Eastern Alps). *Natural Hazards and Earth System Sciences*.

Bosellini, A., Gianolla, P. & Stefani, M., 2003. Geology of the Dolomites. *Episodes,* 26(3), p. 181–185.

Bretar, F. et al., 2013. An advanced photogrammetric method to measure surface roughness: Application to volcanic terrains in the Piton de la Fournaise, Reunion Island. *Remote Sensing of Environment*, Band 135, p. 1–11.

Broili, L., 1974. Ein Felssturz im Großversuch. In: L. Müller-Salzburg, Hrsg. *Felsmechanische Grundlagenforschung Standsicherheit von Böschungen und Hohlraumbauten in Fels / Basic Research in Rock Mechanics Stability of Rock Slopes and Underground Excavations*. *Rock Mechanics / Felsmechanik / Mécanique des Roches*. Wien: Springer, p. 69–78.

Brunsden, D. & Prior, D. B., 1984. *Slope instability*. Chichester: John Wiley & Sons Ltd.

Burtin, A. et al., 2014. Seismic constraints on dynamic links between geomorphic processes and routing of sediment in a steep mountain catchment. *Earth Surface Dynamics,* 2(1), p. 21–33.

Calvari, S. et al., 2016. Monitoring crater-wall collapse at active volcanoes: a study of the 12 January 2013 event at Stromboli. *Bulletin of Volcanology,* 78(39).

Carrivick, J. L. et al., 2013. Contemporary geomorphological activity throughout the proglacial area of an alpine catchment. *Geomorphology*, Band 188, pp. 83-95.

Casagli, N. et al., 2017. Spaceborne, UAV and ground-based remote sensing techniques for landslide mapping, monitoring and early warning. *Geoenvironmental Disasters*, 4(9).

Cassol, M., 2008. [Online] Available at: https://static.provinz.bz.it/natur-raum/managementplaene/Managementplan%20Naturpark%20Drei%20Zinnen.pdf [Zugriff am 17 März 2024].

Caviezel, A. et al., 2019. Reconstruction of four-dimensional rockfall trajectories using remote sensing and rock-based accelerometers and gyroscopes. *Earth Surface Dynamics*, 7(1), p. 199–210.

Caviezel, A. et al., 2021. The relevance of rock shape over mass—implications for rockfall hazard assessments. *Nature Communications*, 12(5546).

Chevrel, M. O. et al., 2021. Lava flow hazard map of Piton de la Fournaise volcano. *Natural Hazards and Earth System Sciences*, 21(8), p. 2355–2377.

Chorley, R., Schumm, S. & Sugden, D., 1984. *Geomorphology*. London, New York: Routledge.

Cirillo, D. et al., 2024. Rockfall Analysis from UAV-Based Photogrammetry and 3D Models of a Cliff Area. *Drones,* 8(1).

Coltelli, M. et al., 2017. The Use of Surveillance Cameras for the Rapid Mapping of Lava Flows: An Application to Mount Etna Volcano. *Remote Sensing,* 9(3).

Copons, R., Vilaplana, M. & Linares, R., 2009. Rockfall travel distance analysis by using empirical models (Solà d'Andorra la Vella, Central Pyrenees). *Natural Hazards and Earth System Sciences,* 9(6), p. 2107–2118.

Corominas, J., Mavrouli, O. & Ruiz-Carulla, R., 2017. Rockfall Occurrence and Fragmentation. In: *Advancing Culture of Living with Landslides*. Cham: Springer, p. 75–97.

Crespi, A. et al., 2021. A high-resolution gridded dataset of daily temperature and precipitation records (1980–2018) for Trentino-South Tyrol (north-eastern Italian Alps). *Earth System Science Data,* 13(6), p. 2801–2818.

Crosta, G. B. & Agliardi, F., 2004. Parametric evaluation of 3D dispersion of rockfall trajectories. *Natural Hazards and Earth System Sciences*, 4(4), p. 583–598.

Crosta, G. B., Agliardi, F., Frattini, P. & Lari, S., 2015. Key Issues in Rock Fall Modeling, Hazard and Risk Assessment for Rockfall Protection. In: *Engineering Geology for Society and Territory - Volume 2*. Cham: Springer, p. 43–58.

Cruden, D. M. & Varnes, D. J., 1996. Landslide types and processes. In: *Landslide investigation and mitigation*. s.l.:National Research Council, Transportation Research Board, p. 36–75.

Cui, S.-h., Pei, X.-j. & Huang, R.-q., 2017. Rolling motion behavior of rockfall on gentle slope: an experimental approach. *Journal of Mountain Science*, Band 14, p. 1550–1562.

de Lima, S. R. et al., 2021. An Evaluation of the Effects of UAS Flight Parameters on Digital Aerial Photogrammetry Processing and Dense-Cloud Production Quality in a Scots Pine Forest. *Remote Sensing,* 13(6).

Derrien, A., Peltier, A., Villeneuve, N. & Staudacher, T., 2020. The 2007 caldera collapse at Piton de la Fournaise: new insights from multi-temporal structure-from-motion. *Volcanica*, 3(1), p. 55–65.

Derrien, A., Villeneuve, N., Peltier, A. & Michon, L., 2018. Multi-temporal airborne structure-from-motion on caldera rim: Hazard, visitor exposure and origins of instabilities at Piton de la Fournaise. *Progress in Physical Geographie: Earth and Environment,* 43(2), p. 193–214.

di Prisco, C. & Vecchiotti, M., 2006. A rheological model for the description of boulder impacts on granular strata. *Géotechnique*, 56(7), p. 469–482.

Dietze, M. et al., 2017. Seismic monitoring of small alpine rockfalls – validity, precision and limitations. *Earth Surface Dynamics*, 5(4), p. 653–668.

Dietze, M., Turowski, J. M., Cook, K. L. & Hovius, N., 2017. Spatiotemporal patterns, triggers and anatomies of seismically detected rockfalls. *Earth Surface Dynamics,* 5(4), p. 757–779.

Dikau, R., Brunsden, D., Schrott, L. & Ibsen, M.-L., 1996. *Landslide Recognition. Identification, Movement and Causes*. 5 Hrsg. Chichester: John Wiley and Sons.

Dikau, R. et al., 2019. *Geomorphologie*. Berlin: Springer Spektrum.

Dorren, L. K. A., 2003. A review of rockfall mechanics and modelling approaches. *Progress in Physical Geography: Earth and Environment*, 27(1), p. 69–87.

Dorren, L. K. A., Berger, F. & Putters, U. S., 2006. Real-size experiments and 3-D simulation of rockfall on forested and non-forested slopes. *Natural Hazards and Earth System Sciences*, 6(1), p. 145–153.

Draebing, D. & Krautblatter, M., 2019. The Efficacy of Frost Weathering Processes in Alpine Rockwalls. *Geophysical Research Letters,* 46(12), p. 6516–6524.

Draebing, D., Krautblatter, M. & Hoffmann, T., 2017. Thermo-cryogenic controls of fracture kinematics in permafrost rockwalls. *Geophysical Research Letters,* Band 44, p. 3535–3544.

Durand, V. et al., 2023. Repetitive small seismicity coupled with rainfall can trigger large slope instabilities on metastable volcanic edifices. *Communications Earth & Environment,* 4(383).

Durand, V. et al., 2018. On the Link Between External Forcings and Slope Instabilities in the Piton de la Fournaise Summit Crater, Reunion Island. *Journal of Geophysical Research: Earth Surface*, 123(10), p. 2422–2442.

EEA, 2009. *Regional climate change and adaptation. The Alps facing the challenge of changing water resources,* Copenhagen: European Environment Agency.

Einstein, A. & Infeld, L., 1938. *Evolution of Physics*. Cambridge: Cambridge University Press.

Eker, R., Aydın, A. & Hübl, J., 2017. Unmanned aerial vehicle (UAV)-based monitoring of a landslide: Gallenzerkogel landslide (Ybbs-Lower Austria) case study. *Environmental Monitoring and Assessment*, 190(28).

Eltner, A., Kaiser, A., Abellan, A. & Schindewolf, M., 2017. Time lapse structure-from-motion photogrammetry for continuous geomorphic monitoring. *Earth Surface Processes and Landforms*, 42(14), pp. 2240-2253.

Eltner, A. et al., 2016. Image-based surface reconstruction in geomorphometry – merits, limits and developments. *Earth Surface Dynamics*, 4(2), p. 359–389.

Erismann, T. H. & Abele, G., 2001. *Dynamics of Rockslides and Rockfalls*. 1 Hrsg. Berlin, Heidelberg: Springer.

Evans, S. G. & Hungr, O., 1993. The assessment of rockfall hazard at the base of talus slopes. *Canadian Geotechnical Journal*, 30(4), p. 620–636.

Falsaperla, S., Neri, M., Pecora, E. & Spampinato, S., 2006. Multidisciplinary study of flank instability phenomena at Stromboli volcano, Italy. *Geophysical Research Letters,* 33(9).

Fischer, L. et al., 2012. On the influence of topographic, geological and cryospheric factors on rock avalanches and rockfalls in high-mountain areas. *Natural Hazards and Earth System Sciences*, 12(1), p. 241–254.

Fityus, S. G., Giacomini, A. & Buzzi, O. P., 2013. The significance of geology for the morphology of potentially. *Engineering Geology*, Band 162, p. 43–52.

Flageollet, J. C. & Weber, D., 1996. Fall. In: *Landslide recognition: identitication, movement and causes*. Chichester: Wiley.

Fleischer, F. et al., 2023. Glaciogenic Periglacial Landform in the Making—Geomorphological Evolution of a Rockfall on a Small Glacier in the Horlachtal, Stubai Alps, Austria. *Remote Sensing,* 15(6).

Fleischer, F. et al., 2021. Multi-decadal (1953–2017) rock glacier kinematics analysed by high-resolution topographic data in the upper Kaunertal, Austria. *The Cryosphere*, 15(12), p. 5345–5369.

Flügel, E., 2010. *Microfacies of Carbonate Rocks. Analysis, Interpretation and Application*. 2. Hrsg. Berlin, Heidelberg: Springer.

Frattini, P., Crosta, G. B. & Agliardi, F., 2012. Rockfall characterization and modeling. In: C. U. Press, Hrsg. *Landslides Types, Mechanisms and Modeling*. Cambridge: Clague, John J.; Stead, Douglas, p. 267–281.

Frattini, P., Crosta, G., Carrara, A. & Agliardi, F., 2008. Assessment of rockfall susceptibility by integrating statistical and physically-based approaches. *Geomorphology,* 94(3–4), p. 419–437.

Fugazza, D. et al., 2018. Combination of UAV and terrestrial photogrammetry to assess rapid glacier evolution and map glacier hazards. *Natural Hazards and Earth System Sciences*, 18(4), p. 1055–1071.

Gailler, L. et al., 2022. Volcano-Magnetic Signal Reveals Rapid Evolution of the Inner Structure of Piton de la Fournaise. *Journal of Geophysical Research: Solid Earth*, 128(1).

Gallach, X. et al., 2020. Climatic and structural controls on Late-glacial and Holocene rockfall occurrence in high-elevated rock walls of the Mont Blanc massif (Western Alps). *Earth Surface Processes and Landforms*, 45(13), p. 3071–3091.

Gallo, I. et al., 2021. An Integration of UAV-Based Photogrammetry and 3D Modelling for Rockfall Hazard Assessment: The Cárcavos Case in 2018 (Spain). *Remote Sensing*, 13(17).

Garcin, M., Poisson, B. & Pouget, R., 2005. High rates of geomorphological processes in a tropical area: the Remparts River case study (Réunion Island, Indian Ocean). *Geomorphology,* 67(3–4), p. 335–350.

Geissler, J. et al., 2021. Analyzing glacier retreat and mass balances using aerial and UAV photogrammetry in the Ötztal Alps, Austria. *The Cryosphere*, 15(8), p. 3699–3717.

Geitner, C., 1999. *Sedimentologische und vegetationsgeschichtliche Untersuchungenan fluvialen Sedimenten in den Hochlagen des Horlachtales(Stubaier Alpen/Tirol) – Ein Beitrag zur zeitlichen Differenzierung der fluvialen Dynamik im Holozän*. München: Ludwig-Maximilians-Universität.

Gianolla, P., Morelli, C., Cucato, M. & Siorpaes, C., 2018. *Erläuterungen zur Geologischen Karte von Italien im Maßstab 1:50000 Blatt 016 Toblach,* Bozen: Autonome Provinz Bozen - Süditalien.

Glade, T. & Crozier, M. J., 2005. The Nature of Landslide Hazard Impact. In: *Landslide Hazard and Risk*. s.l.:John Wiley & Sons, Ltd, p. 41–74.

Glenn, N. F. et al., 2006. Analysis of LiDAR-derived topographic information for characterizing and differentiating landslide morphology and activity. *Geomorphology*, 73(1–2), p. 131–148.

Glover, J., Bartelt, P., Christen, M. & Gerber, W., 2015. Rockfall-Simulation with Irregular Rock Blocks. In: G. Lollino, et al. Hrsg. *Engineering Geology for Society and Territory*. Cham: Springer International Publishing, p. 1729–1733.

Goodbody, T. R., White, J. C., Coops, N. C. & LeBoeuf, A., 2021. Benchmarking acquisition parameters for digital aerial photogrammetric data for forest inventory applications: Impacts of image overlap and resolution. *Remote Sensing of Environment,* Band 265.

Gracchi, T. et al., 2022. UAV-Based Multitemporal Remote Sensing Surveys of Volcano Unstable Flanks: A Case Study from Stromboli. *Remote Sensing,* 14(10).

Gratchev, I. & Saeidi, S., 2019. The effect of surface irregularities on a falling rock motion. *Geomechanics and Geoengineering*, 14(1), p. 52–58.

Guerin, A. et al., 2020. The three-stage rock failure dynamics of the Drus (Mont Blanc massif, France) since the June 2005 large event. *Scientific Reports,* 10(17330).

Guerin, A. et al., 2020. Quantifying 40 years of rockfall activity in Yosemite Valley with historical Structure-from-Motion photogrammetry and terrestrial laser scanning. *Geomorphology*, Band 356.

Guzzetti, F., Reichenbach, P. & Wieczorek, G. F., 2003. Rockfall hazard and risk assessment in the Yosemite Valley, California, USA. *Natural Hazard and Earth System Sciences,* 3(6), p. 491–503.

Haas, F., Heckmann, T., Wichmann, V. & Becht, M., 2012. Runout analysis of a large rockfall in the Dolomites/Italian Alps using LIDAR derived particle sizes and shapes. *Earth Surface Processes and Landforms*, 37(13), p. 1444–1455.

Hanagan, C., La Femina, P. C. & Rodgers, M., 2020. Changes in Crater Morphology Associated With VolcanicActivity at Telica Volcano, Nicaragua. *Geochemistry, Geophysics, Geosystems,* 21(7).

Harvey, A. M., 2001. Coupling between hillslopes and channels in upland fluvial systems: implications for landscape sensitivity, illustrated from the Howgill Fells, northwest England. *Catena*, 42(2–4), p. 225–250.

Heckmann, T., Gegg, K., Gegg, A. & Becht, M., 2014. Sample size matters: investigating the effect of sample size on a logistic regression susceptibility model for debris flows. *Nat. Hazards Earth Syst. Sci.*, Band 14, p. 259–278.

Heckmann, T. & Schwanghart, W., 2013. Geomorphic coupling and sediment connectivity in an alpine catchment - Exploring sediment cascades using graph theory. *Geomorphology*, Band 182, pp. 89-103.

Heiser, M., Scheidl, C. & Kaitna, R., 2017. Evaluation concepts to compare observed and simulated deposition areas of mass movements. *Computational Geosciences*, Band 21, p. 335–343.

Hemmelder, S., Marra, W., Markies, H. & De Jong, S. M., 2018. Monitoring river morphology & bank erosion using UAV imagery – A case study of the river Buëch, Hautes-Alpes, France. *International Journal of Applied Earth Observation and Geoinformation*, Band 73, p. 428–437.

Hergarten, S. & Neugebauer, H. J., 1999. Self-organized criticality in landsliding processes. In: *Process Modelling and Landform Evolution*. *Lecture Notes in Earth Sciences*. Berlin, Heidelberg: Springer, p. 231–249.

Hibert, C. et al., 2014. Automated identification, location, and volume estimation of rockfalls at Piton de la Fournaise volcano. *Journal of Geophysical Research: Earth Surface*, 119(5), p. 1082–1105.

Hibert, C. et al., 2017. Spatio-temporal evolution of rockfall activity from 2007 to 2011 at the Piton de la Fournaise volcano inferred from seismic data. *Journal of Volcanology and Geothermal Research*, Band 333-334, p. 36–52.

Hollaus, M. et al., 2011. Roughness Mapping on Various Vertical Scales Based on Full-Waveform Airborne Laser Scanning Data. *Remote Sensing*, 3(3), p. 503–523.

Hungr, O. & Evans, S. G., 1988. Engineering evaluation of fragmental. *Proceedings of the 5th International Symposium on Landslides*, p. 685–690.

IPCC, 2021. *Climate Change 2021: The Physical Science Basis. Contribution of Working Group I to the Sixth Assessment Report of the Intergovernmental Panel on Climate Change,* Cambridge, United Kingdom and New York, NY, USA: Cambridge University Press.

Jaboyedoff, M. & Derron, M.-H., 2005. Hazard assessment within an Integrated Risk Assessment Process for Landslides (IRAPL). In: *Landslide Risk Management - Proceedings of the International Conference on Landslide Risk Management*. Vancouver: Taylor & Francis Group.

Jaboyedoff, M. & Labiouse, V., 2003. *Preliminary assessment of rockfall hazard based on GIS data*. s.l., s.n.

Jaboyedoff, M. & Labiouse, V., 2011. Technical Note: Preliminary estimation of rockfall runout zones. *Natural Hazards and Earth System Sciences*, 11(3), p. 819–828.

James, M. R., Robson, S. & Smith, M. W., 2017. 3-D uncertainty-based topographic change detection with structure-from-motion photogrammetry: precision maps for ground control and directly georeferenced surveys. *Earth Surface Processes and Landforms*, 42(12), pp. 1769-1788.

James, M. R. & Varley, N., 2012. Identification of structural controls in an active lava dome with high resolution DEMs: Volcán de Colima, Mexico. *Geophysical Research Letters*, 39(22).

Jaud, M. et al., 2019. UAV survey of a coastal cliff face – Selection of the best imaging angle. *Measurement*, Band 139, p. 10–20.

Ji, Z.-M.et al., 2019. Laboratory study on the influencing factors and their control for the coefficient of restitution during rockfall impacts. *Landslides*, Band 16, p. 1939–1963.

Jomelli, V. & Francou, B., 2000. Comparing the characteristics of rockfall talus and snow avalanche landforms in an Alpine environment using a new methodological approach: Massif des Ecrins, French Alps. *Geomorphology*, 35(3–4), p. 181–192.

Jones, A. F., Brewer, P. A., Johnstone, E. & Macklin, M. G., 2007. High-resolution interpretative geomorphological mapping of river valley environments using airborne LiDAR data. *Earth Surface Processes and Landforms*, 32(10), p. 1574–1592.

Kasperski, J. et al., 2010. Application of a Terrestrial Laser Scanner (TLS) to the Study of the Séchilienne Landslide (Isère, France). *Remote Sensing*, 2(12), p. 2785–2802.

Kenner, R., 2019. Mass wasting processes affecting the surface of an alpine talus slope: Annual sediment budgets 2009–2018 at Flüelapass, eastern Swiss Alps. *Land Degradtion & Development*, 31(4), p. 451–462.

Kirkby, M. J. a. S. I., 1975. Surface stone movement and scree formation. *The Journal of Geology*, 83(3), p. 349–362.

Kotlarski, S. et al., 2023. 21st Century alpine climate change. *Climate Dynamics,* Band 86, p. 65–86.

Krautblatter, M. & Dikau, R., 2007. Towards a uniform concept for the comparison and extrapolation of rockwall retreat and rockfall supply. *Geografiska Annaler: Series A, Physical Geography*, 89(1), p. 21–40.

Krautblatter, M., Funk, D. & Günzel, F. K., 2012. Why permafrost rocks become unstable: a rock–ice-mechanical model in time and space. *Earth Surface Processes and Landforms,* 38(8), p. 876–887.

Krautblatter, M. et al., 2012. Significance of rockfall magnitude and carbonate dissolution for rock slope erosion and geomorphic work on Alpine limestone cliffs (Reintal, German Alps). *Geomorphology,* Band 167–168, p. 21–34.

Kromer, R. et al., 2017. Managing rockfall risk through baseline monitoring of precursors using a terrestrial laser scanner. *Canadian Geotechnical Journal,* 54(7), p. 953–967.

Lambert, S., Bourrier, F. & Toe, D., 2013. Improving three-dimensional rockfall trajectory simulation codes for assessing the efficiency of protective embankments. *International Journal of Rock Mechanics & Mining Sciences*, Band 60, p. 26–36.

Laporte-Fauret, Q. et al., 2019. Low-Cost UAV for High-Resolution and Large-Scale Coastal Dune Change Monitoring Using Photogrammetry. *Journal of Marine Science and Engineering*, 7(3), p. 63.

Legay, A., Magnin, F. & Ravanel, L., 2021. Rock temperature prior to failure: Analysis of 209 rockfall events in the Mont Blanc massif (Western European Alps). *Permafrost and Periglacial Processes*, 32(3), p. 520–536.

Leine, R. et al., 2014. Simulation of rockfall trajectories with consideration of rock shape. *Multibody System Dynamics*, Band 32, p. 241–271.

Lénat, J.-F., Bachèlery, P. & Merle, O., 2012. Anatomy of Piton de la Fournaise volcano (La Réunion, Indian Ocean). *Bulletin of Volcanology*, Band 74, p. 1945–1961.

Lucieer, A., Jong, S. M. d. & Turner, D., 2014. Mapping landslide displacements using Structure from Motion (SfM) and image correlation of multi-temporal UAV photography. *Progress in Physical Geography: Earth and Environment*, 38(1), p. 97–116.

Luckman, B. H., 1976. Rockfalls and rockfall inventory data: Some observations from surprise valley, Jasper National Park, Canada. *Earth Surface Processes*, 1(3), p. 287–298.

Luckman, B. H., 2013. Processes, transport, deposition, and landforms: rockfall. *Treatise on Geomorphology*, Band 7, p. 174–182.

Luethi, R., Gruber, S. & Ravanel, L., 2015. Modelling transient ground surface temperatures of past rockfall events: towards a better understanding of failure mechanicsm in changing periglacial environments. *Geografiska Annaler: Series A, Physical Geography,* 97(4), p. 753–767.

Magnin, F. et al., 2017. Modelling rock wall permafrost degradation in the Mont Blanc massif from the LIA to the end of the 21st century. *The Cryosphere*, 11(4), p. 1813–1834.

Mancini, F. et al., 2013. Using Unmanned Aerial Vehicles (UAV) for High-Resolution Reconstruction of Topography: The Structure from Motion Approach on Coastal Environments. *Remote sensing*, 5(12), p. 6880–6898.

Marchi, L. et al., 2008. Rocky Headwaters in the Dolomites, Italy: Field Observations and Topographic Analysis. *Arctic, Antarctic, and Alpine Research,* 40(4), p. 685–694.

Markus, S. J., Wartman, J., Olsen, M. & Darrow, M. M., 2023. Lidar-Derived Rockfall Inventory—An Analysis of the Geomorphic Evolution of Rock Slopes and Modifying the Rockfall Activity Index (RAI). *Remote sensing*, 15(17), p. 4223.

Mastrantoni, G. et al., 2024. Automatic photomonitoring analysis for spatiotemporal evaluation of rockfall failure hazard. *Engineering Geology,* Band 339.

Matsuoka, N. & Murton, J., 2008. Frost weathering: recent advances and future directions. *Permafrost and Periglacial Processes,* 19(2), p. 195–210.

McGuire, B., 2010. Potential for a hazardous geospheric response to projected future climate changes. *Philosophical Transactions of the Royal Society A*, 368(1919), p. 2317–2345.

Meißl, G., 1998. *Modellierung der Reichweite von Felsstürzen, Fallbeispiele zur GIS-gestützten Gefahrenbeurteilung aus dem Bayerischen und Tiroler Alpenraum*. Innsbruck: Institut für Geographie, Universität Innsbruck.

Merle, O. et al., 2010. Calderas, landslides and paleo-canyons on Piton de la Fournaise volcano (La Réunion Island, Indian Ocean). *Journal of Volcanology and Geothermal Research*, 189(1–2), p. 131–142.

Messenzehl, K. & Dikau, R., 2017. Structural and thermal controls of rockfall frequency and magnitude within rockwall–talus systems (Swiss Alps). *Earth Surfaces Processes and Landforms*, 42(13), p. 1963–1981.

Messenzehl, K., Hoffmann, T. & Dikau, R., 2014. Sediment connectivity in the high-alpine valley of Val Müschauns, Swiss National Park — linking geomorphic field mapping with geomorphometric modelling. *Geomorphology*, Band 221, pp. 215-229.

Messenzehl, K. et al., 2018. Linking rock weathering, rockwall instability and rockfall supply on talus slopes in glaciated hanging valleys (Swiss Alps). *Permafrost and Periglacial Processes,* 29(3), p. 135–151.

Michon, L. et al., 2007. April 2007 collapse of Piton de la Fournaise: A new example of caldera formation. *Geographical Research Letters: Solid Earth*, 34(21).

Milenković, M., Pfeifer, N. & Glira, P., 2015. Applying Terrestrial Laser Scanning for Soil Surface Roughness Assessment. *Remote Sensing*, 7(2), p. 2007–2045.

Mourey, J. et al., 2021. Rockfall and vulnerability of mountaineers on the west face of the Aiguille du Goûter (classic route up Mont Blanc, France), an interdisciplinary study. *Natural Hazards and Earth System Sciences Discussions*.

Müller, J., Gärtner-Roer, I., Thee, P. & Ginzler, C., 2014. Accuracy assessment of airborne photogrammetrically derived high-resolution digital elevation models in a high mountain environment. *ISPRS Journal of Photogrammetry and Remote Sensing*, Band 98, pp. 58-69.

Neugirg, F. et al., 2016. Erosion processes in calanchi in the Upper Orcia Valley, Southern Tuscany, Italy based on multitemporal high-resolution terrestrial LiDAR and UAV surveys. *Geomorphology*, Band 269, pp. 8-22.

Niethammer, U. et al., 2012. UAV-based remote sensing of the Super-Sauze landslide: Evaluation and results. *Engineering Geology*, Issue 128, p. 2–11.

Okura, Y., Kitahara, H., Sammori, T. & Kawanami, A., 2000. The effects of rockfall volume on runout distance. *Engineering Geology*, 58(2), p. 109–124.

OVPF & IPGP, 2008. *Seismic, tiltmeter, extensometer, magnetic and weather permanent networks on Piton de la Fournaise volcano and La Réunion*. [Online] Available at: http://volobsis.ipgp.fr/networks/detail/PF/ [Zugriff am 13 April 2025].

Paranunzio, R. et al., 2016. Climate anomalies associated with occurence of rockfalls at high-elevation in the Italian Alps. *Natural Hazards and Earth System Sciences*, 16(9), p. 2085–2106.

Peltier, A., Bachèlery, P. & Staudacher, T., 2009. Magma transport and storage at Piton de La Fournaise (La Réunion) between 1972 and 2007: A review of geophysical and geochemical data. *Journal of Volcanology and Geothermal Research*, 184(1–2), p. 93–108.

Peltier, A. et al., 2018. Changes in the Long-Term Geophysical Eruptive Precursors at Piton de la Fournaise: Implications for the Response Management. *Frontiers in Earth Science*, Band 6.

Pesci, A. et al., 2011. Multitemporal laser scanner-based observation of the Mt. Vesuvius crater: Characterization of overall geometry and recognition of landslide events. *ISPRS Journal of Photogrammetry and Remote Sensing,* 66(3), p. 327–336.

Pfeiffer, T. J. & Bowen, T. D., 1989. Computer simulations of rockfalls. *Environmental & Engineering Geoscience*, Band 26, p. 135–146.

Pichler, B., Hellmich, C. & Mang, H., 2005. Impact of rocks onto gravel Design and evaluation of experiments. *International Journal of Impact Engineering*, 31(5), p. 559–578.

Ponti, S., Girola, I. & Guglielmin, M., 2024. Thermal photogrammetry on a permafrost rock wall for the active layer monitoring. *Science of The Total Environment,* Band 917.

Popescu, R. et al., 2017. Low-altitude permafrost research in an overcooled talus slope–rock glacier system in the Romanian Carpathians (Detunata Goală, Apuseni Mountains). *Geomorphology*, Band 295, p. 840–854.

Rahman, Z., Slob, S. & Hack, R., 2006. *Deriving roughness characteristics of rock mass discontinuities from.* Nottingham, Geological Society of London.

Rapp, A., 1960. Recent development of mountain slopes in Kärkevagge and surroundings, northern Scandinavia. *Geografiska Annaler*, 42(2–3), p. 65–200.

Ravanel, L. & Deline, P., 2008. The West Face of Les Drus (Mont-Blanc massif): slope instability in a high-Alpine steep rock wall since the end of the Little Ice Age. *Géomorphologie: Relief, Processus. Environnement*, 4(17330), p. 261–272.

Ravanel, L. & Deline, P., 2010. Climate influence on rockfalls in high-Alpine steep rockwalls: The north side of the Aiguilles de Chamonix (Mont Blanc massif) since the end of the 'Little Ice Age'. *The Holocene*, 21(2), p. 357–365.

Ravanel, L. & Deline, P., 2015. Rockfall Hazard in the Mont Blanc Massif Increased by the Current Atmospheric Warming. In: G. Lollino, et al. Hrsg. *Engineering Geology for Society and Territory - Volume 1 Climate Change and Engineering Geology*. Cham: Springer, p. 425–428.

Riegl, L. M. S. G., 2010. *LMS-Z420I,* Horn: s.n.

Riegl, L. M. S. G., 2020. *Riegl VZ-4000,* Horn: s.n.

Ritchie, A. M., 1963. Evaluation of Rockfall and Its Control. *Highway Research Board*, Band 17, p. 13–28.

Rom, J. et al., 2023. Spatio-temporal analysis of slope-type debris flow activity in Horlachtal, Austria, based on orthophotos and lidar data since 1947. *Natural Hazards and Earth System Sciences,* 23(2), p. 601–622.

Roult, G. et al., 2012. A new comprehensive classification of the Piton de la Fournaise activity spanning the 1985–2010 period. Search and analysis of short-term precursors from a broad-band seismological station. *Journal of Volcanology and Geothermal Research*, Band 241–242, p. 78–104.

Royán, M. J., Abellán, A. & Vilaplana, J. M., 2015. Progressive failure leading to the 3 December 2013 rockfall at Puigcercós scarp (Catalonia, Spain). *Landslides,* Band 12, p. 585–595.

Ruiz-Carulla, R. & Jordi, C., 2020. Analysis of Rockfalls by Means of a Fractal Fragmentation Model. *Rock Mechanics and Rock Engineering,* Band 53, p. 1433–1455.

Sala, Z., Hutchinson, D. J. & Harrap, R., 2019. Simulation of fragmental rockfalls detected using terrestrial laser scans from rock slopes in south-central British Columbia, Canada. *Natural Hazards and Earth System Sciences*, 19(11), p. 2385–2404.

Salvini, R. et al., 2013. Photogrammetry and laser scanning for analyzing slope stability and rock fall runout along the Domodossola–Iselle railway, the Italian Alps. *Geomorphology*, Issue 185, p. 110–122.

Sandeep, C. S., Luo, L. & Senetakis, K., 2020. Effect of Grain Size and Surface Roughness on the Normal Coefficient of Restitution of Single Grains. *Materials*, 13(4), p. 814.

Sanders, D., Ostermann, M. & Kramers, J., 2009. Quaternary carbonate-rocky talus slope successions (Eastern Alps, Austria): sedimentary facies and facies architecture. *Facies*, Band 55, p. 345–373.

Schellenberg, K., Volkwein, A., Denk, M. & Vogel, T., 2008. *Falling weight tests on rock fall galleries with cushion layers*. Morschach, Schweiz, Volkwein, Axel; Labiouse, Vincent; Schellenberg, Kristian, p. 23–25.

Sens-Schönfelder, C., Pomponi, E. & Peltier, A., 2014. Dynamics of Piton de la Fournaise volcano observed by passive image interferometry with multiple references. *Journal of Volcanology and Geothermal Research*, Band 276, p. 32–45.

Smith, M. W., Carrivick, J. L. & Quincey, D. J., 2016. Structure from motion photogrammetry in physical geography. *Progress in Physical Geography*, 40(2), p. 247–275.

Smith, M. W. & Vericat, D., 2015. From experimental plots to experimental landscapes: topography, erosion and deposition in sub-humid badlands from Structure-from-Motion photogrammetry. *Earth Surface Processes and Lanforms*, 40(12), pp. 1656-1671.

Snavely, N., Seitz, S. M. & Szeliski, R., 2008. Modeling the world from internet photo collections. *International Journal of Computer Vision*, Band 80, pp. 189-210.

Soldati, M., Corsini, A. & Pasuto, A., 2004. Landslides and climate change in the Italian Dolomites since the Late glacial. *CATENA,* 55(2), p. 141–161.

Stark, M. et al., 2022. Long-term assessment of terrain changes and calculation of erosion rates in an alpine catchment based on SfM-MVS processing of historical aerial images. How camera information and processing strategy affect quantitative analysis. *Journal of Geomorphology*, 1(1), p. 43–77.

Statham, I., 1973. Scree Slope Development under Conditions of Surface Particle Movement. *Transactions of the Institute of British Geographers,* Band 59, p. 41–53.

Staudacher, T. et al., 2016. Fifteen Years of Intense Eruptive Activity (1998–2013) at Piton de la Fournaise Volcano: A Review. In: C. Cimarelli & S. Müller, Hrsg. *Active Volcanoes of the Southwest Indian Ocean Piton de la Fournaise and Karthala*. Berlin, Heidelberg: Springer-Verlag GmbH, p. 139–170.

Stock, G. M., Martel, S. J., Collins, B. D. & Harp, E. L., 2012. Progressive failure of sheeted rock slopes: the 2009–2010 Rhombus Wall rock falls in Yosemite Valley, California, USA. *Earth Surface Processes and Landforms,* 37(5), p. 546–561.

Stoffel, M. et al., 2024. Rockfall from an increasingly unstable mountain slope driven by climate warming. *Nature Geoscience,* Band 17, p. 249–254.

Strunden, J., Ehlers, T. A., Brehm, D. & Nettesheim, M., 2015. Spatial and temporal variations in rockfall determined from TLS measurements in a deglaciated valley, Switzerland. *Journal of Geophysical Research: Earth Surface*, 120(7), p. 1251–1273.

Stumpf, A. et al., 2015. Ground-based multi-view photogrammetry for the monitoring of landslide deformation and erosion. *Geomorphology*, Band 231, pp. 130-145.

Terzaghi, K., 1962. Stability of Steep Slopes on Hard Unweathered Rock. *Géotechnique*, 12(4), p. 285–318.

Torres-Sánchez, J., López-Granados, F., Borra-Serrano, I. & Peña, J. M., 2017. Assessing UAV-collected image overlap influence on computation time and digital surface model accuracy in olive orchards. *Precision Agriculture,* Band 19, p. 115–133.

Toschek, P. H., 2012. Sedimentological Investigation of the Ladinian “Wettersteinkalk” of the “Kaiser Gebirge” (Austria). In: *Recent Developments in Carbonate Sedimentology in Central Europe*. Berlin, Heidelberg: Springer, p. 219–227.

Tucker, G. E., 2012. *Hillslope, river, and Mountain: some surprises in Landscape evolution (Ralph Alger Bagnold Medal Lecture)*. Vienna, s.n.

Urai, M., Geshi, N. & Staudacher, T., 2007. Size and volume evaluation of the caldera collapse on Piton de la Fournaise volcano during the April 2007 eruption using ASTER stereo imagery. *Geophysical Research Letters: Solid Earth*, 34(22).

Vanneschi, C. et al., 2019. SfM-MVS Photogrammetry for Rockfall Analysis and Hazard Assessment Along the Ancient Roman Via Flaminia Road at the Furlo Gorge (Italy). *ISPRS International Journal of Geo-Information*, 8(8).

Viani, C. et al., 2020. An integrated approach to investigate climate-driven rockfall occurrence in high alpine slopes: the Bessanese glacial basin, Western Italian Alps. *Journal of Mountain Science*, Band 17, p. 2591–2610.

Vilajosana, I. et al., 2008. Rockfall induced seismic signals: case study in Montserrat, Catalonia. *Natural Hazards and Earth System Sciences*, 8(4), p. 805–812.

Vivero, S. & Lambiel, C., 2019. Monitoring the crisis of a rock glacier with repeated UAV surveys. *Geographica Helvetica*, 74(1), p. 59–69.

Volkwein, A. et al., 2011. Rockfall characterisation and structural protection – a review. *Natural Hazards and Earth System Sciences*, 11(9), p. 2617–2651.

Walter, M., Arnhardt, C. & Joswig, M., 2012. Seismic monitoring of rockfalls, slide quakes, and fissure development at the Super-Sauze mudslide, French Alps. *Engineering Geology*, Band 128, p. 12–22.

Wang, Y. et al., 2018. Effects of the impact angle on the coefficient of restitution in rockfall analysis based on a medium-scale laboratory test. *Natural Hazards and Earth System Sciences*, 18(11), p. 3045–3061.

Wegner, K. et al., 2021. Assessing the effect of lithological setting, block characteristics and slope topography on the runout length of rockfalls in the Alps and on the island of La Réunion. *Natural Hazards and Earth System Sciences*, 21(3), p. 1159–1177.

Wegner, K., Stark, M., Haas, F. & Becht, M., 2023. Suitability of terrestrial archival imagery for SfM-MVS based surface reconstruction of steep rock walls for the detection of rockfalls. *Journal of Geomorphology*.

Westoby, M. J. et al., 2012. 'Structure-from-Motion' photogrammetry: A low-cost, effective tool for geoscience applications. *Geomorphology*, Band 179, pp. 300-314.

Whalley, W. B., 1974. The mechanics of high-magnitude low-frequency rock failure and its importance in mountainous areas. *Reading Geographical Papers*, Band 27.

Whitehouse, I. E. & McSaveney, M., 1983. Diachronous Talus Surfaces in the Southern Alps, New Zealand, and Their Implications to Talus Accumulation. *Arctic and Alpine Research*, 15(1), p. 53–64.

Williams, J. G., Rosser, N. J., Hardy, R. J. & Brain, M. J., 2019. The Importance of Monitoring Interval for Rockfall Magnitude-Frequency Estimation. *JGR Earth Surface,* 124(12), p. 2841–2853.

Wyllie, D. C. & Mah, C. W., 2004. *Rock slope engineering: civil and mining*. 4 Hrsg. London, New York: Spon Press.